Institut de physique
Université de Neuchâtel

Magneto-spectroscopy and development of terahertz quantum cascade lasers

THESE

présentée à la Faculté des Sciences de l'Université de Neuchâtel
pour l'obtention du grade de
Docteur ès Sciences

par

Giacomo Scalari
diploma di Laurea in Fisica
Universitá di Pisa

In presence of a jury composed by

Prof. Jérôme Faist, thesis advisor, Université de Neuchâtel

Prof. Daniel Hofstetter, Université de Neuchâtel

Prof. Piero Martinoli, Université de Neuchâtel

Prof. Carlo Sirtori, Université Paris 7 - Denis Diderot

Prof. Karl Unterrainer, Technical University of Vienna

Neuchâtel, Décembre 2005

Université de Neuchâtel

IMPRIMATUR POUR LA THESE

Magneto-Spectroscopy and Development of Terahertz Quantum Cascade Lasers

Giacomo SCALARI

UNIVERSITE DE NEUCHATEL

FACULTE DES SCIENCES

La Faculté des sciences de l'Université de Neuchâtel,
sur le rapport des membres du jury

MM. J. Faist (directeur de thèse),
P. Martinoli, D. Hofstetter,
C. Sirtori (Paris)
et K. Unterrainer (Vienne)

autorise l'impression de la présente thèse.

Neuchâtel, le 27 février 2006

Le doyen :

J.-P. Derendinger

Faculté des Sciences
■ Rue Emile-Argand 11 ■ CP 158 ■ CH-2009 Neuchâtel
■ Téléphone : +41 32 718 21 00 ■ Fax : +41 32 718 21 03 ■ E-mail : secretariat.sciences@unine.ch ■ www.unine.ch

this work is dedicated to the memory of Harald Willenberg

Keywords: ***laser, intersubband, Terahertz, quantum cascade, magnetic field***

Mots clés: ***laser, intersousbande, Terahertz, cascade quantique, champ magnétique***

Abstract

In this work we concentrate our efforts on the generation of laser emission at low THz frequencies (3-1 THz range) employing the quantum cascade technology. Quantum cascade (QC) lasers are unipolar semiconductor lasers based on intersubband transitions in quantum wells that cover a large portion of the Mid and Far Infrared electromagnetic spectrum. Two main research lines have been followed: (i) the development of quantum cascade lasers based on population inversion between parabolic subbands and (ii) the development of low frequency QC lasers based on a three-dimensional electron confinement induced by an external magnetic field.

(i) Gain and laser action have been demonstrated in different systems at frequencies of 3.4-3.6 THz exploiting bound-to-bound and bound-to-continuum optical transition. A QC laser emitting at 3.6 THz and based on a vertical transition and resonant tunneling in a single quantum well has been demonstrated. To overcome the limitations in performance of such a system, an heterostructure laser based on a bound-to-continuum transition has been developed. The structure was the first one to operate above the technologically important temperature of liquid nitrogen. With a further development of the bound-to-continuum design that includes lower state lifetime reduction by optical phonon emission, laser action was successfully achieved at 115 K. A study of different waveguide mechanisms suitable for different THz frequencies has also been carried out.

(ii) THz quantum cascade lasers based on the in-plane confinement introduced by a strong magnetic field applied perpendiculary to the plane of the layers have been developed. A model system based on large single quantum wells (50-60 nm wide) has been exploited

to study this gain mechanism. Such an approach led to the extension of the frequency range of operation of QC lasers, with the demonstration of laser action at 1.39 THz (220 μm) which is the lowest frequency observed to-date for this kind of technology. The size confinement induced by the magnetic field radically modifies the physics of the system allowing laser action with extremely reduced threshold current densities (0.65 A/cm^2), a factor of 70 lower than any other quantum cascade laser and among the lowest ever observed for a semiconductor laser in general. Electron wavefunction localization is at the basis of the observed effects. Resonances in transport and in laser emission characteristics have been observed and attributed to many-body phenomena. The magnetic field has been used also as a spectroscopic tool to investigate the structures developed in the research line (i). Multi-frequency operation obtained by selectively injecting carriers in the excited states of a single quantum well structure has also been demonstrated.

Riassunto

Questo lavoro di tesi tratta della generazione di emissione laser a basse frequenze nella regione del terahertz (3-1 THz) impiegando la tecnologia della cascata quantica. I laser a cascata quantica sono laser a semiconduttore unipolari basati sulle transizioni intersottobanda in pozzi quantici, e coprono una vasta porzione del medio e lontano infrarosso. Due linee di ricerca principali sono state sviluppate: (i) lo sviluppo di laser a cascata quantica basati su un'inversione di popolazione tra sottobande a dispersione parabolica e (ii) lo sviluppo di laser a cascata quantica a basse frequenze THz basati sul confinamento tridimensionale dell'elettrone indotto da un campo magnetico esterno.

(i) Impiegando transizioni ottiche discreto-a-discreto e discreto-a-continuo sono stati dimostrati guadagno e emissione laser in differenti sistemi alle frequenze di 3.4-3.6 THz. L'azione laser è stata dimostrata in un dispositivo a cascata quantica basato su una transizione ottica verticale e su tunneling risonante in un singolo pozzo quantico alla frequenza di 3.6 THz. Per superare le limitazioni di detta struttura, è stato sviluppato un sistema basato su una transizione ottica discreto-a-continuo. La struttura è stata la prima ad operare ad una temperatura superiore a quella tecnologicamente importante costituita dall'ebollizione dell'azoto liquido. Un ulteriore sviluppo del sistema a cascata quantica basato sulla transizione discreto-a-continuo che include la riduzione del tempo di vita dello stato inferiore della transizione laser ha operato fino alla temperatura di 115 K. Contestualmente è stato condotto uno studio di differenti configurazioni per la guida d'onda alle differenti frequenze THz investigate.

(ii) L'utilizzo di intensi campi magnetici applicati perpendicolarmente al piano degli strati

dell'eterostruttura ha permesso di sviluppare laser CQ con un confinamento tridimensionale dell'elettrone. Lo studio di questo meccanismo di guadagno è stato condotto su un sistema modello costituito da un grande pozzo quantico (50-60 nm di spessore). Questo approccio ha permesso l'estensione della gamma di frequenze generate dai laser a cascata quantica fino a 1.39 THz, corrispondente a una lughezza d'onda di 220 μm circa: questa frequenza è la piú bassa mai raggiunta con questo tipo di tecnologia. Il confinamento dimensionale introdotto dal campo magnetico modifica drasticamente la fisica del sistema consentendo l'azione laser con valori estremamente ridotti della corrente di soglia (0.65 A/cm^2), inferiori di un fattore 70 in rapporto a quelli degli altri laser a cascata quantica e tra i piú bassi mai osservati in un laser a semiconduttore. La localizzazione della funzione d'onda dell'elettrone è alla base degli effetti osservati. Le risonanze osservate nel trasporto e nell'intensitá laser sono state attribuite a fenomeni elastici e a molti corpi. Il campo magnetico è stato anche utilizzato come strumento spettroscopico per l'analisi dei dispositivi sviluppati al punto (i). É stato inoltre possibile realizzare un laser operante su due distinte frequenze iniettando selettivamente gli elettroni negli stati eccitati di un singolo pozzo quantico.

Contents

List of Figures

List of Tables

Chapter 1

Introduction

1.1 Motivation

The region of the electromagnetic spectrum from 0.3 to 20 THz (10 - 600 cm^{-1}, 1 mm - 15 μm wavelength, Fig. 1.1) is a frontier area for research in physics, chemistry, biology, materials science and medicine. Many of the phenomena related to the mentioned domains have their typical energies and/or frequencies lying in the THz region [1]. Most of the interstellar dust clouds emit in the THz region, electrons in highly-excited atomic Rydberg states orbit at THz frequencies, small molecules rotate at THz frequencies, electrons in semiconductors and their nanostructures resonate at THz frequencies. Superconducting energy gaps are found at THz frequencies. An electron in Intel's THz Transistor races under the gate in ∼1 ps. Gaseous and solid-state plasmas oscillate at THz frequencies. Matter at temperatures above 10 K emits black-body radiation at THz frequencies.

All those examples and many others call for an adequate scientific and technological effort. Electromagnetic radiation is the most widespread mean to interact with all those systems, and subsequently grows the need for sources and detectors in this region of the spectrum. The nature of this region, that acts really as a boundary between optics and electronics, has determined a sort of underdevelopment of the key elements for the scientific investigation, often being referred as the THz "gap". There is thus a solid interest in trying to develop reliable, low-cost and flexible sources of THz radiation. In the following section a brief overview of the principal applications of THz radiation is presented.

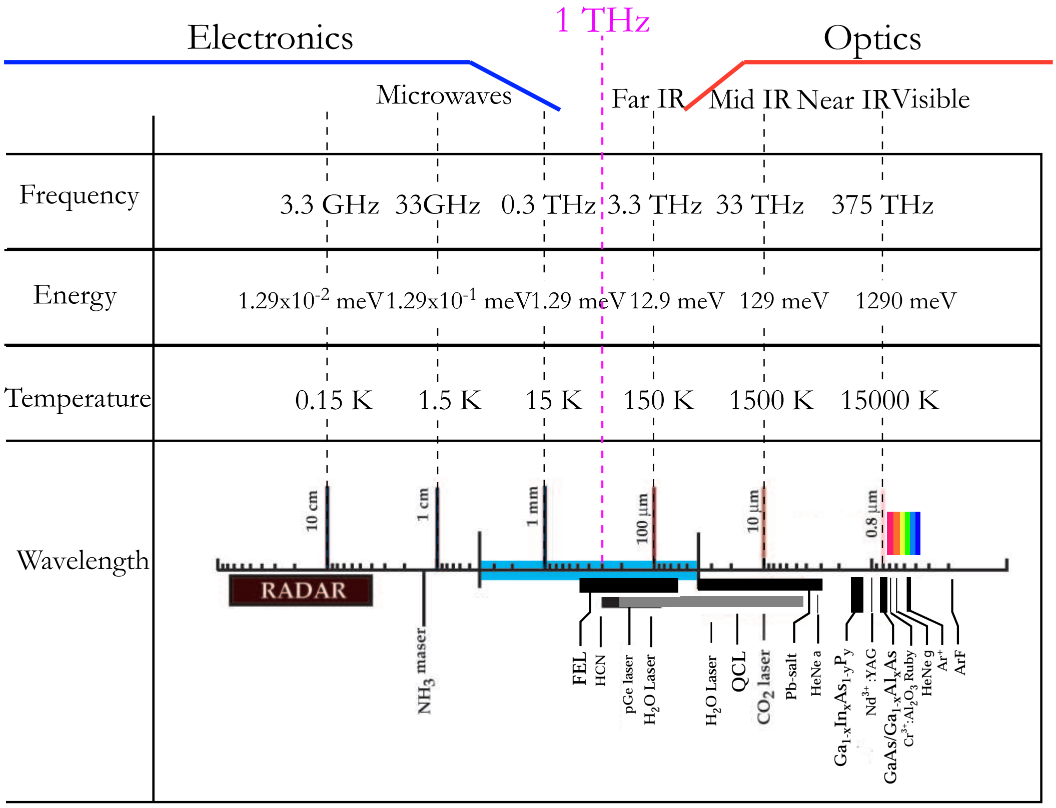

Figure 1.1: Comparative table with electromagnetic spectrum expressed in wavelength, temperature, energy and frequency with principal coherent sources reported on the bottom. The THz region lies clearly inside the gap between optics and electronics.

1.2 Terahertz radiation and its applications

1.2.1 Astronomy

Spectroscopy has been the principal field of application of THz radiation since many molecular species have their absorption lines falling in this region. In particular astronomy would benefit from the presence of compact and reliable THz sources of coherent radiation. It is sufficient to take a look at the spectral signature of an interstellar cloud (see Fig. 1.2) to understand the central importance of the development of terahertz technologies for the astronomy [2]: approximately 98% of the photons emitted since the Big Bang fall in the sub-mm and Far-ir region of the EM spectrum. Many molecules like water, oxygen, carbon monoxide, nitrogen can be probed in the THz range. Individual emission lines, such as the C^+ line at 158 μm-1.9 THz (the brightest line in the Milky way sub-mm spectral range, which is the emission wavelength of a laser developed in this work, greatly discussed in Chapter 6) can provide a detailed look at star forming regions where surrounding dust is illuminated by hot young ultraviolet emitting stars.

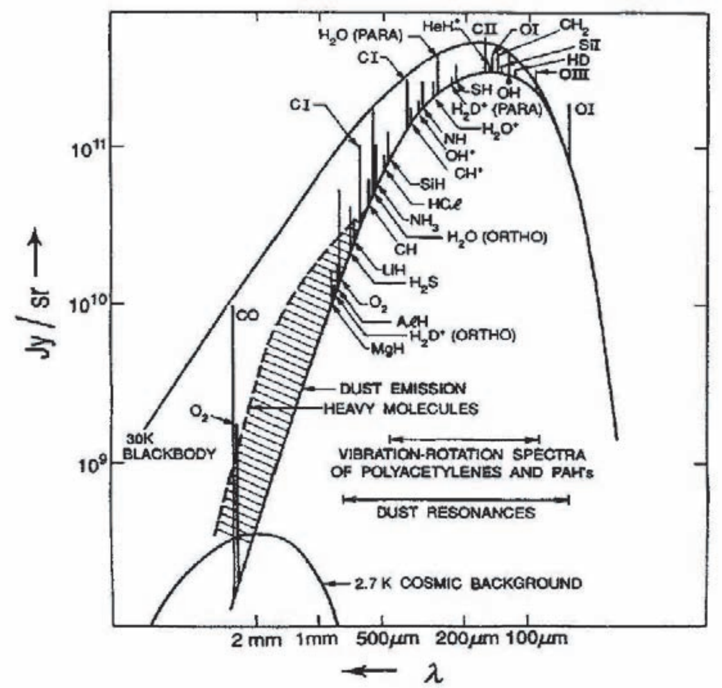

Figure 1.2: Radiated energy versus wavelength showing 30-K blackbody, typical interstellar dust, and key molecular line emissions in the submillimeter wavelength range (reprinted from [2]).

Since these signals are obscured from most Earth-based observations (except from a very few high-altitude observatories, aircraft, or balloon platforms), they provide strong motivation for a number of existing or upcoming space astrophysics instruments. Most notably, the Submillimeter Wave Astronomy Satellite (SWAS) has been launched in December 1998, and is currently sending back data on water, oxygen, neutral carbon, and carbon monoxide in interstellar space; and in the near future, the European Space Agencys (ESA) Herschel scheduled for 2007 and NASAs proposed Submillimeter Probe of the Evolution of Cosmic Structure (SPECS), SPace InfraRed Interferometric Telescope (SPIRIT), and Filled Aperture InfraRed telescope (FAIR), which will examine this spectral region in great detail in the decade beyond 2010. For interstellar and intragalactic observations, both high resolving power (large apertures) and high bandwidth resolution (1100 MHz) are generally required. In the lower terahertz bands, heterodyne detectors are generally preferred, and consequently need stable and reasonably powerful local oscillator sources, that are quite scarce in this portion of the spectrum. There are several major ground- and space-based submillimeter/THz telescopes which have recently been completed or will go on line in the near future. Surprisingly, many of these systems will investigate spectral regions for which very incomplete spectral information is available and laboratory experiments are needed in order to understand the origin / identify the carriers of the spectral features. Additionally, large molecules such as (large) poly-aromatic hydrocarbons are probably abundant in interstellar space and believed to be responsible for many of the features.

1.2.2 Terahertz Imaging

The potential for imaging applications using Terahertz radiation [3] results from a number of characteristics. Terahertz waves penetrate most dry, nonmetallic and nonpolar objects like plastics, paper, cardboard and nonpolar organic substances. In the case of dielectrics, the absorption is governed by optical phonons and depends on the polarity and the optical phonon resonances of the material. On the other hand, metals are completely opaque to THz, and polar liquids such as water strongly absorb in this frequency region. In the gas phase, most polar molecules have very sharp and strong absorption lines in this frequency range, which reflect the unique rotational or roto-vibrational spectra of the absorbing species. One very attractive aspect of THz imaging is its intrinsic safety due to the employment of very low energy photons (non-ionizing radiation). The simplest type of image one can generate in a transmission imaging setup is one in which the transmitted power determines the nature of the image.

A good example of this is shown in Fig.1.3, which shows a terahertz imaging setup together with a transmission image of a leaf from a common houseplant [4]. The color scale is determined by the amplitude of the transmitted terahertz power, which in turn is related to the amount of moisture present at each point on the leaf. This image illustrates the extreme sensitivity of this technique to water content: in this frequency range, water absorbs quite strongly (230 cm^{-1} at 1 THz). The setup and the image come from Agilent Labs, Palo Alto, CA, that use some of the lasers developed in this thesis work (bound-to-continuum design, see Chapter 5) to perform imaging on various kind of materials.
Using terahertz imaging, it is possible to account for inhomogeneities in the sample by performing a spatially resolved measurement. Because these measurements are inherently nondestructive, repeated measurements may be made on the same sample.

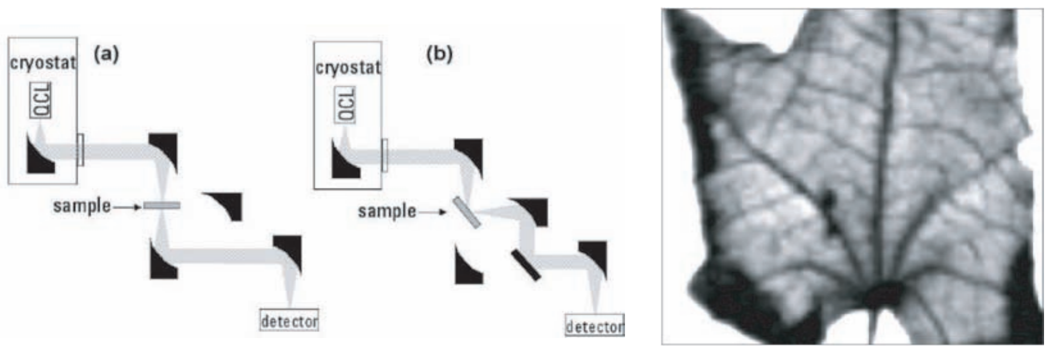

Figure 1.3: Left: Experimental setup for THz imaging employing a quantum cascade laser as a source: (a) transmission configuration, (b) reflection configuration. Right: THz image of a leaf from an abutilon plant. Absorption from water in the veins of the leaf is clearly observed (reprinted from [4]).

Spatially resolved measurements of the terahertz transmission coefficient may also be used in package inspection or quality control applications. Evidently, since many packaging materials such as plastic and cardboard are transparent to terahertz radiation, it is quite simple to image through these materials and detect the contents. In many industries, X-ray imaging is currently used for such tasks. THz imaging may be a desirable alternative simply because of the health and safety issues involved with ionizing radiation. The extreme sensitivity to water content proves important in these types of applications as well. Although numerous methods exist for measuring the water content of moisture-sensitive products, essentially no method exists if the measurement must be performed through a cardboard or thin plastic package.

THz wavelengths can provide information at depths of 1-2 cm in bio-tissue depending on water content. The contrast mechanisms that enable image generation are not well understood. Different wavelengths and pulse structures appear to provide unique information about biological systems. The contrast mechanisms are related to water content, but influence in the local environment, (bound vs. free water, lipid vs. protein) clearly affect the signal. Considerable progress in THz technology now allows access to the technology for image generation and several companies (TeraView Ltd, Picometrix) are selling THz systems.

Identification of unique biologic signatures of disease may be possible leading to improved techniques for cancer screening and surveillance. While the feasibility of imaging has been demonstrated, selection of optimal parameters for imaging has not been achieved. To obtain optimal THz images substantial advances in sources, pulse sequences, imaging algorithms, detectors, and an understanding of contrast mechanisms are essential.

1.2.3 Fundamental physics

The energy scales of several, large interest physical phenomena lie in the sub-mm and THz regions: the electronic transitions in systems that are quantum confined to two, one and zero dimensions have excitations in the THz regime. Well defined collective and single particle excitations emerge as the THz frequency exceeds various relaxation rates and broadening: the response at THz frequencies is dynamic rather than diffusive or relaxed. Fundamental issues include reliable control of carrier injection by doping, electric fields or optical pumping, the relationship between geometry and energy level structure, linewidths of transitions between states, excited state coherence and population lifetimes, superposition states of carriers, and spin excitations. Coherent quantum control of the orbital and spin states (see Appendix A) of carriers in semiconductor nanostructures is particularly attractive at THz frequencies.

The properties of semiconductor nanostructures at visible and near-IR wavelengths can also be controlled with THz-frequency electromagnetic radiation.

1.3 Terahertz sources

Here we propose a rapid overview of the principal sources of THz radiation, classified in reason of their bandwidth. We will not report on accelerator-like sources of THz radiation like the Free-Electron-Laser (FEL) because due to its complexity and dimensions it is out of the technological target of our research, although recently a table-top version of an undulator for producing terahertz radiation has been proposed and discussed [5].

1.3.1 Broadband Terahertz sources

Microwave generation followed by frequency multiplication

High-order harmonics of a microwave oscillator can be generated at frequencies in the THz range: starting at W-band (100 GHz) or below, or alternatively at the highest frequency where mW direct oscillation is available, the oscillator is followed by a power amplifier and a nonlinear solid-state frequency multiplier (typically a Schottky barrier diode or diode array). Current capabilities allow tunable power generation at the 5-10% bandwidth range from 200 GHz to approximately 1600 GHz with power levels from 30 mW (low end) to 1 μW at the highest frequencies. The technique involves significant power at the pump frequency and efficiencies are typically below 1 percent for multiple stages. The sources of power at low frequency, like GUNN diodes or IMPATT, exhibit a decrease of output power that follows a square root dependence with the frequency. This limits the amount of power available at the end of the multiplication chain. However the frequency multiplication technique has been around for as long as microwave spectroscopy (more than 60 years) and is very powerful. With continuing development in pushing oscillator frequencies up into the submillimeter range, or power combining at the pump end, it is possible to generate a few microwatts of tunable cw power up to 2 THz [6].

Recently, another way of generating sub-THz and THz radiation has been demonstrated by

Knap and co-workers [7] by means of resonant, voltage tunable emission from a gated two-dimensional electron gas in a 60 nm InGaAs high electron mobility transistor. The emission is interpreted as resulting from a current driven plasma instability leading to oscillations in the transistor channel (Dyakonov-Shur instability).

Backward wave oscillators

Backward wave oscillators (BWO), (and other tube sources like carcinotrons and klystrons) have been around for more than half a century but are currently only produced in one small remaining arm of a large company, Istok, in Russia. Power levels from 100 mW near 100 GHz to 1mW at 1200 GHz have been commercially achieved in electronically tuned bandwidths from 10 - 25%. Capabilities from 50 GHz to 200 GHz are likely to remain, but tubes between 200 and 1200 GHz may no longer be procurable due to the uniqueness of the provider. Although these electron sources require high voltages (2-10 kV) and large magnetic fields (5 - 12 kG), and their output power is multimode, they have been a mainstay for THz CW work for many years. Several teams are trying to develop electron sources using modern microfabrication and cathode technologies, but to date no working oscillators above 300 GHz have been produced. Theoretical projections indicate that BWO sources can work up to at least 2 THz and that advances in cold cathode and MEMS fabrication may yield designs which cost less and use less power.

Femtosecond pulse generation

It is based on using a short pulse (femtosecond) optical laser (argon-laser-pumped Ti : sapphire laser) to illuminate a gap between closely spaced electrodes on a photoconductor (e.g., silicon-on-sapphire or low temperature grown (LTG) GaAs) generating carriers, which are then accelerated in an applied field (100 V) [8]. The resulting current surge, which is coupled to an RF antenna, has frequency components that reflect the pulse duration, i.e., terahertz rates. The same THz output spectrum can be obtained by applying short laser pulses to a crystal with a large second-order susceptibility (field-induced polarization) like zinc telluride or organic ionic salt 4-N, N-4-dimethylamino-4'-N'-methylstilbazolium tosylate (DAST). Since the higher order susceptibility terms are indicative of nonlinear response, mixing occurs, producing a time-varying polarization with a frequency-response representative of the pulse length, i.e., terahertz oscillation. As with the photomixers, RF power may be radiated by antennas printed on the photoconductor or crystal, and typically have frequency content from 0.2 to 2 THz or higher depending on the laser pulse parameters. Average power levels over the entire spectrum are very low (nanowatts to microwatts) and pulse energies tend to be in the femtojoule to nanojoule range. Fiber coupled systems have been developed and continual improvements are being made to these RF generators in order to increase the signal-to-noise of the THz imagers.

1.3.2 Narrow band Terahertz sources

Photomixing

Photomixing [9] uses offset-frequency-locked CW lasers focused onto a small area of an appropriate photoconductor (one with a very short $<$ 1-ps carrier lifetime e.g., low temperature grown GaAs) to generate carriers between closely spaced ($< 1\mu$m) electrodes (source and drain) printed on the semiconductor. The laser-induced photocarriers short the gap producing a photocurrent, which is modulated at the laser difference frequency. This current is coupled to an RF circuit or antenna that couples out or radiates the THz energy. The resulting power is narrow-band, phase lockable, and readily tuned over the full THz band by slightly shifting the optical frequency of one of the two lasers. Both 780-820 nm Ti : sapphire and 850-nm DBR semiconductor lasers have been used to match the bandgap of the LTG GaAs. Typical optical-to-THz conversion efficiencies are below 10^{-5} for a single device and reported output power falls from ≈ 1 μW at 1 THz to below 0.1 μW at 3 THz, even with the newer distributed or travelling-wave photomixer designs.

Optically pumped gas lasers

Typical IR-pumped gas lasers , such as those produced commercially by DEOS, Edinburgh Instruments, and MPB Technologies are usually based on grating tuned CO_2 pump lasers (20-100 W) injected into low-pressure flowing-gas cavities that lase in the mm and sub-mm wavelength range depending on the molecule used as active medium. Power levels of 120 mW are common depending on the chosen line, with one of the strongest being that of methanol at 2522.78 GHz. In the 500-GHz-3-THz regime, not all frequencies are covered by strong emission lines. Although bulky (linear dimensions > 1m) and power demanding (100-200 W needed), those laser sources have been in use for many years in a variety of applications, from local oscillators in heterodyne detection to radiation source for various spectroscopic applications.

Ge and Si far-infrared laser

Firstly envisioned by B. Lax in 1960 [10], the operation of the p-Ge laser [11, 12, 13] is based on a population inversion between the light and heavy hole valence subbands, created through the application of crossed electric and magnetic fields (E = 0.5 - 3 kV/cm, B = 0.3 - 2 T) at cryogenic temperatures (T = 4 - 40 K). For $|E/B|$ ratios of about 1.5 kV/cmT, the heavy holes are accelerated up to energies above the optical phonon energy and consequently scattered strongly by these phonons. Under these conditions, a few percent of the heavy holes are scattered into the light hole band. The light holes remain at much lower energies and are accumulated on closed trajectories below the optical phonon energy. This effectively results in a continuous pumping of heavy holes into the light hole band - leading to a population inversion - and consequently to laser emission between the two valence sub-bands. The main problem about this source (a real tunable intersubband FIR laser) is the amount of power that has to be dissipated and that limits the operation to pulsed regime with maximum duty cycle of 5% [14].

Recently, stimulated emission and lasing in the Far-IR has been reported [15, 16, 12] also from long lived impurity states of group-V donors in silicon (Si:Bi, Si:P, Si:Sb). The devices are optically pumped by means of a CO_2 laser and tunability can in principle be achieved by means of magnetic field and uniaxial stress. However, those kind of sources are of relatively scarce technological interest because of the optical pumping and cryogenic temperatures (below 30 K) that seem to be unavoidable to obtain laser action.

Optical parametric oscillation

Optical parametric oscillation (OPO) is a second-order non linear effect that transfers the energy from a pump wave oscillating at a frequency ω_3 to an idler ω_2 and a signal ω_1. The condition of energy conservation $\omega_3 = \omega_2 + \omega_1$ ($\lambda_1 = (1/\lambda_3 - 1/\lambda_2)^{-1}$) must be satisfied and the conversion efficiency is maximum when the three waves are phase matched [17]. The non-linear crystal $LiNbO_3$ has been used in a set-up with a pump constituted by a Nd:YAG laser (1.064 μm) and an OPO tuned in the range 1.03 μm 1.06 μm to generate radiation from 0.6 to 2.4 THz. Recently, the change to another non linear material as GaP has extended the generation up to 7 THz [18].

1.4 Quantum wells, intersubband transitions and quantum cascade laser

The basic constituent of the physical systems that we have investigated in this work is the quantum well (QW). The quantum well is a way to create a 2 dimensional system by confining the motion of a particle in one direction [19]. In order to obtain quantum confinement effects, the confining potential must vary on the same order of magnitude of the De Broglie wavelength $\lambda_{dB} = \dfrac{h}{p}$ of the particle one wants to confine: if we work with semiconductors and we want to confine the carriers (electrons, holes), we consider the particle at the Fermi edge and the confining potential should have a characteristic dimension of $\lambda_{dB} = \lambda_F = \frac{2\pi}{k_F} = 2^{3/2}\left(\frac{\pi}{3N}\right)^{1/3} \approx 100$ nm for a typical carrier density of N=10^{16} cm^{-3}. We will end with a structure of the kind of Fig.1.4 (a), where both electrons and holes have discrete energy levels in the z direction: the spacing of these levels can be tuned by changing the thickness of the layers [20] and the bandgap by changing the material system. One symmetric single quantum well admits at least one bound state for any width L, and its energy spectrum in the case of infinite barriers, calculated by solving the one-dimensional Schrödinger equation is [20]:

$$E_n = \frac{\hbar^2\pi^2}{2m^*L^2}n^2 \qquad n \geq 1 \tag{1.4.1}$$

It is then necessary to be able to build a structure where a semiconductor layer with a certain bandgap is sandwiched between two layers of another semiconductor with a larger bandgap: all this has to be done at the atomic scale.

The ability to grow such single-crystal semiconductor nanostructures with atomic layer precision came with the development of the molecular beam epitaxy (MBE) technique, pioneered in the 60-70's at Bell labs [21] by A. Y. Cho. MBE is basically an extremely sophisticated thermal evaporation technique: effusion cells of different materials (III-V and II-VI groups for the semiconductors, MBE is used also for other kind of materials) are opened and closed and individually controlled. The material is evaporated on a rotating substrate and all the process happens in ultra-high vacuum (UHV) (base pressure P$\approx 10^{-11}$ mbar). The presence of the UHV environment allows also the implementation of powerful *in situ* analytical techniques such as reflection high-energy electron diffraction (RHEED) and mass spectrometry. The first evidences of quantum confined states in semiconductor quantum wells were then

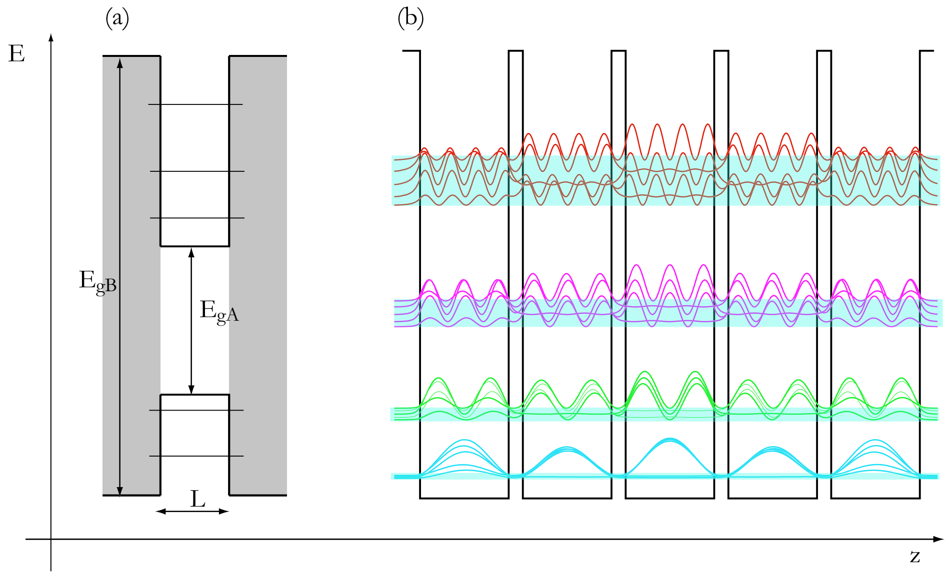

Figure 1.4: (a): Semiconductor quantum well (type I) obtained by sandwiching a layer of a material A with band gap E$_{gA}$ between two layers of material B with band gap E$_{gB}$. Note the discrete energy states in the z direction. (b): Superlattice (in the conduction band) obtained by an indefinite repetition of quantum wells. Note the formation of minibands whose energy dispersion grows with the height in the quantum well.

presented in the early 70's by Esaki [22] (in transport) and by Dingle [23] (optical absorption). The same growth technique allows also the creation of more complex structures, where the quantum well is the basic building block. Following the proposal of Esaki and Tsu [24], the repetition of many coupled quantum wells can give rise to a structure, the *superlattice* , where energy subbands are formed in analogy of what happens when atoms are brought together to form a solid (see Fig.1.4 (b)).

The intra-band transitions (both in conduction band and in valence band) between states formed by these repeated quantum well structures are called *intersubband transitions*. Although intersubband transitions were already observed in the far-infrared between the levels of a Si accumulation layer 1974 by Kamgar [25], the first intersubband absorption measurement on a GaAs-AlGaAs QW dates 1985 [26]: after this demonstration this research field had a tremendous development [27]. The design flexibility introduced by the exploitation of this kind of transitions and technologically mature epitaxial growth techniques such MBE and more recently metal-organic-vapor-phase-epitaxy (MOVPE-MOCVD) gave rise to a new sector of research that relies on the so-called *band-structure engineering* [28]. Among the many realizations important for both basic research and applications achieved via the band structure engineering, the most impressive is the realization of an intersubband laser, the *quantum cascade laser* (QCL).

1.4.1 Quantum cascade lasers

In a conventional laser diode [29, 30] the emission wavelength is determined by the characteristics of the employed material because the light emission is based on the electron-hole recombination across the semiconductor's bandgap. Some tuning is possible by employing strained structures or by varying the composition of the alloys but especially towards low photon energies, in the Mid-Infrared range (MIR) (below 300 meV, $\lambda \geq 4$ μm) it is difficult to find a suitable material to achieve laser emission. The idea is then to employ the intersubband transitions, where the photon energy can be tuned simply by varying the energy spacing between the levels of the quantum well, i.e. by changing its thickness. The tunability of the intersubband transitions is then only limited by the band offset achievable from the different materials. One important aspect of employing the intersubband transitions to achieve laser action is the shape of the joint density of states (see Fig.1.5): the states belong to the same band (conduction or valence) and have the same curvature (neglecting non-parabolicity). In the reciprocal space the density of states of such a transition is atomic-like, in contrast to an interband transition where the different curvature of the bands give rise to a broad joint density of states and subsequently a broad gain spectrum. The first

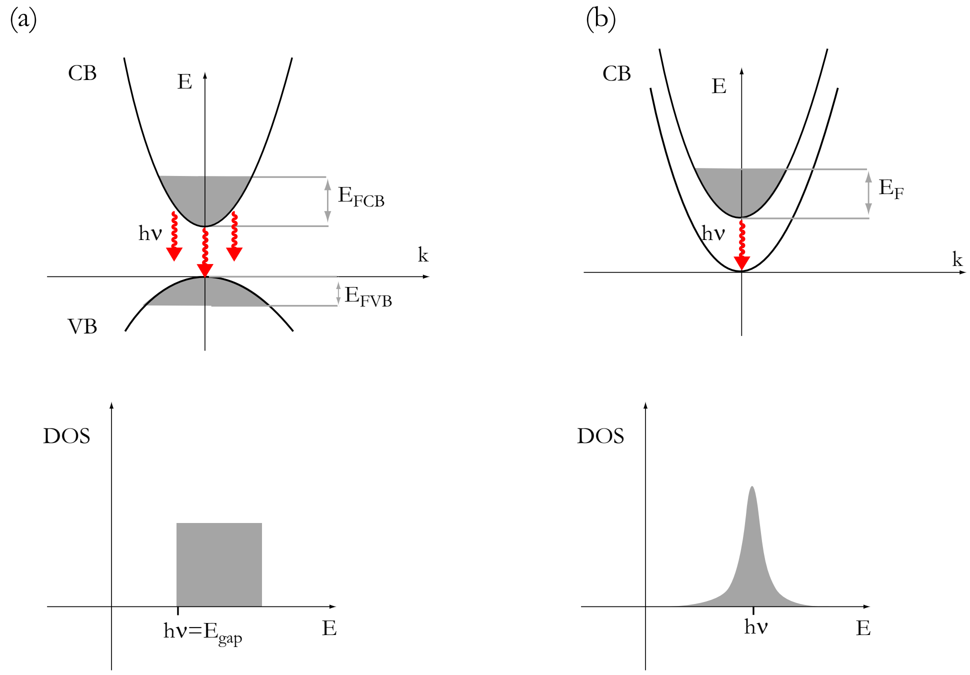

Figure 1.5: (a): interband radiative transition in the reciprocal space (up) at the energy $h\nu$ with associated density of states (down). Note the different parabolic subband dispersion for conduction band and valence band that lead to a broad and flat joint DOS. (b): intersubband radiative transition in the reciprocal space (up) at the energy $h\nu$ with associated density of states (down). The shape of the joint density of states now is narrow and peaked around the transition energy at the bottom of the upper subband.

proposal of light amplification by using intersubband transitions in a superlattice is reported in the seminal paper of R. Kazarinov and R. Suris of 1971 [31], only one year after Esaki and Tsu's superlattice proposal. In this proposal, light emission takes place between the states of a superlattice via an interwell, photon assisted tunnelling transition. The electrons in the conduction band can emit as many photons as the number of QW constituting the superlattice (cascading scheme). More details about this proposal can be found in Chapter 4. The quest for the intersubband laser started, and other proposals [32, 33, 34, 35] of electrically pumped superlattice IR emitters based on resonant tunnelling were made. Optical pumping was considered as well [36]. Experimental efforts led to the demonstration of intersubband electroluminescence in a superlattice excited by sequential tunnelling by Helm et al. in 1989 [37].

The breakthrough however came in 1994 with the first demonstration of an intersubband heterostructure laser from Jérôme Faist and co workers in the group of Federico Capasso at Bell Labs [38]. The quantum design of this laser differs substantially from the many proposals cited before: here we try to summarize the relevant points that makes this kind of device so unique. We already pointed out the unipolarity intrinsic to a device exploiting intersubband transition. The most striking point is the achievement of the population inversion by careful quantum engineering of the lifetimes of the states (typically in the ps range), while in an interband laser the inversion condition comes from an intrinsic property of the material [39]. Then there is the electron recycling intrinsic to the cascading scheme and as a third important point the intersubband gain is only limited from the quantity of carriers one is able to inject in the upper state and does not saturate as it happens for interband lasers [29].

A scheme of the first QCL is reported in Fig.1.6. The device, realized by $In_{0.48}Ga_{0.52}As$ wells and $In_{0.47}Al_{0.53}As$ barriers lattice matched to InP, is constituted by one basic structure, called "period", repeated N=25 times. One period is then split in an **active region** where the optical transition occurs, and an **relaxation-injection region**, where the carriers can relax after having completed the optical transition and be reinjected in the next period. The carriers are injected by resonant tunnelling in the state $|3\rangle$, where they can relax to state $|2\rangle$ by means of photon-assisted tunnelling [40] or by scattering, mainly from LO phonon if the condition $E_{32} \geq \hbar\omega_{LO}$ is satisfied. In order to achieve population inversion the lifetimes of the electrons in the quantum states must satisfy the relation $\tau_{32} > \tau_2$: this condition is achieved by means of two key points:

1. The lifetime τ_{32} is increased by employing a transition with a reduced spatial overlap of the wavefunctions.

2. The lifetime τ_2 is reduced by making the energy E_{21} resonant with the optical phonon energy, that is the most efficient scattering mechanism.

The injector region is doped, acting as an electron reservoir and preventing the formation of space-charge domains. The cascaded geometry obtained by repeating N times the period allows electron recycling that can be re-injected in the subsequent period after performing the optical transition, thus giving rise to an internal quantum efficiency in principle greater than one and equal to the number of periods: the same electron can emit N photons.

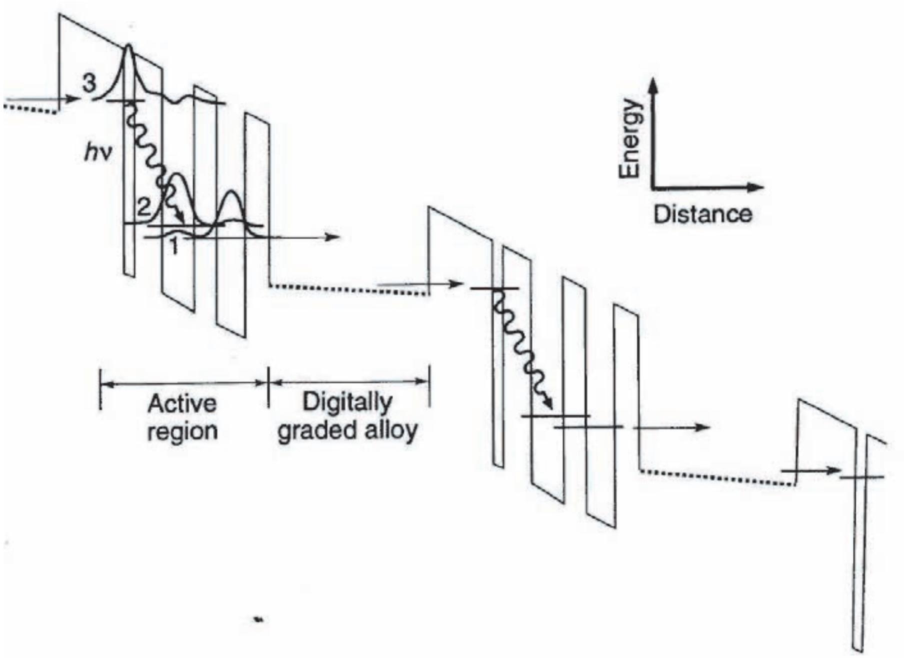

Figure 1.6: Band diagram of the first quantum cascade laser reprinted from Ref. [38]. The structure aligns for an applied electric field of about 95 kV/cm. Note the diagonal nature of the radiative transition in real space and the energy distance of one LO phonon between states 1 and 2. The digitally graded alloy is where the doping resides.

After this first demonstration, the Mid-IR QCLs showed an impressive development. Many active region designs were proposed and allowed an increase of the performances: some of the main innovations were the introduction of a vertical transition in the real space together with an electron Bragg reflector [41] constituted by the injector superlattice that suppresses the electron escape from the upper state of the lasing transition [42].

Design freedom has allowed the realization of active regions based on superlattices [43], diagonal transitions [44], QCL's without global population inversion [45] and QC lasers capable of multi-wavelength operation [46]. However, the goal being room temperature (RT) continuous-wave (CW) operation, a special active region design together with appropriate thermal management and facet coating techniques were necessaries to achieve the first CW-RT QCL at 9.2 μm in 2002 [47]. The active region design takes advantage of a two-phonon resonance [48] in the lower state of the lasing transition and the technique of the buried-heterostructure [49] laser is employed, embedding the whole laser ridge in an heatsink by laterally regrowing undoped InP in order to maximize heatsinking.

Among other designs, it is worth to cite two superlattice-based active regions, the chirped superlattice demonstrated by Tredicucci et al. in 1998 [50] and the bound-to-continuum of Faist et al. in 2001 [51]. Those two designs show very good performances also at low photon energies in the Mid-IR and will be proficiently used in the realization of THz quantum cascade lasers. The chirped superlattice design is an upgrade of the QCL based on the doped intrinsic superlattice of Ref.[43]: it is based on compensating the applied electric field in the superlattice with an effective quasi electric field generated by "chirping" the superlattice period to reach a flat miniband condition without having to dope heavily the superlattice itself. Previous research already showed the detrimental effect of a huge doping of the structure that will result in a broadening of the optical transition and a subsequent loss of gain [52]. The optical transition (wavy black arrow in Fig.1.7) takes place between two minibands delocalized over 6 wells. The population inversion is sustained also at high temperatures because of the very efficient intra-miniband scattering that ensures fast depletion of the lower state and avoids the backfilling problem that can affect structures based on resonant tunnelling for extraction of the carriers like the three quantum well design [53].

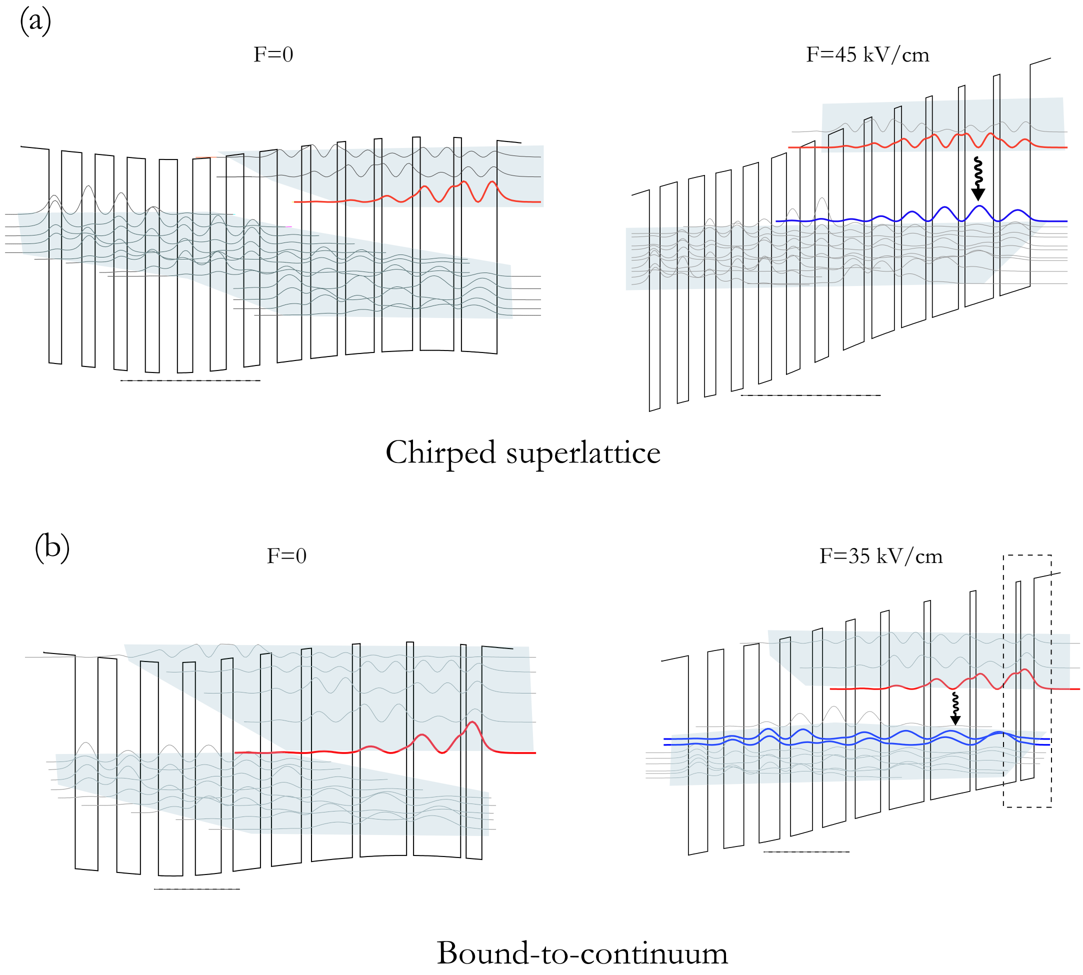

Figure 1.7: (a) Band diagram of the chirped superlattice design of Ref. [50] with no applied electric field (F=0) and with the structure aligned (F=45 kV/cm). Note the bands formed by the confined states (grey regions) that reach the flat condition when the correct bias is applied. Horizontal dashed line marks the doped layers, red line is the upper state of the lasing transition. (b) Band diagram of the bound-to-continuum design of Ref. [51] with no applied electric field (F=0) and with the structure aligned (F=35 kV/cm)

The other high-performance, superlattice-based design is the one that relies on a photonic bound-to-continuum transition, whose band profile is shown in Fig.1.7 (b). Here the lower state of the lasing transition is still constituted by a miniband obtained by chirping a superlattice, but the upper state is an isolated state created by inserting a narrow quantum well (highlighted by a dashed rectangle in Fig.1.7 (b)) just behind the injection barrier. There is no sharp separation between active region and injection-relaxation region and a good injection efficiency is ensured by the resonant tunnelling into the upper state of the lasing transition. The narrow well creates also a huge gap above the upper state of the lasing transition that contributes to minimize carrier injection in the higher energy states of the superlattice.

In parallel, a significant milestone of the development of QCLs was the demonstration of laser action in the GaAs/AlGaAs material system in 1998 by Sirtori et al. [54]. GaAs-based Mid-IR QC's have improved a lot since their demonstration [55], but still they are outperformed by almost a factor of 4 in threshold current density by InP based devices. The large discrepancy in performance is most likely due to the lighter effective mass (i.e. larger oscillator strength, $m^*_{GaAs} = 0.0665m_0$, $m^*_{InGaAs} = 0.0427m_0$), smaller optical phonon scattering cross section, lower waveguide losses and better heat conductivity of the InP with respect to the GaAs.

Recently, QC lasers have been demonstrated in different material systems such InAs/AlSb [56, 57], InGaAs/AlAsSb [58], and also realized with a growth technique different from MBE, the MOVPE [59, 60]. Especially MOVPE-grown InP based devices recently showed excellent performances comparable to the best MBE results [61]. All these experimental realizations show the solidity and the validity of the QC concept that is in some sense really independent from the material system and starts also to show some very good performances with a different growth technique. It is worth to cite intersubband lasing achieved by means of optical pumping, "the quantum fountain" laser [62]. An interesting project is also the one aimed to develop a QC laser in the Si/SiGe material system [63], with some experimental report also about THz emission from such structures [64]. This would be the ultimate demonstration that the QC concept does not depend on the nature (direct-indirect) of the bandgap of the semiconductor involved and also on the type of carrier (in this system it is the valence band that gives reasonable band offsets to work with).

To date, state-of-the-art InP Mid-IR QCLs are emitting from 3.4 μm [65] to 24 μm [66],

with CW-RT operation and high power at several wavelengths [67, 68]. Distributed feedback operation, very important for spectroscopy, has also been demonstrated at RT with large output powers [69, 70]; the Mid-IR QCL is really gaining the status of ”device” in the industrial sense.
Some interesting directions of development for the Mid-IR QC lasers research besides the pure performance increase are the investigation on broad gain curves in order to obtain wide tunability [71, 72], the non-linear processes for short wavelength generation [73, 74] and the investigations on the gain mechanism of QCLs and its relation to the Bloch oscillator [75]. The study of quantum cascade systems of reduced dimensionality will be the subject of a subsequent section (Sec. 1.5.2).

1.4.2 Terahertz quantum cascade lasers

Our choice for the generation of coherent terahertz radiation is to employ the quantum cascade laser (QCL) concept.
In the following section we give an overview of the evolution and the state of the art of terahertz quantum cascade lasers. Although luminescence in the far infrared (2.6 THz, 4.5 THz and 6 THz) from a superlattice excited by sequential tunnelling was demonstrated already in 1989 by Helm [37] it took almost eight years to demonstrate laser action below the reststrahlen band after the first demonstration of the QC in 1994 [38]. Different proposals [33, 76, 77] of far-infrared intersubband lasers were made during the 13 years between 1989 and 2002. Electroluminescence from a cascade-like structure based on a diagonal transition was observed in Qing Hu’s group in 1997 [78], then narrow electroluminescence was demonstrated by Faist’s group in 1998 [79] (from an intrawell transition) and by the Vienna group in 1999 and 2000 [80, 81] (both diagonal and vertical transitions). Both AlGaAs/GaAs and AlInAs/AlGaAs/InP material system were investigated. Those structures were all based on different designs, but the common point was that all the energy states of the active region lied below the LO phonon energy. Successively far-infrared electroluminescence was demonstrated in a structure based on lower state depopulation assisted by an LO-phonon resonance [82], in analogy to what is used in the Mid-IR. Other approaches based on emission

in parabolic quantum wells [83] were also explored.

Up to that point no lasing was demonstrated: besides the difficulty to selectively inject the carriers in the upper state and to selectively depopulate the lower state, the challenging point in the realization of a THz QC is the waveguiding mechanism. Dielectric waveguides such as the ones used in conventional laser diodes or Mid-IR QC's are not feasible because at the wavelengths of the Far-IR (50 μm-300 μm) the thickness of the cladding layers is not compatible with the epitaxial techniques employed for the realization of the heterostructures. One solution is to clad the active region between two heavily doped layers of semiconductor that will act as a "quasi-metal" confining all the radiation inside the active region. Since the free carrier absorption is the main responsible for the waveguide losses at these long-wavelengths as it scales with λ^2 (see Sec.3.3.1), such a waveguide would present unacceptably high losses of the order of 50 cm^{-1}, mainly due to the penetration of the electromagnetic wave in the heavily doped region. The validity of the simulations were confirmed by experimental measurements of waveguide losses in the Far-IR by means of a single pass technique [84]. The first laser demonstration came in late 2001 from the group of A. Tredicucci in Pisa [85]: the achievement of the first terahertz laser at 67 μm relied on the combination of a carefully designed active region based on a chirped superlattice [50] (already described for the Mid-IR region in Sec.1.4.1) and, most important, on a smart solution for the waveguide that allowed to reach values of $\frac{\Gamma}{\alpha_{tot}} = 0.47/16 \simeq 3 \times 10^{-2}$ cm, compatible with the modal gain of the structure. The waveguiding mechanism chosen by Tredicucci et al. is somewhat an hybrid solution between the microstrip resonator widely used in the microwave range and a plasmon confinement waveguide as the one used in long-wavelength Mid-IR QC lasers [86, 66, 87]. The active region of the laser is sandwiched between two heavily doped layers: one is very narrow (80 nm, 5 $\times 10^{18}$ cm^{-3}, Si) and bounds the optical mode together with a gold layer that constitues also the top contact of the laser ridge. The other heavily doped layer (2 $\times 10^{18}$ cm^{-3}, Si) is 800 nm thick: the careful choice of the doping and the thickness of this layer inverts the sign of the dielectric constant and merges the two interface plasmons bounding the mode, which partially leaks into the substrate. If the growth is performed on a semi-insulating (SI) substrate, the part of the mode that does not overlap with the active region does not contribute to the losses due to the absence of free carrier absorption. This waveguiding solution was firstly proposed by Ulrich et al. in 1999 [80]. Typical performances of this kind of device were 50 K of maximum temperature pulsed operation with some milliwatts of output power. Another THz QC laser was demonstrated [88] by our group shortly after the breakthrough of Köhler et al.: it was based also on a chirped superlattice design and will be described in more details in Chapter 7. The next step of the evolution of the THz Qc's were the demonstration of a 3.6 THz QC laser based on a bound-to-continuum transition [89] by Scalari et al. that will be extensively described in Chapter 5. It was the first THz QC to reach liquid nitrogen temperature (T_{max} = 90 K) in pulsed operation with 25 mW of peak power at 10 K. At the same time Williams et al. demonstrated laser action at 3.4 THz with a quite different approach, employing a short-period structure based on optical phonon depopulation of the lower state of the lasing transition [90].

In the successive 3 years, an impressive development led to a variety of results that are summarized in Figures 1.8 and 1.10. Figure 1.8 presents an overview of the different active region designs that showed laser action to-date. The active regions can be essentially filed in two categories: one where the overall energy spacing of the photon transition+injector dispersion is **below** the LO-phonon energy of the host material and the other category where this limit is exceeded. In the case of the total energy below the LO phonon population inversion relies on lifetimes regulated by elastic scattering mechanisms: the exact weight of the different phenomena (carrier-carrier scattering, interface roughness, impurity scattering) is still unclear and subject of active research. A very important aspect of the increase in performance of THz QCL's is the waveguiding mechanism: the realization of a low loss-high confinement resonator is crucial for the achievement of pulsed and CW high temperature operation. Significative steps in this direction have been made by the MIT group with the realization [94] and optimization of the double metal waveguide [95] that led to the demonstration of the highest temperature operation both in pulsed (164 K) and in CW (114 K) operation [96]. Another approach towards an efficient mode confinement and heatsinking is presented in Ref. [97], where the surface plasmon waveguide is combined with proton

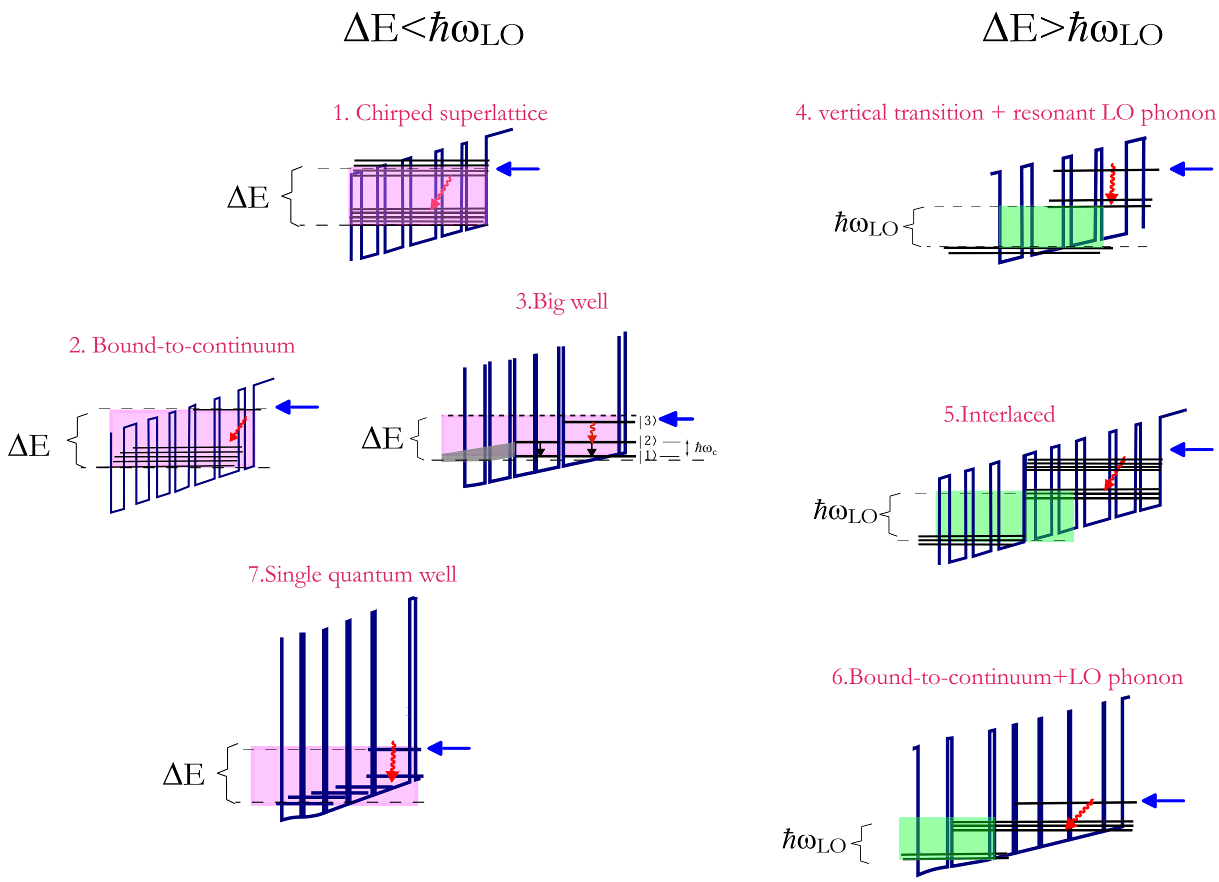

Figure 1.8: Overview of the THz QCL's designs. References are: 1 is [85], 2 is [89], 3 is [91], 4 is [90], 5 is [92], 6 is [93]. For number 7, the single quantum well, the design is almost the same as in [79] and it will be discussed in Chapter 4.

implantation to achieve a "buried strip" geometry, with a beneficial effect on the heatsinking side and also on the mode confinement. Recently the same idea has been combined with the double metal waveguide to obtain very low threshold currents on the bound-to-continuum structure of Ref.[98, 99].

On the cavities side, another interesting approach is the use of 2-dimensional photonic confinement. This approach has shown already interesting results in the Mid-IR [100] and our group recently realized a single-mode THz laser that uses 2-dimensional photonic crystals as mirrors/Bragg reflectors [101].

The possibility to achieve gain in the THz with multi-dimensional confinement is largely dis-

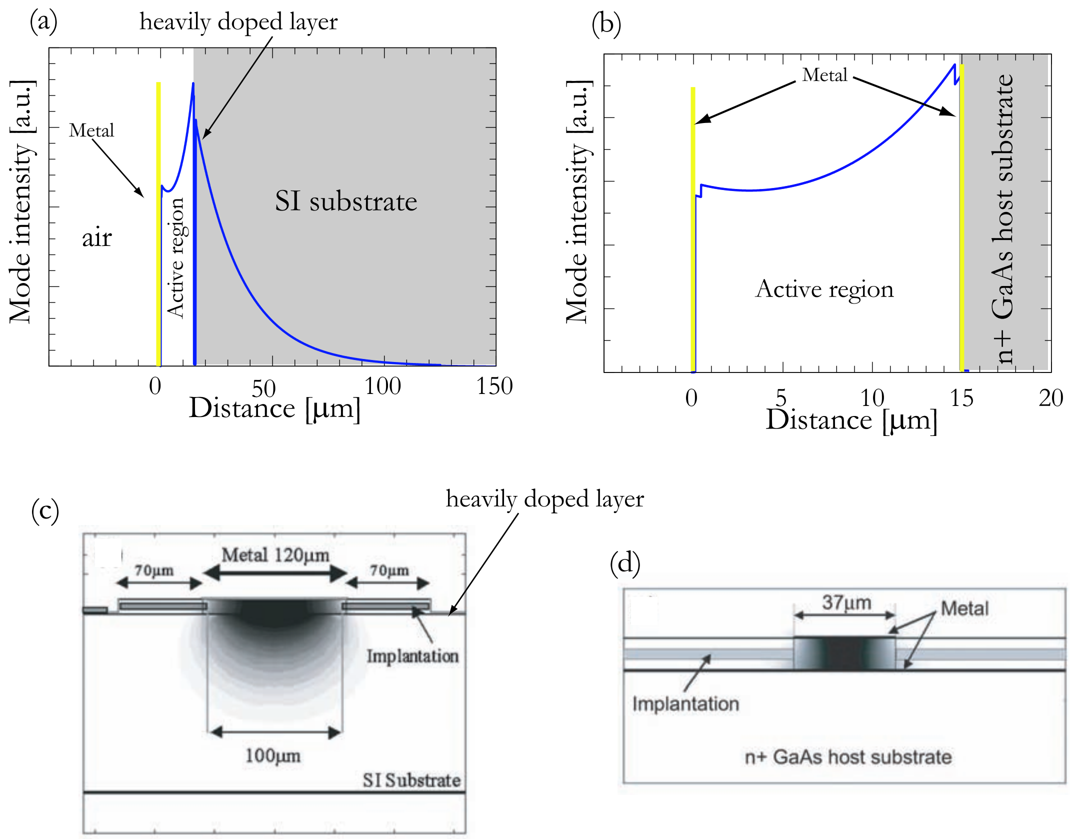

Figure 1.9: Overview of the THz QCL's waveguides. (a) Single plasmon waveguide (from [85]). (b) Double metal waveguide (from [94]). (c) Buried single plasmon waveguide (reprinted from [97]). (d) Buried double metal waveguide (reprinted from [98])

cussed throughout this thesis work; it is interesting to note that recently we have achieved laser action with extremely low threshold current densities in a very simple structure constituted by a single quantum well plus injector. This is a model system reminiscent of the very early proposals of intersubband lasers [31] and will be discussed in Chapter 4.

Figure 1.10 shows the present status of the performances of THz QC lasers. The highest operating temperatures are achieved by designs based on LO-phonon scattering and double metal waveguide. Although the laser system is a non-equilibrium system, it is interesting to note that the limit where the thermal broadening exceeds the photon energy ($k_BT > h\nu$) has already been passed, giving positive indications on the possibility to achieve laser action at room temperature or at least at temperatures attainable with thermoelectric coolers (240-250 K). Recently our group also demonstrated lasing action at 3.5 THz in the InP/AlInAs/AlGaAs material system [102] with a design derived from the one of Ref.[93]: performances are still poor but evidences of a high material gain makes us confident about a great improvement for this kind of material system also in the THz region.

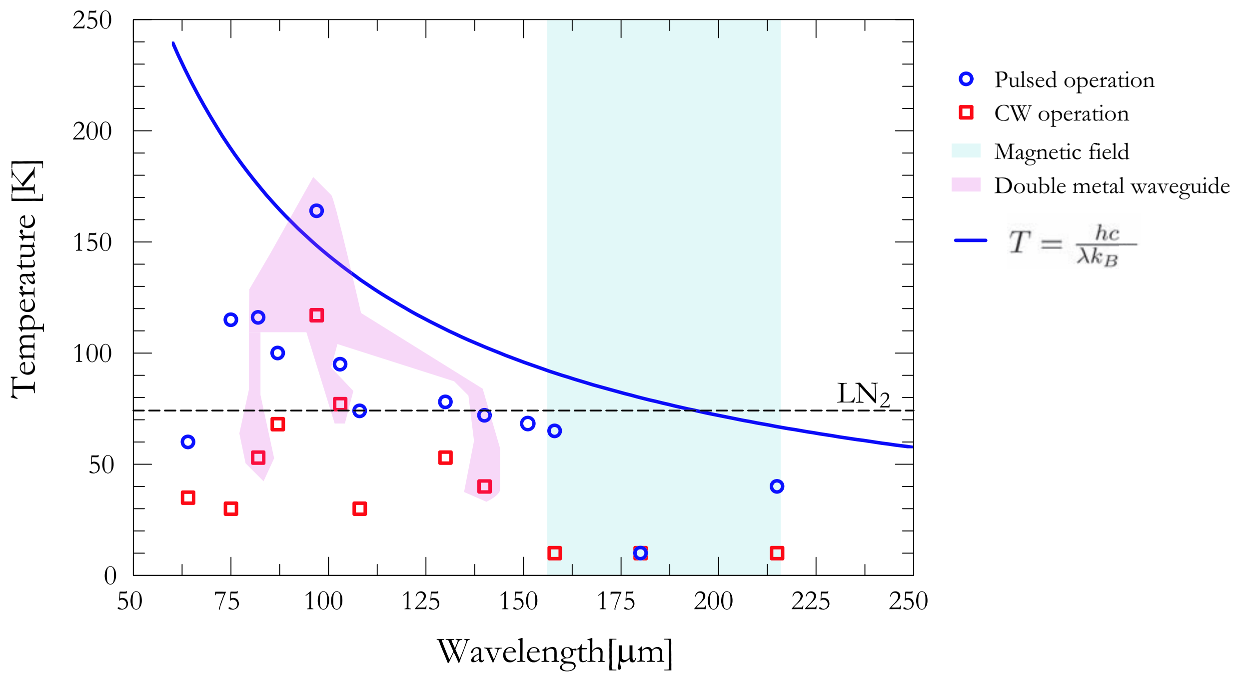

Figure 1.10: Overview of the AlGaAs/GaAs THz QCL's performances at the various wavelengths in function of the heatsink temperature. Blue circles represent pulsed operation, red squares CW operation. The light blue region denotes laser action in magnetic field, the pink region marks the devices relying on double metal resonators. The continuous blue line is the Boltzmann factor as a function of the wavelength $T = \frac{hc}{\lambda k_B}$.

1.5 Multi-dimensional confined systems and devices

One of the scopes of this thesis is the study and the realization of quantum cascade structure operating in the THz range that benefit from an additional dimensional confinement in the plane of the layers in order to provide a 3-dimensional confinement to the electrons.

In our case, the confinement has been obtained by means of a magnetic field applied perpendicularly to the layers (see Chapter 2 for details). One of the main themes of the last 20 years of semiconductors research has been the realization of nanostructures in order to tailor the properties of the materials [39]. The low dimensional semiconductor systems have unique properties in reason of their density of states and up to now we have illustrated the heterostructures based on coupled quantum wells where the confinement is 1-dimensional.

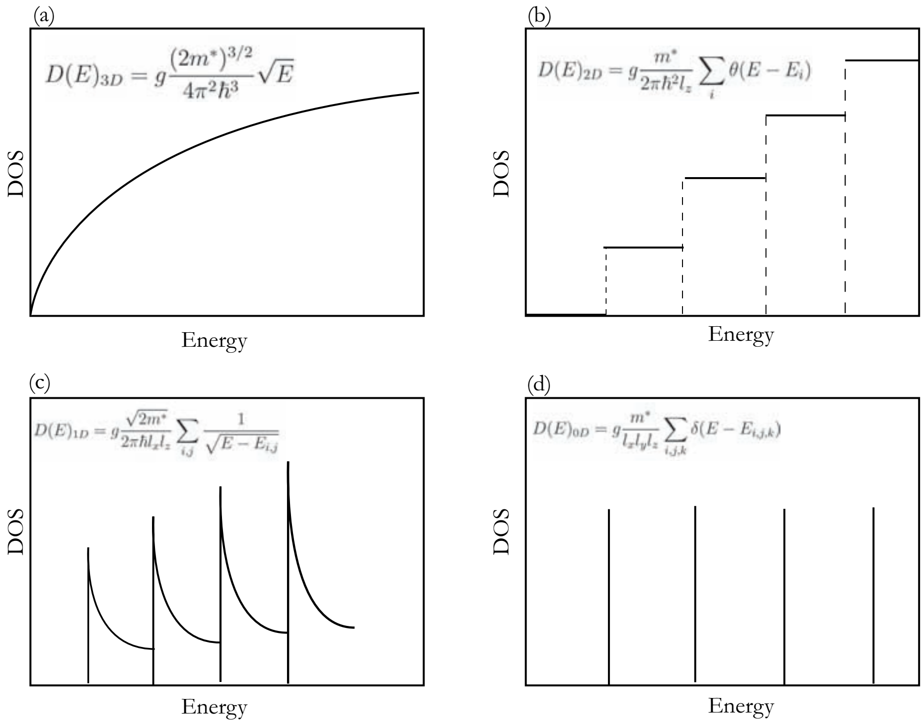

Figure 1.11: Density of states for a parabolic energy dispersion $E(\vec{k}) = \frac{\hbar^2 k^2}{2m^*}$ with an isotropic effective mass m^* in the case of (a) bulk, (b) quantum well, (c) quantum wire and (d) quantum dot.

The density of states (DOS) for the electrons as a function of the dimensionality of the structure is reported in Fig.1.11. Especially for light emitting and lasing systems, calculation showed that the peaked DOS in the 1D and 0D case should allow a high differential optical gain with low temperature dependence [39]. The possibility to use 3D confinement to quench many of the non-radiative channels offers unique possibilities both to interband

and intersubband photonic systems.

1.5.1 Interband lasing in multi-dimensional confined systems

In their seminal paper from 1982 [103] Arakawa and Sakaki proposed the reduction of the dimensionality of the active gain medium of a laser diode in order to reduce Auger processes and decrease the temperature dependence of the threshold current of a such a lasing system. Actually they proposed and realized experiments [104] using a magnetic field perpendicular to the plane of a heterostructure laser diode in order to observe reduced dimensionality effects. The realization of the first quantum wire laser in 1989 [105] and the lasing from the ground state of a self-assembled quantum dot demonstrated in 1994 [106] represent some of the milestones for the lasing in systems of reduced dimensionality. To-date, extremely low threshold current densities can be achieved with quantum dot lasers (InAs-GaAs dots, 17 A/cm^2 CW-RT) [107]. Although the performances of the quantum dot lasers are constantly improving, one of the open issues in this field of research is the so-called "phonon bottleneck" [108]: the quenching of the relaxation paths due to the dimensional confinement can be detrimental and moreover the improvement in the luminescence linewidth of a quantum dot system is difficult to achieve. However, in the case of intersubband transitions the carriers do not need to reach the bandgap to emit photons and then the quenching of all non-radiative processes and especially LO-phonon emission can be extremely advantageous.

1.5.2 Intersubband lasing in multi-dimensional confined systems

Even before the realization of the first Mid-IR quantum cascade laser in 1994, there were already proposals and studies for an intersubband infrared laser that would have benefit from a reduction of the dimensionality and specifically by a perpendicular magnetic field in order to increase the radiative efficiency. The first proposal of an intersubband laser relying on 3D confinement coming from an applied magnetic field on a 2D electron gas is the one from Aoki [109] in 1986. The proposal is to achieve population inversion between the Landau levels of a 2DEG in the quantum Hall regime (see section. 2.6.2): the emission should be tunable with the magnetic field since it happens between Landau levels.

The case of a magnetic field and superlattice-based emitters is treated by Kastalsky and Efros [110] (1991): they calculated the rate of suppression of acoustic phonon emission in a superlattice by means of a perpendicular magnetic field and proposed to use this method to achieve stimulated emission between minibands. Blank and Feng in 1993 [111] analyze the possible advantages of a perpendicular magnetic field on the structure of Ref.[76] and treat the suppression of LO-phonon emission and the tunnelling in presence of magnetic field. Some other authors propose slightly different schemes all taking advantage of the reduction of non-radiative processes [112]. For example, quite recently has been proposed an intersubband quantum wire laser [113] based on the cleaved edge overgrowth technique, with some experimental results reported on electroluminescence [114].

Quantum dot-quantum cascade lasers have been the object of a large number of proposals [115, 116, 117], both obtained via nanopatterning of the material or via seeded growth like self-assembled quanum dots, but to date there is no evidence of lasing in such systems and only electroluminescence [118, 119] has been demonstrated.

The application of a magnetic field on a quantum cascade structure, especially the ones emitting in the THz region, would be desirable in order to quench the many non-radiative channels that inhibit population inversion between closely spaced subbands. For the Mid-IR quantum cascade lasers, a large of effort has been made in the group of C. Sirtori [120] and more details can be found in Section 2.7.1. Magnetic-field enhanced THz emission from a quantum cascade structure was firstly demonstrated in 2000 by the Vienna group [121] and later from our group by Blaser et al. [122].

1.6 Scope and organization of this work

The objective of this thesis work is to extend the frequency and temperature ranges of operation of THz quantum cascade lasers and to study the physics of these systems in presence of a further dimensional confinement provided by a perpendicular magnetic field. The achievement of laser action on a wide span of frequencies and temperatures requires a profound knowledge of the key elements of a laser oscillator constituted by the gain medium and the optical resonators. Different active region design approaches have been developed combined with different waveguide configurations.

In Chapter 2, a few theoretical aspects about intersubband transitions and gain are presented, together with a basic analysis of heterostructures immersed in a perpendicular magnetic field. Some details about Landau level coupling and intersubband lifetime modulation are discussed. Chapter 3 is devoted to the discussion of the different experimental setups used throughout the work together with a discussion of the waveguides and the processing of the samples. The single quantum well THz laser is presented and analyzed in Chapter 4, together with a simple model describing transport in a two-level lasing structure. In Chapter 5, the results obtained with two designs based on a superlattice active region are presented . One design presents a depletion mechanism of the lower state based on elastic scattering and the other on LO phonon emission. The development of long wavelength THz quantum cascade lasers based on magnetic confinement is treated in Chapter 6. Four laser structures emitting at 3.6 THZ, 1.9 THz, 1.66 THz and 1.39 THz are presented together with measurements in high magnetic fields up to 28 T. Chapter 7 treats the magneto-spectroscopy of superlattice-based design. In Appendix A are presented two magneto-spectroscopy experiments that use the THz QC laser developed during this thesis work: one is an electron spin resonance experiment and the other is a magnetospectroscopy of a THz quantum well detector.

Chapter 2

Theory

2.1 Introduction

In this chapter I will present some basic theoretical tools necessary to the design of THz quantum cascade lasers and for the interpretation of the results achieved. The chapter starts by presenting a more quantitative discussion of the operation of a quantum cascade laser, followed by an analysis of the intersubband relaxation mechanisms in the THz energy range. The second part of the chapter is devoted to a review of the effects of a magnetic field applied perpendicularly to the plane of an heterostructure system.

2.2 Basic principles of quantum cascade lasers

2.2.1 Energy states in heterostructures

As already discussed in Chapter 1, the quantum cascade laser is a complex heterostructure constituted by coupled quantum wells. The structures presented in this thesis work are lattice matched-MBE grown multiquantum wells in the AlGaAs/GaAs material system. We then need to calculate the allowed energy states for the electrons in the conduction band of such structures: the solutions to the Schrödinger equation are searched in the framework of the envelope function Hamiltonian in the Kane approximation [20], where the wavefunction

$\psi(\vec{r}) = \psi_n(\vec{r}) u_{n,\vec{k}}(\vec{r})$ is the product of an envelope function $\psi_n(\vec{r})$ and a periodic Bloch part $u_{n,\vec{k}}(\vec{r})$. Over large distances the QW is not periodic, the periodicity being at the atomic level, so the envelope function varies slowly and averages over atomic distances. When the material changes, at the interface barrier/well, we make the basic assumption that the Bloch part of the wavefunction is the same $u^A_{n,\vec{k}}(\vec{r}) = u^B_{n,\vec{k}}(\vec{r})$. The non-parabolicity is included through an energy dependent effective mass [123]:

$$m^*(E) = m^*(0)\left(1 + \frac{E - V}{E_G}\right) \tag{2.2.1}$$

where $m^*(0)$ is the effective mass at the bottom of the conduction band, (E-V) is the energy of the eigenstate measured from the bottom of the conduction band, E_G is the energy gap of the considered material. If we introduce a system of axes with direction z parallel to the growth direction, the potential due to the alternating materials in the heterostructure will be expressed by a function of z only V(z). We can then separate completely the in-plane (x,y) solution and the z solution, ending up with a system of coupled one-dimensional equations for the envelope function of the conduction band:

$$\left(-\frac{\hbar^2}{2}\frac{d}{dz}\frac{1}{m^*(E,z)}\frac{d}{dz} + V(z) + V_C(z)\right)\psi(z) = E\psi(z) \tag{2.2.2}$$

$$\frac{\partial^2\psi(z)}{\partial z^2} = \frac{e}{\epsilon(z)\epsilon_0}\left[\sum_i n_i|\psi(z)|^2 - N_D(z)\right] \tag{2.2.3}$$

Strictly speaking, when using the energy and position-dependent effective mass $m^*(E,z)$ the total wavefunction $\psi(\vec{r})$ is calculated over conduction band, light-hole and split-off bands (see Ref.[123]). Then Eq.2.2.2 is referred to the conduction band part and Eq.2.2.3 is on the total wavefunction. The first equation is the Schrödinger equation for the z direction: it includes also a Coulomb term $V_C(z) = e\phi(z)$ that takes into account charging effect due to the population of electronic levels (our structures are doped). The second equation is the Poisson equation written for the doping profile $N_D(z)$: the charge density can be calculated via $Q(z) = e(N_D(z) - \sum_i n_i|\psi_i(z)|^2)$ where i is the subband index, n_i is the subband electron density and $|\psi_i(z)|^2$ the subband probability density. The temperature is introduced from the charge conservation via the Fermi distribution

$$\sum_i n_i = \sum_i \int \rho_i^{2D}(E) f(E) dE = \int N_D(z) dz = n_s \tag{2.2.4}$$

where ρ_i^{2D} is the quantum well density of states (see Sec.1.5 and Fig.1.11), $f(E) = \left(e^{\frac{E-E_F}{k_B T}} + 1\right)^{-1}$ is the Fermi-Dirac distribution and n_s is the sheet carrier density. The corrections due to the self-consistent calculations are usually negligible when we deal with relatively high energy states (MId-IR QCL's): for our long wavelength, low frequency THz lasers (with typical energies $E = h\nu = 6 \div 10$ meV) it is very important to include the effects of the band population and of the dopants because they can lead to relevant differences in the subband position, especially in the design of the injector region.

2.2.2 Intersubband gain

In order to achieve laser action it is necessary to induce stimulated emission of photons between two states of our heterostructure that lie at the desired energy spacing: we have thus to express the spontaneous and stimulated emission rates in order to obtain the gain for an intersubband transition. We consider two states i and j: starting from Fermi's golden rule $W_{ij} = \frac{2\pi}{\hbar}|\langle\psi_i|\widehat{H}|\psi_j\rangle|^2\delta(Ei - E_j - \hbar\omega)$ applied to the coupling of the two states by an electromagnetic field $\widehat{H}$ (the intersubband selection rule requires a TM polarized wave, i.e. a component of the electric field parallel to the growth axis [27]) we obtain for the spontaneous emission transition rate, (as extensively treated in Yariv [29] for an atomic system):

$$W_{ij}^{sp} = \frac{e^2\omega^3 n^3}{3\pi c^3 \hbar \epsilon_0}|z_{ij}|^2 = \frac{e^2 n^3 \omega_0^2}{6\pi m_0 \epsilon_0 c^3} f_{ij} \tag{2.2.5}$$

where we have introduce the **oscillator strength**, a very important quantity proportional to the square of the dipole matrix element:

$$f_{ij} = \frac{2m_0(E_j - E_i)|z_{ij}|^2}{\hbar^2} \tag{2.2.6}$$

The oscillator strength obeys the sum rule $\sum_{i \neq j} f_{ij} = \frac{m_0}{m^*}$ and it is a useful quantity to compare different laser designs because it is proportional to the gain. Ref.[123] illustrates how the sum rule has to be modified in a system where a spatially dependent effective mass and non-parabolicity are present. Typical values for the intersubband spontaneous emission lifetime $\tau_{ij} = W_{ij}^{-1}$ are 13 μs at 2 THz (8.2 meV) for $f_{ij} = 22$ (GaAs QW): this process has negligible influence on the transport and it is evident that the radiative efficiency for an intersubband transition is very poor. As we will see in the following, the order of magnitude for the non-radiative lifetime for intersubband transitions (both MIR and FIR) is in the ps (10^{-12} s) range, so the radiative efficiency at THz frequencies is $\eta_r = \frac{\tau_{nr}}{\tau_{nr}+\tau_r} \approx 10^{-7}$. The intersubband light emitting diode is therefore very inefficient. For the stimulated emission it is possible to calculate the following expression [29]:

$$W_{ij}^{st} = W_{ij}^{sp} \frac{\lambda^2 I(\nu)}{8\pi h \nu n^2} L(\nu) \tag{2.2.7}$$

where $I(\nu)$ is the intensity of the radiation at the frequency ν and $L(\nu) = \dfrac{\frac{2}{\pi}\gamma}{(\nu-\nu_0)^2+\gamma^2}$ is the Lorentzian lineshape that replaces the Dirac's delta for finite state lifetimes (homogeneous broadening). At this point the expression for the gain can be deduced by writing the intensity variation for an electromagnetic wave propagating by a distance dz in the heterostructure medium:

$$dI(\nu) = \alpha I(\nu) dz \tag{2.2.8}$$

If we express the absorption coefficient α using the stimulated emission and absorption rates $W_{ij}^{st} = W_{ji}^{st}$, we obtain for the power

$$\begin{aligned} P = (W_{ij}^{st} N_i - W_{ji}^{st} N_j) h\nu = h\nu W_{ij}^{st} (N_i - N_j) \Longrightarrow \\ \Longrightarrow dP = h\nu W_{ij}^{sp} \frac{\lambda^2}{8\pi h \nu n^2} L(\nu)(N_i - N_j) I(\nu) dz \Longrightarrow \\ \Longrightarrow \alpha = \frac{e^2 \nu_0 \pi z_{ij}^2}{\hbar c n \epsilon_0} L(\nu) \Delta N \end{aligned}$$

These quantities are still referred to a volume: the population inversion factor written explicitly in terms of surface densities is $\Delta N = \Delta n/L_p = (n_i - n_j)/L_p$ where L_p is the length of one period of the laser. If the inversion factor is positive (population inversion condition) $\alpha > 0$ and we have gain in the structure. Finally, for the peak gain ($\nu = \nu_0$) between subbands i and j we can write [53]:

$$G_p = \frac{4\pi e^2}{\epsilon_0 n_{eff} \lambda 2\gamma_{ij} L_p} z_{ij}^2 (n_i - n_j) \propto z_{ij}^2 \cdot \Delta n \cdot \frac{1}{2\gamma_{ij}} \frac{1}{L_p} \tag{2.2.9}$$

where λ is the emission wavelength, n_{eff} is the real part of the refractive index of the material, $2\gamma_{ij}$ is the full width at half maximum of the spontaneous emission in energy units, Γ is the overlap factor, z_{ij} is the dipole matrix element, $n_{i,j}$ are the subband electron sheet densities. To obtain the modal gain G_M it is sufficient to multiply Eq. 2.2.9 by the overlap factor [1] Γ of the given optical mode in the laser cavity

$$G_M = \frac{G_p}{\Delta n}\Gamma = \frac{g_c}{\Delta n} \tag{2.2.10}$$

With this equation we have also defined g_c as the gain cross section. Equation 2.2.9 shows that, in order to maximize the gain, we have to operate in a multi-dimensional parameter space, where the parameters are not decoupled. The inversion term $\Delta n(\tau_i, j)$ contains the dependence on the lifetimes of the electronic states. The dipole element z_{ij} is also connected to the lifetimes because it depends on the wavefunction overlap. The period length is related to the energy dispersion of the injector and to the electric field. Then there is one partially phenomenological parameter $2\gamma_{ij}$, the luminescence linewidth. This number depends obviously on the quality of the growth but depends also strongly on the kind of optical transition that is chosen. In Fig.2.1 the four kinds of optical transition that are employed in the active regions of quantum cascade lasers are reported. The vertical transition maximizes the wavefunction overlap, resulting in a strong dipole coupling between the two

[1]The overlap factor is defined as follows: $\Gamma = \frac{\int_{core} |\vec{E}|^2 dV}{\int_{space} |\vec{E}|^2 dV}$ where $\vec{E}$ is the electric field vector of the optical mode in the cavity and *core* is N times the volume of one period, where N is the number of periods in the laser.

states. Generally speaking vertical transitions are also less sensitive to surface roughness (their delocalization is limited to one well and the interfaces touched are 2) and present the narrowest spontaneous emission linewidths (~ 1 meV), positively affecting the gain (see Formula 2.2.9). The drawback is that the strong wavefunction overlap decreases the upper state lifetime, calling for an efficient depletion mechanism for the lower state. One variant of the vertical transition that proves to be highly efficient is the two-well vertical transition employed in the MIT design [90]. Here the optical transition is still vertical but the wavefunction is delocalized over two wells: here the luminescence linewidth is kept quite broad (~ 4 meV) with the advantage of a better design for the extraction of the carriers from the lower state. This active region relies in fact on a doubly resonant condition at the injection and extraction of the carriers.

The optical transition can also be made more "diagonal" in real space, reducing the overlap with the lower state, either by anticrossing the excited state of one quantum well with the ground state of a neighboring one, or by relying on a photon assisted tunnelling transition.

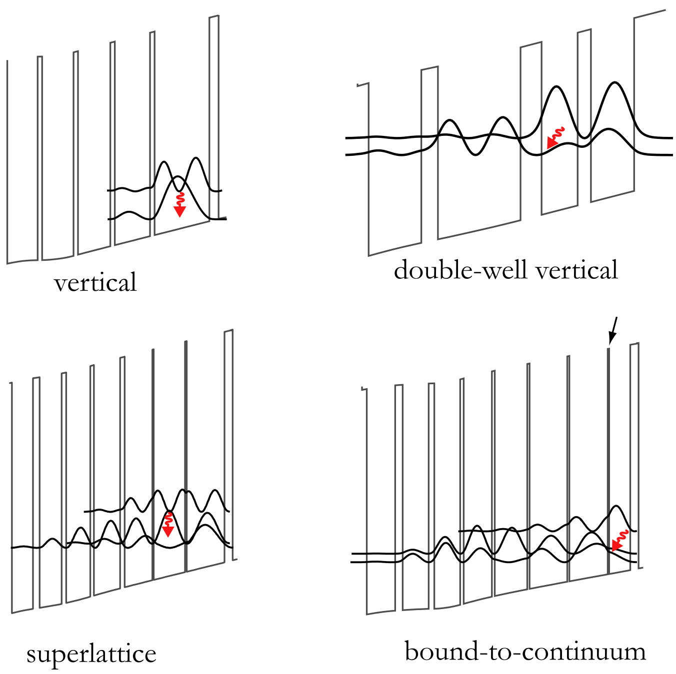

Figure 2.1: Different kinds of radiative transitions in THz QCLs.

The upper state lifetime will then increase, at the expenses of a weaker dipole (which is squared in the gain formula) and a broader luminescence linewidth. To-date no "pure diagonal" transition has demonstrated lasing action in the THz. Optical transitions between edge states of a miniband, like in the chirped superlattice design, present high values of the oscillator strength but the injection selectivity is reduced. Also in this case, due to the large delocalization of the wavefunction, typical values of electroluminescence linewidth are higher than in the vertical case (~ 2 meV, Ref.[124]). The bound-to-continuum optical transition is slightly more diagonal than the superlattice one, due to the choice of having one isolated upper state: in this case there is some more control in the upper state lifetime by tuning the first barrier thickness(black arrow in Fig.2.1), and typical values of the luminescence linewidth are in the 2 meV range. The price to pay is a lower oscillator strength with respect to the superlattice case.

2.3 Intersubband relaxation mechanisms in the far-IR

The determination of the electronic lifetimes of both the excited and the ground state of the optical transition in a structure is a key issue in understanding the carrier dynamics. When the subband energy spacing results equal or higher to the energy of a longitudinal optical phonon $\hbar\omega_{LO}$, the electron can emit very efficiently an optical phonon. This process is named Fröhlich interaction and the corresponding scattering rate reads (for $k_{\|} = 0$):

$$\frac{1}{\tau_{ij}} = \frac{m^* e^2 \omega_{LO}}{2\hbar\epsilon_0 \sqrt{2m^*(E_{ij} - \hbar\omega_{LO})}} \int dz \int \psi_i^*(z)\psi_j^*(z) e^{-\frac{\sqrt{2m^*(E_{ij}-\hbar\omega_{LO})}}{\hbar}|z-z'|} \psi_i(z')\psi_j(z') dz' \tag{2.3.11}$$

where phonon dispersion is neglected. It describes the emission of a bulk phonon from an electron: the mid-IR QCL designs that were described in the introduction make extensive use of this formula to calculate the lifetimes of the states. Good agreement is found between experimental data and calculation although this formula ignores the complex phonon spectrum of the heterostructure. Record linewidth for intersubband transitions in the Mid-IR lie in the 2-3 meV range ([125, 126]).

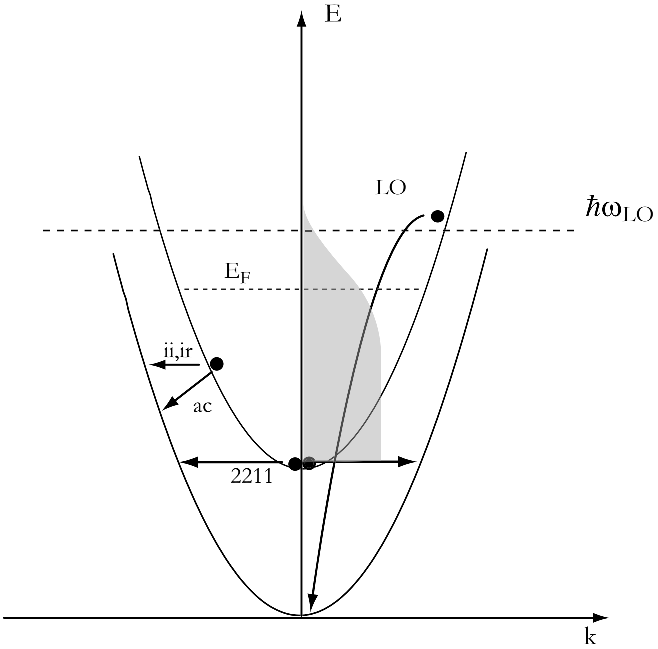

Figure 2.2: Parabolic dispersion of two subbands with an energy spacing ΔE. Different scattering mechanisms are illustrated: ionized impurity scattering (ii), interface roughness scattering (ir), e-e scattering (process 2211), optical phonon emission from hot tail of Fermi distribution, acoustic phonon (ac).

In the far-infrared, the subband energy spacing of the optical transition is less than the optical phonon energy: this in principle, at low temperatures, forbids scattering involving optical phonons and consequently this process is no longer the main non-radiative coupling between the states. Other scattering channels are therefore responsible for the non-radiative depopulation of the excited state. A schematic of the possible non-radiative paths connecting two subbands separated by an energy spacing ΔE is reported in Fig.2.2. Scattering from ionized impurities, acoustic phonon or interface roughness lie in the same order of magnitude, giving linewidth broadening of the order of 1 meV or less in wide quantum wells. The situation in those systems is far from being well understood and experimental results report lifetimes that span a wide range from a few ps to more than 100 ps [27]. The key point is that among the various relaxation mechanism that can play a role with far-IR subband separation, only acoustic phonon emission and optical phonon emission from the high energy tail of the electron distribution can effectively cool the carrier distribution.

Regarding the acoustic phonons, their emission is allowed for any carrier energy because they present no gap in their dispersion curve. Calculations show however that their scattering rate is as low as 4×10^{-3} ps^{-1} for a 20 nm thick $Al_{0.3}Ga_{0.7}As/GaAs$ quantum well and the scattering rate decreases with the well width [127, 128]. This source of scattering will play a negligible role in our structures, especially in the long wavelength THz lasers in magnetic field where the well width of the vertical transition is > 50 nm.

Electron-electron scattering, impurity scattering or interface roughness scattering are elastic processes that can only thermalize the distribution. It is important then to note that the electronic temperature will mostly be higher than the lattice one even at cryogenic temperatures. In the following sections we will give some details about those scattering mechanisms starting with electron-electrons scattering.

2.3.1 Electron-electron scattering

Electron-electron (e-e) interaction is an elastic process mediated by a Coulomb potential, which is screened by the surrounding potential. Hence, electron-electron scattering rates will depend on carrier density into the subbands. The most effective process in e-e scattering is the one where both carriers change subbands going from 2 to 1 (indicated as 2211 in Fig.2.2, where ijkl means carrier in subband i scatters in subband j and carrier in subband k scatters in subband l). On the contrary, processes like 2221 where only one carrier changes subband are forbidden [128]. Experimental work with pump and probe measurements on wide quantum wells as a function of carrier concentration (10^9-10^{11} cm^{-2}) [129] yield intersubband relaxation times in the range of 30-10 ps. The calculation of the e-e scattering rates are quite complex especially if the effect of dynamical screening has to be included. Smet et al. [128] calculated e-e scattering rates for single and coupled quantum wells with different kinds of static screening deducing lifetimes of $10 \div 20$ ps for a subband energy spacings of 10 meV with a density $1.4 \cdot 10^{11}$ cm^{-2} in the upper subband.

In low density systems (single particle approximation) the scaling of the scattering rate can be evaluated by Fermi's golden rule: following the treatment of Hyldgaard [130] the rate is proportional to the square of the matrix element $|U(q_{\Delta E})|$ (unscreened potential) weighted by the measure of the available phase space $I_p(0)$, and is expressed by the formula:

$$\frac{1}{\tau_{ee}} = W_{ee}(\Delta E) = n_2 \frac{Ry^*}{\Delta E} \frac{\hbar |U(q_{\Delta E})|^2 I_p(0)}{\pi m^*} \tag{2.3.12}$$

where ΔE is the subband energy separation and Ry^* is the excitonic Rydberg. The scattering rate for moderate electron densities ($\leq 10^{11}$ cm^{-2}) is then directly proportional to the subband density and inversely proportional to the subband energy separation ΔE. This kind of dependence leads to a square-root dependence of the emitted electroluminescence power from the injected current: this signature of electron-electron scattering has been found in vertical transition terahertz emitters at low temperatures (see Ref.[79] and Sec.4.3). Experimental work on THz emitters points toward a low temperature lifetime dominated by e-e scattering: typical values for upper state lifetime of far-infrared THz emitters lie in the 2-10 ps range [131]. Electron-electron scattering can reduce the lifetime of the upper subband also by promoting a hot electron above the LO phonon energy, where it can finally relax in the lower subband by emitting a phonon and effectively cooling the distribution. e-e scattering has been claimed to be essential in order to obtain laser action in superlattice-based structures [85] within the framework of a Monte Carlo (MC) simulation employing a model that includes only e-e and LO phonon scattering as diffusion mechanisms. The same model was applied to predict no gain in the vertical structure of Ref.[79]. We will see in Chapter 4 that this prediction was proved to be wrong, since we demonstrated laser action in such a structure. The complex interplay between e-e scattering and the other elastic scattering mechanisms as impurity scattering and interface roughness has to be taken into account, as recently pointed out also by other theoretical analyses and MC simulations [132, 133].

2.3.2 Interface roughness and impurity scattering

Evaluation of interface roughness scattering is a difficult task since the diffusion mechanism depends on a microscopic description of the interfaces that give rise to the confining potential.

However some general statements can be made: the scattering rate will depend strongly on the electron wavefunction delocalization (number of surfaces involved) and can contribute considerably to intra-subband broadening. The effect should be stronger in narrow quantum wells and should depend also on the bias applied on the structure that will change the wavefunction distribution inside the QW, changing its interaction length with the barriers [127].

Scattering from ionized impurities can play also a role in the intersubband relaxation below the LO phonon energy. The dopants are normally placed away from the region where optical transition occurs, in order to avoid electroluminescence linewidth broadening. The contribution of the impurity scattering can then be significant on the transport characteristics of the QC structure especially in the injector region. Recent results from MC simulations of MIT group [133] that include the effect of remote impurity scattering show that this mechanism cannot be ignored and, depending on the active region design, can also exceed e-e scattering. Impurity scattering is then another elastic mechanism that can indirectly contribute to the rising of the electronic temperature, thus favoring a reduction of the excited subband lifetime via LO phonon emission.

2.4 Rate equations for a QCL

In this section we will present a rate equation model for a QC laser active region [53] that will allow us to express the threshold condition as a function of the gain cross section (Eq. 2.2.10) and of the lifetimes of the structure. The active region is schematically represented as a three level system with the associated scattering rates τ_j^{-1} and sheet level densities n_j illustrated in Fig.2.3. Carriers are injected with 100% efficiency in state $|3\rangle$ which is the upper state of the lasing transition. The overall scattering rate out of this state is expressed by:

$$\tau_3^{-1} = \tau_{32}^{-1} + \tau_{31}^{-1} + \tau_{esc}^{-1} \tag{2.4.13}$$

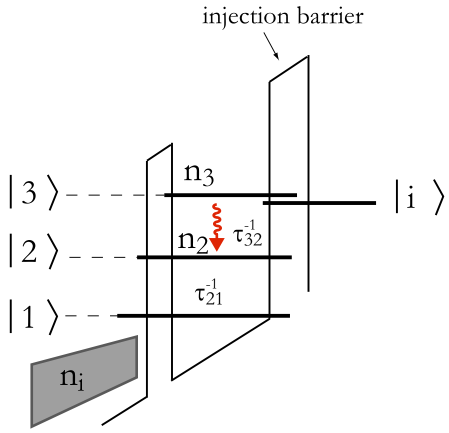

Figure 2.3: Active region of a QCL schematized as a three-level system with relevant scattering rates and level populations indicated.

where τ_{esc}^{-1} describes the possible carrier loss towards states different than $|2\rangle$ and $|1\rangle$. In analogy, scattering rate out of level $|2\rangle$ is given by:

$$\tau_2^{-1} = \tau_{21}^{-1} + \tau_{2i}^{-1} \tag{2.4.14}$$

where the coupling with the injector is accounted by the term τ_{2i}^{-1}. We introduce the electromagnetic field by the term S that represent the photon density per unit length per period. The set of rate equations to solve at stationary state is then:

$$\frac{dn_3}{dt} = \frac{J}{e} - \frac{n_3}{\tau_3} - Sg_c(n_3 - n_2) \tag{2.4.15}$$

$$\frac{dn_2}{dt} = \frac{n_3}{\tau_{32}} + Sg_c(n_3 - n_2) - \frac{n_2 - n_i e^{-\Delta/k_B T}}{\tau_2} \tag{2.4.16}$$

$$\frac{dS}{dt} = \frac{c}{n}\left(g_c(n_3 - n_2) - \alpha)S\right) \tag{2.4.17}$$

where we neglect spontaneous emission (well justified for ISB transitions, see Sec.2.2.2). The total losses are expressed by $\alpha = \alpha_w - \frac{1}{2L} ln(R_1\ R_2)$ and the factor $n_i e^{-\Delta/k_B T}$ accounts for a thermally populated injector miniband of energy width Δ. The solution at steady state of the system for $S = 0$ gives then the threshold condition:

$$J_{thresh} = \frac{e}{\tau_3} \frac{(\alpha_w + \alpha_m)/g_c + n_2^{\text{therm}}}{1 - \tau_2/\tau_{32}} \tag{2.4.18}$$

From this expression, the importance of the lifetime ratio τ_2/τ_{32} together with an efficient depleting mechanism for the lower state in order to avoid thermal backfilling that can induce reabsorption and suppress gain becomes clear. If we write the population inversion as a function of the threshold current $n_3 - n_2 = \frac{J_{thresh}}{q}\tau_3 \left(1 - \frac{\tau_2}{\tau_{32}}\right) = \frac{J_{thresh}}{q}\tau_{eff}$ we can point out one of the main aspects of the QCL: if the lifetimes are suitably engineered, the device can lase for an arbitrarily low value of the injected current J. In the case of a QCL, the **transparency current**, that sets the limit to the threshold of conventional interband laser diodes [39], translates into the minimum current that has to flow into the structure in order to align the injector with the upper state of the lasing transition. This parameter can then be engineered as well: a demonstration of this concept is given in Chapter 6 where laser action with extremely reduced thresholds is demonstrated by employing a highly favorable ratio of lifetimes.

2.5 Resonant tunnelling: Kazarinov and Suris model

The transport in a quantum cascade laser relies on a complex interplay between scattering mechanisms and resonant tunnelling that couple the different states of the heterostructure. The selective injection of carriers in the upper state of the lasing transition of the majority of THz QC laser designs (see Sec.1.4.2) happens via scattering-assisted resonant tunnelling: it is therefore very important to understand which are the relevant parameters that control this process. The description of the tunnel coupling of two states across the injection barrier can be performed in a full quantum mechanical way by describing the system in a tight-binding approach and using the density matrix formalism. For a schematic of the relevant states in our injection-active region model we refer to Fig.2.4. When the electric field F applied to the

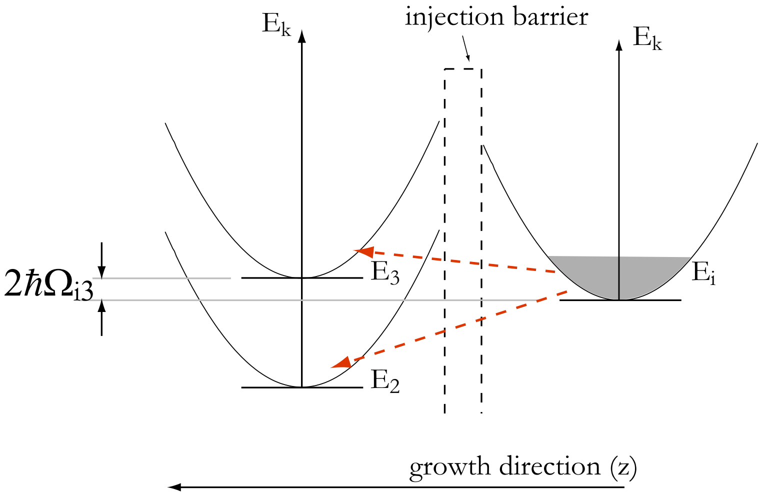

Figure 2.4: In-plane parabolic dispersion of the injector-active region coupling for a QCL: the red arrows represent possible scattering mechanisms responsible for the transport.

heterostructure is increased, the state $|i\rangle$ (ground state of the injector) and the upper state of the lasing transition $|3\rangle$ are brought closer in energy: at the resonance ($F = F_0$) they form a doublet spaced by an anticrossing gap $E_{i3} = 2\hbar\Omega_{i3}$ determined by the barrier thickness. The electron oscillates back and forth with a characteristic time that is the half of the Rabi period $\dfrac{\hbar\pi}{E_{i3}} = \dfrac{\pi}{\Omega_{i3}}$. The presence of different scattering mechanisms can modify this picture of "coherent" transport depending on the rate of the scattering mechanism considered relative to the Rabi frequency. An analytical expression for the tunnelling current between these two levels coupled via a tunnelling barrier in the density matrix formalism was derived by Kazarinov and Suris [134]:

$$J = qn_s \frac{2|\Omega_{i3}|^2\tau_p}{1 + \Delta^2\tau_p^2 + 4|\Omega_{i3}|^2\tau_p\tau_3} \tag{2.5.19}$$

$$\hbar\Delta(F) = E_i(F) - E_3(F) = qd(F - F_0) \tag{2.5.20}$$

where τ_p is the in-plane dephasing time (corresponding to the T_2 time in the formalism of the optical Bloch equation for a two level system [19]), d is the spatial separation of the centroids of the two wavefunctions ($d = |\langle \mathbf{p}, i|z|\mathbf{p}, i\rangle| - |\langle \mathbf{p}, 3|z|\mathbf{p}, 3\rangle|$), n_s is the sheet carrier density and τ_3 is the total lifetime of state $|3\rangle$. The current density as a function of applied voltage is thus a Lorentzian with a full-width-half-maximum given by $2/\tau_p\sqrt{1 + 4|\Omega_{i3}|^2\tau_p\tau_3}$. The maximum current J_{max} is reached at resonance ($\Delta = 0$) and is expressed by the relation:

$$J_{max} = q\ n_s \frac{2|\Omega_{i3}|^2\tau_p}{1 + 4|\Omega_{i3}|^2\tau_p\tau_3} \tag{2.5.21}$$

Depending on the relative weight of the different parameters, the coupling of the levels $|i\rangle$ and $|3\rangle$ can be divided in two regimes: the **weak** and the **strong** coupling regimes [135]:

$$4|\Omega_{i3}|^2\tau_p\tau_3 \ll 1 \longrightarrow J^w_{max} = 2q\ n_s|\Omega_{i3}|^2\tau_p \qquad \text{weak coupling} \tag{2.5.22}$$

$$4|\Omega_{i3}|^2\tau_p\tau_3 \gg 1 \longrightarrow J^s_{max} = \frac{q\ n_s}{2\tau_3} \qquad \text{strong coupling} \tag{2.5.23}$$

The in-plane dephasing time τ_p depends essentially on the quality of the growth and can be estimated, in the far-infrared, from the linewidth of the spontaneous emission in the case of a vertical transition. Our spontaneous emission linewidths range from 3 meV to less than 1 meV, yielding typical values τ_p ∼400 fs-1.5 ps (see also Sec.4.3 for a more extended discussion). The coupling regime is then controlled by the product between the overall lifetime τ_3 and the squared value of the anticrossing gap in frequency units. In the case of weak coupling, described by relation 2.5.22, the transport is controlled by scattering (the levels are broader than the energy splitting), the tunnelling rate $2|\Omega_{i3}|^2\tau_p$ is much smaller than τ_3^{-1} and almost all carriers reside in the injector. On the other side, when relation 2.5.23 is satisfied the total current is controlled by the intersubband relaxation time τ_3: the tunnelling rate $2|\Omega_{i3}|^2\tau_p$ is much larger than τ_3^{-1} and the carriers can be almost equally distributed between the ground state of the injector $|i\rangle$ and the upper state of the lasing transition $|3\rangle$. The strong coupling regime is the one where we achieve the fastest injection of carriers in the upper state of the laser transition and thus the best one for laser operation [135]. It is worth to note that also the in-plane dephasing time τ_p controls the coupling regime of the resonant tunnelling: this dependence will be further analyzed in the Chapters relative to magnetic field measurements. Equation 2.5.21 can be used either to estimate the maximum current density J_{max} for the onset of space-charge accumulation (given τ_3) or to infer the lifetime τ_3 by measuring the maximum current at the breaking point of the J-V curve. When $J > J_{max}$ the electron sheet density is not sufficient to sustain the desired current and states i and n = 3 are populated with an excess negative charge. This results in the breaking of the charge neutrality condition, giving rise to an additional built-in electric field which can substantially modify the alignment of the levels and thus deteriorate the injection mechanism. Knowing n_s, τ_p and the splitting Ω_{i3}, upper state lifetime τ_3 can be written as:

$$\tau_3 = \frac{q\ n_s}{2J_{max}} - \frac{1}{4|\Omega_{i3}|^2\tau_p} \tag{2.5.24}$$

Generally the strong coupling regime is assumed and the relation 2.5.24 reduces to $\tau_3 = \frac{q\ n_s}{2J_{max}}$ but it is important to notice that a small variation of the splitting Ω_{i3} can reduce the deduced lifetime. In Fig.2.5 the upper state lifetime and the coupling parameter $4|\Omega_{i3}|^2\tau_p\tau_3$ are calculated via Eq.2.5.24 as a function of $2\hbar\Omega_{i3}$ employing typical values for our THz laser structures of Chapter 5 ($\tau_p = 500fs$, $J_{max} = 600$ A/cm^2, $n_s = 3 \times 10^{10}$ cm^{-2}). We notice

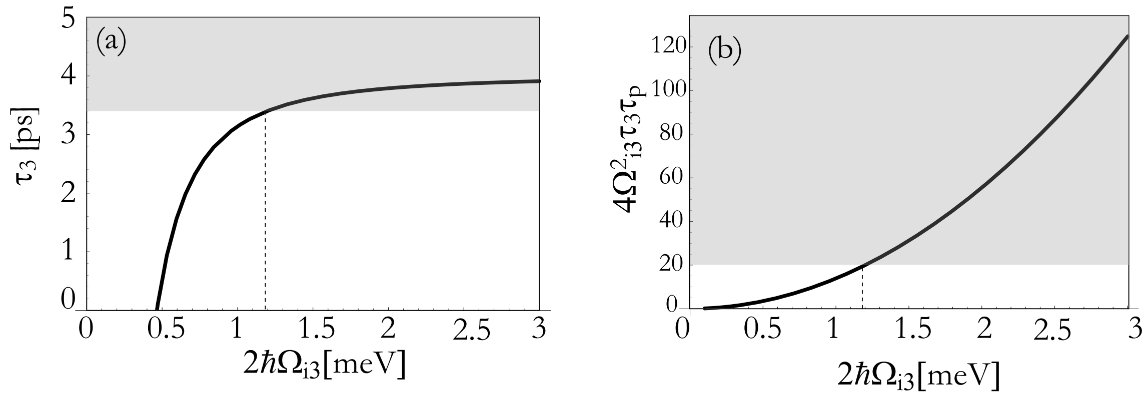

Figure 2.5: (a): Upper state lifetime deduced from J_{max} in function of the anticrossing energy $2\hbar\Omega_{i3}$. (b): Coupling parameter $4|\Omega_{i3}|^2\tau_p\tau_3$ as a function of the anticrossing energy $2\hbar\Omega_{i3}$. Strong coupling of the injector is highlighted by grey area.

that the deduced upper state lifetime value saturates when the system enters the strong coupling regime. In THz QC structures, the energy splitting at the anticrossing is often small, so care must be taken when estimating upper state lifetime from transport features.

2.6 Magnetic field effects in heterostructure systems

In this section we analyze the effects of an external magnetic field on a quantum well system. Since the quantum well is the building block of a generic heterostructure and particularly of the quantum cascade laser we are interested in the evolution of the energy levels and in the couplings between the electronic states of such an heterostructure whenever a magnetic field is applied. We will treat the case of a magnetic field applied perpendicularly to the plane of the layers of the heterostructure (parallel to growth axis) because our experimental work corresponds to this configuration.

2.6.1 Perpendicular magnetic field: energy spectrum

In order to evaluate the effect of a static magnetic field on the electronic states of an heterostructure, let us consider a quasi bi-dimensional electron system [20, 136, 137]. The axes are oriented as in Fig. 2.6. A static magnetic field $\mathbf{B}$ can be defined via the vector potential $\mathbf{A}$ via the relation

$$\mathbf{B} = \nabla \times \mathbf{A} \tag{2.6.25}$$

($\nabla \cdot \mathbf{B} = 0$ still holds). The freedom given by the definition 2.6.25 leave us the choice of a suitable gauge due to the invariance of $\mathbf{B}$ in respect to a transformation $\mathbf{A}' = \mathbf{A} + \nabla\Lambda$ where Λ is an arbitrary scalar function. We choose the so-called Landau gauge $\mathbf{A} = (-BY, 0, 0)$ where the magnetic field reads $\mathbf{B} = (0, 0, B)$. We also define $V(Z)$ as the heterostructure potential due to the presence of the confining barriers.

With the canonical transformation $\mathbf{p} \longrightarrow \mathbf{p} - (-e)\mathbf{A} = \mathbf{p} + e\mathbf{A}$ where e is the absolute value of the electron charge the Schrödinger equation of the single-particle system reads:

$$\left(\frac{(\mathbf{p} + e\mathbf{A})^2}{2m^*} + V(Z) + g^*\mu_B\sigma\mathbf{B}\right)\phi(\mathbf{R}) = E\phi(\mathbf{R}) \tag{2.6.26}$$

The operator σ (with eigenvalues $\pm\frac{1}{2}$) is the Pauli operator for the spin, $\mu_B = \frac{e\hbar}{2m_0}$ is the Bohr magneton and g^* is the effective Landé factor (g=2 for a free electron, $g^* = -0.44$ for GaAs,

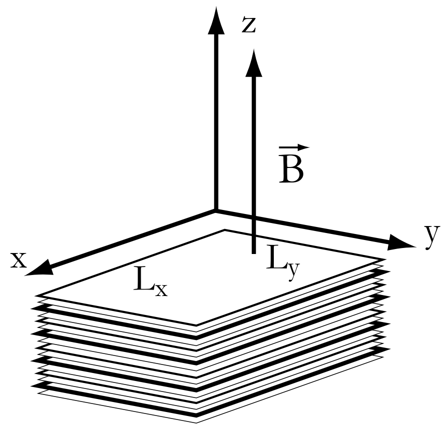

Figure 2.6: Magnetic field $\vec{B}$ applied perpendicularly to the layers of the heterostructure (parallel to the growth axis z). The linear dimensions of the sample are L_x and L_y.

g^* depends on magnetic field). Since spin is rotationally invariant we can find the solutions to the orbital part of the Schrödinger equation 2.6.26; the effect of the spin will be included later simply by taking the tensorial product $|x, y\rangle \bigotimes |\uparrow\downarrow\rangle$ between the eigenvectors of the orbital equation $|x, y\rangle$ and the eigenvectors of the spin part $|\uparrow\downarrow\rangle$. Let us now concentrate on the orbital part of Eq.2.6.26: the motion of an electron can be decoupled in x-y and z directions due to the fact that the magnetic field is not influencing the motion of the electron in the z-direction. The Hamiltonian for the x-y directions is:

$$H_{xy} = \frac{1}{2m^*}((p_x - eBy)^2 + p_y^2) \tag{2.6.27}$$

We work in the Schrödinger representation and the operators are defined as $\mathbf{p} \equiv -i\hbar\nabla$, $\mathbf{R} \equiv \mathbf{r}$. Inspection of the Hamiltonian 2.6.27 reveals that it is x-independent: then we take the ansatz $\Phi(x, y) = \Psi(y)e^{ik_x x}$ for the $\Phi(x, y)$ wavefunction, with plane waves as solutions on the x direction. The Schrödinger equation 2.6.26 reduces to:

$$\left(-\frac{\hbar^2}{2m^*}\frac{\partial^2}{\partial y^2} + \frac{\hbar^2 k_x^2}{2m^*} - \frac{\hbar k_x eBy}{m^*} + \frac{e^2B^2y^2}{2m^*}\right)\Psi(y) = (E - E_z)\Psi(y) \tag{2.6.28}$$

We can now map this equation onto the harmonic oscillator Schrödinger equation:

$$\left(-\frac{\hbar^2}{2m^*}\frac{\partial^2}{\partial v^2}+\frac{1}{2}m^*\omega^2 v^2\right)u(v)=Eu(v)$$

by the substitutions:

$$\begin{aligned}\omega &\longrightarrow \omega_c=\frac{eB}{m^*}\\ v &\longrightarrow y-\frac{\hbar k_x}{m^*\omega_c}\end{aligned}$$

The quantity ω_c is called the *cyclotron frequency* . The eigenfunctions of the xy Hamiltonian are the well known Hermite polynomials in the y-direction multiplied by the plane waves on x:

$$\Phi(x,y)=e^{ik_x x}(2^n n!\sqrt{\pi}l_B)^{-1/2}e^{\left(-\frac{(y-y_0)^2}{2l_B^2}\right)}H_n\left(\frac{y-y_0}{l_B}\right) \tag{2.6.29}$$

where $l_B=\sqrt{\frac{\hbar}{eB}}$ is the magnetic length that represents the width of the ground state of a Landau level. For the eigenvalues we reintroduce the spin degree of freedom and we obtain the expression for the energy values of the eigenstates, called *Landau levels*, of an electron in the envelope function approximation in a magnetic field:

$$E_{n,z,B}=E_z+\hbar\omega_c\left(n+\frac{1}{2}\right)\pm\frac{1}{2}g^*\mu_B B \qquad n=0,1,2,.... \tag{2.6.30}$$

This expression neglects the effects of the non-parabolicity: we will take them into account in Section 6.6.2. In general we will neglect the spin degree of freedom because for GaAs (the material of the wells of our structures) $g^*=-0.44$ and the spin splitting at 28 T is 1.5 meV, well inside the broadening of the Landau levels. Let us now specify the quantities we have used in writing the solution and analyze its physics. For simplicity we will put the boundary conditions on the x-y plane assuming L_x,L_y as the linear dimensions of the sample. The quantization on x will be expressed by $k_{x,n}=\frac{n\pi}{L_x}$ and the harmonic oscillators on the y-axis will be centered at the positions $y_n = \frac{n\pi\hbar}{m^*\omega_c L_y}$. The Landau levels are highly degenerate, and the degeneracy of the level E can be evaluated by counting the states that lie within $E \pm \frac{\hbar\omega_C}{2}$ and that will collapse in the same Landau state. If we recover the density of states for a 2D system [137] $D_0 = \frac{\eta_s \eta_v m^*}{2\pi\hbar^2}$ (η_s and η_v spin and valley degeneracy, respectively) we can give the expression for the density of states of a Landau level by multiplying by $\hbar\omega_c$ and we obtain:

$$D = \frac{\eta_s \eta_v eB}{2\pi\hbar} \Longrightarrow D(E) = \frac{\eta_s \eta_v eB}{2\pi\hbar} \delta(E - E_n) \tag{2.6.31}$$

which is valid for an ideal 2DEG in presence of a magnetic field.
If we introduce the carrier density per unit area n_s we can define a very important quantity called the *filling factor* ν:

$$\nu = \frac{n_s}{D} = \frac{2\pi\hbar n_s}{\eta_s \eta_v eB} \tag{2.6.32}$$

which measures the number of Landau levels filled for a given value of the magnetic field B and the electron density n_s. If the system is in presence of disorder caused by impurities or interface roughness or other nonidealities, Eq.2.6.31 is no longer valid and the δ's will broaden; Ando [138] has calculated the density of states in the condition of short range impurities: the calculation has the effect to replace the δ functions with the semi-ellipses:

$$D(E) = \frac{1}{2\pi l_B^2} \sum_n \left[1 - \left(\frac{E - E_n}{\Gamma_n}\right)^2\right]^{1/2} \tag{2.6.33}$$

where Γ_n is the broadening of the levels that depends on B and n. An empirical formula that overcomes the abrupt cutoff of 2.6.33 is the one that uses Gaussian functions to describe the broadened Landau states.

$$D(E) = \frac{2eB}{h} \sum_n \frac{1}{\Gamma_n \sqrt{2\pi}} e^{-\frac{(E-E_n)^2}{2\Gamma_n^2}} \tag{2.6.34}$$

This approach has proven to be quite accurate and experimental measurements point towards a square root dependence of the level width from the magnetic field $\Gamma(B) = \Gamma_0 \sqrt{B}$ as in

Ref.[139]. A representation of the density of states of Landau levels is given in Fig.2.7(a). It is interesting to note that, if the potential range d is sufficiently short ($d < \frac{l_B}{(2n+1)^{1/2}}$) we can relate the Γ_n to a scattering time for the impurities τ_f

$$\Gamma^2 = \frac{2}{\pi}\hbar\omega_c\frac{\hbar}{\tau_f}$$

and give a condition for the observability of the Landau levels [137] . More generally, for being able to observe magnetoquantization effects we need

$$\Gamma \leq \hbar\omega_c \Longrightarrow \frac{2}{\pi}\hbar\omega_c\frac{\hbar}{\tau_f} \leq (\hbar\omega_c)^2 \Longrightarrow \frac{2}{\pi}\frac{1}{\tau_f} \leq \omega_c \Longrightarrow \omega_c\tau_f \geq \frac{2}{\pi} \Longrightarrow B \geq \frac{1}{\mu}$$

where we used the definition of mobility $\mu = \frac{e\tau_f}{m^*}$. It is evident that the poorer the mobility the higher the magnetic field we have to apply in order to observe these effects. It is not easy to evaluate the mobility for a QC sample; for the GaAs structures grown at the Cavendish laboratory in Cambridge, the average mobility measured on High Electron Mobility Transistors (HEMT) grown in-between laser structures are above 10^6 cm^2/V·s, so the condition on the magnetic field reads $B \geq \frac{1}{10^2} = 10^{-2}$ T.

In summary we conclude that for sufficiently high mobilities and magnetic fields the electrons will exhibit a completely quantized energy spectrum given by Formula 2.6.30 and will perform closed orbits in the x-y plane with a frequency ω_c and a typical orbit length that is given by the magnetic length l_B. Another important quantity is the cyclotron radius $r_c = k_F l_B^2 = \frac{2\pi}{\lambda_F}\frac{\hbar}{eB} = \sqrt{\frac{n_s}{2\pi}}\frac{h}{eB}$ that connects the magnetic length l_B to the Fermi wavelength $\lambda_F = \sqrt{\frac{2\pi}{n_s}}$.

2.6.2 Shubnikov-de Haas oscillations and quantum Hall effect

Once we have defined our energy scheme for a 2D electron gas in a magnetic field, the most common way to observe the effects of the Landau quantization is via transport measurements at low temperatures ($k_BT \leq \Delta E$). A typical experimental configuration is shown in Fig.2.7(b). Two striking phenomena can be detected by measuring the longitudinal resistivity of a 2DEG sample (ρ_{xx}, parallel to the current flow $\vec{J}$) and at the transverse, or Hall, resistivity (ρ_{xy}, perpendicular to the current flow $\vec{J}$) at low temperatures. The Hall resis-

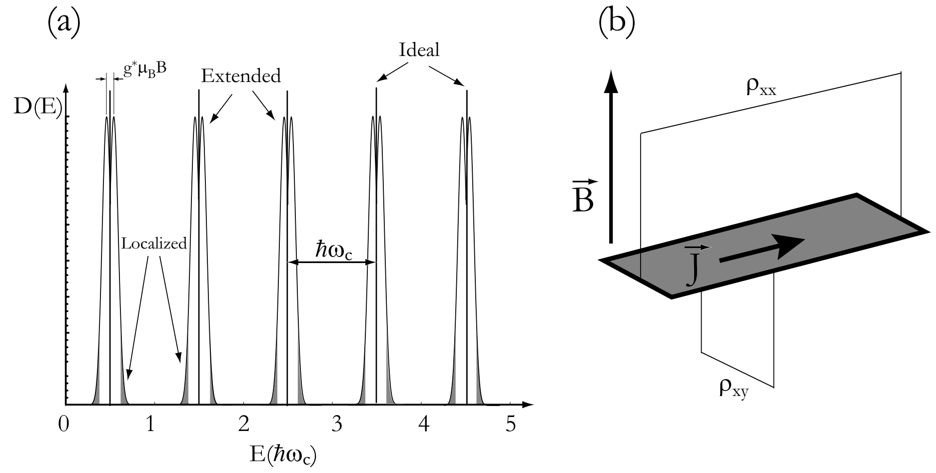

Figure 2.7: (a): Density of states of a 2DEG with perpendicular magnetic field in the ideal case (vertical lines) and in the case of disorder and imperfection (including spin splitting). The localized states (grey regions) lie in the tails of the Gaussian linewidth (see Eq.2.6.34). The extended states are more centered on the energy of the Landau level. (b): typical experimental arrangement for the measurement of Hall and longitudinal resistance of a 2DEG sample.

tance turns out to be quantized in units of $\frac{h}{e^2}$: plateaux are observed in ρ_{xy} as the magnetic field or the Fermi level is changed, whenever the filling factor ν (see formula 2.6.32) is an integer. This phenomenon is known as the quantum Hall effect [140] (QHE) and represents a whole field of study *per se*: here we only recall the basics and its origin in order to try to give a correct interpretation of our measurements of THz QC lasers in strong magnetic fields. The observed quantization is universal since it does not depend on the material system provided that the carrier gas is bi-dimensional: its value at the $\nu = 1$ Hall plateau has been adopted as the resistance standard. The exact determination of $\frac{h}{e^2}$ is full of interest also for quantum electrodynamics since this ratio is contained in the fine-structure constant $\alpha = \frac{\mu_0 c}{2} \frac{h}{e^2} \approx \frac{1}{137}$. In essence, the transport features are the result of transitions between alternating metallic and insulating phases. There is another effect that is closely related to the QHE: the longitudinal resistivity ρ_{xx} oscillates as a function of the magnetic field or the Fermi level and in the regions of quantized Hall resistance it falls to zero. These oscillation are know as Shubnikov-de Haas oscillations : the whole behavior of a 2DEG in perpendicular magnetic field is reported in the celebrated Fig.2.8 reprinted from [141].

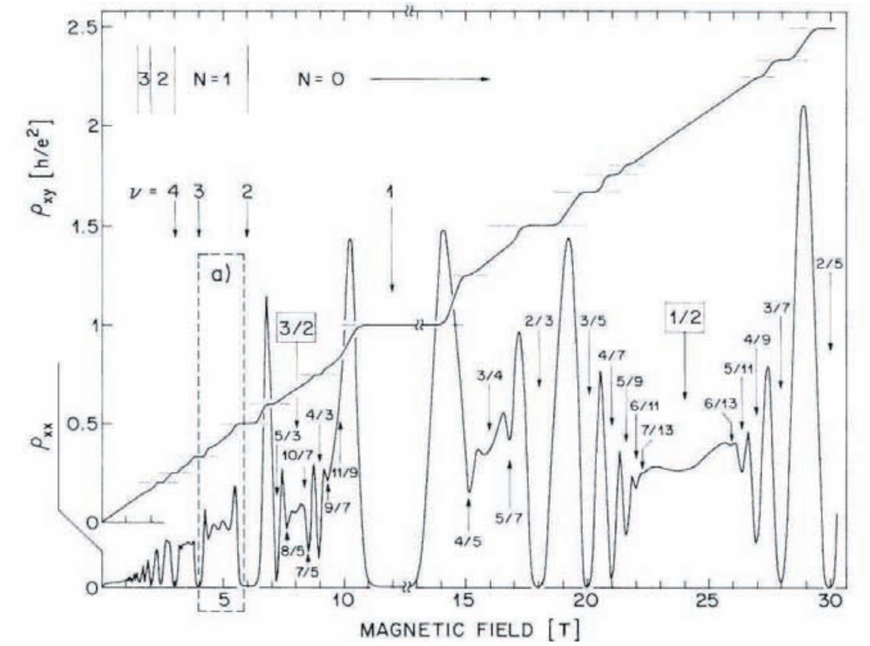

Figure 2.8: Evolution of longitudinal resistivity ρ_{xx} and Hall resistivity ρ_{xy} of a 2DEG at T=150 mK as a function of the applied magnetic field. The density $n_s = 3.0 \times 10^{11}$ cm^{-2} and the mobility 1.6×10^6 cm^2/V·s. Note the integer filling factor ν in correspondence of the plateaux and the Landau index N. Above 12 T ($\nu < 1$) the system enters the fractional regime. Reprinted from [141].

Two elements are essential in order to observe the QHE: one is the Landau quantization that we discussed in Section 2.6.1. The other essential ingredient is the disorder.

2.6.3 Disorder and localization

In spite of the extreme care with which our 2DEG is prepared, there remain some energetic valleys and hillocks along the interfaces, due to residual defects, steps or impurities, and each Landau level maps this irregular landscape. As we change the filling of the Landau level (either changing the Fermi level or adjusting the magnetic field) the electrons keep orbiting on contours that encircle hills or valleys and do not transfer from one side of the sample to another, being then **localized** in those regions. The density of these localized states depends on the amount of disorder and is smaller than the one of the states that can carry current: the situation is sketched in Fig.2.9. Localized electrons provide a reservoir of carriers that keep the Landau levels in the energetically flat part of the sample exactly filled for finite intervals of magnetic field, giving rise to finite Hall plateaus (and not points as the ideal situation). Localized electronic states then lie in the "tails" of the broadened Landau levels.

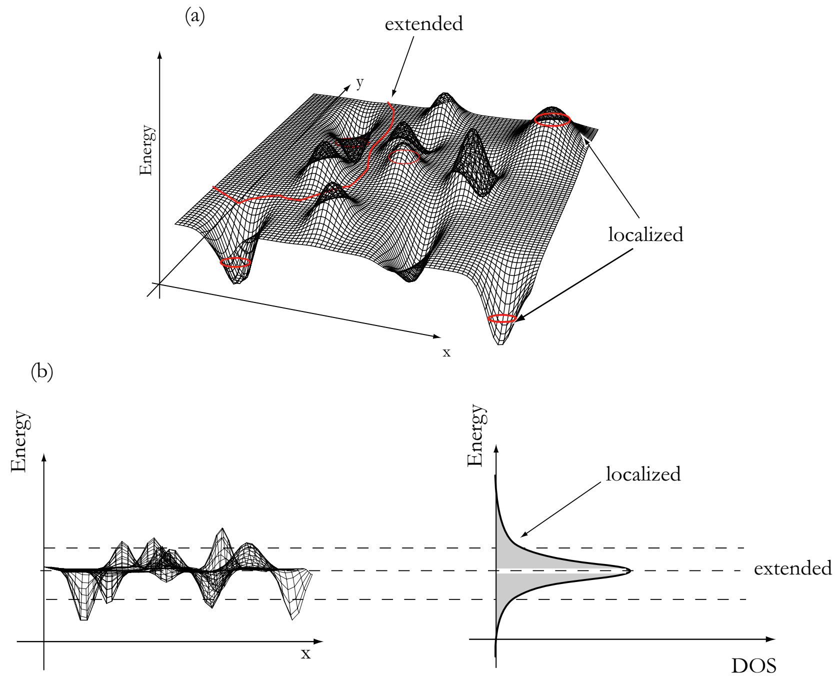

Figure 2.9: (a):Disorder-induced potential landscape with some localized (red circles around valleys and hillocks) and extended electron orbits (red line). (b): cross section of the potential landscape; the Landau level follows the oscillations of the conduction band bottom and the resulting distribution of the density of states is displayed on the right.

It is possible to infer some characteristics of the potential induced by the disorder. Since the electrons are usually separated from the ionized donors by a spacer layer (modulation doping technique [142], we find it also in some of our quantum cascade structures), the core of the Coulomb potential is cut off and leaving only tails. The random potential fluctuations due to the remote ionized donors should have a characteristic lateral scale of approximately the spacer width [143]. One important quantity is the localization length that is the average length over which an electronic state extends in the sample: this value can be tuned by the magnetic field over wide ranges and depends on the landscape of the potential. The scenario that we will find when dealing with long-wavelength THz quantum cascade lasers in strong magnetic field is the one with a strongly diluted 2DEG with sub-unitary filling factor. The typical sheet carrier densities for the injectors of our devices are $5 \cdot 10^{10}$ cm^{-2} (at extremely low temperatures similar low densities led to claim the observation of a Wigner crystal in a 2DEG [144]), giving us a unitary filling factor for an applied magnetic field of B = 2 T. Recent research on imaging of quantum Hall states [145, 146] allowed the construction of a phase diagram of the quantum Hall localization that goes beyond the single particle picture where electrons populate the states of a fixed disorder-induced potential. Coulomb repulsion produces a potential landscape that varies with the filling factor in an attempt to minimize the total electrostatic energy. For our regime of low densities and high magnetic fields the consequence is a formation of dot-like structures with an insulating phase and a mutual spatial separation in the sub-μm range, as visible in Fig.2.10, reprinted from [146].

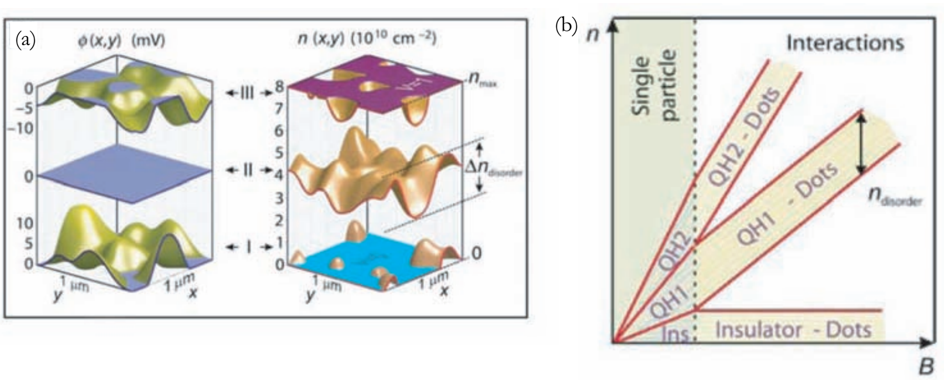

Figure 2.10: (a): Density profile and electrostatic profile for an almost-empty (I), half-full (II), almost-full Landau level (III) in a typical disorder potential (b): a generalized phase diagram for QH localization. Both graphs reprinted from [146]

In Table 2.1 we resume the relevant quantities related to the presence of the magnetic field:

Quantity	Expression
Fermi energy for a free 2DEG E_F	$\frac{n_s \pi \hbar^2}{m^*}$
Cyclotron energy, E_c	$\frac{\hbar e B}{m^*}$
Cyclotron radius, r_c	$\sqrt{\frac{n_s}{2\pi}}\frac{h}{eB}$
Magnetic length, l_B	$\sqrt{\frac{\hbar}{eB}}$
Density of states (2DEG, ideal), D(E)	$\frac{g_S}{2\pi l_B^2}\delta(E-E_n)$
Density of states (2DEG, impurities), D(E)	$\frac{1}{2\pi l_B^2}\sum_n \left[1-\left(\frac{E-E_n}{\Gamma_n}\right)^2\right]^{1/2}$
Filling factor, ν	$\frac{g_s E_F}{\hbar\omega_c} \Longrightarrow \frac{h n_s}{eB}$

Table 2.1: Relevant quantities in presence of a magnetic field applied on a 2-dimensional electron gas.

2.7 Landau level coupling in quantum cascade structures

Up to this point we have given the description of the main phenomena that arise when a quantum well is immersed in a strong perpendicular magnetic field. Now we try to connect the previous information to the QC system that is in fact constituted by coupled quantum wells. The motivation that led us to put a quantum cascade structure in a magnetic field is clear: the confinement induced by magnetic field and disorder in the x-y plane adds to the one ($V(z)$) induced by the heterostructure offering the possibility to change radically the lifetimes of the electrons in the various subbands. Moreover, the confinement induced by the magnetic field is also tunable, adding in fact another "knob" to the toolbox for the engineering of the lifetimes (see before where we talk about population inversion engineering in THz QC's).

Let us consider two subbands denoted by $|1\rangle$ and $|2\rangle$ and separated by an energy difference ΔE_{12}: the application of a magnetic field on this system will give rise to a ladder of Landau states attached to each subband and identified with $|i, l\rangle$ where $i = 1, 2$ is the subband index and $l = 0, 1, 2, ..$ is the Landau index. The scenario of the two subbands in a magnetic field

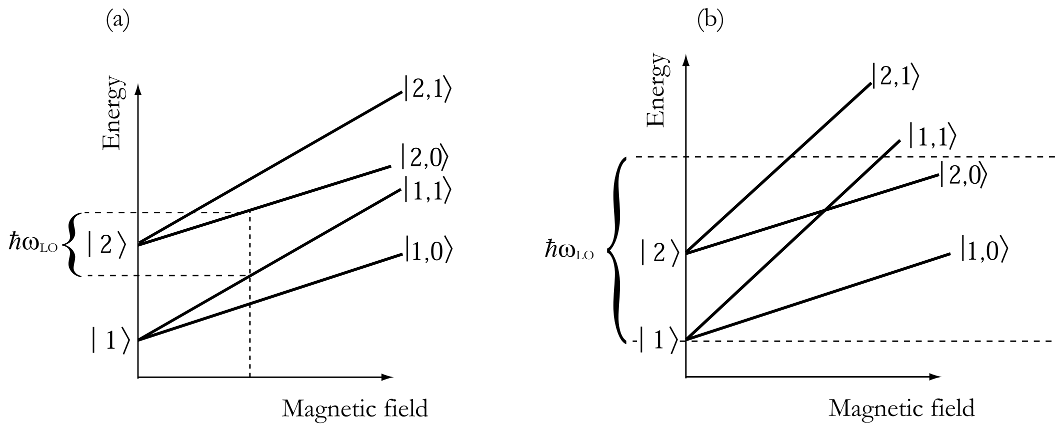

Figure 2.11: (a): evolution of the energy levels of two subbands when the energy spacing ΔE_{12} exceeds the LO phonon energy $\hbar\omega_{LO}$, as it happens in the radiative states of a Mid-IR quantum cascade laser. (b):evolution of the energy levels of two subbands when the energy spacing ΔE_{12} is less than one longitudinal optical phonon, as it happens in the active region of a THz quantum cascade laser.

is depicted in Fig.2.11. We classify the possible transitions between the Landau states in radiative and non-radiative. For the radiative transitions, their selection rules and associated phenomena see section 2.9. Now we will discuss the non-radiative coupling between the Landau levels: the nature of the coupling will strongly depend on the energy separation ΔE_{12}. If $\Delta E_{12} \geq \hbar\omega_{LO}$ (as in Mid-IR quantum cascade lasers) optical phonon assisted scattering is allowed also at low temperatures and this inelastic process will dominate the physics of the system. If the subband separation fulfills the condition $\Delta E_{12} < \hbar\omega_{LO}$ (as for the radiative transition in THz quantum cascade lasers) another mechanism comes into play and the coupling will be elastic via the magnetointersubband scattering.

2.7.1 Inelastic coupling: magnetophonon resonance

Magnetotransport measurements have always been an important tool for the investigation of the physics of semiconductor systems and heterostructures. One effect that is fundamental for the electron-phonon interaction is the so-called magnetophonon effect. In a quantum well, the effect arises whenever the intersubband energy exceeds the LO-phonon energy:

the presence of the magnetic field changes the relaxation spectrum of the carriers and the relaxation is enhanced when an emission of an LO-phonon allows one electron to relax from the ground state of the upper subband $|i, 0\rangle$ to one of the excited states of the lower subband $|i-1, l\rangle$, as depicted in Fig.2.11 (a) for the transition $|2, 0\rangle \longrightarrow |1, 1\rangle$. This effect has been observed in a double quantum well [147] and also via a bipolar process in the intersubband luminescence of a double barrier resonant tunnelling structure [148]. In quantum cascade lasers, such phenomenon has been largely investigated by the group of C. Sirtori in Paris. They observed magnetophonon effects both in transport[149] and light emission [150, 120] on a lasing structure. Especially the light emission measurements constitute a spectacular proof of the "phonon bottleneck" for Mid-IR QC lasers, showing that the freezing of the LO-phonon emission increases the upper state lifetime of the lasing transition. The same group provided also a theoretical framework for the interpretation of the results, [151] studying the electron-phonon interaction between Landau levels in the weak-coupling scenario between electron and phonon (no polaron effects). The energy conservation condition gives rise to the selection rule

$$\Delta E_{21} - \hbar\omega_{LO} = n\hbar e \frac{B}{m^*(E)} \qquad n = 0, 1, 2, ... \tag{2.7.35}$$

and the 1/B analysis of any quantity related to the scattering rate between the two subbands will show peaks separated by $\frac{e\hbar}{m^*(\Delta_0 - \hbar\omega_{LO})}$[151, 120].

For the purpose of our work on THz QC's, this kind of coupling of the levels is of little relevance, because in the structures that we developed the overall energy spacing of the active region plus injector is below the energy of the LO phonon and then this kind of coupling is forbidden. There is a case where the intersubband magnetophonon resonance could play a role in the THz lasers: the structures that include an LO-phonon scattering to depopulate the lower state of the lasing transition (Sec.5.2) could show some resonances related to LO-phonon emission: Those devices will be analyzed in strong magnetic fields in Sec.7.3.1.

2.8 Elastic coupling

2.8.1 Magnetointersubband scattering

If we are in a situation where the subband separation satisfies $\Delta E_{12} < \hbar\omega_{LO}$ as depicted in Fig.2.11 (b), the LO phonon scattering is forbidden by the energy conservation, at least at low temperatures. Direct resonant transfer between Landau states of different index n is in principle forbidden because of the Landau index conservation selection rule $\delta n = 0$ [152]. The presence of scattering by impurities or interface roughness relaxes this condition and magnetotransport evidences of this inter-Landau level scattering were first observed in undoped GaAs-AlGaAs superlattices [153](named Stark-cyclotron resonances due to the Wannier-Stark basis of the superlattice) and then in far-infrared quantum cascade structures by the Vienna group [121] and our group [154, 122]. The selection rule for the energy conservation then becomes:

$$\Delta E_{12} = \hbar\omega_c \delta n \qquad \delta n = 1, 2, 3, ... \tag{2.8.36}$$

Whenever the energy spacing between two levels is a multiple of the cyclotron energy we should observe an enhancement of the scattering rate and a consequent reduction of the lifetime of the upper subband $|2, l\rangle$. A theoretical framework for this phenomenon in a 2DEG has been provided by Raikh and Shahbazyan [155]. They called the enhancement of the intersubband scattering that satisfies Eq.2.8.36 magnetointersubband scattering (MIS). Their calculations include short-range potentials because the intersubband scattering requires a large momentum transfer and occurs in samples dominated by short range disorder caused by impurities or interface roughness. Another key point of the MIS is, in contrast to the Shubnikov-de Haas oscillations (2.6.2) the independence from the Fermi level (see Eq.2.8.36) which should make this scattering event much less sensitive to the temperature leading to the observation of MIS oscillations well above T=4.2 K. The limit of this calculation[155] is set from the condition that the subband energy separation should be much larger than the cyclotron energy $\Delta E_{12} >> \hbar\omega_c$: indeed many experimental observations [121, 122, 156, 157] report observation of conductance oscillations also in the regime where $\Delta E_{12} \approx \hbar\omega_c$. This effect is clearly observed in several experiments both in magnetotransport measurements and in light emission measurements. For the magnetotransport, if we sweep the magnetic field, the experimental signature of the magnetointersubband scattering is a local increase of the current at constant bias due to the opening of this relaxation channel. The general reduction of current as a function of applied magnetic field (positive magnetoresistance) is due to the progressive localization of the electron wavefunction. The strength of the scattering should scale with the inverse of the Landau index change but we [91] and other authors [158] observe quite strong features also for $\delta n = 6$.

2.8.2 Electron-electron scattering in magnetic field

Another theoretical approach, based on the random phase approximation (RPA) has been proposed by Kempa and coworkers. They treat the intersubband electron-electron scattering [159] in quantum wells and its extension to the presence of a strong perpendicular magnetic field [160, 161]. The theoretical treatment leads to the following expression for the scattering rate γ_k out of state k [160]:

$$\gamma_k = \frac{4\pi}{\hbar} \sum_{l,m,p} |V_{kl,mp}|^2 F_{m,p,l} \delta(E_k + E_m - E_p - E_l) \tag{2.8.37}$$

where $|V_{kl,mp}|$ is the term containing the wavefunctions and $F_{m,p,l}$ contains the subband occupations. If we express the Landau energy levels with Eq.2.6.30 ($E_{i,k} = E_i + (k + \frac{1}{2})\hbar\omega_c$) and include level broadening, Eq.2.8.37 will represent maxima of scattering rate versus magnetic field. The energy conservation term expressed by the δ function produces the selection rule for the e-e scattering as a function of the applied magnetic field that includes what found by Raikh with formula 2.8.36: the energy conservation according to Kempa's calculation leads to an enhancement of the e-e scattering rate γ_{el-el} whenever the condition [2]:

[2] The denominator 2 of the fraction n/2 comes from the fact a 2 electron process is considered. Energy conservation then reads: $E_2 + (k+1/2)\hbar\omega_c + E_2 + (m+1/2)\hbar\omega_c - E_1 + (p+1/2)\hbar\omega_c - E_1 + (l+1/2)\hbar\omega_c =$

$$\Delta E_{12} = \frac{n}{2}\hbar\omega_c \qquad n = 1, 2, 3, ... \tag{2.8.38}$$

is satisfied. Specifically, for **odd** values of n the scattering is a Coulomb scattering that only involves two electrons.

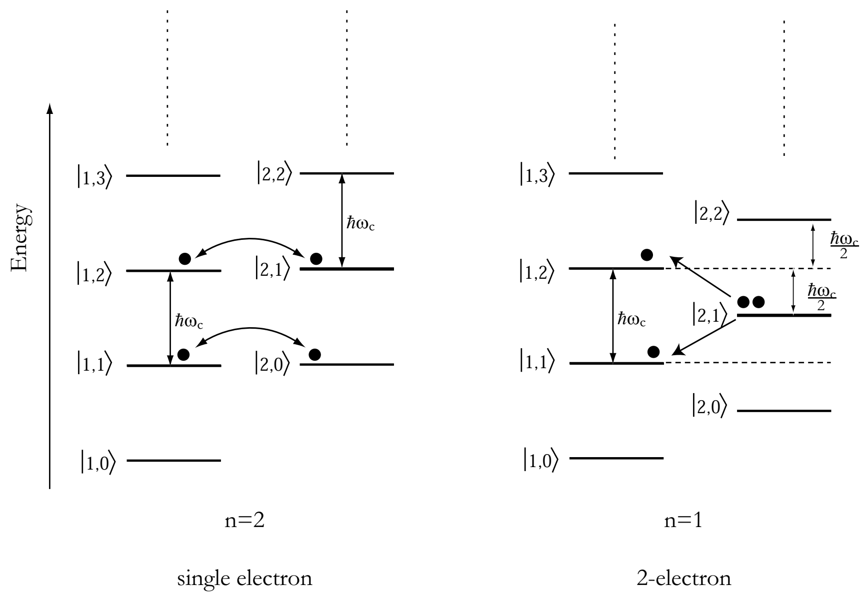

Figure 2.12: Left: Landau level arrangement for our 2-subband model system for n even (n=2) in formula 2.8.38: the Landau ladders are aligned. Right: Landau level arrangement in the case of n odd (n=1): the Landau ladders are midway misaligned. The spin degree of freedom is neglected in this picture.

For **even** values of n the scattering is of mixed type (single-electron coming from interface roughness and impurity scattering). It is worth to note that if we observe the series of values for n even we recover the result of Raikh's paper[155]: whenever we have the ladders of Landau states that are aligned the intersubband scattering rate is enhanced. This is what the Golden Rule would also predict. What is new in the Kempa's theory is the n odd series that accounts for these multi-electron scattering events. In this situation the Landau states attached to the two subbands are midway misaligned. The physical picture of this

---

$2E_2 - 2E_1 + \hbar\omega_c(k + m - p - l) \Longrightarrow 2\Delta = \hbar\omega_c(l - k + p - m)$ where l-k+p-m must be an integer.

selection rule is summarized in Fig.2.12. The strength of this scattering phenomenon has been calculated in Ref.[160] for a two subband system with an energy spacing of 18 meV: two series of scattering rate maxima appear corresponding to even and odd n, as visible in Fig.2.13. The strength of the scattering due to the n even series which correspond to single and double electron events (analogous to Raikh) is higher than the odd series representing the two electron phenomena only.

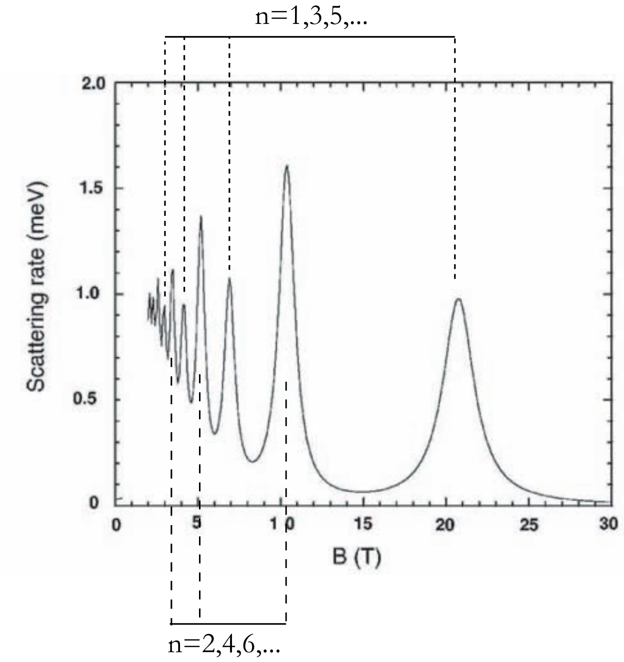

Figure 2.13: Electron-electron scattering rate according to Kempa's theory for a two subband system with an energy spacing of 18 meV: note the different scattering rate for even and odd series. Graph reprinted from [160].

2.9 Optical transitions in Landau levels

Now that the principal non-radiative coupling mechanisms have been analyzed, let us discuss which kind of optical transitions are possible between Landau states and which ones can be observed in our intersubband system.

To find the transition rate and the selection rules when an electromagnetic field couples the eigenstates that we have found in Sec.2.6 we can write Fermi's golden rule as in Ref. [27]

$$\frac{2\pi}{\hbar}|\langle\Psi_i|H|\Psi_f\rangle|^2\delta(E_f - E_i - \hbar\omega) \tag{2.9.39}$$

where this time the eigenfunctions Ψ_i, Ψ_f are constituted by $\Psi_i(x, y, z) = \psi_i(z)\Phi_i(x, y)$ (see Eq.2.6.29). Our electromagnetic radiation field can be expressed [162] in terms of a vector potential $\vec{A}$ with the choice of gauge $\nabla\vec{A} = 0$ that implies $[\vec{A}, \vec{p}] = 0$. The plane monochromatic wave is expressed by $\vec{A} = A_0\widehat{e}[e^{i(\vec{q}\cdot\vec{r}-\omega t)} + e^{-i(\vec{q}\cdot\vec{r}-\omega t)}] = \frac{E_0 e}{2\omega}\widehat{e}[e^{i(\vec{q}\cdot\vec{r}-\omega t)} + e^{-i(\vec{q}\cdot\vec{r}-\omega t)}]$ where $\widehat{e}$ is the unity polarization vector and $\vec{q}$ is the propagation vector of the e.m. wave. The choice of the axes is the same as in Fig.2.6: a linearly polarized electromagnetic wave in the TM mode will have the polarization vector $(0, 0, 1)$. From the complete hamiltonian we can retain the term $H' = -\frac{e}{m^*}\vec{A}\cdot\vec{p}$ neglecting the terms of the order $|\vec{A}|^2$. Following the same line of Ref.[27, 162] we can use the dipole approximation (well justified in the case of THz QC lasers where $\lambda \geq 65\ \mu$m $\gg 50$ nm for a wide quantum well) and the term $e^{i\vec{q}\cdot\vec{r}} = 1 + i\vec{q}\cdot\vec{r} + ...$ can be approximated to 1. We can write the complete expression:

$$\begin{aligned} W_{if} = \frac{2\pi}{\hbar}\frac{e^2E_0^2}{4m^*\omega^2}|\langle\Psi_i|\widehat{e}\cdot\vec{p}|\Psi_f\rangle|^2\delta(E_f - E_i - \hbar\omega) \propto \frac{2\pi}{\hbar}\frac{e^2E_0^2}{4m^*\omega^2}\delta(E_f - E_i - \hbar\omega)\cdot \\ \cdot\left(|\langle\psi_i|\psi_f\rangle\langle k_x, n|p_x|k'_x, n'\rangle|^2 + \right. \\ + |\langle\psi_i|\psi_f\rangle\langle k_x, n|p_y|k'_x, n'\rangle|^2 + \\ \left. + |\langle\psi_i|p_z|\psi_f\rangle\langle k_x, n|k'_x, n'\rangle|^2\right) + \text{mixed terms} \end{aligned} \tag{2.9.40}$$

If we apply the selection rules for the harmonic oscillator $\langle k_x, n|k'_x, n'\rangle \propto \delta_{n,n'}\delta_{k_x,k'_x}$, $\langle k_x, n|p_x|k'_x, n'\rangle \propto \delta_{k_x,k'_x}\delta_{n,n\pm1}$ and $\langle k_x, n|p_y|k'_x, n'\rangle \propto \delta_{k_x,k'_x}\delta_{n,n\pm1}$ we obtain the final expression:

$$W_{if} \propto \delta(E_f - E_i - \hbar\omega) \cdot (\langle\psi_i|\psi_f\rangle\delta_{k_x,k'_x}\delta_{n,n\pm1} + \\ + \langle\psi_i|\psi_f\rangle\delta_{k_x,k'_x}\delta_{n,n\pm1} + \\ + \langle\psi_i|p_z|\psi_f\rangle\delta_{n,n'}\delta_{k_x,k'_x}) \tag{2.9.41}$$

Depending on the polarization of the electromagnetic wave we can observe different optical transitions between the Landau states. If we consider a cavity for a THz laser the polarization is TM, i.e. the electric field is parallel to the growth axis z. Then, the last line of equation 2.9.41 tells us that we can observe transitions only between Landau states with the same index ($\delta_{N,N'}$ gives the selection rule $\Delta N = 0$). Hence, for a THz QC laser there is no possibility to tune the emission with the applied magnetic field because the selection rule allows transitions only between Landau levels that remain equidistant with the applied magnetic field (always neglecting non parabolicity effects that will be treated in Section 6.6.2). It is worth to note that this is the main difference between the Landau level lasers we discussed in the introduction and the THz QC laser developed in this work: it is the breaking of the translational invariance in the growth direction [163] that gives rise to the selection rule on the TM polarization for the intersubband heterostructure laser and makes them not tunable with the magnetic field as it happens with the bulk Ge and Si cyclotron lasers. We are forced to use a cavity which does not allow Landau index change in optical transitions. For the TE polarization (with the electric field vector lying in the plane x-y) we can observe transitions between Landau levels with different index because the selection rule $\Delta N = \pm 1$ holds. In emission we have the phenomenon of Landau emission [164] first observed by Gornik [165]in bulk n-doped InSb.

In absorption, the inter-Landau level absorption or cyclotron resonance is one of the most powerful techniques for the determination of the effective mass in metals and semiconductors [166, 20]. For III-V semiconductors all the frequencies of interest lie in the far infrared or mm parts of the spectrum and mainly two experimental techniques are used: one is to use

Fourier transform infrared spectroscopy with the sample immersed in a magnetic field and then measure the absorption spectrum for different magnetic fields. The other and more simpler technique consists in using a set of narrow band frequency sources (see Chapter 1) that illuminate the sample while the applied magnetic field is swept. By plotting the photon energy $\hbar\omega$ versus the observed resonance field it is possible to determine (in a parabolic subband dispersion) the value of the effective mass with high accuracy $\hbar\omega = \hbar\frac{eB}{m^*}$. Actually one of our THz lasers has been used for a cyclotron resonance experiment [167] demonstrating the suitability of THz QC's as sources for this kind of spectroscopy. Also our own magnetic field measurement setup includes, as an internal detector, a cyclotron resonance detector based on an n-doped InSb element [168] immersed in a magnetic field that can tune the cyclotron energy from 0 to about 22 meV spanning the whole range of frequencies of interest in the FIR and sub-mm region.

Chapter 3

Experimental setup, sample processing and waveguides

In this Chapter I will give some details about the various experimental setups used to perform the measurements presented in this thesis. A section will be devoted to sample processing together with an analysis of the different waveguides employed in the different wavelength range covered by the fabricated devices.

3.1 Electroluminescence and laser emission measurements

For Far-Infrared spectral emission measurements a Fourier transform infrared (FTIR) spectrometer has been used. The main advantage of the FTIR is its high resolution capabilities as it consists of a *Michelson-Morley* interferometer where the resolution is given by the optical path length difference between two interfering light beams. For electroluminescence characterization, an under-vacuum, home-made FTIR has been used: it is described in detail in Ref. [169]. The advantage of measuring under vacuum is clear, given the fact that we have to measure very low signals (some pW, ISB LED has a very poor efficiency) and the THz frequencies are strongly absorbed by water vapor (see Sec.1.2.2). A step-scan technique is used to increase the setup sensitivity. The samples, soldered on a copper mount and electrically connected to two gold pads by gold wire bonding are mounted on the cold finger of a He flow Janis JT-100 cryostat with a maximum testing capacity of four samples. The electrical power is provided by a HP-8114A pulse generator. The injected current is measured using a Model 711 calibrated current probe by American Laser Society. The probe is an electrical transformer placed around the injection current line. The current and the bias on the device are measured by a digital oscilloscope. A phase-sensitive detection scheme is employed, with an EG&G 7260 DSP lock-in amplifier synchronized with the pulse generator. The detection of THz radiation is a challenge by itself: direct coupling into circuitry is difficult because of diffractive limits and conventional photodiodes are impossible to fabricate due to the very low energy of the photons. Pyroelectric infrared detectors are used, but their Noise Equivalent Power (NEP) is in the μW/Hz$^{1/2}$ range. There is active research also in the field of intersubband detectors for THz radiation, and in Sec.A.2 one example is briefly discussed. The extremely small powers that we have to measure in spontaneous emission mode in the THz range are detected with a bolometer, which shows a NEP in the pW/Hz$^{1/2}$ range. We have employed two different liquid He-cooled bolometers based on Si and Ge active elements (IRLabs, Inc. 1808 E. 17th Street Tucson, AZ). The Si-based is the one with the higher responsivity (17550 V/W, [169]) and has been used in the electroluminescence setup. The Ge one has been employed in the magnetic field setup, where laser signals are observed. Being based on a thermal effect, the bolometer is intrinsically a slow detector. Due to its slow response time, the current injected in the sample is modulated into low frequency macro pulses with a repetition rate that matches the bolometer maximum recovery time ($1/\tau_{bol}^{Si}$=416 Hz for the Si, $1/\tau_{bol}^{Ge}$=49 Hz for the Ge). To prevent as much as possible device heating, trains of N micro-pulses with a repetition rate of $1/T$ with $NT = \tau_{bol}/2$ are produced. The maximum possible overall duty factor is 50%.

For laser emission and power measurement, a very simple setup is adopted where a lightpipe collects the THz emission directly from the laser facet, guiding it through a polyethylene window and then to a calibrated thermopile (Ophir, SH5).

3.2 Magnetic field measurements: the setup

The magnetic field measurement setup used throughout this thesis work is the evolution of an existing apparatus extensively described in Ref.[168]. The core of the setup is constituted by a He cryostat equipped by a superconducting coil (Janis Research Company, INC. 2 Jewel Drive, Wilmington, MA) capable to generate a magnetic field of 12 T (14 T employing the Lambda plate refrigerator). The whole setup is illustrated in Fig.3.1. The optical characterization of the samples can be performed in two ways: one insert probe is equipped with an InSb cyclotron resonance detector [164]. The principle of operation of this detector is to induce transitions between the Landau levels created by applying an auxiliary magnetic field on the InSb. By tuning the applied field we tune consequently the energy spacing of the levels that can match the electromagnetic radiation and produce a change in the detector's conductivity. This detector provides great sensitivity but limits the temperature of the measurements to 4.2 K because the auxiliary superconducting coil that provides the magnetic field necessary to tune the detector has to be immersed in liquid He. The wavelength range covered by this detector depends on the intensity of the magnetic field applied: the InSb effective mass is $m^*_{InSb} = 0.0139 m_0$ and this translates in an energy per magnetic field unit of $\hbar\omega_c = 8.324 \cdot B[meV]$. Our tuning superconducting coil is capable of 2.5 T, which limits our bandwidth to about 21 meV (59 μm, 5.1 THz). In this configuration the intersubband signal does not leave the sample tube: electroluminescence measurements in the THz range are possible [168] and further pumping on the sample tube reaching 3 K allows increased sensitivity. The InSb detector allows also spectral characterization but the intrinsic linewidth of our InSb slab is very large (≈ 2.5 meV) which translates in rough information about emission spectra.

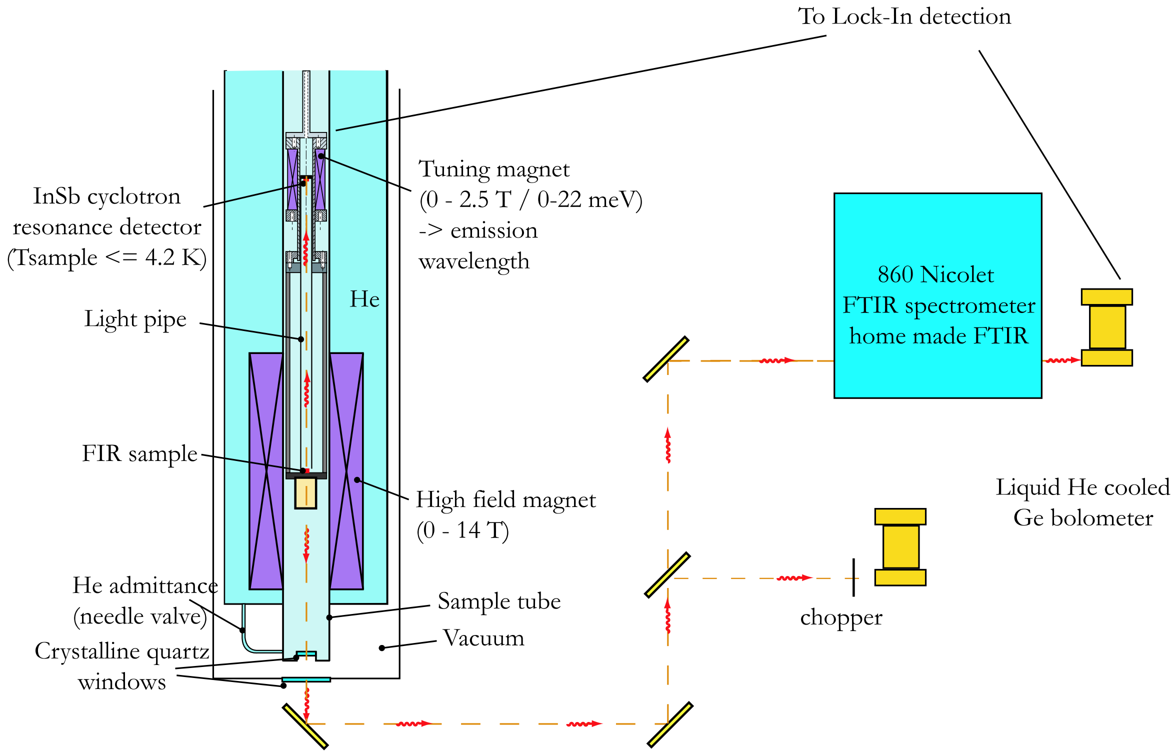

Figure 3.1: Magnetic field measurement setup: radiation path is marked with dashed lines and wavy arrows

The other setup configuration is the one that takes advantage of an optical window at the bottom of the sample tube. The cryostat in the Far-Ir configuration has been equipped with a set of three crystalline quartz windows (2.5 inch diameter, 5 mm thick, Crystran Ltd.) with the transmissivity spectrum shown in Fig.3.2. The sample holder is provided with a mirror that directs the light emission along the axis of the cryostat: the laser emission is then collected by a Fresnel lens (fresnel technologies inc. 101 West Morningside drive, Forth Worth, Texas) of focal length 2.5 cm: the quasi-parallel beam at the exit of the lens is guided with reflective optics and feeded into a Ge bolometer or into an FTIR spectrometer (either Nicolet 860 or custom built). This experimental arrangement allows us to perform measurements in function of the temperature, that can be in principle adjusted between 2.2 K and 300 K.

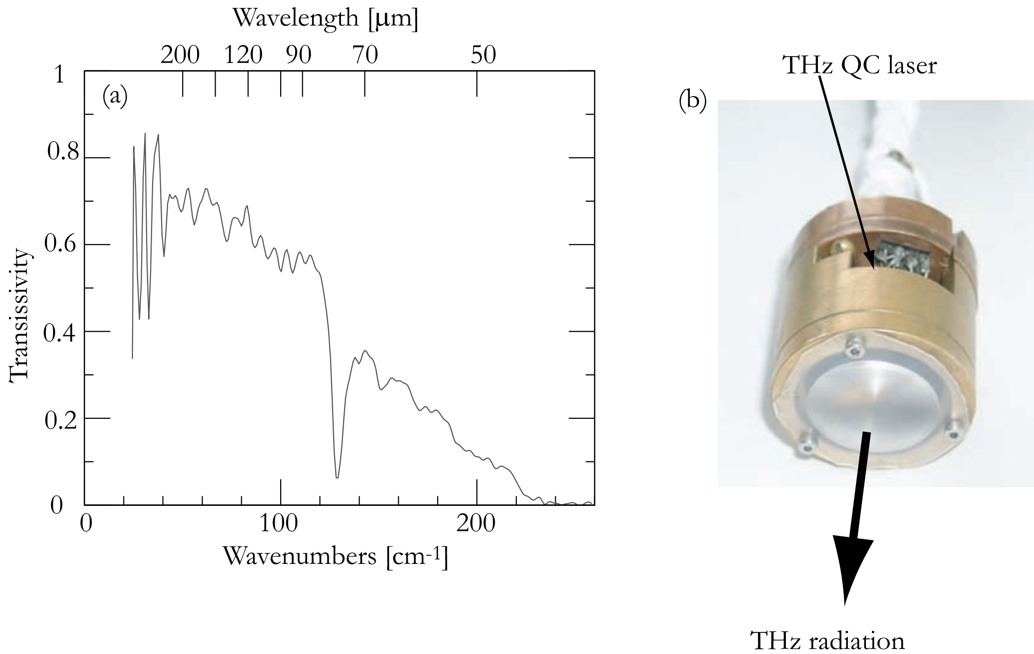

Figure 3.2: (a): Transmissivity of one crystalline quartz window. (b): magnetic field probe equipped with a Fresnel lens of 2.5 cm focal length.

A chopper can be inserted in the light path in order to perform continuous-wave emission experiments in function of the magnetic field. The possibility to use an external FTIR spectrometer increases the spectral resolution of our measurements: in the latest version the apparatus resolution is 0.045 cm^{-1} with an home-made FTIR.

3.3 Waveguides

As exposed in Section 1.4.2, the possible choices for waveguiding in THz QC lasers are essentially two: the single plasmon waveguide [85, 80] and the double metal waveguide [94, 95]. The key point of the single plasmon waveguide is having the optical mode partially overlapping with the active region, while the remaining part of the mode propagating in a virtually lossless region, the semi insulating (SI) substrate. There are at least three parameters that can affect the single plasmon waveguide efficiency: buried layer thickness, buried layer doping and substrate thickness. The buried layer thickness and doping control essentially the overlap and the losses for the optical mode. The substrate thickness has to be chosen in order to avoid high-order modes to be excited in the cavity because, depending on the wavelength, the optical mode starts to bind on the back-metallization (unless this is the desired effect: see Sec.3.3.1 for a waveguide based on the second TM mode).

The double metal waveguide confines the mode almost entirely within the active region (almost 100 % overlap) at the expenses of higher waveguide losses. The situation is resumed in Fig.3.3 where we calculate [1] the waveguide losses α_w and overlap factor Γ for the same active layer (sample N314 presented in Sec. 5.2) in the two cases at a wavelength of 80 μm. The merit factor Γ/α results to be nearly the same in the two cases: what is claimed to be the main advantage of the double metal waveguide is the fact that when writing the complete lasing threshold condition $g = \alpha_w/\Gamma + \alpha_m/\Gamma$ the mirror losses α_m are also reduced by a high value of the overlap factor. The evaluation of the mirror losses in the double metal

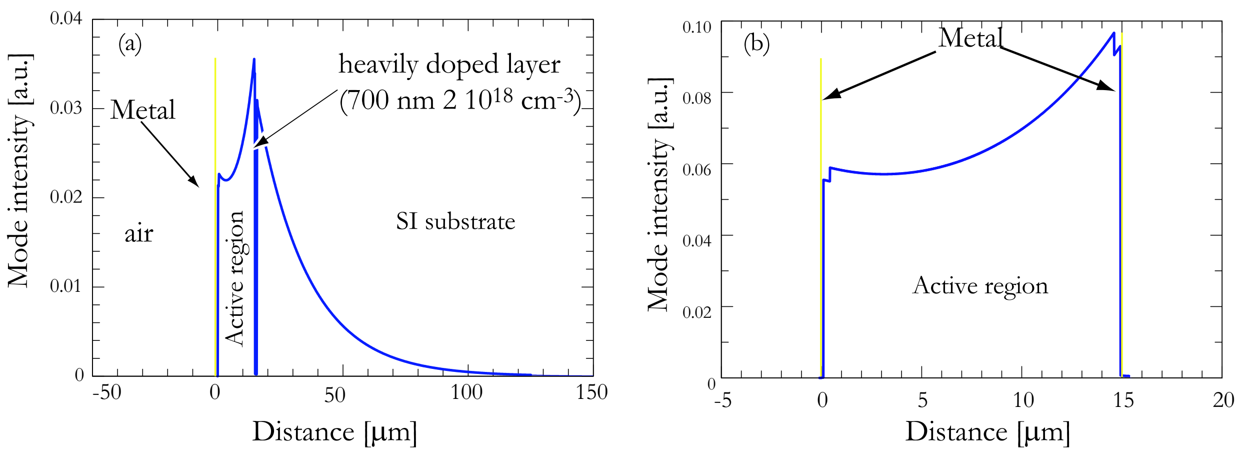

Figure 3.3: (a): Calculated mode intensity for a single plasmon waveguide at 82 μmn for sample N314. (b): Calculated mode intensity for a double metal waveguide at 82 μm with the same epilayer as the single plasmon case.

case necessitates some care because the impedance mismatch created by the narrow aperture and the two metallizations gives rise to a higher reflectivity, and the usual expression that

[1]The calculation of the mode intensity in the cavity is performed numerically solving the Maxwell equation with the transfer matrix method [29]. The losses are evaluated with the Drude-Lorentz model.

employs the refactive index $R = \left(\frac{n_a - n_b}{n_a + n_b}\right)^2$ does not apply anymore. Calculation of the mirror losses based on a mode matching method [170] in the double metal case show higher values for the facet reflectivity [171]. For structure N314 we calculate R=0.97 for each facet. The double metal waveguide is then a "high Q-factor" cavity with respect to the single plasmon: this fact has the drawback that the extracted power is intrinsically low because of the high reflectivity. In any case, mirror losses can be reduced by means of a high reflection coating also in the single plasmon cavity.

Another important aspect of the double metal waveguide is the pumping efficiency of the laser ridge. The "vertical injection" assures a more homogeneous distribution of the electric field in the laser ridge and consequently of the injected current, surely superior with respect to the "lateral" injection in the case of a single plasmon waveguide that uses the buried layer as the current carrying channel. Effects of an asymmetric current injection in a single plasmon THz QC are discussed in Ref.[172]. The buried layer can also introduce a series resistance [173] that can have detrimental effects especially when operating devices at high values of injection current, increasing the amount of heat that has to be dissipated.

3.3.1 Waveguiding at low THz freqencies

Going towards longer wavelengths (low THz frequencies) the waveguide losses will strongly increase because they scale quadratically with the wavelength. With the Drude model [166] it is possible to calculate a frequency dependent permittivity of a material that will translate into a free carrier loss expression [174]:

$$\alpha_{fc} = \frac{n_s e^2 \lambda^2}{8\pi^2 m^* c^3 \tau n} \tag{3.3.1}$$

where τ is the Drude scattering time, m* the effective mass of the electrons in the semiconductor and n is the refractive index. Employing the double metal waveguide below 10 meV could result in a very low extracted power from the device.

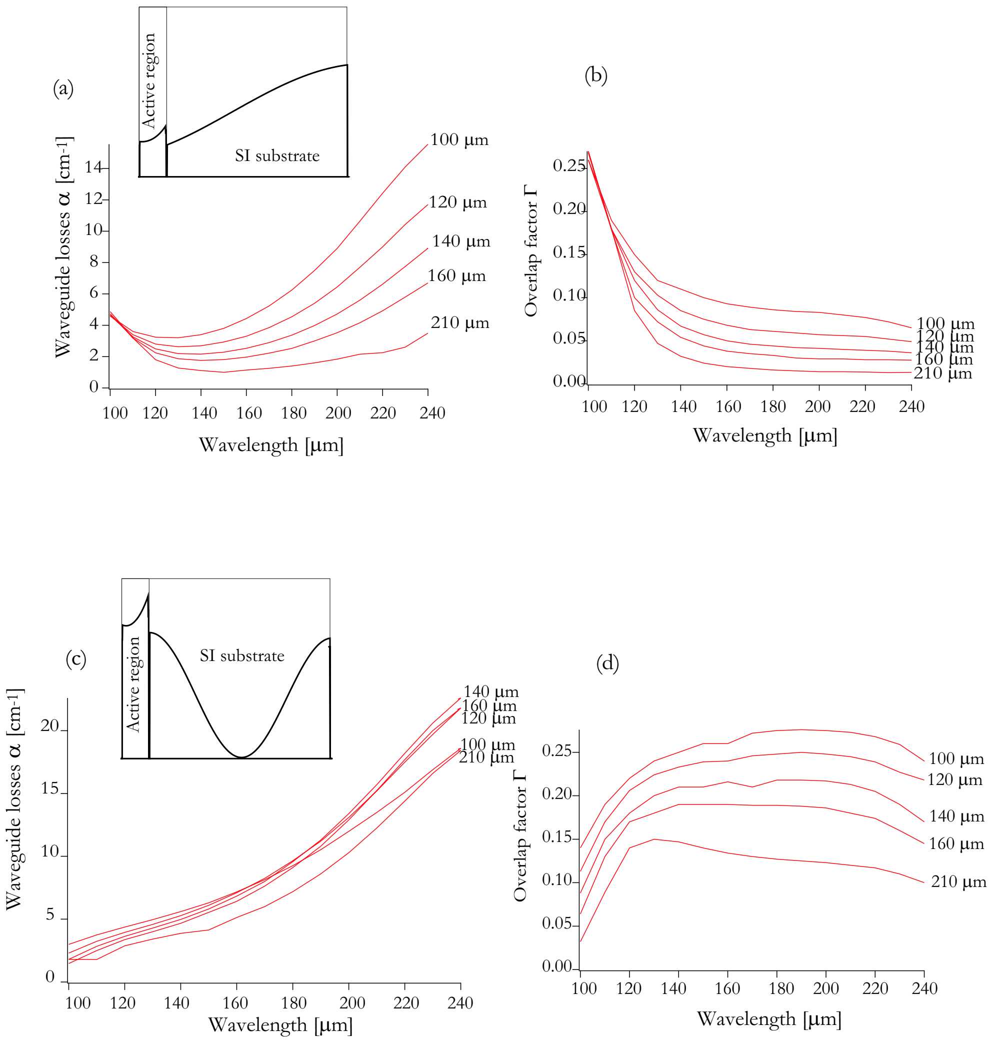

Figure 3.4: (a): calculated waveguide losses in function of the wavelength for different substrate thicknesses for the TM mode n=1 of single plasmon waveguide. (b): calculated overlap factor in function of the wavelength for different substrate thicknesses for the TM mode n=1 of single plasmon waveguide. (c): calculated waveguide losses in function of the wavelength for different substrate thicknesses for the TM mode n=2 of single plasmon waveguide. (d): calculated waveguide losses in function of the wavelength for different substrate thicknesses for the TM mode n=2 of single plasmon waveguide.

On the other side, the single plasmon waveguide is less and less effective as the wavelength is increased. In Fig.3.4(a,b) the overlap factor and the waveguide losses calculated for different substrate thickness for the first TM mode of a single plasmon waveguide in function of various wavelength are reported. The heterostructure used is the 160 μm big well design that will be the object of Section 6.4. The long wavelengths are clearly disfavored by this waveguiding solution. A sort of compromise between the single plasmon and the double metal waveguide is the one that we adopted for the long wavelength big well devices. We exploit the second mode (TM n=2) of a single plasmon waveguide tuning the losses and the overlap factor by changing the substrate thickness. This kind of solution allows to keep a reasonable figure of merit up to very long wavelengths with still a good outcoupling (calculated reflectivity at 160 μm wavelength is 0.67 for n=2 TM mode) and consequently good values of the emitted power.

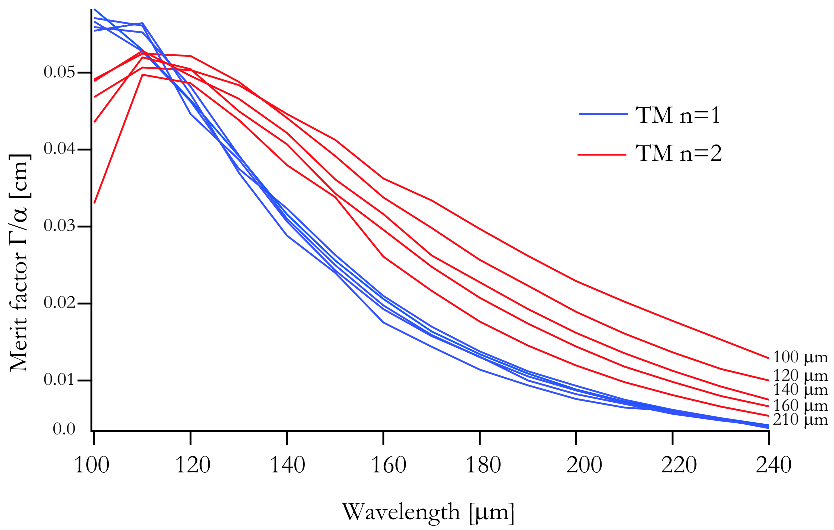

Figure 3.5: Figure of merit for the first (blue lines) and second order mode (red lines) of the single plasmon waveguide in function of the wavelength and of the substrate thickness.

In Fig.3.4(c,d) the values of Γ and α_w for this waveguide solution are reported. Fig.3.5 is a comparative graph for the first and the second mode of the single plasmon waveguide in function of the wavelength and of the substrate thickness. It is evident that above 120 μm the second mode is more advantageous, with still some room for improvement by playing with the substrate thickness. Another couple of parameters that can be advantageously used to fine tune the figure of merit of the single plasmon waveguide are the doping and the thickness of the buried layer.

3.4 Sample fabrication

The structures fabricated throughout this thesis work are semiconductor mesas that are metallized in order to provide electrical contacts and which can be equipped by metallic diffraction gratings (for electroluminescence measurements) or with cleaved facets in order to form ridge optical resonators. To fabricate our structures we use conventional optical litographic processes; the metallizations for waveguiding and/or contacting the structures are performed either via electron beam evaporation or via thermal evaporation. Several ridge widths are employed depending on the wavelength of emission of the device. Roughly speaking, larger ridges are more indicated for longer wavelengths, especially if the single plasmon waveguide is employed [171].

In the case of the single plasmon waveguide, device processing starts by wet etching through the active region in order to expose the buried contact layer, thereby creating $70-110-160-210-320-420-520\,\mu$m wide ridges. The solution $H_2SO_4/H_2O_2/H_2O$ (1:8:1) presents a typical etching speed of 0.14 μm/s when shaking the sample vertically at $\sim$ 1 Hz. This high etching speed is desirable when dealing with very thick epilayer: the typical etch depth is 15 μm but the ridge height can reach 18 μm in the long wavelength devices. Etching is isotropic in respect to the crystallographic directions: in order to have ridges with a positive slope on the sides the wafer has to be aligned with the big flat that indicates $(0\bar{1}1)$ direction parallel to the laser ridges. Two bottom contacts are then evaporated on both sides of the stripes (Ge/Au/Ag/Au 12/27/50/400 nm alloyed at 400 °C during 1 minute). The top contact is provided by two 10 μm wide stripes (Ge/Au 6/13 nm alloyed at 320 °C for 1 minute) deposited along the edges of the ridge. Depending on the growth, an InGaAs top contact layer is present, and the two annealed stripes are not employed. A Ti/Au confining layer is furthermore evaporated which completely covers the top of the stripe. Substrate thinning varies depending on which kind of waveguide is employed. If the first TM mode is used (wavelength range 60-120 μm), the substrate is thinned down to $220 - 240, \mu$m. Backside metallization (Ti/Au) completes the processing of the devices. In the case of longer wavelength devices that exploit the second TM mode, the substrate thinning is pushed down to typically $70 - 100$ μm and the backside is finely polished with a fine diamond disk (1 μm size). Ti/Au back metallization with a thick (500 nm) Au layer completes the mode confinement layer on the substrate side. The devices are then cleaved in laser bars of various lengths and soldered on copper mounts using indium. Au wire wedge bonding (current carrying capability is 250 mA CW at room temperature for a 25 μm $\emptyset$ wire) completes the processing. A SEM picture of a mounted, long wavelength THz QCL is presented in Fig.3.6

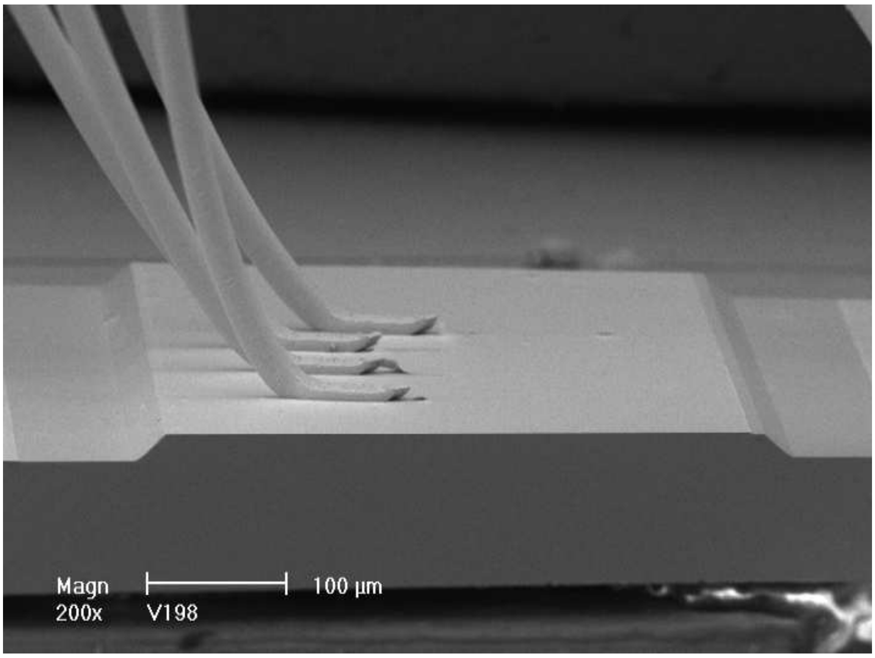

Figure 3.6: Electronic microscope picture of a mounted, long-wavelength THz QCL

The double metal process follows in major lines the one described in Ref. [94]: the epilayer is metallized with Cr/Au (20/1000 nm) and then soldered (10 mins at 250° C) to an n^+ GaAs substrate provided with an In/Au (1200/120 nm) metallization. GaAs substrate is mechanically thinned down to a residual thickness of about 40 μm and then removed with an etchant solution of citric acid and hydrogen peroxyde (H_2O:Citric Acid:H_2O_2 3:3:2 in mass) that is selective on the GaAs/$Al_{0.3}Ga_{0.7}As$ layer. This etching solution has a very good selectivity on 30% aluminium but it is extremely slow ($\sim 0.2\ \mu$m/min). The etch stop layer is then removed together with a part of the doped layer, leaving 400 nm thick of doped GaAs (Si, $2{\cdot}10^{18}$ cm^{-3}). The device is then processed in the standard way defining ridges of various widths (70-220 μm) by lithography, wet etching and a top Cr/Au metallization. For the final result see Fig. 3.7

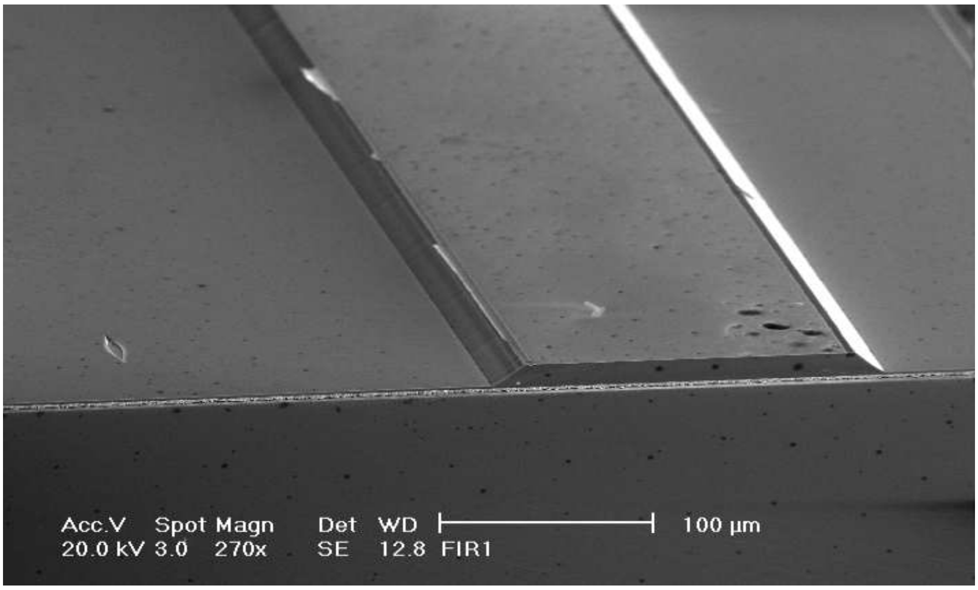

Figure 3.7: SEM image of one double metal ridge waveguide of sample N314; the brighter layer under the ridge is the In/Au soldering layer.

Chapter 4

Single quantum well THz laser

4.1 Introduction

Kazarinov and Suris' proposal of light amplification by means of photon-assisted tunnelling in a biased superlattice found its realization in the quantum cascade laser. A slight variation of the same concept is to obtain laser action via an intra-well transition, injecting carriers in the first excited state of the quantum well that will emit photons relaxing on the ground state of the well, as proposed by Capasso et al.[32]. If the energy of the photon is larger than the LO phonon energy, population inversion will be difficult to achieve because the efficiency of the LO phonon scattering will make the upper state lifetime shorter than the average tunnelling time of the electron out of the ground state (see Fig. 4.1). As suggested in Ref.[32], a more favorable situation would be achieved if the photon energy was smaller than the LO phonon, quenching this fast relaxation channel at least at low temperatures. In this scheme the population inversion will rely solely on the interplay between inter-subband elastic scattering (see Chapter 2) and resonant tunnelling at the injection and at the extraction of carriers from the quantum well. The structure will be divided in two sections: one active region, where the optical transition occurs, constituted by a single quantum well and a four-well injector which will act as a carrier reservoir and will contain the dopants. The design is an almost exact replica of one of the first THz intersubband emitters (Ref.[79]).

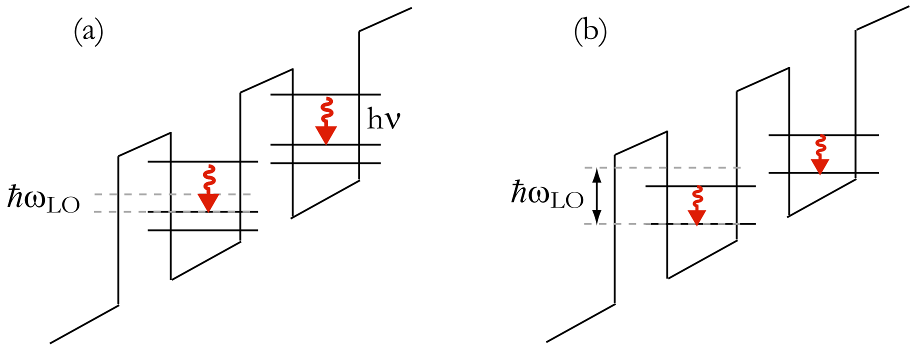

Figure 4.1: (a): schematic of the proposal for an intersubband laser from a biased superlattice with $h\nu > \hbar\omega_{LO}$. (b): proposal for an intersubband laser with $h\nu < \hbar\omega_{LO}$

4.2 Bandstructure analysis

The structure of sample N471 is constituted by five quantum wells and the layer sequence is reported in the caption of Fig. 4.2. The upper state of the lasing transition is constituted by the first excited state of the 28 nm-wide GaAs quantum well (state $|6\rangle$) that anticrosses with the ground state of the adjacent injector well ((state $|1'\rangle$) for an applied electric field of E_{res}=2.9 kV/cm giving rise to a doublet with a calculated energy splitting of $2\hbar\Omega_{61'} = 0.69$ meV . The lower lasing state is the ground state of the same well (state $|5\rangle$) and the extraction of the carriers is achieved via tunnelling in the adjacent quantum well (state $|4\rangle$). The strong doublet formed by the extraction barrier ($Al_{0.15}Ga_{0.85}As$, 2.3 nm) yields a value of $2\hbar\Omega_{54} = 2.7$ meV for the energy splitting. The photon energy $E_{65} = 15.2$ meV and the dipole matrix element $z_{ij} = 6.6$ nm yield a value of 18 for the oscillator strength. The growth has been performed on a semi-insulating substrate in order to exploit the low-loss single-plasmon waveguide configuration [85]: the intensity of the first transverse magnetic (TM) mode in the cavity is reported in the inset of Fig 4.4 : for the chosen buried contact layer thickness (500 nm) and doping (Si, 2×10^{18} cm^{-3}) we obtain a theoretical value for the waveguide losses $\alpha_w = 4.4$ cm^{-1} and an overlap factor $\Gamma = 0.35$.

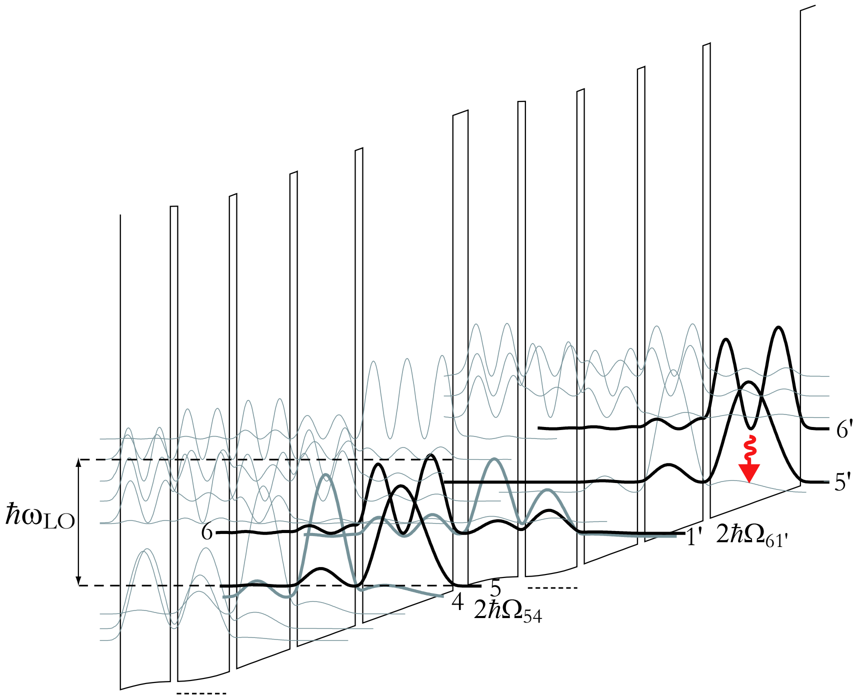

Figure 4.2: Computed conduction band profile at T= 20 K of two periods of the structure under an average applied electric field of 2.9 kV/cm. The GaAs/$Al_{0.15}Ga_{0.85}As$ layer sequence of one period of the active layers starting from the injection barrier is as follows: **4.7**/28.0/**2.3**/18.0/**2.3**/16.5/**2.3**/<u>16.0</u>/**2.3**/15.5/**1.5**. Thicknesses are in nanometers, GaAs wells are in roman, $Al_{0.15}Ga_{0.85}As$ barriers in bold and doped layer (Si $2.4 \cdot 10^{16}$ cm^{-3}, Ns=3.84 $\times 10^{10}$ cm^{-2}) is underlined.

4.3 Experimental results

The transport and spontaneous emission characteristics for sample N471 are reported in Fig.4.3 for a short, side cleaved device [175] measured at T=10 K. The electroluminescence intensity presents a typical square root dependence on injected current, signature of the presence of electron-electron scattering [79] that affects the upper state lifetime. The spontaneous emission spectrum can be fitted by a Lorentzian, centered at 15.5 meV and with a full-width at half-maximum $2\gamma \cong 1$ meV. The linewidth is very narrow as expected for a vertical transition in the Far-IR [79]. The full-width at half maximum can be written (in energy units):

$$2\gamma = \hbar \left(\frac{1}{T_1} + \frac{2}{T_2} \right) \tag{4.3.1}$$

where the T_1 is the relaxation time that accounts for intersubband processes and T_2 is the intraband dephasing time, also described as in-plane relaxation time τ_p. In the Far-IR, where optical phonon emission is forbidden at low temperatures, we expect, as already discussed in Sec. 2.3.1, an intersubband lifetime in the range of tens of ps for vertical structures with electron densities of 3-8 10^{10} cm^{-2}. From previous work on quantum well system and QC lasers [176, 135], the value of T_2 sits in the 100-200 fs range for relatively narrow quantum wells. Interface roughness surely plays a major role in this context, and the wide QW used in this design should present a longer dephasing time. The condition $T_1 >> T_2$ allows us to calculate the value of T_2 from the luminescence linewidth, and Formula 4.3.1 yields $T_2 = \tau_p \cong \frac{\hbar}{\gamma} \approx 1.3$ ps.

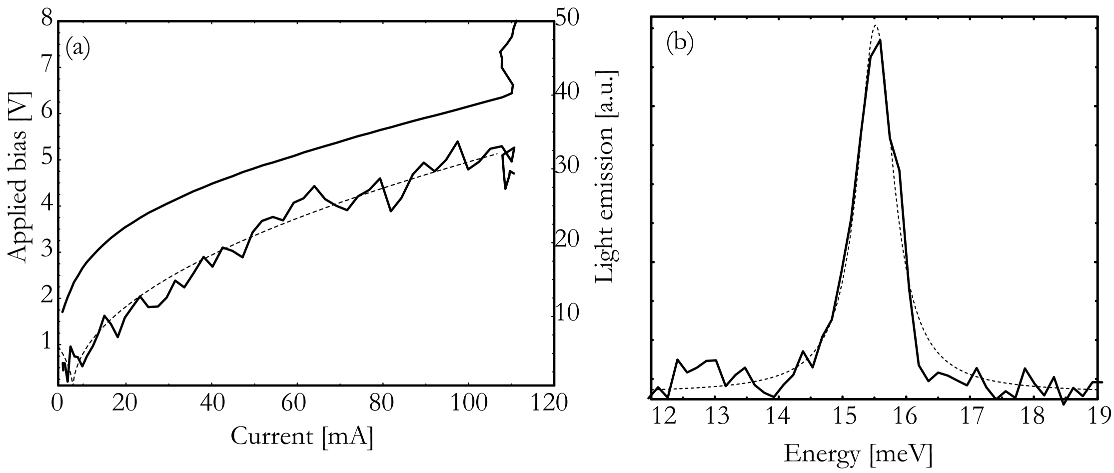

Figure 4.3: (a): I-V curve and spontaneous emission intensity for a side-cleaved device. The dashed line is a square-root fit of the spontaneous emission. (b): Spontaneous emission spectrum measured at I=130 mA. Full width at half maximum is 2γ =1 meV. The dashed line is a Lorentzian fit. The slight asymmetric shape of the spectrum on the high energy side is due to an absorption line of the bolometer window at 16.3 meV.

Laser processing follows the usual guidelines already described in Chapter 3, with ridge widths varying from 100 to 520 μm. Laser action takes place at 15.5 meV ($\lambda \simeq 79.7$ μm) (see Fig.4.4(b)), in the center of the electroluminescence spectrum 15.5 meV and is in very good agreement with the calculated value of the $|6\rangle \longrightarrow |5\rangle$ transition. Pulsed operation up to 30 K and CW operation up to 15 K are demonstrated in narrow stripes (160 μm): typical CW characteristics are shown in Fig.4.4(a).

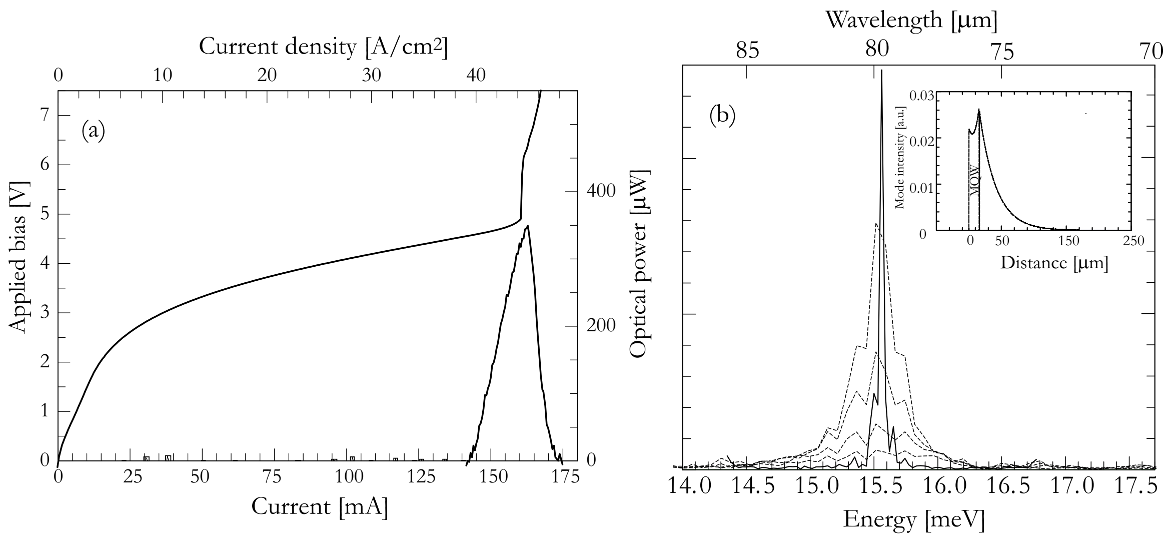

Figure 4.4: (a): CW L-I-V curve for a for a 2.24 mm long, 160 μm wide stripe. (b): Subthreshold electroluminescence spectra (dashed lines) for different values of the injected current and lasing spectra(full line)just above threshold at T = 10 K. Note the progressive narrowing of the spectrum as injected current grows. Inset: calculated mode profile for the single plasmon waveguide: at 80 μm we obtain α_w=4.4 cm^{-1} and $\Gamma = 0.35$.

The threshold current density is $J_{thresh} = 37$ A/cm^2, very low as expected from a vertical transition structure with large oscillator strength and narrow electroluminescence linewidth. Optical power reaches 350 μW for a dissipated power of 750 mW. Laser action is quenched as the injector state is out of resonance with the upper state of the lasing transition at 45 A/cm^2. The bias at threshold is 4.45 V and matches well the theoretical value $V_{theo} = F_{res} N_p L_p =$ 4.36 V obtained by multiplying the electric field just before the resonance between injector and upper state by the number of periods N$_{per}$=140 and the period length $L_p = 1079$ Å.

This good agreement shows that the series resistance is almost negligible for this cavity width. Processing the sample in larger stripes reduces the waveguide losses and allows the demonstration of pulsed operation up to 40 K with slightly lower values for the threshold current density reaching 30 A/cm^2 in the larger stripes (520 μm): typical characteristics for a wide stripe are plotted in Fig.4.5(a). Emitted peak power in pulsed mode reaches 3 mW for very low duty cycles (10^{-4}). CW operation is also possible up to 30 K with optical powers that reach 3 mW, thanks to the very low threshold current density that allow CW operation also in sizeable devices. The increased cavity width introduces a series resistance that is detectable from the increased bias at threshold. Surprisingly, the dynamic range of the samples is increased, showing pronounced misalignment feature at about 80 A/cm^2. It is interesting to note that rollover in light emission happens much before, at about 60 A/cm^2.

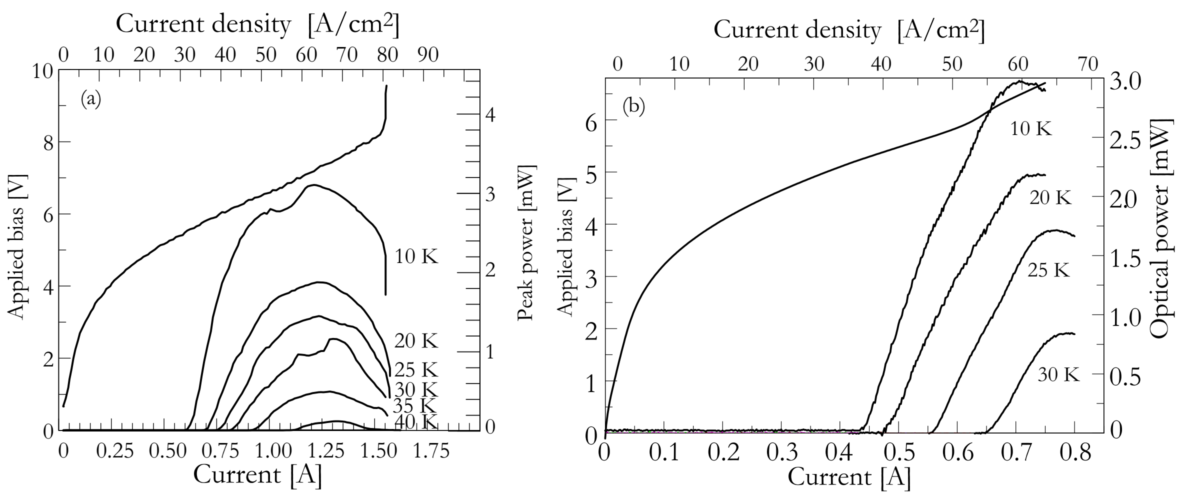

Figure 4.5: (a): pulsed optical power as a function of injection current of a 3.6 mm long, 520 μm wide device at various temperatures together with IV curve of the device at 10 K. (b): continuous wave optical power and applied voltage as a function of injected current from a single facet of a 3.6 mm long, 320 μm wide device, at various temperatures, as indicated.

4.4 Model

The single quantum well laser is the QC laser which comes closest to the original proposal of Kazarinov and Suris. Here we propose a semiclassical modelling of the structure that includes the transport description at the injection barrier illustrated in Sec.2.5 together with the presence of the optical field, as previously done by Sirtori et al.[135]. We will try to go one step further analyzing the transport of a lasing device in order to deduce the lifetimes at threshold. Adopting the same nomenclature as in Ref.[135], we can write the system of coupled equation comprehending Kazarinov and Suris formula for the resonant tunnelling at injection together with a 2-level rate equation system. The photon flux per period per stripe width is denoted by S, τ_p is the in-plane dephasing time, n_s is the sheet carrier density, $\hbar\Delta$ is the energy detuning from resonance and $\sigma = g_c\bar{c}$ ($\bar{c} = c/n$). If we label with V_c the applied bias at resonance (with $V_c = N_p L_p F_c$), the applied bias V and Δ are related by the equation $\Delta = \left(\frac{V}{V_c} - 1\right) \frac{V_c e}{N_p \hbar} \frac{d_{61'}}{L_p}$ where N_p=140 is the number of periods of the active region in the laser structure and $d_{61'} = 28$ nm the distance between the wavefunctions centroids.

$$J = e\ n_s\ \frac{2|\Omega|^2\ \tau_p}{1 + \Delta^2\ \tau_p^2 + 4|\Omega|^2\ \tau_p\tau_6} \tag{4.4.2}$$

$$n_6 = \tau_6 \left(\frac{J}{e} - S\bar{c}\alpha_{tot}\right) \tag{4.4.3}$$

$$S = \frac{1}{\bar{c}\alpha_{tot}\tau_6}\left[\frac{J}{e}\left(\tau_6 - \tau_5\right) - \frac{\alpha_{tot}\bar{c}}{\sigma}\right] \tag{4.4.4}$$

The basic assumptions beyond this model are the unity injection efficiency in the state $|6\rangle$ and the presence of only two scattering times: τ_6 describes the upper state lifetime of the lasing transition and τ_5 represents the extraction time from state $|5\rangle$. The current density J circulating in the structure is related to the lifetime τ_6 by the equation $\tau_6 = \frac{en_6}{J}$. The solution of the system of equations 4.4.2,4.4.3 and 4.4.4 allows us to obtain an expression for the transport below (S=0) and above (S>0) the lasing threshold. For the transport in the lasing regime spontaneous emission has been neglected. Equation 4.4.5 accounts for the transport below lasing threshold, depending only on the in-plane scattering time τ_p and on the overall upper state lifetime τ_6.

$$\Delta_{S=0} = -\sqrt{\frac{2\Omega^2 n_s e}{J\tau_p} - \frac{4\Omega^2\tau_6}{\tau_p} - \frac{1}{\tau_p^2}} \tag{4.4.5}$$

The inspection of Eq. 4.4.6 shows that the presence of the photon field and the lasing condition introduces the dependence on the lifetime of the lower state τ_5 that accounts for the population inversion.

$$\Delta_{S>0} = -\sqrt{\frac{4\Omega^2\tau_6^2}{\tau_5\tau_p} - \frac{4\Omega^2 e\tau_6}{J\tau_5\tau_p}\frac{\alpha_{tot}\bar{c}}{\sigma} - \frac{(J - 2\Omega^2(n_s e - 4J\tau_6))}{J\tau_p}} \tag{4.4.6}$$

Now the transport of a lasing structure can be fitted. By calculating the gain cross section g_c (see Section 2.2.2) and using the parameters measured on the luminescence sample we can reproduce the I-V curve of the lasing sample discussed in the previous Section. For the total losses $\alpha_{tot} = \alpha_w + \alpha_m$ we used the value of 9.5 cm^{-1}, where the contribution of the waveguide losses is $\alpha_w \cong 4.4$ cm^{-1} [1] and the mirror losses are evaluated for a $L_{\text{cav}} = 2.24$ mm long cavity with the usual formula

$$\alpha_m = -\frac{1}{2\,L_{\text{cav}}} ln\,(R_1 R_2) \tag{4.4.7}$$

where the facet reflectivity R=0.32 has been evaluated with the mode matching method [170].

The parameters left free in the transport model are the upper state lifetime τ_6 and the energy splitting at resonance $2\hbar\Omega_{61'}$. To highlight the presence of the optical field in the laser cavity and its influence on the transport, we performed an analysis of the differential resistance of the device. The results are plotted in Fig.4.6(a).

The agreement between the experimental curve and the calculated one is good. The deduced upper state lifetime is $\tau_6 = 65.4$ ps with an energy splitting $(2\hbar\Omega_{61'})_{\text{exp}} = 0.26$ meV. The deduced value of the anticrossing splitting is smaller than the calculated one $(2\hbar\Omega_{61'})_{\text{theo}} =$

[1] The consistency with experimental results has been verified with a 1/L measurement technique.

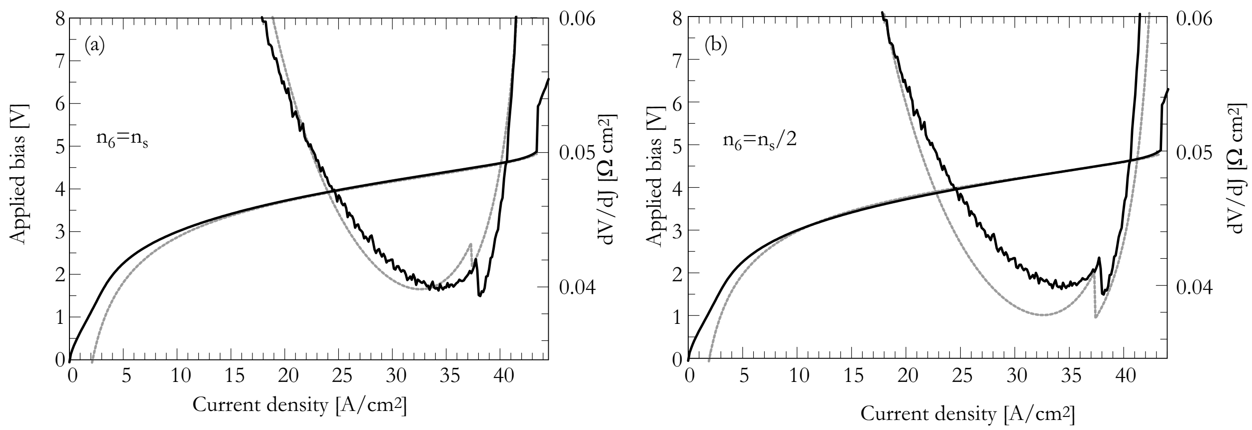

Figure 4.6: (a): a): V-J and dV/dJ curves at T = 10 K (solid line) together with the theoretical curves (dashed grey line) expressed by equations 4.4.6 and 4.4.5 and their derivatives for $n_6 = n_s$. (b): V-J and dV/dJ curves at T = 10 K (solid line) together with the theoretical curves (dashed grey line) expressed by equations 4.4.6 and 4.4.5 and their derivatives for $n_6 = n_s/2$.

0.7 meV. From the analysis of the differential resistance we observe the typical discontinuity at threshold caused by the reduction of the upper state lifetime due to stimulated emission [135]. The model accounts for this quantity and we can deduce also the lower state lifetime being equal to $\tau_5 = 62$ ps. As already demonstrated elsewhere [173] using this same model, the ratio of differential resistances above ($R_{S>0}$) and below ($R_{S=0}$) threshold is directly related to the slope efficiency and it is a measurement of the population inversion via the relation

$$\frac{R_{S>0}}{R_{S=0}} = \frac{\tau_5}{\tau_{eff} + \tau_5} \Longrightarrow \tau_5 = \frac{\tau_{eff}\frac{R_{S>0}}{R_{S=0}}}{1 - \frac{R_{S>0}}{R_{S=0}}} \tag{4.4.8}$$

where in our case the effective lifetime is $\tau_{\text{eff}} = \tau_6 - \tau_5$. From a systematic measurement of the threshold current density as a function of the cavity length we can deduce the quantity $g\Gamma$ using the formula:

$$J_{tresh} g\Gamma = \alpha_w - -\frac{1}{2\,L_{\text{cav}}} ln\left(R_1 R_2\right) \tag{4.4.9}$$

With the measured value $g\Gamma = 0.23$ cm/A we can estimate the effective lifetime value via the expression $\tau_{eff} = (g\Gamma)_{exp} e/g_c \cong 3$ ps. This value for τ_{eff} matches well with the one that we deduce from the fitted lifetimes $\tau_6^{fit} - \tau_5^{fit} \cong 3.4$ ps. Using equation 4.4.8 and the measured values for the differential resistance we can again deduce the lower state lifetime $\tau_5 = 43$ ps. There is a mismatch in the deduced lifetimes that look quite long if compared to previously deduced values on very similar structures using activation energy and the comparison with LO phonon scattering rates [131]. One clear source of an artificially long lifetime is intrinsic to the model we have used. The upper state lifetime is essentially fixed from the critical current density J_{max} (see Sec.2.5): at resonance the Kazarinov model equally distributes all electrons between the injector state and the upper state ($J_{max} \propto \frac{en_s}{\mathbf{2}\tau_6}$). This assumption is justified in the case where we have very short extraction times and the electrons can cross the entire injector region in a very short time: those condition are quite well satisfied in Mid-IR QCL's. In the Far-IR this assumption is too strong: there is a non-negligible part of the electrons that populate the lower state and the rest of the injector. This will lead to a reduced population of the upper state at resonance, that will translate in a shorter lifetime. To give an idea of the importance of this effect, we run the model by supposing the upper state density being half of the nominal value. This is done in order to account for the missing electrons.

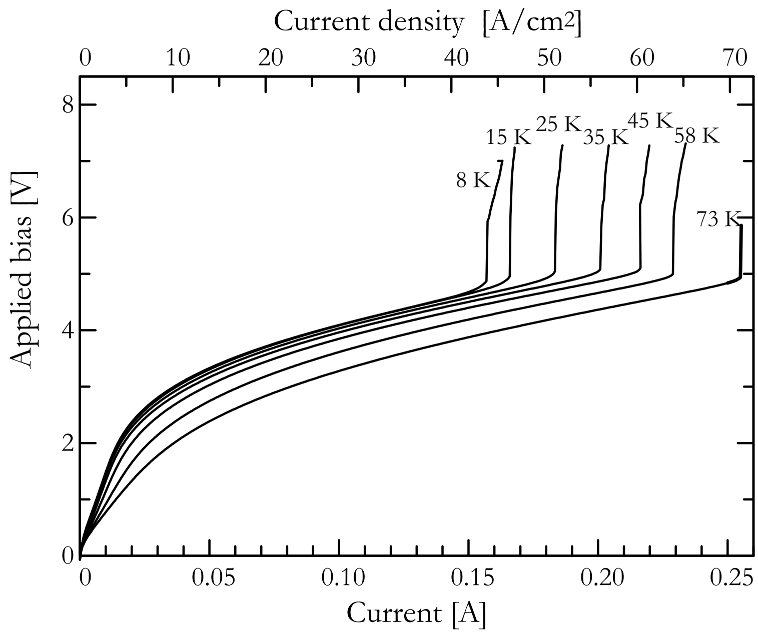

Figure 4.7: Transport as a function of heatsink temperature for sample N471.

The results are reported in Fig.4.6(b). The agreement of the model with the data is still good and the deduced values for the lifetimes are $\tau_6^{n_s/2} = 34.3$ ps and $\tau_5^{n_s/2} = 30.9$ ps (with a deduced $2\hbar\Omega_{61'} = 0.38$ meV). It is interesting to note that the effective lifetime $\tau_{eff}^{n_s/2} = \tau_6^{n_s/2} - \tau_5^{n_s/2} = 3.4$ ps remains the same. Another condition of the model that can be relaxed in future simulations is the assumption of a constant upper state lifetime. As shown in the first part of the Chapter, there are signatures of electron-electron scattering that affects the upper state lifetime and will most likely change as a function of the carrier density. It is interesting to observe the change in transport as a function of temperature and deduce some indications on the evolution of the lifetimes. The I-V curves as a function of temperature are plotted in Fig.4.7. The critical current at resonance J_{max} increases considerably already in the interval 8-15 K confirming a strong temperature dependence of the upper state lifetime. This dependence is the principal cause of the fast degradation of the laser performances: the upper state lifetime decreases rapidly and population inversion is lost already at 40 K.

4.5 Conclusions

We demonstrated laser action in the THz range for a structure closely related to the early proposals for the QC laser. A simple model based on resonant tunnelling and rate equations accounts for the observed results and yields values for the relevant lifetimes in the structure. Deduced lifetimes are elevated but still in good agreement with what observed by pump and probe experiments. The overall simplicity and cleanliness of the system makes it an ideal model for the study of electron dynamics in the Far-IR.

The devices exhibit remarkably low values for the threshold current density that allow CW operation with reasonable values of the output powers (1 mW) with an extremely low electric power dissipation (typically 500 mW-1 W) at cryogenic temperatures. This aspect, together with the narrow gain spectrum due to the vertical nature of the radiative transition makes this device also a good candidate as a local oscillator source for heterodyne spectroscopy [177].

Chapter 5

Bound-to-continuum THz quantum cascade lasers

5.1 Bound-to-continuum design

With the objective of increasing the performance of the THz QC lasers both from the point of view of the maximum operation temperature and of the emitted power, a change in the design strategy of the active region is necessary in order to overcome the issues highlighted in the analysis of the single quantum well device. The design freedom inherent to intersubband transitions and the results of the research on Mid-IR QCL's lead to a solution where the optical transition takes place between states delocalized over more than one quantum well. The first active region that showed laser action at terahertz frequencies [85] was based on a chirped superlattice design [50, 157]. In such designs the upper and lower state wavefunctions extend over several (three for the terahertz lasers) coupled quantum wells. "Chirping" the quantum well and barrier thickness then restores the large dipole matrix element existing between the states at the edge of the minigap [50]. Terahertz quantum cascade lasers based on these designs demonstrated good performance levels with maximum pulsed operation temperatures of about 60 K and peak powers of the order of 4 mW. CW operation was also demonstrated in such designs [178, 172, 179] with reasonable output powers ($\simeq$ 4 mW at 10 K) up to 40 K [179]. The main limitations in the performance of these devices, namely the poor slope efficiency ($\frac{dP}{dI}$) and the low maximum operating temperatures, are attributed to thermal backfilling of the lower miniband and a weak population inversion.

To overcome these problems, an active region based on a bound-to-continuum transition[51] has been conceived. Long-wavelength ($\lambda \simeq 16\mu m$), high performance QC lasers operating above room temperature have already been demonstrated using this design concept [180, 181]. In this design, electrons are injected into an isolated state created inside the minigap by a thin well adjacent to the injection barrier, whilst electron extraction occurs through a lower miniband (see Fig. 5.1). Owing to the diagonal nature of the laser transition, both the injection efficiency and lifetime ratio (upper to lower state) are maximized, whilst miniband transport is employed as an efficient extraction mechanism to minimize the lower state population. It is the combination of long lifetime and good injection efficiency of the upper state with an excellent extraction efficiency of the lower state that is especially advantageous in terahertz QC lasers, where population inversion is difficult to achieve.

5.1.1 Bound-to-continuum QC laser at 87 μm

The bandstructure of such a QC laser, sample A2771 , emitting at $\lambda \simeq 87\mu$m (3.5 THz, $h\nu \simeq 14.5$ meV) is presented in Fig. 5.1 and is obtained by solving Schrödinger and Poisson's equations self-consistently, assuming a thermal electron distribution in the injector region of the structure. The radiative transition occurs between level n= 8, isolated in the minigap, and a group of three states n=7,6 and 5 in the lower miniband. Because of level broadening, caused by interface roughness and impurities, we were not able to identify these states individually in the intersubband luminescence or magnetotransport measurements. Furthermore, because of the diagonal nature of the laser transition, the total oscillator strength of the radiative transitions, f = 29, is significantly lower than the one computed in our previous work on chirped superlattices (f = 40, with $h\nu$ = 19 meV), but larger than in the single QW case.

Fabrication of the devices relied on molecular beam epitaxy (MBE) in the GaAs/AlGaAs material system. The structure consisted of 120 repetitions of the active region embedded in

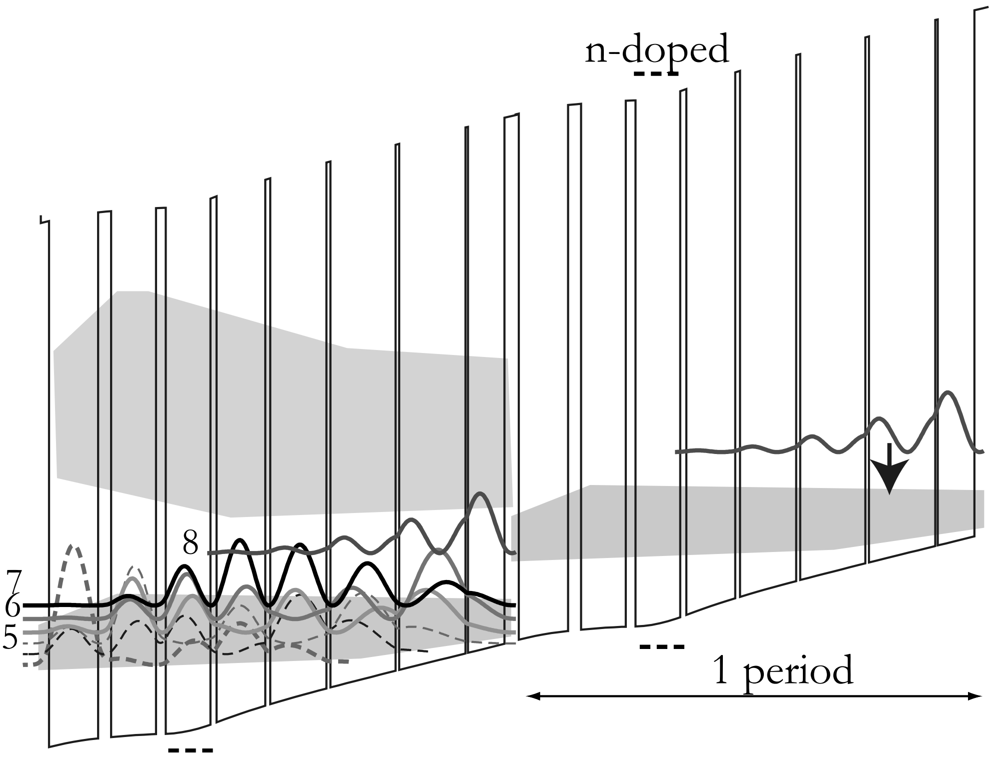

Figure 5.1: Computed conduction band profile at T=40 K of one stage of the structure under an average applied electric field of 2.55 kV/cm. The GaAs/$Al_{0.15}Ga_{0.85}As$ layer sequence of one period of the active layers starting from the injection barrier is as follows: **3.5**/9.0/**0.6**/16.3/**0.9**/16.0/**1.0**/13.8/ **1.2**/12.0/**1.5**/<u>11.0</u>/**2.4**/11.0/**3.2**/12.1. Thicknesses are in nanometers, GaAs wells are in roman, $Al_{0.15}Ga_{0.85}As$ barriers in bold and doped layer (Si $2.5 \cdot 10^{16}$ cm^{-3}) is underlined.

a single plasmon waveguide, using the same approach as described in Ref. [88]. Compared to the structure already published [88], the longer operating wavelength of this laser enabled the use of a waveguide that employed a thicker (700 nm instead of 300 nm) buried heavily ($2 \cdot 10^{18} cm^{-3}$ Si) doped layer whilst still maintaining a large value of the Γ/α_w parameter (where Γ is the overlap factor and α_w are the waveguide losses). The ridge waveguide devices with lateral contacts are processed using wet etching and three metallization steps [178]. After junction-up soldering onto a copper block and wire bonding, the devices are mounted on the cold finger of a helium-flow cryostat.

5.1.2 Optical measurements

In a first set of experiments, the devices were driven by 200-ns-long pulses at a 125 kHz repetition rate. Light versus current characteristics for a 2.7 mm long and 200 μm wide device are shown in Fig. 5.2 for various temperatures. In these experiments, the light was collected (with an estimated collection efficiency of about 60%) through a light pipe and sent to a broadband thermopile power meter. As shown in Fig. 5.2, the device operated up to a maximum temperature of 90 K, exhibiting a peak power of 22 mW at 10 K. The peak power had a very small dependence on duty cycle up to 40%. Measurements of continuous wave operation were performed in a smaller device (165 μm wide and 1.5 mm long) fitted with a dielectric/metal high reflectivity coating on the back facet (ZnSe/Au, 100/60 nm), in order to decrease the heat load to the cryostat. As shown in Fig. 5.3, CW operation is achieved at 10 K with a threshold current density of 260 A/cm^2 and a maximum power of 15 mW. The maximum operating temperature is as high as 55 K.

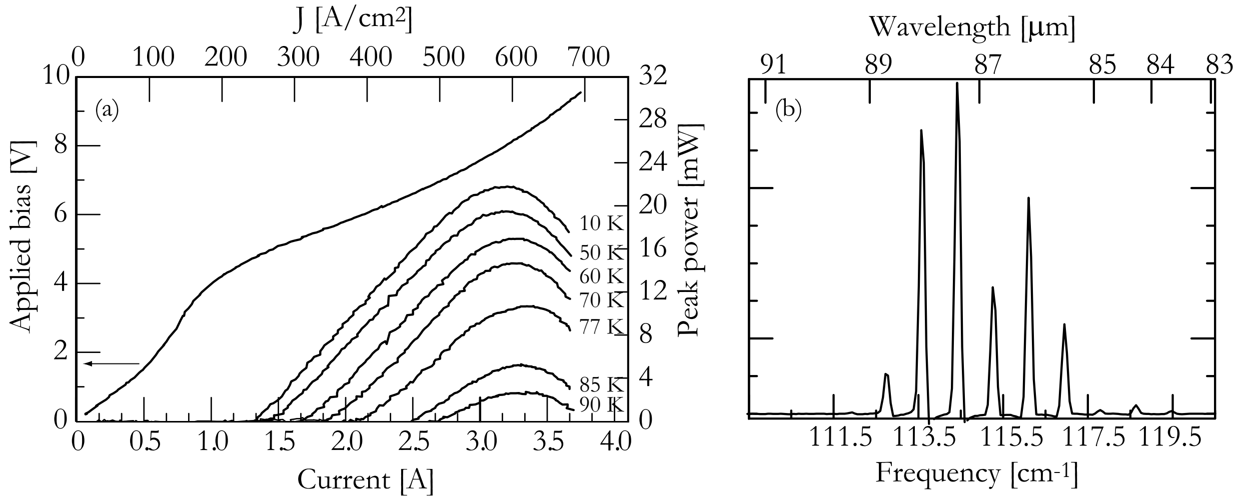

Figure 5.2: (a) Pulsed optical power as a function of injection current of a 2.7 mm long, 200 μm wide device at various temperatures together with IV curve of the device at 10K. Decrease of emitted power at 600 A/cm^2 is due to the beginning of band misalignment. (b): Spectrum of a 1.5 mm long, 165 μm wide device in pulsed mode at 10 K.

The voltage-current characteristics, shown in Fig. 5.3(b), indicate a significant leakage current (about 100 A/cm^2) flowing before the structure aligns at approximately 4 V. This current can be reduced by increasing the injection barrier thickness, as shown later in Sec.5.1.4. High resolution (0.09 cm^{-1}) spectrum of the device was taken with a Fourier transform infrared spectrometer and is reported in Fig.5.2 (b). From the mode spacing and the cavity length, a value of the group velocity index $n_g = 4.02$ could be deduced, in good agreement with the value reported in the literature corrected with the dispersion (n=3.89) [182]. The device remains multimode in both pulsed and CW operation, with a fairly large spectral width (of about 5 cm^{-1}). This is to be expected from a device that employs a gain region based on a bound-to-continuum transition, where the oscillator strength is spread over 2-3 transition, as also shown by the relatively broad electroluminescence curve (see Fig. 5.4).

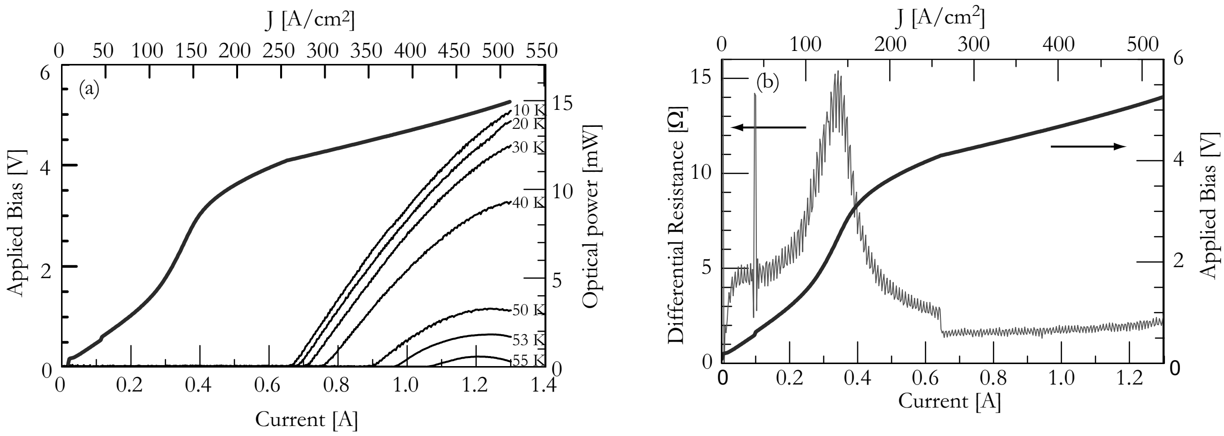

Figure 5.3: Continuous wave optical power and applied voltage as a function of injected current from a single facet of a high reflectivity coated, 1.5 mm long, 165 μm wide device, at various temperatures, as indicated. Inset: Voltage-Current characteristics at T = 10 K of the device (continuous line) and the differential resistance (dashed line) deduced from it as function of current.

5.1.3 Device analysis

Previous studies of terahertz quantum cascade lasers, based on chirped superlattice active regions, suggested that population inversion in these devices was very poor. This poor population inversion most likely arises from the small difference between upper and lower state lifetimes, together with a non-optimal injection efficiency into the upper state. The higher maximum operating temperature and larger differential slope efficiency (by about an order of magnitude) of our bound-to-continuum structures are consistent with devices operating with a much improved ratio of upper to lower state lifetimes. An indirect indication of the large slope efficiency is the clear slope discontinuity of the current-voltage characteristics at threshold (the size of this discontinuity is 1 Ω, much lager than the value of 0.2 Ω obtained from a device with similar dimensions and chirped superlattice based active region). As shown theoretically [183, 173], the size of this discontinuity is ultimately limited by the ratio of the upper to lower state lifetimes.

In order to investigate this point further, electroluminescence was measured as a function of temperature using an experimental technique [175] where the luminescence is extracted from the edge of a device which has been cleaved along the length of the stripe. This geometry has the advantage of allowing luminescence measurements in lasing devices with a negligible contribution from the gain. Luminescence spectra as a function of temperature are shown in Fig. 5.4 a). Luminescence is observed up to a maximum temperature of 110 K.

The inverse luminescence intensity is plotted, along with the threshold current, as a function of temperature in Fig. 5.4 b). Because of the very low electron densities involved, the intensity of the electroluminescence at fixed current is proportional to the upper state lifetime, in contrast to the gain which is proportional to the difference between the upper and lower state occupancies. The data of Fig. 5.4, together with transport characteristics, show clearly that both quantities have very similar temperature dependences, demonstrating that this bound-to-continuum design has a performance limited by the upper state lifetime. Because of the extended nature of the wavefunctions, we expect the low temperature ISB lifetime to be limited by interface roughness. Indeed, unlike vertical transition structures where electroluminescence intensity has characteristic square root dependence on current [79], we observe this dependence to be linear, as shown in Fig.5.5.

At liquid nitrogen temperatures and above, optical phonon scattering is expected to be the dominant scattering mechanism. In this simplified model, the electron temperature was assumed to be equal to that of the lattice. Using the energies and wavefunctions computed

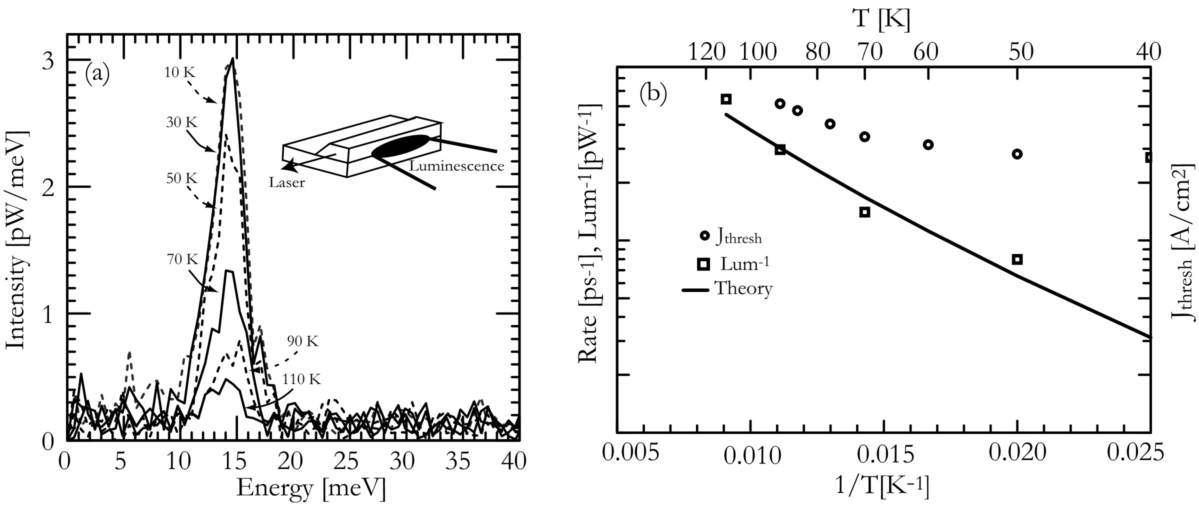

Figure 5.4: a) Electroluminescence spectra, taken from the edge of the device, for various temperatures. Inset: schematic of the experimental configuration for luminescence measurements. b) Luminescence intensity, measured from the spectra shown in the upper figure (squares), threshold current (circles) shown as a function of inverse temperature. The full line shows a computation of the total optical phonon scattering rate from the upper state.

using the self-consistent model, the total optical phonon scattering rate from the n=8 upper state of the laser transition was calculated. For every final state of the active region, the optical phonon scattering rate was computed from an energy corresponding to the onset of optical phonon emission (as the transition energy is lower than the optical phonon energy for all transitions inside the active region). For each temperature, these individual rates were added with a weight $(exp(-(\hbar\omega_{LO} - E_{8j})/k_B T))$ corresponding to the activation of electrons above the energy corresponding to the emission of an optical phonon. Finally, the scattering rate by absorption of optical phonons was included. The total intersubband scattering rate, computed according to this procedure, is plotted along with the luminescence and threshold data. As expected, the corresponding lifetime drops rapidly, and is 4.3 ps at 80 K and 2.1 ps at 110 K. However, in contrast to previous results obtained in the luminescence from a single quantum well, where a very good fit to the temperature dependence [131] was observed, the temperature dependence of the threshold current and luminescence is stronger than that

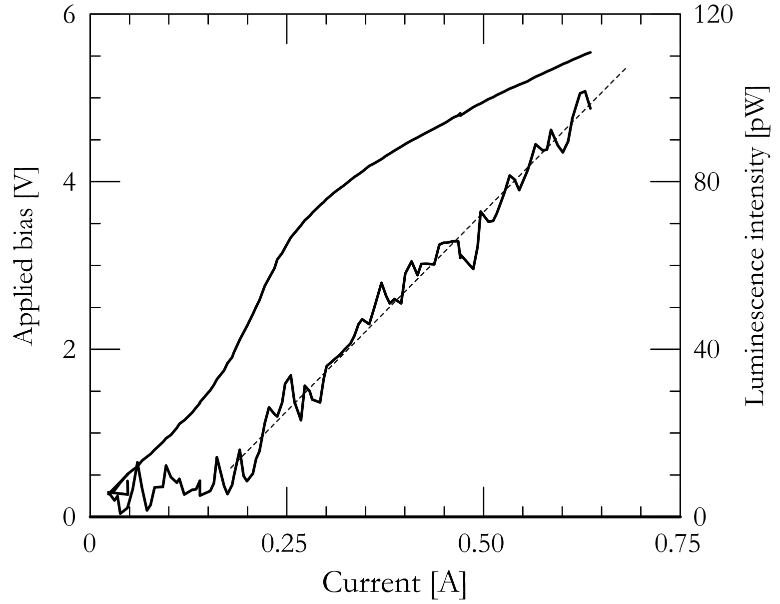

Figure 5.5: Electroluminescence intensity at T=10 K for sample A2771 (open ridge, no cavity effetcs). The dashed line is a linear fit of the emission.

predicted theoretically. As each transition has its own specific activation energy, it is not possible to define a single activation energy for the total scattering rate. However, taking the average slope of the data at high temperature, we find an equivalent activation energy of 21 meV for the experimental data and only 16 meV for the theoretical curve. The low value of the activation energy derived from the theoretical curve comes from high energy intersubband transitions that occur from states deep in the injector that have a low activation energy but, at the same time, a low overlap with the upper laser state. A possible interpretation of the discrepancy is that these transitions do not come into play because of the loss of coherence owing to collision broadening.

5.1.4 Design improvement: injection barrier tuning

As mentioned in Sec.5.1.2, the transport of the bound-to-continuum design can be optimized by the tuning of the injection barrier thickness that controls the very important parameter $2\hbar\Omega_{i8}$ described in Sec.2.5. Also the doping plays an important role, governing the maximum quantity of carriers we can inject in the upper state. Keeping this in mind, a regrowth of structure A2771 with a thicker injection barrier (4.2 nm instead of 3.7 nm) and a slightly increased doping density (3.0×10^{16} instead of 2.5×10^{16} cm^{-3}) was realized. Sample

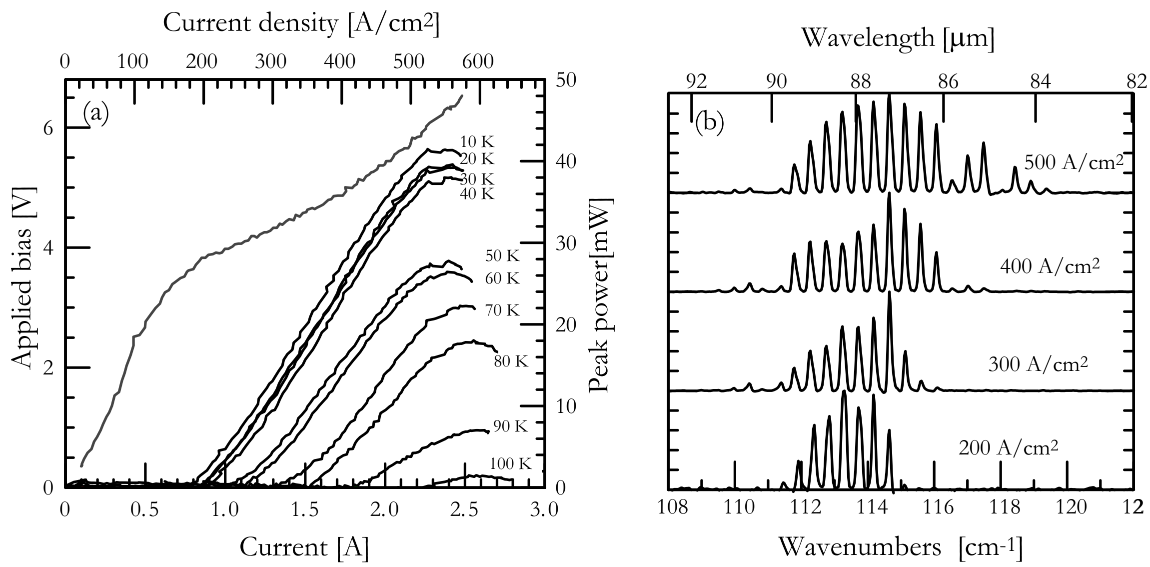

Figure 5.6: a) Pulsed optical power as a function of injection current of a 2.7 mm long, 160 μm wide device with HR backfacet coating at various temperatures together with IV curve of the device at 10K. b) Spectral emission in pulsed mode ar T=10 K as a function of injected current density for sample A2986, 2.7 mm long, 160 μm wide device with HR backfacet coating.

A2986 showed improved temperature dependence with a $T_{max} = 100$ K in pulsed mode (see Fig.5.6(a)) and T=68 K in CW and a maximum peak power of 50 mW both in pulsed and CW operation. A detailed comparison of these two structures can be found in Ref.[173]: here we briefly discuss some features of the improved coupling of the injector with the upper state of the lasing transition that can be deduced from the transport. In Fig.5.7(a), two DC I-V curves are plotted for two samples A2771 and A2986 with identical dimensions. The reduction of the leakage current can be easily noticed looking at the first peak in the differential resistance marked with the vertical black arrow: band alignement occurs at 100 A/cm^2 instead of 125 A/cm^2. Threshold bias is also reduced (3.9 V instead of 4.2 V) with positive effects on CW operation (less Joule heating). In Fig.5.6(b) spectral emission for sample A2986 in function of injected current density is shown: the broad emission bandwidth observed at high current density values and consequently at high emitted power values suggest inhomogeneous broadening of the gain profile due to spatial hole burning phenomena [29]. The blue shift of the mode envelope with the bias is consistent with a Stark shift induced by the diagonal nature of the transition.

The discontinuity at threshold is bigger in size and its evolution as a function of the temperature, displayed in Fig.5.7(b) clearly shows an improved ratio of lifetimes for structure A2986. In order to achieve CW operation at liquid nitrogen temperature the current carrying capabilities should be improved (doping calibration) together with a further optimization of the design.

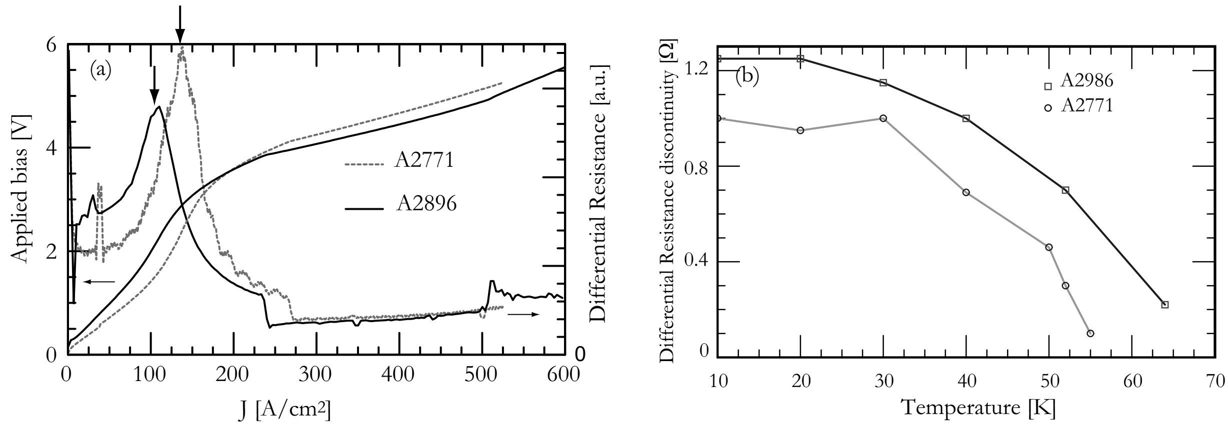

Figure 5.7: (a): CW I-V curves for samples A2771 and A2986 together with differential resistance: vertical black arrows indicate the band alignement with an evident reduction of the leakage current for sample A2986. (b): Differential resistance discontinuity at threshold for samples A2986 and A2771 as a function of temperature.

Another issue that should be addressed is the thermal dependence of waveguide losses: in Fig.5.8 two series of measurements of the threshold current density for sample A2986 in function of the inverse cavity length are reported. Exploiting the threshold condition expressed by Eq.4.4.9 and the calculated facet reflectivities we can extract the modal gain and the value of the waveguide losses: the results are summarized in Table 5.1.

Already at T=70 K we note an increase in the waveguide loss and a decrease in the modal

	α_w (cm^{-1})	Γg (cm/A)	calculated α_w
10 K	5.4	4.4 $\times 10^{-2}$	6.1
70 K	6.6	3 $\times 10^{-2}$	

Table 5.1: Waveguide losses and modal gain for structure A2986 for two different temperatures.

gain. The increase in waveguide loss can both come from an activated reabsorption in the active region (see Sec.5.2.2) and from activated free carrier absorption in the semi-insulating substrate. Some preliminary measurements of the semi-insulating substrate absorption seem to confirm the existence of this loss. The bound-to-continuum design has shown its efficiency

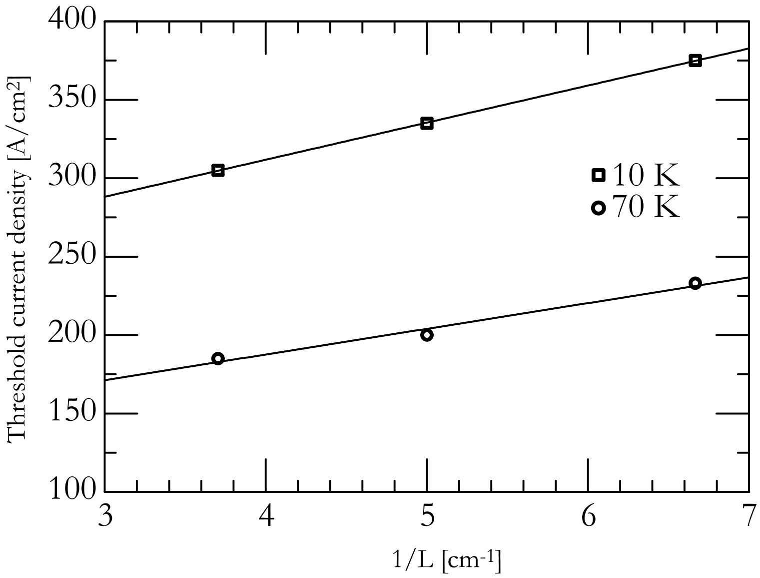

Figure 5.8: Waveguide losses and modal gain as a function of temperature for sample A2986

also at longer wavelengths: in Ref.[173] is described a device emitting at 9.5 meV ($\lambda \simeq 130\mu$m) with very good performances that is the direct rescaling of the concepts illustrated in this Section.

5.2 Bound-to-continuum with optical phonon extraction

In this Section we present a design that combines the advantages of the bound-to-continuum [89] approach together with the use of an LO phonon resonance to enable fast scattering of the carriers out of the lower miniband.

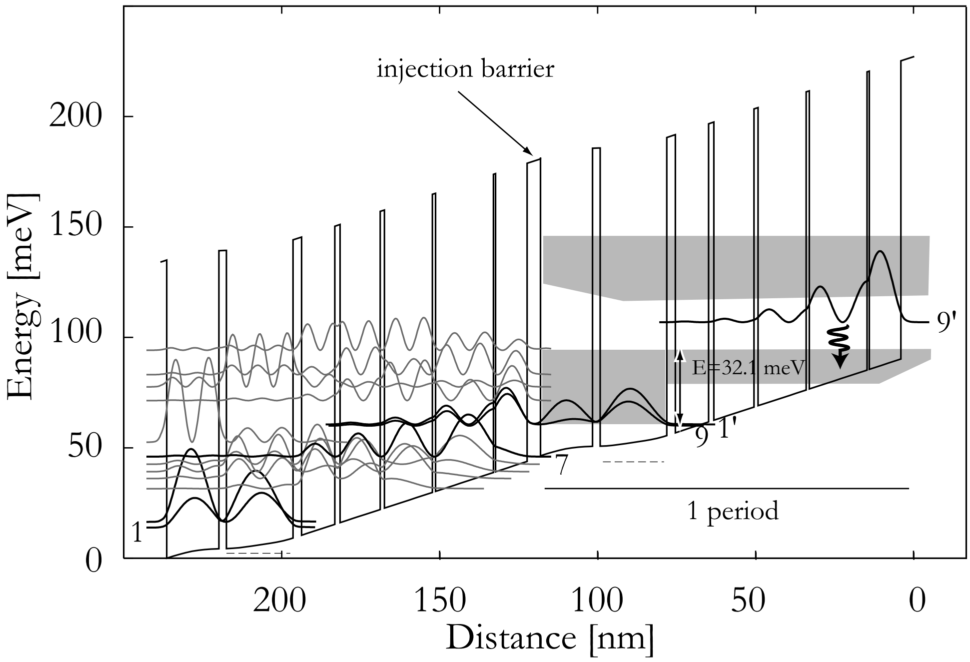

Figure 5.9: Self-consistent solution of coupled Schrödinger and Poisson's equations for two periods of the structure N314 at a temperature T=20 K. Layer sequence in nm starting from injection barrier is as follows: **4.2**/10.0/**0.7**/18.3/**1.0**/15.2/**1.3**/12.7/**1.7**/10.5/**2.7**/<u>21.1</u>/**2.4**/ 16.5/ (underlined layer is Si doped at 3.8×10^{16} cm^{-3}, figures in bold type are $Al_{0.15}Ga_{0.85}As$ layers).

The bandstructure of the sample N314, computed solving self-consistently Schrödinger and Poisson's equations, is reported in Fig.5.9. In this structure the extraction miniband of the bound-to-continuum transition is aligned resonantly with the first excited state of a large coupled quantum well that exhibits a transition E_{71}=32.1 meV at roughly the optical phonon energy in GaAs. The anticrossing between states $|9\rangle$ and $|1'\rangle$ ($\Delta E_{91'}$=0.65 meV) is reached for an applied electric field of F=4.15 kV/cm: at this field the design photon energy is E_{97}=14.6 meV with a computed dipole of z_{97}=76 Å and an oscillator strength equal to 22.6. As compared to the previous bound-to-continuum designs [173, 89, 99] the large energy separation E_{71} significantly reduces the lower state lifetime by allowing optical phonon scattering from electrons with very small in-plane kinetic energy and reduces the thermal backfilling of the lower state. The GaAs/$Al_{0.15}Ga_{0.85}As$ structure is grown on a GaAs semi-insulating substrate. The growth begins with a 300 nm $Al_{0.3}Ga_{0.7}As$ etch-stop layer that allows the processing of the device also with a double-metal waveguide [95], followed by an heavily doped ($2 \cdot 10^{18}$ cm^{-3}, Si) 700 nm thick layer that defines the lower contact of the laser in the case of a single-plasmon waveguide processing [85]. The active region is repeated 120 times and the growth ends with an heavily doped ($2 \times 10^{18}/2 \times 10^{19}$ cm^{-3}, Si) GaAs/InGaAs (40/40 nm) contact layer. Processing of the devices has been performed in two ways: the usual single plasmon waveguide already described elsewhere [89] and the double metal one. In the single-plasmon case the GaAs/InGaAs contact layer allowed us to deposit only a Cr/Au (10/300 nm) top metallization without Ge, removing one annealing step. The double metal process is described in Section 3.4. It is worth to note here that the thick doped layer left in this process (400 nm) after substrate removal contributes substantially to waveguide losses. From the simulation we obtain a value of $\alpha_w^{400} = 25.2$ cm^{-1} and only $\alpha_w^{100} = 20.5$ cm^{-1} for a 100 nm thick contact layer. Future process will reduce this thickness to at least 100 nm and laser performances will certainly gain from this process modification.

5.2.1 Optical measurements

Laser emission takes place at an energy of 14.9 meV just above threshold, in good agreement with the designed photon energy. Performances of lasers with single-plasmon waveguide are reported in Fig. 5.10: a 2.2 mm-long and 220 μm-wide ridge with back facet coating reached 98 K of pulsed operation with peak powers of about 36 mW at 10 K with still 6 mW detected at 85 K. In the single-plasmon case, the lowest measured threshold current density in pulsed operation is J_{thresh} = 178 A/cm^2, significantly lower than the other optical-phonon based structures [92, 184] and even lower than previous results obtained on a bound-to-continuum structure [89].

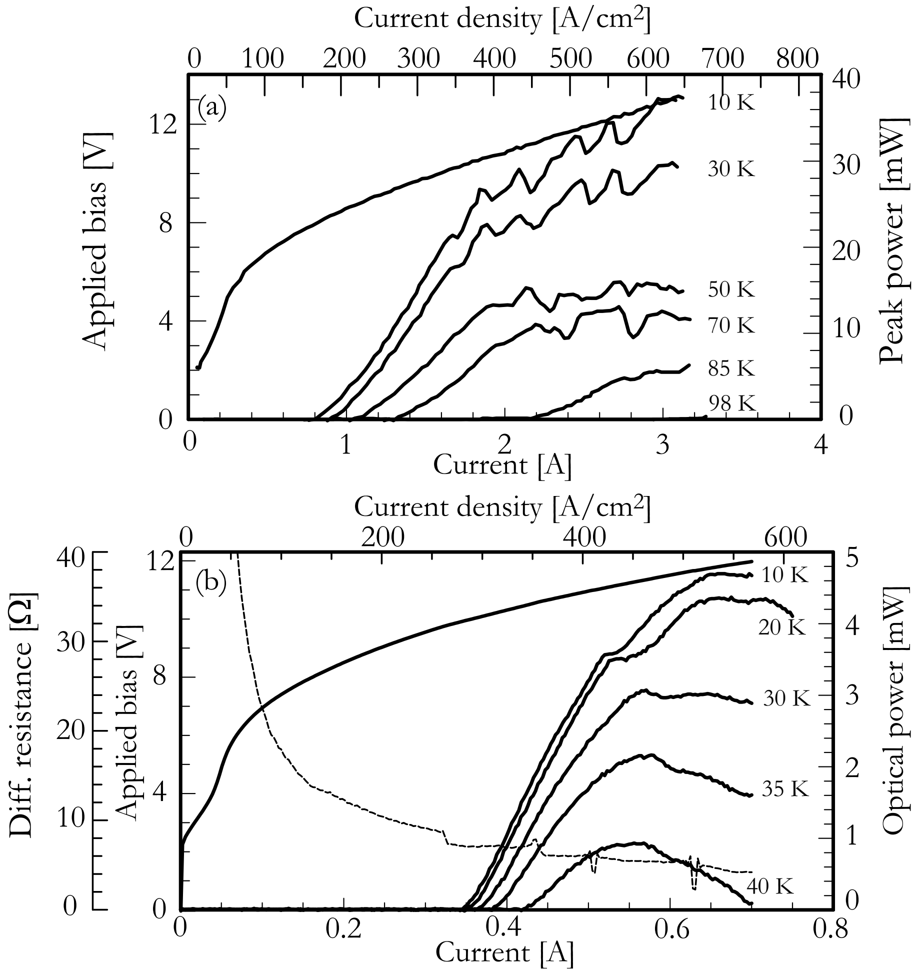

Figure 5.10: (a) pulsed LI-IV curves of a 2.2 mm-long, 220 μm-wide single-plasmon laser ridge with high-reflection (HR) backfacet coating measured with a calibrated thermopile powermeter at a 2.5% duty cycle (125 KHz repetition rate). (b) CW operation of a 1.12 mm-long, 110 μm-wide single-plasmon waveguide device with HR backfacet coating together with differential resistance (left axis) that shows typical discontinuity at threshold. The features in light emission and differential resistance correspond to mode jumps.

Current dynamic range is large, and after a broad plateau emitted power begins to drop at a current density value of about 700 A/cm^2. Continuous-wave (CW) operation could be reached in smaller devices, yielding a maximum operating temperature of 40 K with peak powers of the order of 5 mW for a 1.12 mm-long, 110 μm wide laser ridge equipped of high reflectivity (HR) backfacet coating (ZnSe/Au 100/60 nm). Assuming the same thermal conductivity as our previously published results [89, 173], the lower CW temperature range could be explained by the higher electrical power dissipated due to a threshold bias that results to be 8.95 V, 2.4 times higher than in the bound-to-continuum case. Inspection of the CW-LI curve at 40 K confirms this hypothesis, clearly showing a power saturation due to thermal rollover. The differential resistance shows a discontinuity at threshold typical of a high ratio of lifetimes. A series of measurement of the threshold current at T = 10 K as a function of the cavity length yields a value of 9.3 cm^{-1} for the waveguide losses α_w for a ridge width of 160 μm, in good agreement with the calculated value of 9.4 cm^{-1} for the single plasmon waveguide. Laser performances in the case of a double-metal waveguide are reported in Fig.5.11. Pulsed operation could be observed up to an heatsink temperature of 116 K in a 1.5 mm-long, 110 μm-wide laser ridge with HR backfacet coating. Due to the slightly diagonal nature of the $|9\rangle \longrightarrow |7\rangle$ transition the device is tunable with the applied bias from 78 μm to 82 μm as visible from the inset of Fig 5.11(b). Total collected output power is much lower (about 1/10) than in the single plasmon case, due to the impedance mismatch condition present at the facet, where the THz mode reflectivity is significantly different from the single plasmon case. A numerical calculation based on the mode matching method [170] yields a value of R=0.97 for the reflectivity of the first mode of the cavity in the double-metal case, that partially accounts for the observed decrease in emitted power. Comparison of the transport characteristics of the single-plasmon and double metal waveguide shows an excess bias at threshold of 0.8 V in the double metal case, that comes from the directly polarized Schottky barrier created by the Cr/Au top contact. CW operation is possible in narrow stripes [185] because of the high lateral mode confinement provided by the double-metal waveguide and maximum operating temperature rises up to 53 K in a 0.75 mm-long, 70 μm-wide laser ridge.

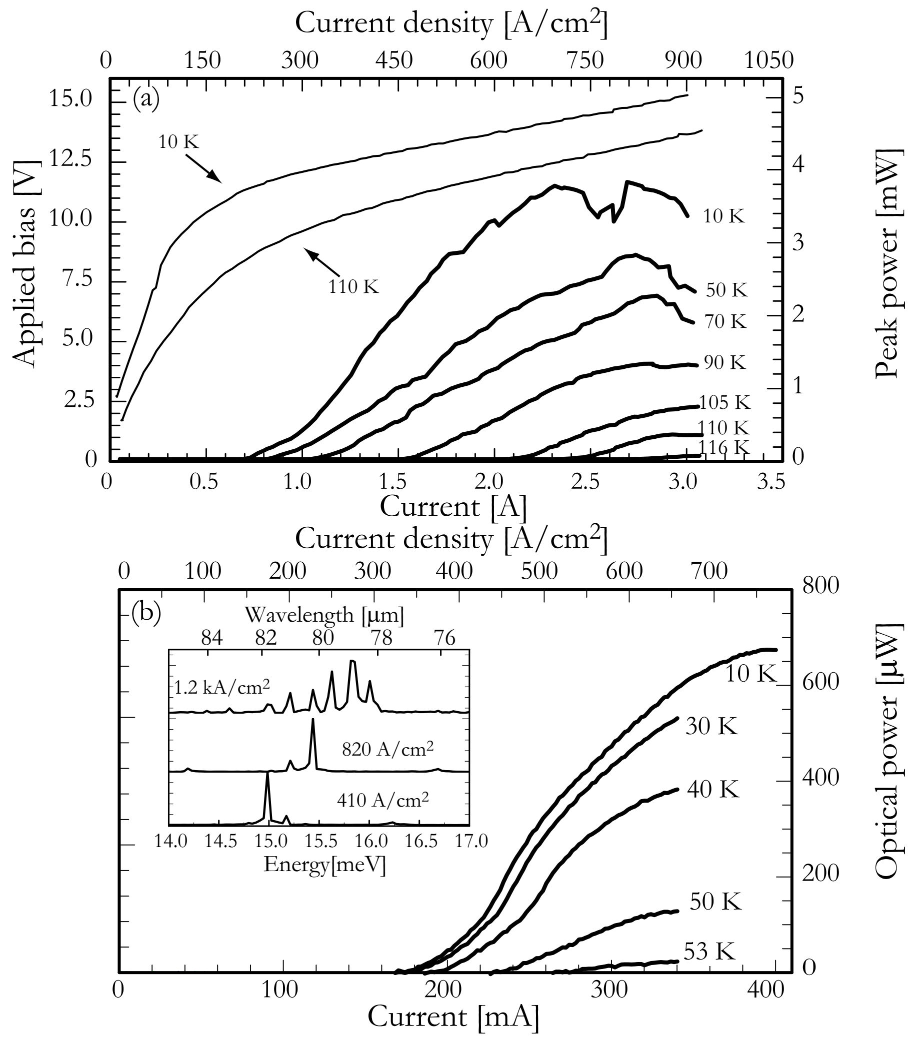

Figure 5.11: (a) pulsed LI-IV curves of a 1.5 mm-long, 220 μm-wide double-metal waveguide laser ridge with HR backfacet coating: a duty cycle of 0.01% has been chosen in order to avoid bolometer saturation. (b) CW-LI curves of a 0.75 mm-long, 70 μm-wide double-metal waveguide laser ridge: emitted power has been measured with a calibrated thermopile. Inset: emission spectra in pulsed mode for the same device at different injection current densities at T = 10 K. The mode spacing suggests that the laser is operating on a high order lateral mode.

As stated before, output coupled power is lower compared to the single-plasmon case, leading to a measured maximum optical power of 700 μW at 10 K. A comparison of the average thermal resistance (deduced from CW-pulsed threshold current temperature dependence) $R_{th} \simeq 8.6$ K/W with the value 6.3 K/W of Ref. [185] shows that substantial improvement will be possible optimizing both substrate thinning and In/Au soldering. In order to understand and to quantify the effective improvement of the double metal waveguide, a set of measurements of threshold current versus cavity length has been performed. The results are too scattered to be reliable and this shows that the process has to be greatly improved in order to give homogenous results on different laser ridges.

5.2.2 Device analysis

Device performances are expected to depend on both design and MBE growth. To disentangle the separate influences of these factors, we compare this structure (N314) to our previous one based on a smaller miniband width ($\Delta E \simeq 15$ meV)[89, 173] but grown in the same run (N310)[186]. Sample N310 exhibits a maximum operating temperature significantly lower (80 K instead of 103 K) than the same design grown in a different machine (sample A2896, Ref. [173]). We attribute this difference to a higher background doping of our MBE equipment. We plotted the temperature dependence of the threshold current density for the three samples (N310 single plasmon, N314 single plasmon and double metal) in Fig.5.12. The importance of the optical phonon stage is clear: the pulsed operation range of N314 outperforms sample N310 by about 20 K in the same single plasmon waveguide. Slope efficiency reflects this improvement, yielding $\left(\frac{dP}{dI}\right)_{N314} \simeq 25.5$ mW/A and $\left(\frac{dP}{dI}\right)_{N310} \simeq 20.4$ mW/A. We find another signature of an improved ratio of lifetimes looking at the size of the discontinuity in differential resistance at CW threshold: for the same device dimensions this parameter results more than twice as large in sample N314 with respect to sample N310. An absolute comparison of our design N314 with the structure of Ref.[184] should be made under the same growth conditions: from the comparison with the results of bound-to-continuum structures N310 and A2986 it is plausible that sample N314 grown in a cleaner chamber would yield a significantly higher T_{max}. In Fig.5.12 we plot the calculated temperature dependence of the threshold current for the structure N314, using the

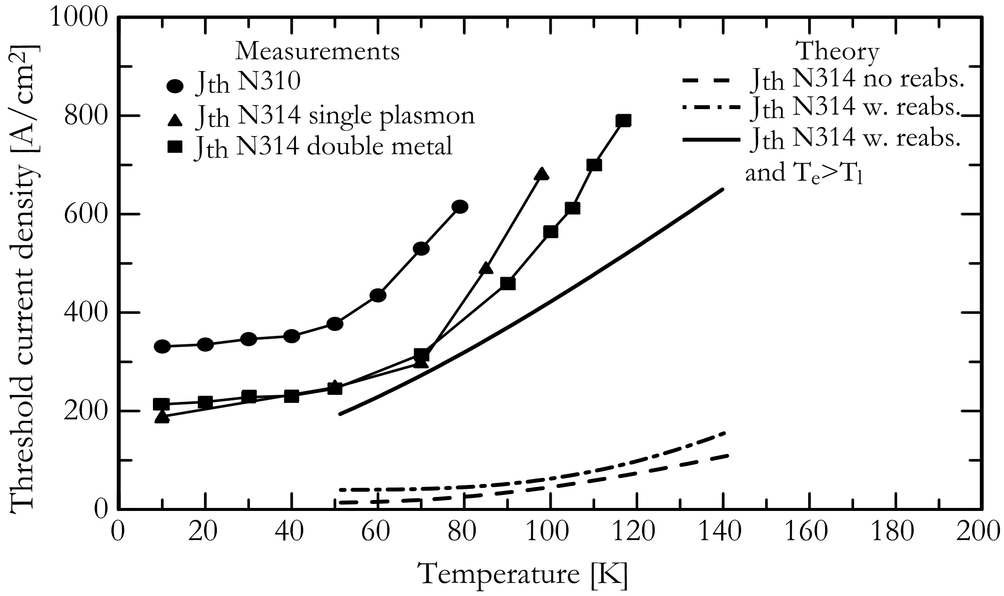

Figure 5.12: Experimental temperature dependence of the threshold current density for sample N310 (bound-to-continuum design of Ref.[89]) in a single-plasmon waveguide (disks), experimental temperature dependence for sample N314 in single-plasmon waveguide (triangles) and double metal waveguide (squares). Theoretical modelling of the threshold current temperature dependence (dashed curve) including thermally activated waveguide losses from free carrier absorption (dashed-dotted curve) and hot electrons effects (solid curve).

expression $J_{thresh}(T) = \frac{e}{\tau_9(T)} \frac{(\alpha_w(T)+\alpha_m)/g_c}{\left(1-\tau_7(T)/\tau_{9_{67}}(T)\right)}$ where $\alpha_w + \alpha_m$ are the calculated losses, e is the electron charge and g_c is the gain cross-section [53] that includes the experimental value of the linewidth of the spontaneous emission $2\gamma_{97} = 1.9$ meV measured at T = 10 K. The lifetimes τ_9, τ_7 and $\tau_{9_{67}} = \left(\frac{1}{\tau_{97}} + \frac{1}{\tau_{96}}\right)^{-1}$ are calculated as a function of the temperature supposing a thermal distribution of the carriers in each one of the subbands and including only longitudinal optical phonon scattering at $k \neq 0$. The double-metal waveguide has been simulated with the active region undoped, calculating α_w^{bare}. Then the losses of the active region $\alpha_w^{active}(T)$ are evaluated via the complete absorption spectrum calculated at different temperatures with the self-consistant computation of the active region. The results for the activated absorption of the active region are plotted in Fig.5.13. Finally the total waveguide losses are obtained via $\alpha_w^{tot}(T) = \alpha_w^{bare} + \alpha_w^{active}(T)$. This procedure can be applied to the double metal waveguide since the changing in dielectric constant due to the removing of the doping from the active region does not change significantly the mode distribution and consequently the overlap. Three different calculated curves are presented in Fig.5.12: the

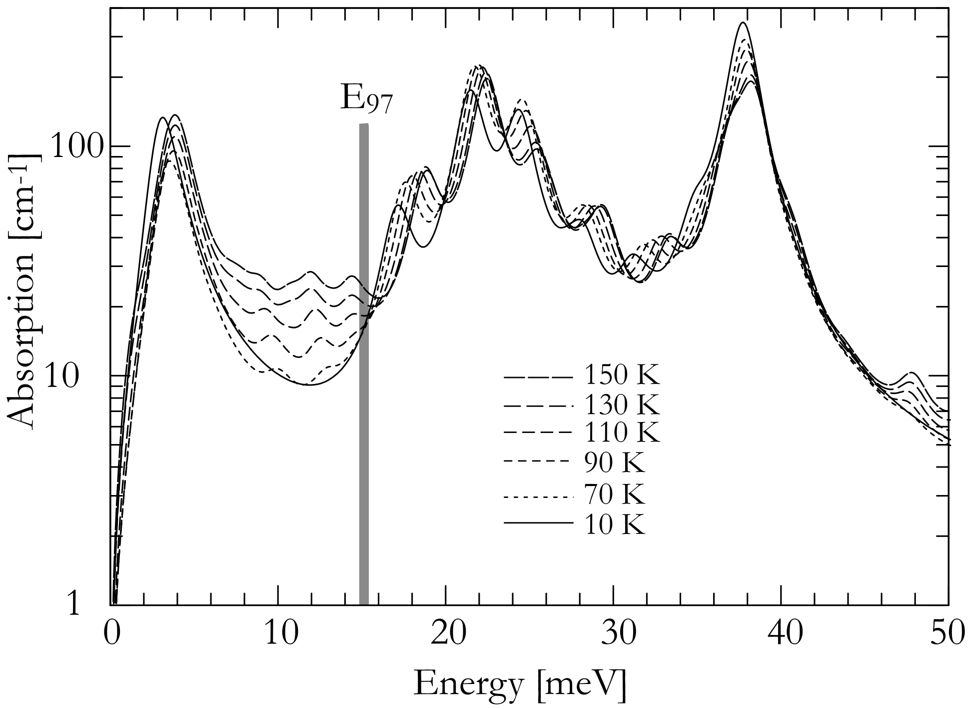

Figure 5.13: Calculated absorption spectrum of the active region for sample N314 as a function of the lattice temperature. E_{97} is the energy of the emitted photons.

dashed one assumes a fixed value for the waveguide losses α_w and an electronic temperature T_e equal to the lattice one T_l. The dashed-dotted curve includes a temperature dependence $\alpha_w(T)$ calculated from the absorption of the active region as a function of the temperature. The solid curve finally accounts also for an electronic temperature much higher than the lattice one ($T_e=T_l+100$ K) as suggested in Refs. [187, 133] and measured in Ref. [188]. The strong temperature dependence for structure N314 is partly recovered only when both thermally activated reabsorption and hot carriers are included in the model. The observed drop in the slope efficiency can also be due to additional filling of the lower states either by non-resonant injection or by mentioned hot carriers.

5.2.3 Design improvement: injection barrier and waveguide tuning

As in the bound-to-continuum design, a new growth with optimized injection barrier thickness (sample N470) and the buried layer contact thickness has been performed in order to obtain a better coupling between the injector and the upper state and to increase the confinement of the waveguide (overlap factor grows with buried layer thickness). The combined effect of these two changes has yielded a lower value of the bias at threshold that passed from 9 V for N314 to 7.8 V for N470. Maximum pulsed operation still reaches 100 K but the lower bias at threshold allows CW operation up to 53 K in a single plasmon waveguide (N314 stopped at 40 K) with an optical power that is twice the one recorded on the previous sample.

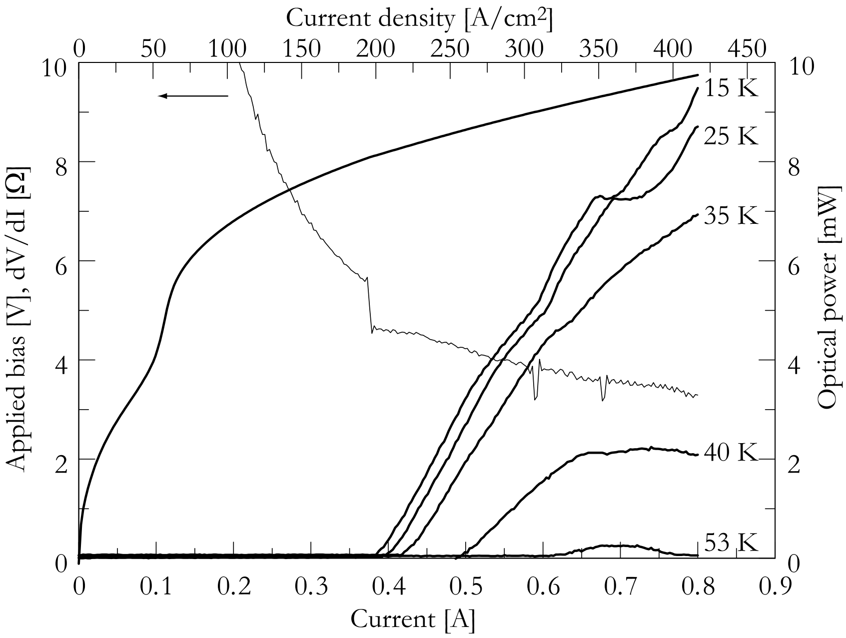

Figure 5.14: (a) pulsed LI-IV curves of a 1.6 mm-long, 120 μm-wide single plasmon waveguide laser ridge with HR backfacet coating. Emitted power has been measured with a calibrated thermopile detector.

5.3 Conclusions

In this Chapter we have analyzed the research activity on THz quantum cascade lasers based on a bound-to-continuum transition. The main achievements in this field have been the liquid nitrogen and high power operation of THz QC lasers at wavelengths between 80 and 90 μm (3.5 THz). Two designs have been presented and analyzed, together with comparative study of different waveguide configurations. The phonon-depletion scheme seems to be the most promising way to achieve high temperature operation, but the temperature dependence of the threshold current is still too strong. One possible design modification would be to shrink the quantum wells in order to achieve a larger separation between the upper state of the laser transition and the higher excited states. Those states can be populated by hot electrons reducing injection efficiency and contributing to parasitic injection in the lower miniband with consequent backfilling.

Chapter 6

Population inversion by resonant magnetic confinement: big well design

6.1 Magnetic field measurements; motivation and typical dimensions

High temperature operation of THz QC lasers as well as the prospect of reaching lower frequencies may depend on the development of new concepts for population inversion. An attractive possibility is offered by introducing an additional in-plane confinement potential that, at these low photon energies ($h\nu < 15$ meV), may be achieved by lithography (with a characteristic size of about 50 nm) or by the application of a magnetic field perpendicular to the layers. In Chapter 2 we have extensively discussed the consequences of the application of a perpendicular magnetic field on an heterostructure. We know that, in the presence of this additional confinement, the intersubband scattering rate strongly depends on the respective energies of the Landau levels associated with the separate subbands. The quenching of the scattering mechanisms due to the reduction of available phase space is strongly related to the energy separation of the levels. Let us take a look at the magnitudes associated with this additional confinement: in Fig.6.1 (a) the magnetic length and the cyclotron radius (for a typical sheet carrier density of $3 \cdot 10^{10}$ cm^{-2}) are reported as a function of the magnetic field together with the width of a GaAs quantum well that has the two first level separated by 15 meV (3.6 THz). In Fig.6.1 (b) the cyclotron energy for the GaAs ($m^* = 0.067$) as a function of the magnetic field is reported. The application of a perpendicular magnetic field on a THz QC laser splits the parameter space in two distinct regions: when the cyclotron energy $\hbar\omega_c$ is smaller than the energy separation ΔE that encloses the upper state of the lasing transition and the ground state of the injector (see Section 1.4.2 and Fig.1.8), inter-Landau level scattering is allowed and the lifetimes of the Landau states are modulated according to what was exposed in Sec. 2.8: this means that the first excited Landau level $|1,1\rangle$ of the ground state $|1\rangle$ of the active region of our structure has not yet crossed the Landau ground state $|j,0\rangle$ that represents the doublet injector-upper state. When the condition $\hbar\omega_c > \Delta E$

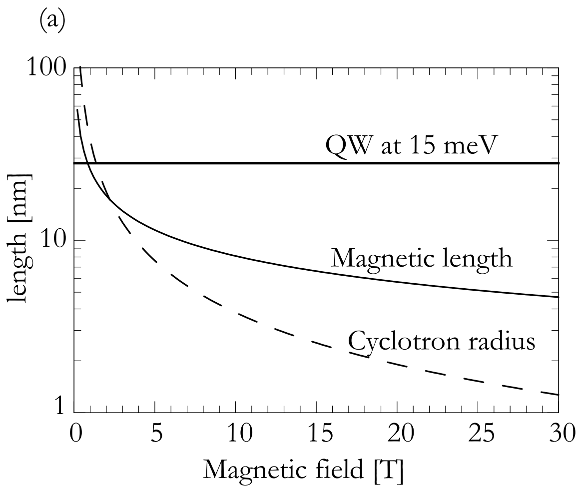

Figure 6.1: (a): Cyclotron radius (dashed line) and magnetic length (full line) as a function of magnetic field together with the width (horizontal line) of a $GaAs/Al_{0.15}Ga_{0.85}As$ quantum well with the first two levels spaced by 15 meV (3.6 THz) (b): Cyclotron energy as a function of magnetic field and LO phonon energy (horizontal line)

is satisfied no more Landau levels can cross the upper state of the lasing transition and modulation of the lifetime of the levels is possible only in the case of multi-electron scattering events (see Sec. 2.8.2). In this regime the lifetime should increase monotonically with the applied magnetic field. A structure that has to benefit from the applied magnetic field has to be designed in order to exploit the lifetime modulation possibilities offered by these two regimes. It is worth to note that if we want to reach the condition of strong confinement on a structure with a $\Delta E = 15$ meV, a magnetic field greater than 9 T has to be applied (see Fig.6.1). As we will see in the following chapters, the detailed architecture of the active region and the nature of the optical transition (vertical or delocalized) will produce relevant differences also when this condition is fulfilled. The resonance condition with the longitudinal optical phonon in GaAs is matched at 20.8 T: this, together with the experimental results found at lower fields, motivates the use of intense magnetic fields.

This chapter is organized as follows: first we illustrate the principle of the resonant magnetic confinement, then we present and discuss four designs of THz lasers based on vertical transitions and the magnetic field effect that lase with extremely low threshold current densities in a frequency range from 3.6 THz to 1.39 THz. Experiments in very high magnetic fields up to 28 T will be also presented together with their interpretation. A comparative study of the structures is then presented.

6.2 Resonant magnetic confinement

A three-level rate equation approach to describe the active region of a quantum cascade laser gives us the inversion condition as a function of the lifetimes of the three states (see Sec. 2.4): in order to maximize the population inversion the upper state lifetime τ_{32} has to be maximized together with the minimization of the lower state lifetime τ_2. A resonant scattering mechanism would be desirable in order to efficiently minimize the lower state lifetime: we can think of mimicking the LO-phonon resonance substituting the LO-phonon energy by the cyclotron energy $\hbar\omega_c = \hbar\frac{eB'}{m^*}$ for a given value B' of the magnetic field and making the energy spacing of the extraction levels resonant

$$E_{21} = \Delta n\hbar\frac{eB'}{m^*} \qquad n = 1, 2, 3, ...$$

At the same time, in order to increase the upper state lifetime the energy spacing E_{32} will be adjusted in order to have the Landau states completely off resonance, i.e. $E_{32} \neq n\hbar\frac{eB'}{m^*}$

and to minimize the scattering rate [1]. Such modulation of the upper state lifetime by these resonances has been demonstrated experimentally by THz electroluminescence measurements [121, 122] in vertical transition QC THz emitters. This translates into a condition between the energies of the three states

$$E_{32} = \frac{3}{2}E_{21} = \frac{3}{2}n\hbar\frac{eB'}{m^*} \tag{6.2.1}$$

The concept of the resonant magnetic confinement aimed to maximize the population inversion is illustrated in Fig.6.2 A large single quantum well ("big well") will naturally provide

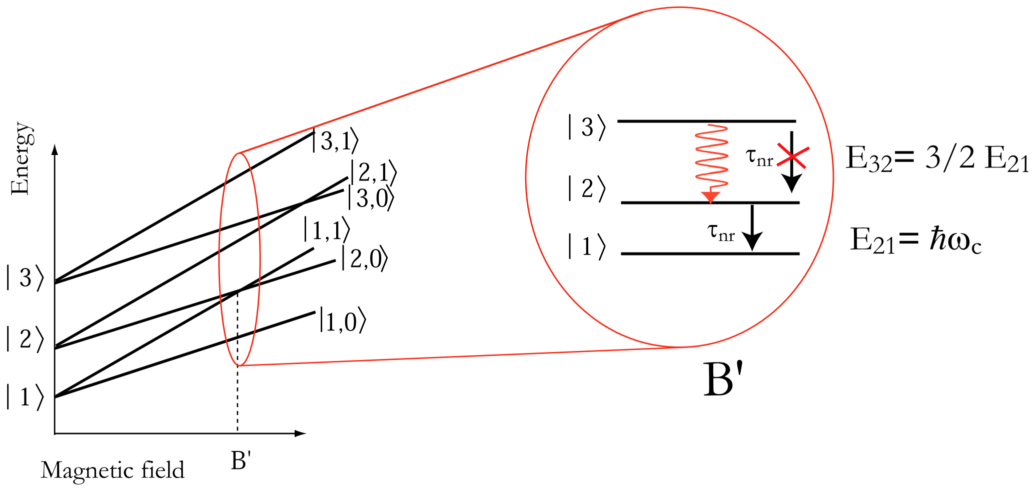

Figure 6.2: Landau states for a three-level system arranged in order to satisfy the resonant confinement condition 6.2.1.

an energy spectrum compatible with this concept, since in the limit of infinite barrier height, the ratio of the 3-2 to the 2-1 transition energy is $E_{32}/E_{21} = 5/3$. With finite barrier height and an applied electric field, a thin well adjacent to the large single quantum well enables this ratio to be tuned towards the ideal value of 3/2. Adjusting the magnetic field to the lowest (i.e. with $\Delta n = 1$) resonant condition between the n = 2 and n = 1 states ($\Delta E_{21} = \hbar\omega_c$) will

[1]This off-resonance condition is restricted to the one electron scattering processes and at the first order for the two electron processes, see Sec.2.8.2

then simultaneously decrease the n = 2 and enhance the n = 3 state lifetimes [189]. This condition does not take into account multi-electron scattering events that reduce the n=3 lifetime for the Landau level arrangement $E_{32} = n/2\hbar\omega_c \; n = 1$(see Section 2.8.2). The effect is in any case weaker than the n=2 resonance for the extraction levels.

6.3 Big well at 80 μm

The band profile of a QC laser structure, computed by solving self-consistently Poisson's and Schrödinger's equations, and designed with an active region based on a 36 nm thick GaAs well is shown in Fig. 6.3. The computed transition energies are $E_{32} = 15.2$ meV and $E_{21} = 10.6$ meV.

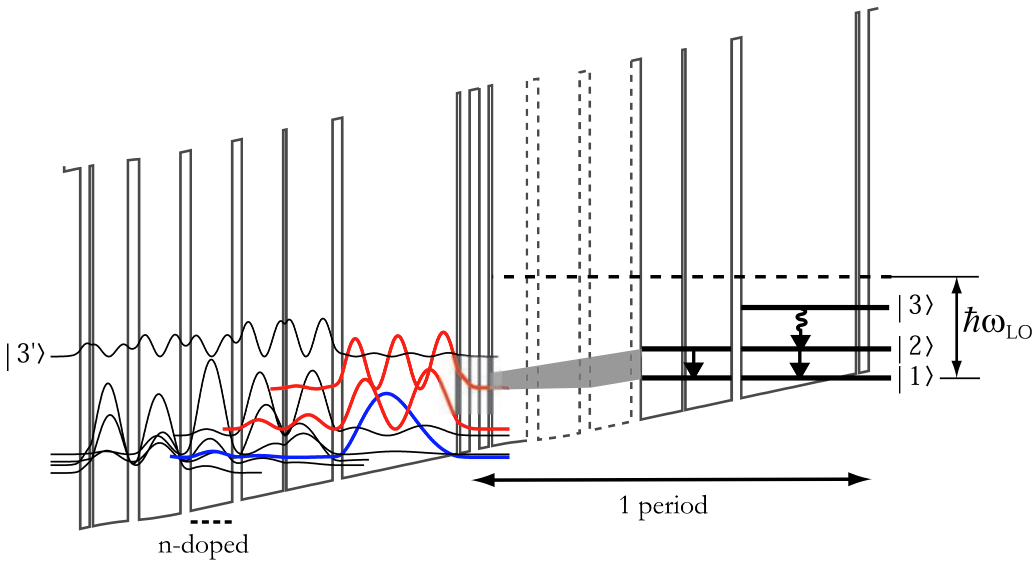

Figure 6.3: Computed conduction band profile of two stages of the structure A2664 under an average applied electric field of 2.55 kV/cm. The GaAs/$Al_{0.15}Ga_{0.85}As$ layer sequence of one period of the active layers starting from the injection barrier is as follows: **3.0**/3.0/**1.0**/36.0/**3.0**/14.5/**1.0**/ 13.0/**3.0**/13.0/**3.2**/<u>13.0</u>/**3.5**/11.0/**1.0**/3.0. Thicknesses are in nanometers, GaAs wells are in roman, $Al_{0.15}Ga_{0.85}As$ barriers in bold and the doped layer (Si: 2 $\times 10^{16}$ cm^{-3}) is underlined.

To enhance population inversion at B = 0, the large single quantum well is coupled to a coupled well system with an identical E_{21} energy but a much larger $E_{3'2}$ spacing (= 27 meV). An injector formed by three coupled quantum wells completes the structure. The GaAs/$Al_{0.15}Ga_{0.85}As$ heterostructure is grown onto an undoped GaAs substrate by molecular beam epitaxy. Sample A2664 consists of 120 repetitions of the active region embedded in a single plasmon waveguide of the kind described in Section 3.3, with a buried contact layer consisting of a 300 nm thick GaAs layer Si doped to $2 \times 10^{18}cm^{-3}$. Ridge laser structures, 110-160-210 μm wide, were processed using wet chemical etching [178]. Sample A2770 had a very similar active region design but with thinner injection and extraction barriers, a higher injector doping level (Si, $3 \times 10^{16}cm^{-3}$ instead of $2 \times 10^{16}cm^{-3}$), and a thicker waveguide (700 nm) contact layer. Both structures were measured with x-ray diffraction and layer thicknesses proved to be in very good agreement with the specified parameters (below 1% difference for both structures).

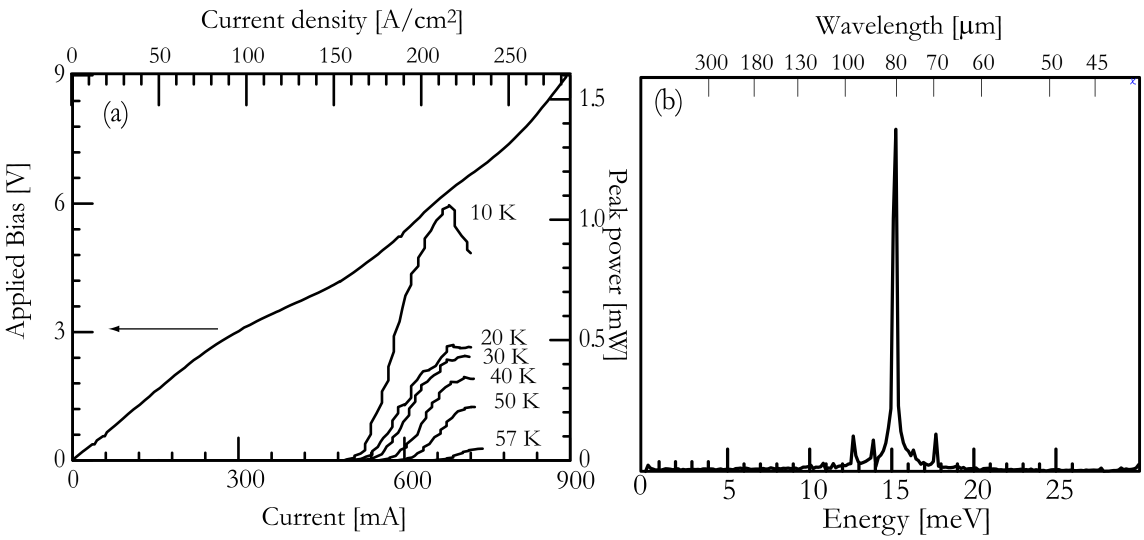

Figure 6.4: (a): pulsed LIV curves as a function of temperature for structure A2770 (1.7 mm long and 200 μm wide ridge). (b) Spectral emission at T = 10 K for the same device

Without an applied magnetic field, laser action was observed in sample A2770 with, for a 1.7 mm long and 210 μm wide device, a threshold current density of 150 A/cm^2 at $T = 10$ K, and a maximum operating temperature of 57 K. It is interesting to compare this result with the one discussed in Chapter 4 where the photon energy is the same. Here the effect of having one more level in the extraction part improves the lifetime of the lower state and the maximum operating temperature is increased by 17 K. The laser emission characteristics together with an emission spectrum are reported in Fig.6.4. The differential slope efficiency at 10 K was $\frac{dP}{dI} = 8.4$ mW/A (where P is the emitted optical power and I is the current). Sample A2664 also lased in the absence of an applied magnetic field but only in a very long device (4.1 mm) with high reflection coatings on both facets, and overall it displayed a very poor performance, showing however a very low threshold current density of 30 A/cm^2. The energy levels of the active region were measured by spectral emission and by tracking the location of the magneto-intersubband resonances [154]: the measured transition energies were $E_{32} = 15.3$ meV and $E_{21} = 9.7$ meV, in good agreement with the theory.

6.3.1 Laser emission in magnetic field

Light emission as a function of magnetic field is reported in Fig.6.5 for sample A2770, that shows laser action with no applied magnetic field. Huge oscillations of the laser emission due to inter-Landau level resonances are observed together with a modulation of the threshold current. A detailed analysis of these oscillations is reported afterwards referring to sample A2664 that shows the same behavior with better performance. A 2 mm long, 165 μm wide laser ridge with backfacet coating was measured for sample A2664: this device lased for applied magnetic fields > 0.8 T. The intensity of the laser emission was then measured at fixed voltage [2] as a function of applied magnetic field, with the InSb detector kept locked at the laser emission energy. Such measurements were performed between 0 T and 12 T for several values of applied bias. Fig. 6.6 shows these results up to 7 T; no laser action was observed at higher fields (the sample has been tested up to 28 T).

[2] Variation of the applied bias on the whole magnetic field sweep are within 5% of the initial value reported in Fig.6.6

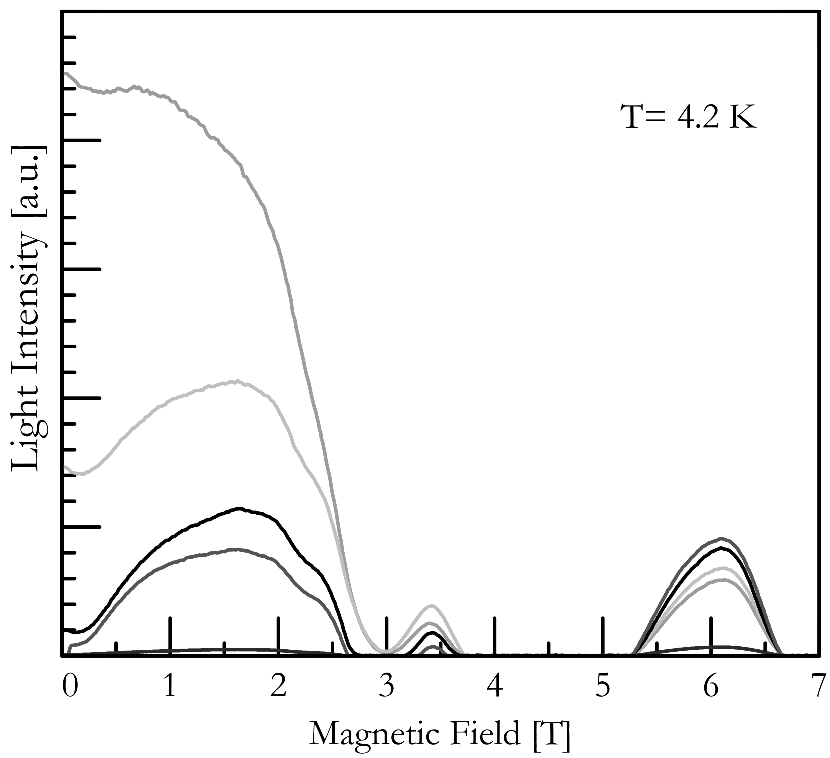

Figure 6.5: Light emission as a function of applied magnetic field for sample A2770 at various applied bias at T=4.2 K.

To clarify the interpretation of Fig.6.6(a), a Landau fan of the active region of the structure has been calculated and shown in Fig.6.6(b). The values of the energies used to calculate the Landau levels are those extracted from magnetotransport and spectral measurements. A Gaussian broadening scaling with $\Gamma = \Gamma_0 \cdot \sqrt{B}$ has been used for the Landau levels, with $\Gamma_0 = 1$ meV$/T^{1/2}$ [139]. In the Landau fan different resonance conditions are indicated by different colors. This graph highlights how the resonance condition affects laser emission. The main intensity peak corresponds to the field (B = 5.65 T) at which the transition energy E_{12} = 9.7 meV, extracted from magneto-transport measurement, matches the cyclotron energy. The peak at 2 T does corresponds to δn = 3 resonances from the lower state of the laser transition, namely $|1,3\rangle \rightarrow |2,0\rangle$ and $|1,4\rangle \rightarrow |2,1\rangle$. To support the last point, we note that no lasing action was detected at any applied bias on the laser at a field of 4.9 T, where resonance condition is satisfied among states $|3\rangle$ and $|2\rangle$, responsible of the optical transition.

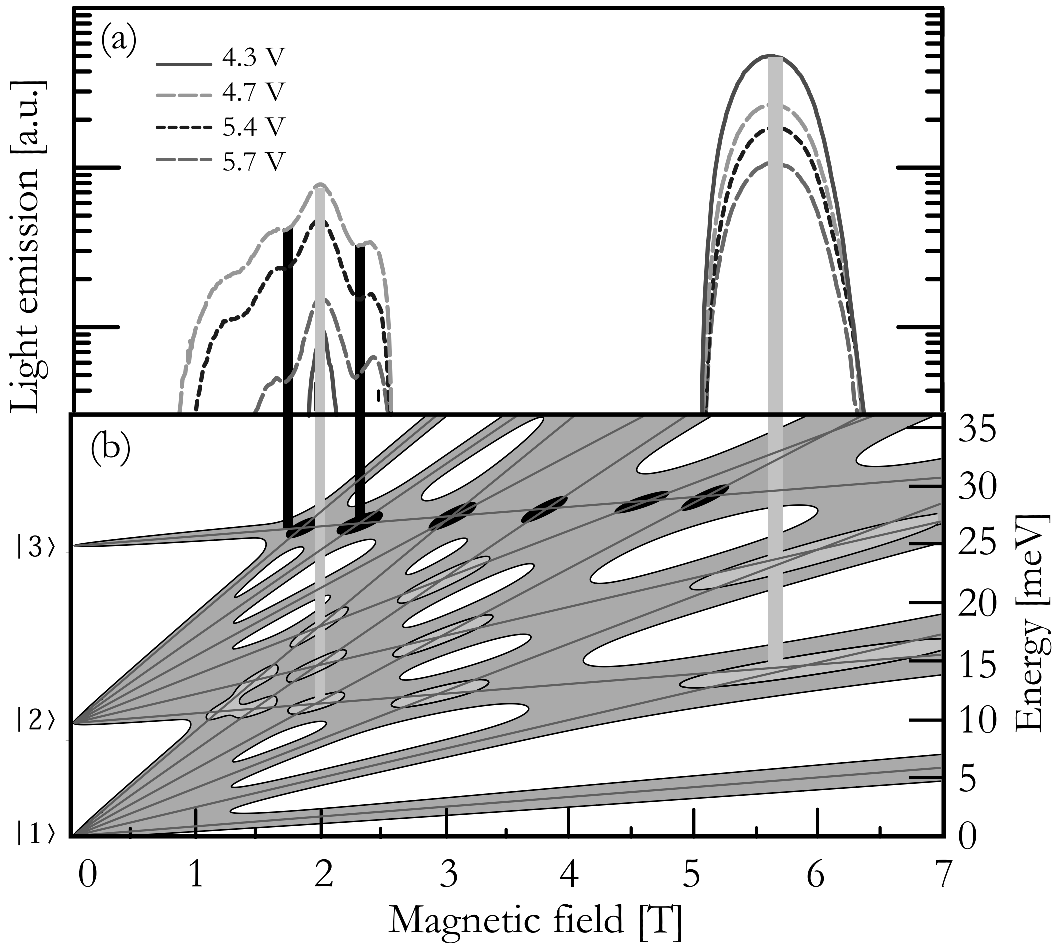

Figure 6.6: (a) Laser emission vs. magnetic field for sample A2664 at different biases measured at T = 4.2 K with InSb detector. (b) Landau fan of the active region: grey lines represent the center of the Landau levels together with the broadening. Light grey ellipses indicate the resonance condition for the extraction levels, where maxima in light emission occur. Black ellipses highlight the crossing of the Landau level of the upper state with the states originated from levels 1 and 2 where a decrease of light efficiency is produced. Lines of respective colors are a guide to the eye to ease identification of features in (a).

As shown in Fig. 6.6, the location of these resonances is independent on the applied bias as expected for a structure based on a vertical transition where Stark shifts are second order with respect to the applied electric field. Spectral emission is centered around 15.3 meV and the mode envelope of the laser emission shows a small redshift with increasing magnetic field, as visible from Fig.6.7(a). The light versus magnetic field characteristics of sample A2770 are very similar, presenting a main peak at 6.1 T and another peak at 1.54 T (see Fig.6.5). The difference in the location of the peaks is attributed to a different spacing of the levels responsible for electron extraction. In Fig. 6.7(b) LI curves for sample A2664 as a function of the temperature at the magnetic field where threshold current reduction is maximum are reported. In pulsed operation the device reaches a temperature of 60 K with a threshold current density of 30 A/cm^2, demonstrating the robustness of the resonant magnetic confinement also at high temperatures.

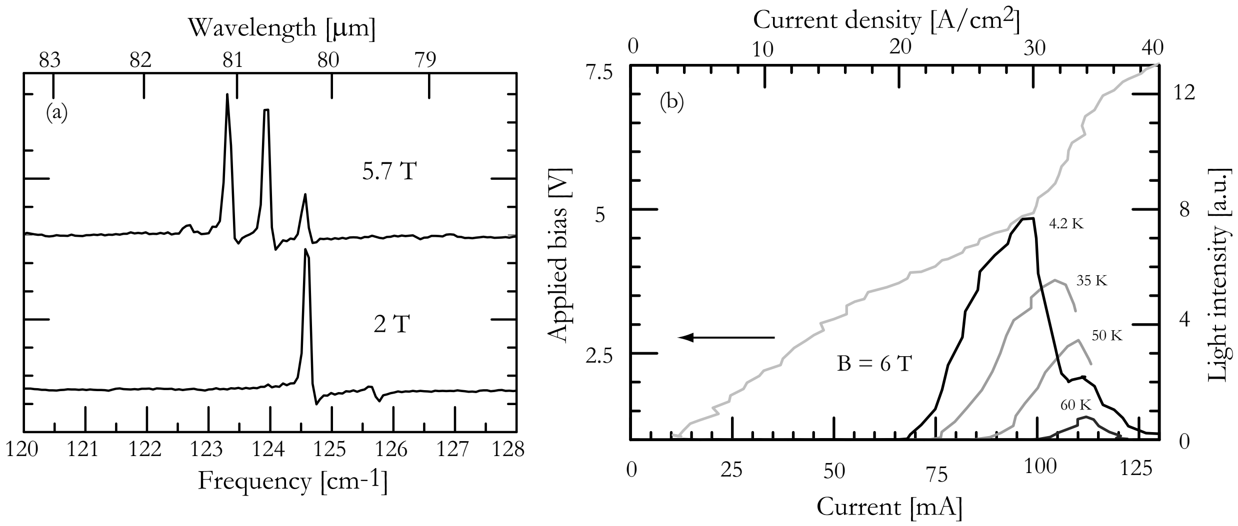

Figure 6.7: (a) Spectral emission at 2 and 5.7 T for sample A2664 at T=4.2 K. (b):L-I-V curves for sample A2664 measured as a function of temperature at 6 T with Ge bolometer (IV curve is at 4.2 K)

6.3.2 Lifetimes analysis

A more quantitative analysis of the influence of magnetic confinement can be achieved by a study of the laser parameters. Threshold current densities as a function of magnetic field are plotted for samples A2664 and A2770 in Fig. 6.8 (a). As expected, the maximum of light intensity in Fig. 6.6 corresponds to a minimum in threshold current density in Fig. 6.8. The overall lower threshold of device A2664 is attributed to its lower doping, and thicker injection and extraction barriers, which together yield a narrow luminescence linewidth. As can be seen from threshold current as a function of magnetic field, laser action is present for sample A2770 also in the region 3 T-3.7 T, where resonance and off resonance condition occur simultaneously. Here the value of the threshold current is higher than the one at zero field: lifetime modulations do not cooperate and more carriers are needed to reach threshold. In a simplified three-level model that assumes unity injection efficiency in level n=3, the threshold current density will depend on the lifetimes τ_3, τ_2 and the scattering time τ_{32} that are *a priori* unknown:

$$J_{thresh} = \frac{e}{\tau_3} \cdot \frac{\alpha/g_c}{1-\tau_2/\tau_{32}}$$

Waveguide losses α and gain cross-section g_c may be computed[3] by the standard approach illustrated in Section.2.2.2. We obtain τ_3 independently by a measurement of the temperature dependence (from T = 10 K to T = 110 K) of the luminescence intensity from a side-cleaved laser [175]. At liquid nitrogen temperature and above, the intersubband lifetime is limited by optical phonon emission; computation of the scattering rate and comparison with previous research [131] enables us to deduce the low temperature lifetime. Values of $\tau_3 = 8$ ps for sample A2664 and $\tau_3 = 5.3$ ps for sample A2770 are found. From the data of Fig. 6.6 and Fig. 6.8, it is clear that most of the improvement in laser performance comes from a modification of the lower state lifetime. Assuming a constant value of τ_3 mentioned above, we find that, for sample A2664 the ratio τ_2/τ_{32} improves from $\tau_2/\tau_{32}\ |_{0T}= 0.9$ and $\tau_2/\tau_{32}\ |_{5.65T}= 0.4$. Similarly, for sample A2770 we find the values $\tau_2/\tau_{32}\ |_{0T}= 0.8$ and $\tau_2/\tau_{32}\ |_{6.1T}= 0.6$.

[3]For sample A2664 we used the values $2\gamma_{32} = 0.77$ meV, $z_{32} = 85$ Å, $\alpha = 5.2$ cm^{-1}, $\Gamma = 0.16$, $L_p = 1252$ Å, while for sample A2770 the values were $2\gamma_{32} = 1.3$ meV, $z_{32} = 91$ Å, $\alpha = 13.2$ cm^{-1}, $\Gamma = 0.32$, $L_p = 1184$ Å: this numbers yield $g_c\ |_{A2664}= 9.5 \times 10^{-13}$ cm and $g_c\ |_{A2770}= 1.5 \times 10^{-12}$ cm.

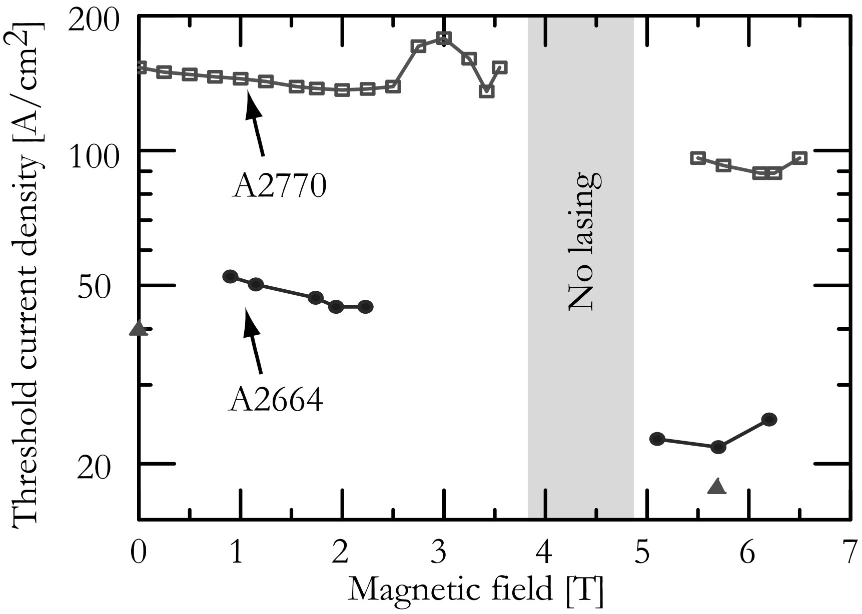

Figure 6.8: Threshold current density vs magnetic field for samples A2664 (2 mm long, 165 μm wide with HR coating), in dots, and for sample A2770 (1.7 mm long, 200 μm wide),in open squares (T= 4.2 K). The two triangles represent data points for sample A2664 obtained from a 4.1 mm device with both facets fitted with HR coating.

Lower state doublet: detailed analysis

From the comparison between measurements and calculations we notice that there is a good agreement between simulated data and experiment: one discrepancy is the energy spacing E_{21} for sample A2664 as deduced from magnetotransport and laser emission in magnetic field. It was already stated elsewhere that at the resonant field where the extraction levels are exactly spaced by the cyclotron energy the lifetime of the lower level is greatly reduced and lasing action becomes possible: in fact the measurement of the position of the peak of light emission in function of the magnetic field could be used to *deduce* information on energy spacing between the electron levels. Let's look at the measurement of laser emission from both samples A2770 and A2664 as a function of magnetic field. The main features are around 2 Tesla and 6 Tesla and especially the feature around 6 Tesla is a clean one: there are no near resonances between Landau levels $|3, i\rangle$ and $|2, i-1\rangle$ that could perturb the laser emission reducing the upper state lifetime of the transition. In sample A2664 measured immersed in liquid helium the maximum peaks at 5.65 T, and could be fitted by a gaussian function, giving a width of $\Gamma_{5.65T} = 0.37$ T. The value of the magnetic field at the peak of the laser

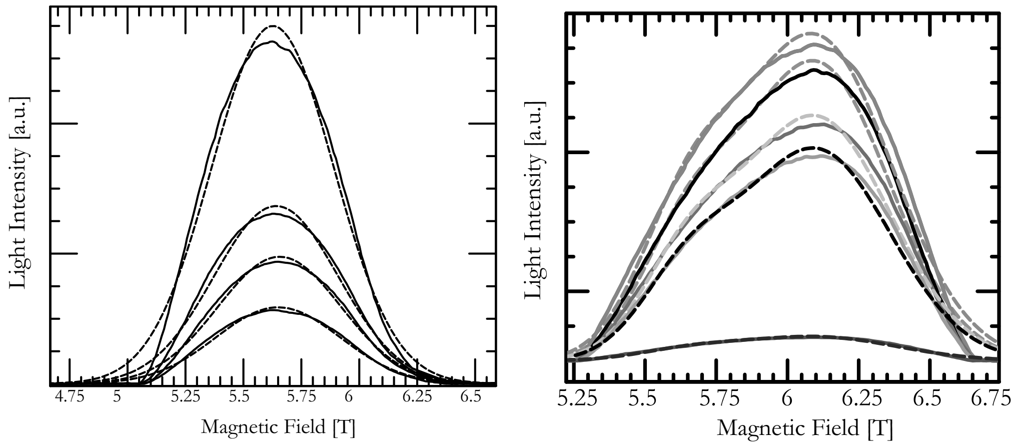

Figure 6.9: Left: peak light intensity at 5.65 T for sample A2664, together with Gaussian fit. The width of the peak in magnetic field unity is Γ =0.37 T for any applied bias. Right: peak light intensity for sample A2770, together with a fit with two Gaussian functions centered at 5.65 T and 6.1 T, respectively. Fitted curves are in dashed.

emission can be used to deduce the spacing of the extraction levels $E_{21}^{A2664} = E_c(5.65T) = 9.7$ meV. The same procedure on sample A2770 yields $E_{21}^{A2770} = E_c(6.1T) = 10.5$ meV [4]. There seems to be a difference in the energy spacing of the extraction levels but the situation is more intricated. To clarify that, let us look carefully at the measurement for sample A2770: the maximum around 6.1 T has an asymmetric shape that clearly suggests the envelope of two maxima. A fit of the peak with two gaussian functions centered respectively around 5.65 T and 6.1 T is reported in Fig 6.9 and results in very good agreement with the observed features. The explanation for that has to be found in the bandstructure diagram: in fact the

[4]The agreement between the fit and the experimental curve is worse on the low magnetic field side of the peak: this can be explained by the fact that at 5 T there is a crossing between the Landau levels $|3,0\rangle$ and $|2,2\rangle$, that acts in the sense of reducing the upper state lifetime, and results in a perturbation of the lower state lifetime reduction due to resonances among levels $|2\rangle$ and $|1\rangle$. The high magnetic field side of the peak agrees better with the gaussian fit, because the next crossing between Landau levels $|3,i\rangle$ and $|2,j\rangle$ is further away (7 T).

level 2 of the laser is constituted by a doublet spaced by 1.9 meV. This doublet is "seen" by

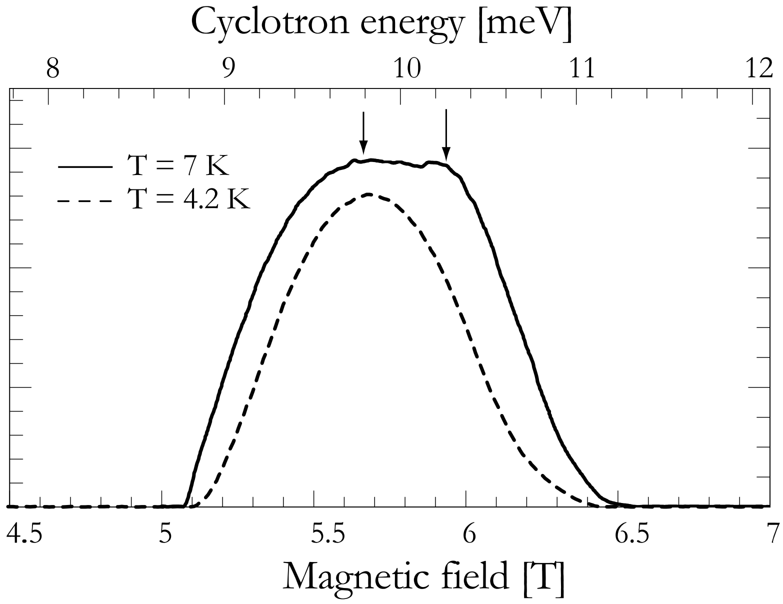

Figure 6.10: LB curves as a function of temperature for sample A2664 around the principal extraction resonance. Black arrows indicate the position of the two extraction resonances

the laser structure, producing an enhancement of the scattering also in correspondence of a magnetic field value lower than the designed one. This phenomenon is due to the coupling of this doublet of levels, that provides the necessary phase space for the electrons to scatter and then reduce the lifetime of the lower level of the lasing transition. This measurement can be verified also on structure A2664: changing temperature and bias we can change the shape of the peak also in this sample (see Fig.6.10). The peak switches from 5.65 T to both resonances. The presence of this doublet of levels can be detected also from an analysis of the electroluminescence of sample A2664 as a function of the applied bias. In Fig. 6.11 (a) a redshift of the emission peak as a function of the applied bias is clearly visible (the asymmetric shape of the peak is due to an absorption line of the bolometer's window at 16.2 meV). We expect no Stark shift in this structure (in the same quantum well it is second order in the applied field) and moreover it should be a blue shift. Plotting the calculated values of the energy and the dipole element z_{3j} for the two states $|2\rangle$ and $|2'\rangle$ as a function

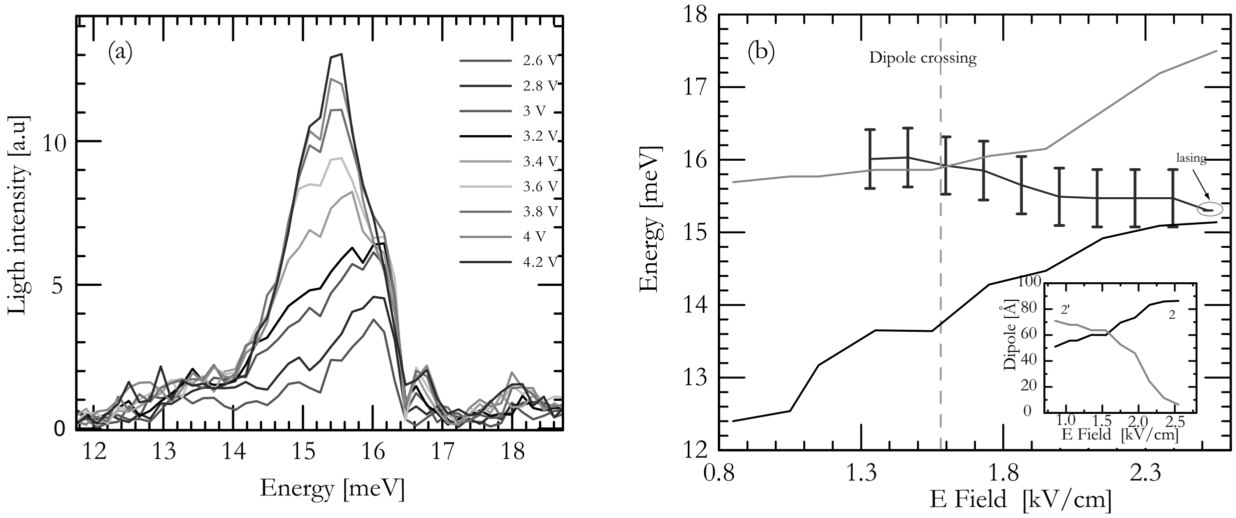

Figure 6.11: (a):Electroluminescence for sample A2664 at T = 10 K. Redshift of the peak as a function of the applied bias is clearly visible. The asymmetric shape of the spectra is due to absorption line in the bolometer's window at 16.5 meV. (b):Calculated energies E_{32} and $E_{32'}$ (solid lines) as a function of the applied electric field together with peak position of the luminescence with error bars. Inset: dipole element for the two transitions 32 and 32' as a function of the electric field.

of the electric field, we notice that the dipole at low field is higher for the level $|2'\rangle$ which has a higher calculated energy spacing $E_{32'}$. Increasing the electric field, the states show an anticrossing behavior and the relative intensities of the dipoles interchanges at about 1.6 kV/cm. The trend of the peak of the luminescence follows this picture: it starts from a higher energy value and then it saturates at the final value $|32\rangle$ = 15.2 meV, where laser emission occurs (see Fig. 6.11(b)). This redshift of the emission is not attributable to many body effects like depolarization shift[27] because the electron densities are too low (typical upper state density $n_{s,up} \approx 10^9$ cm^{-2}). For a more detailed discussion of this topic see Sec. 6.6.2.

6.4 Big well at 159 μm

In the previous experiments, we studied the behavior of the laser for cyclotron energies smaller or equal to the photon energy [150, 190, 158, 191]. In this Section we investigate a similar device, but designed to operate at 1.91 THz (7.9 meV, $\lambda \simeq 160$ μm) in the regime of strong magnetic confinement. The temperatures, mobilities and magnetic fields correspond to the physics of resonant tunnelling in the quantum Hall regime [192]. In contrast to previous

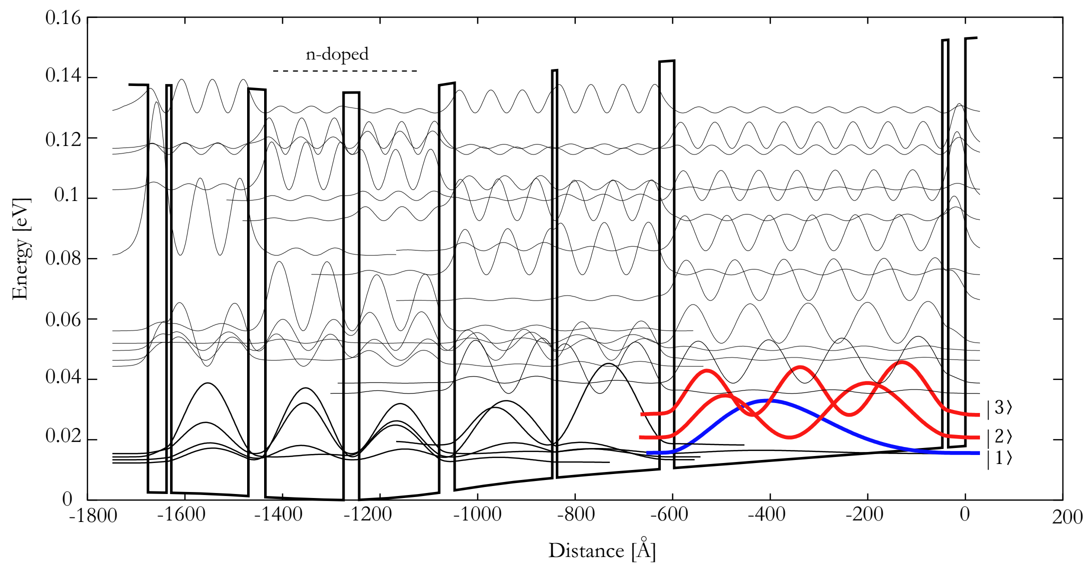

Figure 6.12: Bandstructure for sample A3096 calculated self-consistently at T=10 K for an applied electric field of 0.86 kV/cm. Dashed line marks the doped layers. The layer sequence in nm starting from the injection barrier is (from right to left) as follows: **2.5**/3.5/**1.2**/55.0/**3**/21.0/**1.0**/20.0/**3.2**/<u>16.4/**3.2**/16.0</u>/**3.5**/15.8/**1.0**/3.8/ (underlined layers are Si doped at 1.5 $\times$ 10^{16} cm^{-3}, figures in bold type are $Al_{0.15}Ga_{0.85}As$ layers).

work, where an intermediate regime was achieved in which the magnetic confinement was strong enough to modulate the intersubband lifetime but no qualitative change was observed in the laser behavior, we will observe two dramatic new features unique to these devices that can operate in the strong confinement regime: a strong reduction of the waveguide losses and an increase in the gain attributed to carrier localization, and a resonant electron-electron scattering effect. As shown in Fig.6.12, the active region of sample A3096 , similar in concept to the one presented in Section 6.3, consists of a 55 nm thick undoped GaAs quantum well followed in sequence by a coupled well extractor and a three quantum well injector. The dipole matrix element for the $|3\rangle \longrightarrow |2\rangle$ transition is $z_{32} = 119.3$ Å for an oscillator strength f_{32}=29.7. The exact layer sequence is given in the caption of Fig. 6.12. The device is originally designed to operate at a field of 2.9 T where the cyclotron energy matches the E_{21} energy spacing, reducing the n=2 lifetime. At the same time, the energy spacings E_{32} and E_{31} are respectively equal to one and a half times and two and a half times the cyclotron energy, enhancing the n=3 lifetime. This combination of level alignment therefore enhances the n=3 to n=2 population inversion. The structure was grown by molecular

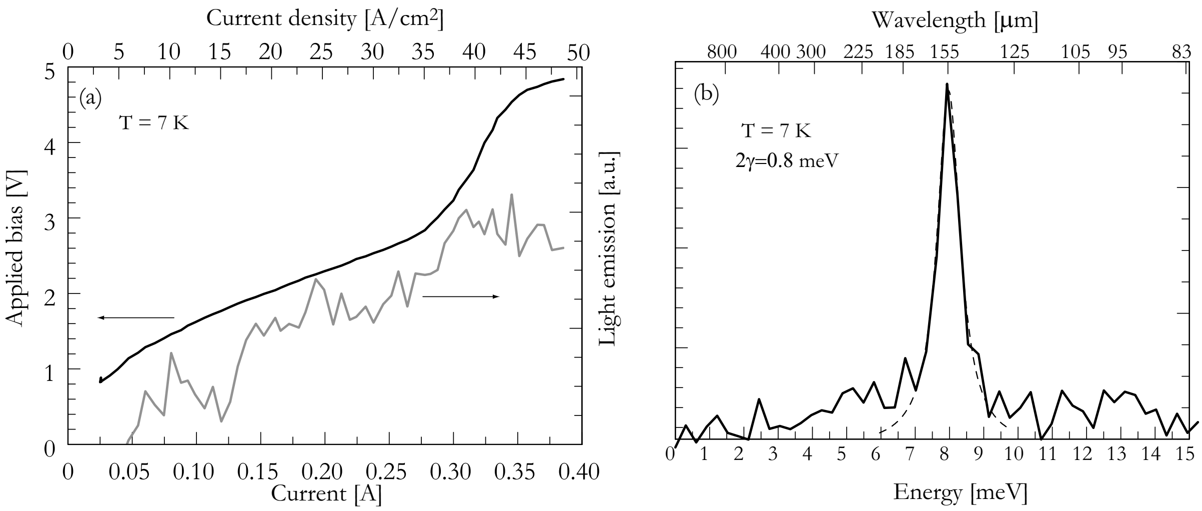

Figure 6.13: (a): L-I-V curve for sample A3096 at B=0. Device dimensions are 3.6 mm length and 220 μm width. Note the very low current density injected in the device. (b): Electroluminescence spectrum for sample A3096 at T=7 K for B=0. Full width at half maximun is 2γ=0.8 meV.

beam epitaxy on a semi-insulating GaAs substrate. 100 periods of the active region were deposited between 0.7 μm thick (Si doped, 9×10^{17} cm^{-3}) lower and 0.08 μm thick (Si doped, 5×10^{18} cm^{-3}) upper GaAs contact layers. The devices were then processed into 100-520 μm wide and 0.5-4.7 mm long ridge stripes by wet chemical etching. The thinning was pushed down to a substrate thickness of 100 μm in order to exploit the second mode of the single plasmon waveguide, as described in Section 3.3. The laser ridges did not show laser action without applied magnetic field. Electroluminescence measurements in a waveguide configuration showed a very narrow emission peaked around 7.9 meV. A spectrum of such emission together with an I-V curve with no applied magnetic field is reported in Fig.6.13 for a 3.6 mm long, 220 μm wide device. The current density circulating in the structure is extremely reduced: the injector is aligned for $J_{align} \approx 10$ A/cm^2 and the pronounced feature observed at $J_{max} = 40$ A/cm^2 marks the misalignment of the ground state of the injector with the upper state $|3\rangle$. From this value and the calculated value of the injection-upper state coupling (see Table 6.1 in the following) we can already infer a quite long value for the upper state lifetime $\tau_3 \cong 95$ ps.

6.4.1 Laser emission in magnetic field

Light intensity characteristics, obtained by ramping the magnetic field applied perpendicularly to the epilayers, are displayed in Fig. 6.4.1(a) for various applied biases. As expected, the device displays a first maximum of intensity at an applied magnetic field of 2.9 T, corresponding to the design field at which the lifetime of the n=2 state is reduced by enhanced scattering [155] at the crossing of the Landau levels $|1, i\rangle \rightarrow |2, i-1\rangle$. The laser then switches off until a field value of 5.5 T, at which point a series of oscillations starts. As shown in Fig. 6.4.1, the extinction of the laser between 3.3 and 5.5 T, as well as the minimum at 7.4 T, can be attributed to resonances between the n=3 state and an excited Landau level of the n =1 and n=2 levels, and n=1 level, respectively [122, 190, 191, 91, 158]. For fields larger than 3 T, $\hbar\omega_c > E_{21}$ and no resonances between the n=2 and n=1 states are allowed.

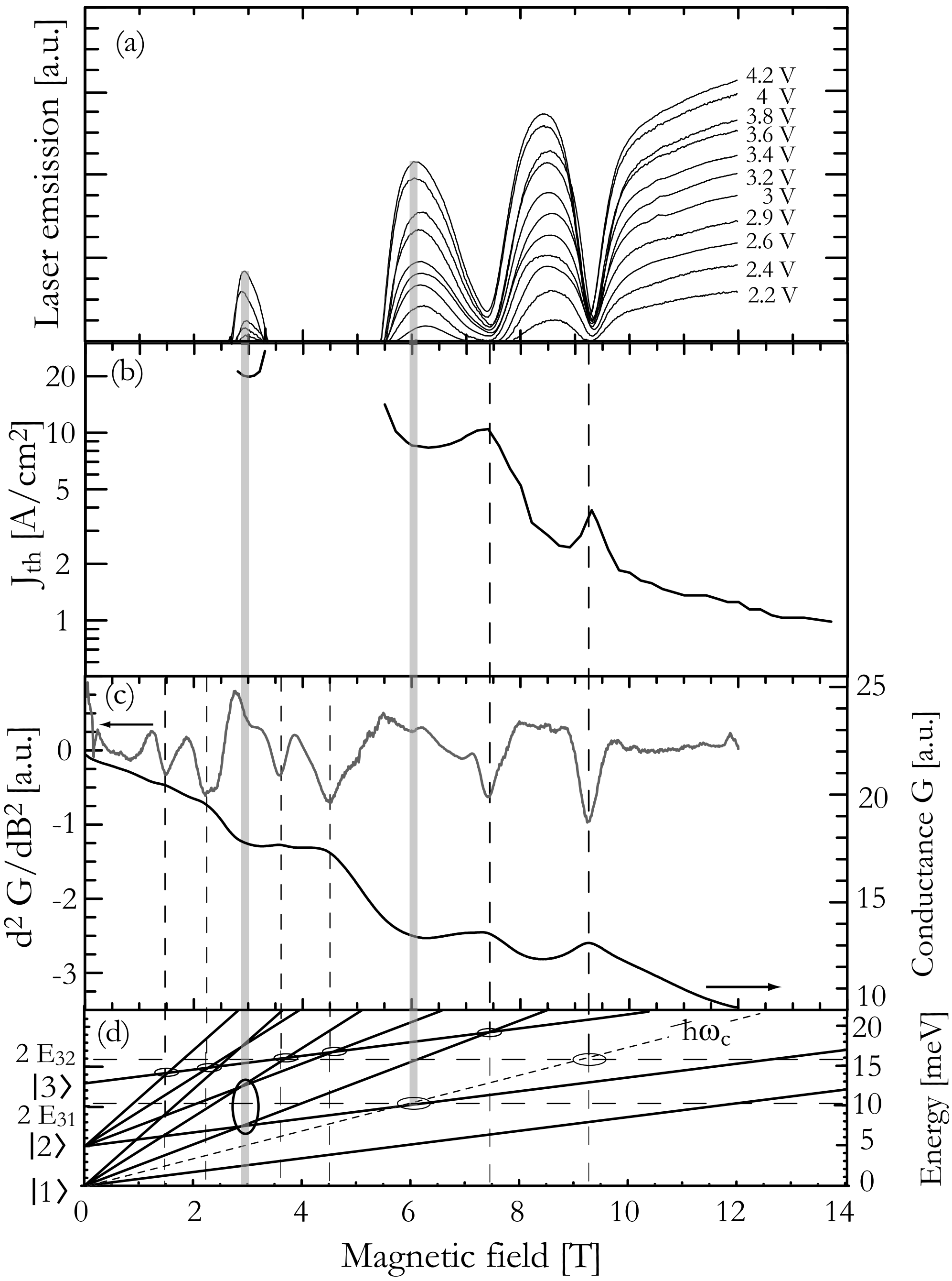

Figure 6.14: (a) Light emission in pulsed mode as a function of magnetic field for various applied biases for a 3.5 mm long, 520 μm wide laser stripe at 4.2 K.(b) Threshold current density as a function of magnetic field for the same device as in (a). (c) Conductance, together with its second derivative, as a function of magnetic field at 4.2 K measured on a 320 $\times$ 400 μm^2 mesa at 1.5 V applied bias. (d) Landau fan plot of the active region: the dashed line is the cyclotron energy. Note the crossing at 9.3 T of the cyclotron energy with the horizontal wide dashed line representing two times the photon energy $2E_{32}$ and the same kind of resonance happening at 6 T for $2E_{21}$.

The conductance, measured directly by a lock-in technique, is displayed in Fig. 6.4.1 (c), together with its second derivative in magnetic field $\frac{\partial^2 G}{\partial B^2}$. This quantity reflects the variation of the n=3 lifetime with applied magnetic field. As expected, an excellent agreement is found between the conductance and laser emission data whenever a Landau level crossing involving the n=3 state occurs. The minimum at 7.4 T marks the crossing of the first excited Landau level of state 1 with the ground Landau level of state 3 $|3,0\rangle \longrightarrow |1,1\rangle$ above which the in-plane confinement energy is greater than E_{31}. For this reason, for fields larger than 7.4 T, no more inter-Landau-level resonances should be observed. However, a very strong feature is present at 9.3 T, corresponding to a field where the photon energy is half of the cyclotron energy, $\hbar\omega_c(9.3T) = 15.9$ meV $=2h\nu = 2E_{32}$. In fact, this resonance was predicted theoretically [161] as a signature of an electron-electron scattering event in which energy and momentum are conserved with one electron scattering to the lower Landau level and a second electron scattering up to the higher Landau level. A signature of this effect in transport only was observed previously at very large magnetic field values [161]. In our data, this resonance appears not only in transport but also in the light intensity for the first time. A similar resonance arising between n=2 and n=1 states is at the origin of the abrupt increase in light intensity above 5.5 T when the condition $2E_{21} = \hbar\omega_c$ is satisfied, reducing the lower state lifetime. No features are to be expected in the conductance data in this case since the n=3 lifetime is not affected.

The threshold current density J_{th} of the device (Fig. 6.4.1(b)) also exhibits the resonances displayed in the light intensity data, and steadily decreases from a value of 20 A/cm^2 at B = 3 T to less than 1 A/cm^2 at 13 T. This value of threshold is extremely low, even compared to record values $J_{th} = 5$ A/cm^2 obtained from quantum box interband devices at similarly low temperatures [30]. This decrease in threshold current originates both from a reduction of the waveguide losses as well as from a strong increase of the gain, caused by the increase of the upper state lifetime with magnetic field. To further understand the behavior of the threshold current, we measured the threshold current density J_{th} in a series of five samples of various lengths between L = 4.7 mm and L = 1.8 mm, extracting the waveguide loss α_w and gain $g\Gamma$ (see Formula 4.4.9).

Waveguide losses and differential gain are plotted as a function of magnetic field in Fig. 6.15 for 420 μm wide laser stripes [5]. Two regimes are apparent. The main waveguide loss mechanism is, at these low THz frequencies, free carrier absorption. We believe that this is effectively quenched by the localization of carriers induced by magnetic field. This phenomenon should become significant as soon as $\omega_c\tau > 1$, i.e. the cyclotron energy is larger than the broadening of the levels of the injector; this condition is well fulfilled at B = 6 T. However, as expected, at the resonant condition where cyclotron energy matches the photon energy $\hbar\omega_c(7.4T) = h\nu = 7.9$ meV we observe a strong increase of the waveguide losses due to the coupling of the in-plane component of the electric field. At large fields (B > 9.3 T), the waveguide loss is limited by the metal waveguide and no further reduction of the loss is possible. However, the dielectric constant of the semiconductor is anisotropic owing to the Landau quantization and therefore an exact solution for the waveguide behavior is difficult . Solutions have been proposed for specific geometries different from ours [193]. However, in our geometry where the field is constrained by two metal boundaries it would be difficult to change significantly the field distribution. An experimental indication of this unchanged field distribution is that the group velocity index $n_g = 4.03$, obtained from the spacing of Fabry-Perot interference fringes, does not change with magnetic field (see inset Fig. 6.15(b)). It agrees well to the computed value (n = 3.97) using the n=2 TM mode and tabulated refractive index values [194].

Below B = 9.3 T, the measured differential gain, displayed in Fig. 6.15(b), exhibits the same oscillations as the laser emission due to the modulation of lifetimes in the excited subbands caused by the coupling of the Landau levels. Specifically, we observe a decrease of the gain and lifetime by a factor of 2 at the field (9.3 T) where resonant e-e scattering is occurring. Above 9.3 T, gain increases dramatically by a factor of 5, attributed to an increase of the lifetime of the upper state by the same factor. Shown, alongside the gain data, is the lifetime deduced from magnetotransport measurements of the diagonal THz emitter studied in Ref. [154] with an energy spacing of 14 meV, very close to the energy spacing $E_{31} = 12.9$ meV

[5] The calculation of the gain and losses over the whole set of five lasers is possible only above 5.5 T , because for the shortest cavity length there is no laser action at 2.9 T. The same kind of analysis has been performed on 320 μm wide ridges with similar results

of our laser. The behavior of the two quantities is very similar, confirming a dependence of the gain on the overall lifetime τ_3.

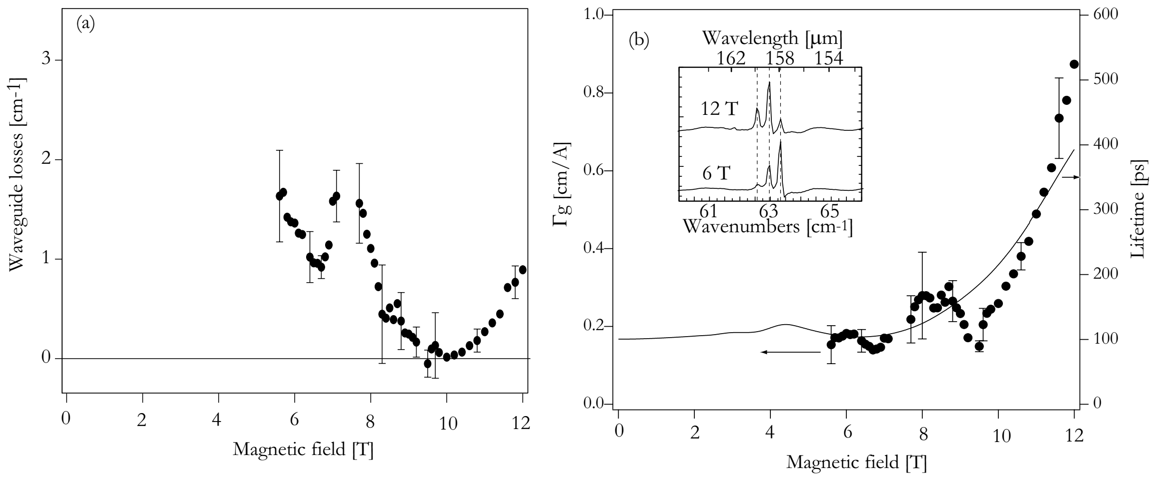

Figure 6.15: (a) Waveguide losses as a function of magnetic field for a ridge width of 420 μm. Inset: intensity profile for the n=2 TM mode (black line) which has a calculated value of losses of 7.9 cm^{-1} and a mode overlap of $\Gamma = 0.29$. (b) Left axis (disks): differential gain as a function of applied magnetic field for a ridge width of 420 μm. Right axis (full line): lifetime deduced from the magnetotransport of the diagonal terahertz emitter studied in Ref. [154]. Inset: laser spectra recorded at 6 T and 12 T for a 3.18 mm long, 220 μm wide cavity at T = 4.2 K with an FTIR spectrometer (resolution 0.125 cm^{-1}).

The origin of this strong increase in the lifetime may be understood by looking at the dependence of the threshold current density on magnetic field and temperature. In Fig. 6.16, the threshold current density is shown between 4.2 and 65 K for the various magnetic fields corresponding to a local maxima in the optical intensity.

For magnetic field below 6 T or temperatures above about 20 K, the threshold current density remains above a value of 10 A/cm^2, increasing as the temperature is raised and showing a very weak temperature dependence below 50 K. This is the behavior exhibited by all THz quantum cascade lasers [85], and reflects the increase in threshold current density caused by the activation of optical phonon processes above a temperature of about 50 K. However, in our sample, for low temperatures and large magnetic fields, a strong reduction of threshold current density is observed, with the threshold varying by a factor of five between 4.2 K

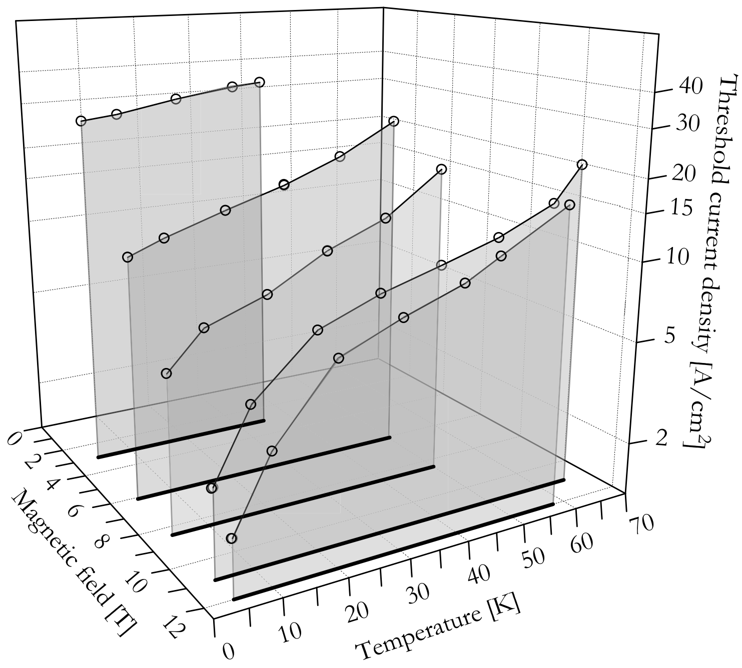

Figure 6.16: Dependence of threshold current density on temperature and magnetic field for a 3.5 mm, 320 μm wide device. The change in lasing regime is evident above 6 T and below 20 K. The measurements at 4.2 K are performed with the sample immersed in liquid He.

and 20 K. This temperature range corresponds to an energy much lower than the cyclotron energy, but is compatible with the typical localization energy of $\approx$ 1 meV resulting from residual disorder in the sample.

From knowledge of the dipole matrix element, and measurement of the waveguide and mirror losses, an estimated upper state sheet density of $n_3 \simeq 1.05 \times 10^8$ cm^{-2} is obtained [6]. This corresponds to an effective upper state lifetime of $\tau_3 \approx 20$ ps and an average inter-electron distance of 0.97 μm. Furthermore, recent work has shown that the localization of electrons on such a scale does occur even at much lower magnetic fields [146]. In reality, the situation is more complex than this since each of these electrons pockets will be coupled by tunnelling

[6] With the parameters n=4.03, $2\gamma_{32} = 0.7$ meV, $\lambda = 159$ μm, L = 0.35 cm, α_w=0.5 cm^{-1}, $L_{per} = 1701$ Å, $z_{ij} = 119.86$ Å, $\Gamma = 0.3$, $R_1 = 0.67$, $R_2 = 0.98$ (backfacet HR coated) we can calculate the upper state sheet density $\Delta n = \frac{\epsilon_0 \ n \ \lambda \ 2\gamma_{32} \ L_{per}}{4\pi e^2 \ z_{ij}^2} \cdot \frac{1}{\Gamma}(\alpha_w + \frac{1}{2L} \cdot ln\frac{1}{R_1 \ R_2}) = 1.05 \cdot 10^8$ cm^{-2}

to a common reservoir of electrons in the lower injector state, where a sheet density of $n_{inj} = 5.3 \times 10^{10}$ cm^{-2} resides.

The nature of the main non-radiative channel between subbands, key to the performance of THz quantum cascade emitters at low temperatures is still a matter of controversy. The observation in our data of clear electron-electron scattering resonances points to the importance of this process and is in agreement with indirect evidence obtained from light-current characteristics of non-lasing structures based on a vertical transition in a square well [79], whereas such behavior has never been observed in chirped superlattice or bound-to-continuum structures [124, 89]. Actually, the largest increase in gain and lifetime is observed at large magnetic fields and low temperatures, i.e. in a situation where interface roughness and impurities do not lead to intersubband scattering but to an inhomogeneous broadening of the gain because of carrier localization. It is worth noting that this localization is at least as efficient for high excited states since the population inversion improves with magnetic field. Electron-electron scattering is also efficiently suppressed except for the resonant condition at 9.3 T.

6.4.2 Device analysis and continuous wave operation

Due to its extremely reduced threshold current density, sample A3096 is a natural candidate for CW operation with ultra-low threshold. A special sample has been prepared with an epoxy protection on the bond wires in order to avoid eventual failure coming from Lorentz force acting on wires continuously excited by currents of some hundreds of milliamps. The setup has been provided by a chopper and CW laser emission has been recorded over the whole magnetic field range from 0 to 12 T. The CW operation is represented in a three dimensional graph reported in Fig.6.17 for a 4.7 mm long, 420 μm wide laser ridge with a backfacet high reflection coating. The threshold current density results to be the same as in pulsed mode, and the CW operation allows to observe several new features both in light emission and in transport. This kind of measurement resulted to be really useful and will be used also in the characterization of samples in very high magnetic field up to 28 T. The transport measurements especially benefit from the use of a high precision

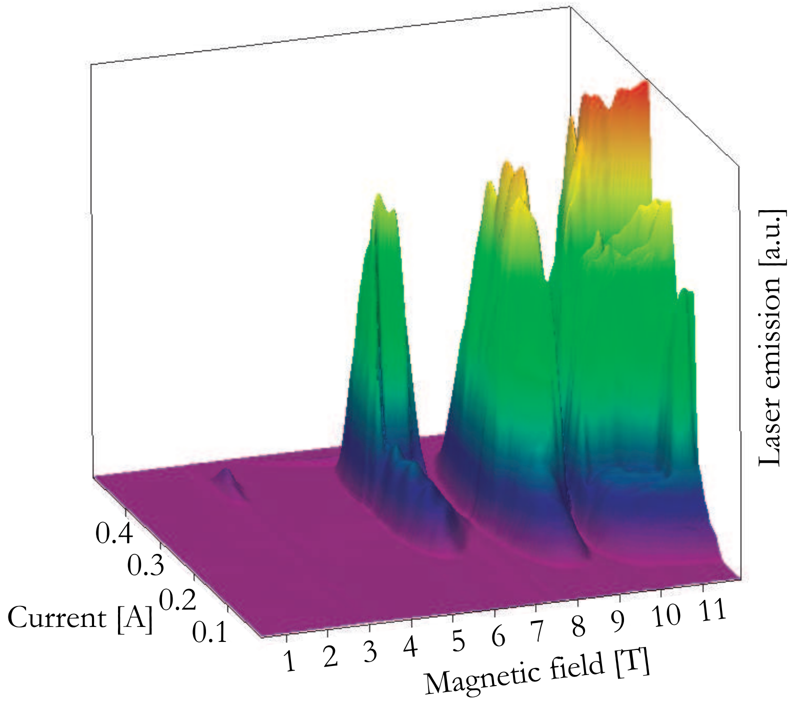

Figure 6.17: Three dimensional plot of CW emission of sample A3096 as a function of injected current and applied magnetic field.

current source (Keithley 2400 source meter). From the light emission as a function of the magnetic field several features are observed: (i) the dynamic range of the laser emission increases with the magnetic field, (ii) the L-I curves at constant magnetic field show a steplike behavior, (iii) the slope efficiency dP/dI increases with increasing magnetic field. The increased dynamic range of the device is due to the strong reduction of the threshold current. The reason for the abrupt increasing of the light emission in "steps" has to be searched in the structure of the injector (see Sec.6.4.3). The transport measured in continuous wave can also yield important informations. Direct analysis of IV curves as a function of the magnetic field show a progressive smoothing of NDR feature, together with a pronounced magnetoresistance. Besides the signatures of the inter Landau level resonances analyzed before on a mesa structure, it is interesting to investigate the influence of the strong photon field due to the laser action in the transport behavior. To do that it is convenient to perform a differential analysis of the I-V curve. We will present this kind of analysis first on one specific L-I-V curve (representing a "section" at constant B of the whole, 4-dimensional L-I-V-B plot), then we will make use of three dimensional and density plot to show the evolution of the features we detect. In Fig.6.18(a) the L-I-V curve at 12 T together with the calculated differential resistance is presented. The strong discontinuity (J_{thresh} = 1.5 A/cm^2) at laser threshold caused by the reduction of the upper state lifetime in consequence of stimulated emission is evident. The huge drop of differential resistance at threshold is a clear signature of an high lifetime ratio and a strong population inversion. Another peculiarity of this lasing

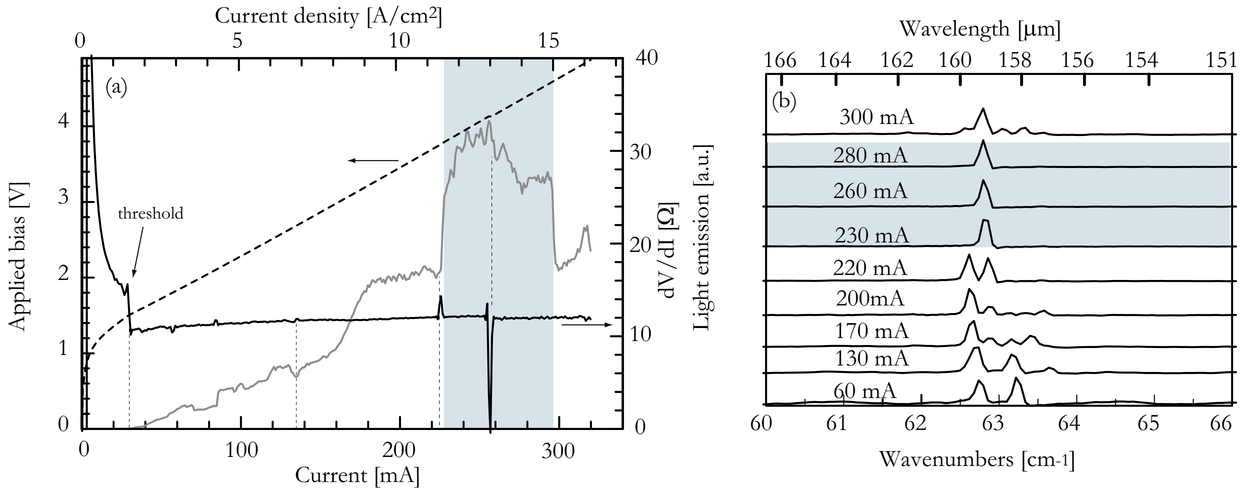

Figure 6.18: (a): L-I-V curve in CW for sample A3096 at 12 T together with differential resistance. Ridge length is 4.9 mm and ridge width is 420 μm. Laser emission is in grey, while I-V curve is dashed. Steplike behavior of the L-I curve is evident together with correspondent features in the differential resistance. The grey area is where single mode emission occurs (b): Spectral emission at different injection currents.

regime can be observed analyzing the spectral emission, reported in Fig.6.18(b). The laser emission just above threshold is multimode, then when the laser reaches is last alignment step and its maximum output power the emission switches to single mode. This region is highlighted by a grey shading in the figure. After the highest plateau the lasing comes back to multimode emission. This behavior is observed for every magnetic field value above the

2-electron scattering event at 9.3 T [7]. Usually in a QC laser the opposite phenomenon is observed: changing from single mode to multi-mode emission is attributed to spatial hole burning (variation of the carrier density due to the variation of the power). What we observe here suggests in fact that on the last plateau the optical power inside the cavity is distributed more uniformly than at low injection currents. This aspect needs obviously more research for a satisfying explanation.

6.4.3 Alignement of injector states

If we look carefully at the structure of the injector of the sample A3096, we can see that there are three states that can couple with the upper state of the lasing transition and thus inject carriers. The successive alignement of these states in function of the applied electric field allow us to calculate anticrossing values and then injection coupling constants $2\hbar\Omega_{i3}$. We observe indeed features due to this "multi-level" injector when we look at the L-I-V curve in CW of Fig.6.18: the kinks on the light emission and the corresponding features in the differential resistance can be attributed to successive couplings of the injector states with level $|3\rangle$. Looking at the voltage at threshold in function of the applied magnetic field we can also see that at low field values, where we need more carriers to reach threshold, the corresponding bias is higher. Increasing the magnetic field and the lifetimes, we improve the population inversion and the structure can lase starting with the higher injector state (see Fig.6.19). It is interesting to note that the slope efficiency changes whenever we reach a new injector resonance: this is the signature of an improved coupling of the upper state with the electron reservoir.

Moreover, by increasing the electric field we bring into resonance the upper state $|3\rangle$ with states with lower energy with respect to the ground state of the injector, and consequently more populated at low temperatures. The possibility to observe these resonances comes again from the increased lifetimes due to magnetic confinement: the reduction of the threshold allows lasing with lower biases. It is not straightforward to deduce the values of the

[7] For lower magnetic fields the laser spectrum is multimode

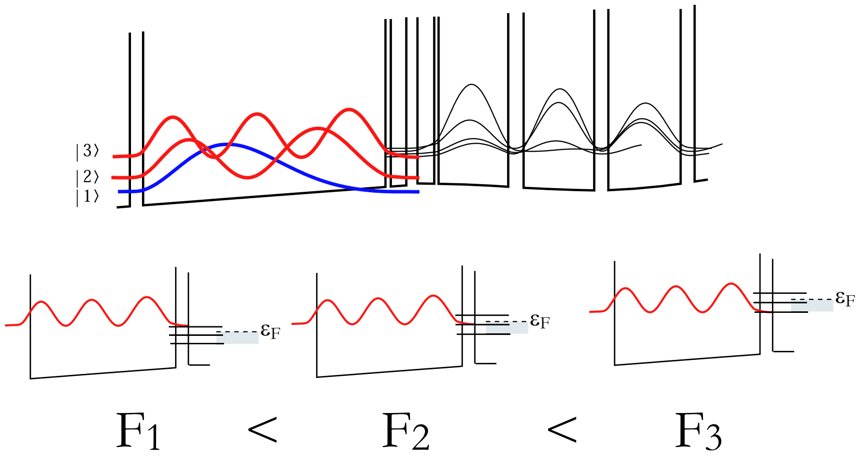

Figure 6.19: Successive alignement of the injector states with the upper state of the lasing transition $|3\rangle$ for increasing values of the applied electric field $F_1 < F_2 < F_3$.

	$2\hbar\Omega_{A3096}$ [meV]	Ω_{A3096} [THz]	$2\hbar\Omega_{A3520}$ [meV] [meV]	Ω_{A3520} [THz]	$2\hbar\Omega_{V198}$ [meV] [meV]	Ω_{V198} [THz]
E_{31}	0.12	0.09	0.11	0.08	0.14	0.11
$E_{31'}$	0.16	0.12	0.21	0.16	0.20	0.16
$E_{31''}$	0.21	0.16	0.16	0.12	0.08	0.06

Table 6.1: Energy couplings of the injector states with the upper state of the lasing transition $|3\rangle$ for samples A3096, A3520 and V198.

electric field corresponding to the various alignements (F_i) from the voltage at threshold beacause when we increase the magnetic field a huge magnetoresistance is present masking the real voltage drop on the structure and the consequent alignment condition. The nature of the magnetoresistance is related to the localization of the carriers and will be discussed later in the text. The described behavior of step-like L-I curves was observed in many devices of sample A3096 and also on the longer wavelength big wells that will be presented in the following of the Chapter. To give a more quantitative description of the phenomenon, we calculated the couplings of the injector states with the upper state of the lasing transition for the three big well structures. The results, shown in Table 6.1, show relevant couplings for three states in the injector for the three designs. This demonstrates the nature of this effect because we purposely kept the design of the injectors as close as possible changing mainly the width of the big well and the coupling with the extraction wells. Now that the features

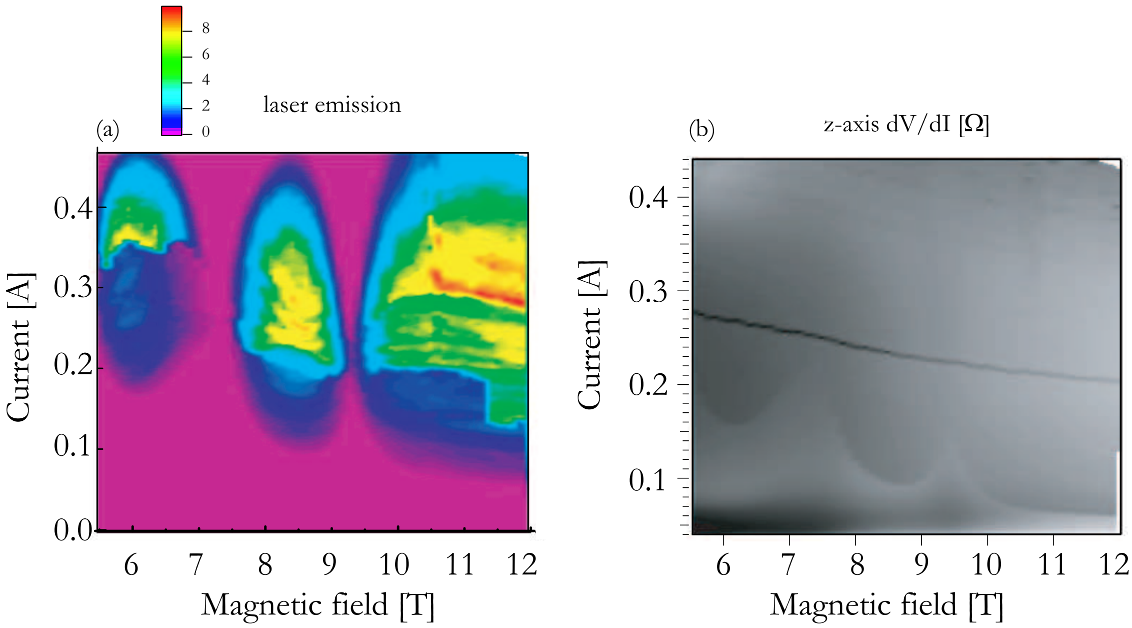

Figure 6.20: (a): CW laser intensity plot as a function of applied magnetic field and injected current. (b): differential resistance as a function of injected current and applied magnetic field. The discontinuity at threshold is evident also form the comparison with panel (a). The strong black feature is the beginning of the band misalignment.

are identified, a strong link has been demonstrated between laser emission and transport. The complete picture of the evolution of these features can be obtained by looking at the two density plots of Fig.6.20. In Fig.6.20 (a) a color plot of the laser emission as a function of the current and the applied magnetic field is reported. In panel (b) of the same figure the differential resistance as a function of the magnetic field is reported . The threshold current is identified by the discontinuity in the differential resistance: the amplitude of this discontinuity is modulated by the inter Landau level resonances, demonstrating the modulation of the lifetimes in the laser structure. We recall that the discontinuity at threshold is directly related to the slope efficiency, as discussed in Chapter 4: this means that a transport measurement as a function of the magnetic field can provide a complete picture of the lasing emission including the slope efficiency.

6.5 Strong confinement limit: lasing in magnetic fields up to 28 T

The results of the previous section demonstrate the importance of an in-plane confinement in order to increase intersubband lifetimes and obtain laser action with low photon energies. The extremely reduced values of the threshold current obtained in the strong confinement regime clearly motivate the extension of the experiments to higher values of the applied magnetic field. At the same time the possibility to achieve laser action at longer wavelengths exploiting the magnetic confinement pushed us to design two rescaled versions of the long wavelength big well. Going towards low photon energies is a difficult task: the achievement of selective injection and extraction of carriers becomes more difficult as the energy spacing of the levels begins to approach their broadening. In this respect the possibility offered by the magnetic confinement to increase the lifetime of the states narrowing their width and really simulating a "quantum box" structure seems to be a viable way for reaching the goal of 1 THz emission. In this section we will analyze the results we obtained on the structure A3096 in very high magnetic field up to 28 T. Then we will introduce two new laser designs that operate at 1.66 THz ($h\nu$= 7 meV) and 1.39 THz ($h\nu$= 5.9 meV) and analyze their performance in strong magnetic field. A comparative analysis of the big well devices will then be performed. The high magnetic field measurements have been performed at the Grenoble High Magnetic Field Laboratory (GHMFL) in Grenoble, France. In Appendix B some details about the facility and the experimental setup we used to perform the experiments are reported.

6.5.1 1.9 THz big well in strong magnetic field

The investigation of sample A3096 provides insights into the physics of intersubband transitions in high magnetic fields. In Fig.6.21 a three dimensional graph of the laser emission as a function of applied magnetic field and injected current density is reported. The output power has been calibrated measuring in the same apparatus a well-characterized device of the bound-to-continuum type described in Section 5.1. The calibration is still inaccurate (at least 20% of uncertainty) due to the difficulties of knowing the exact focal length of the Fresnel lens and the collection efficiency of the apparatus and should be taken as indicative. The output power is probably underestimated. Laser emission rises abruptly above the 12 T limit and keeps increasing towards high values of the magnetic field. At the maximum field value of 27 T laser emission is still increasing and its derivative with respect to the field is positive, indicating that the maximum of the emission has not been reached yet. This kind of measurement has been performed with two different detectors (one internal and one external, see Appendix B) and on two different samples showing the same trend. No more resonances are observed after the 2-electron scattering event at 9.3 T. One more resonance should be expected, the 2-electron resonance that couples the levels 1-3 of the big well structure that should appear for a magnetic field value (see Eq. 2.8.38) $2E_{32} = 2\times 12.9 = \hbar\omega_c \Longrightarrow B = 14.9$ T. The absence of this resonance, which is indeed observed on longer wavelengths samples, could be due to the high energy separation of the levels ($E_{31} = 12.9$ meV), since electron-electron scattering rate scales with the inverse of the energy separation ΔE^{-1} (see Section 2.3.1). Threshold current density steadily decreases down to the value of 0.625 A/cm^2 observed at 27 T: with this complete picture we can affirm that the changing in lasing regime is the one observed when the system enters the strong confinement region. The total reduction of threshold current density from the first peak of lasing at 2.9 T to the maximum value of 27 T is more than 30 times. Besides the point at 7.46 T where the first Landau level of the ground state $|1,1\rangle$ crosses the Landau level $|3,0\rangle$ of the upper state the system shows a uniform increase in radiative efficiency. An L-I-V curve for the same device is reported in Fig.6.22(a): the device shows a huge dynamic range ($J_{rollover}/J_{thresh} \cong 30$) as a consequence of the extremely low threshold current. The current density at which rollover occurs (about 20 A/cm^2) is half of the value at which we observe band misalignment at B=0. Moreover, there is no signature of band misalignment in the transport. To gain insight into the physics

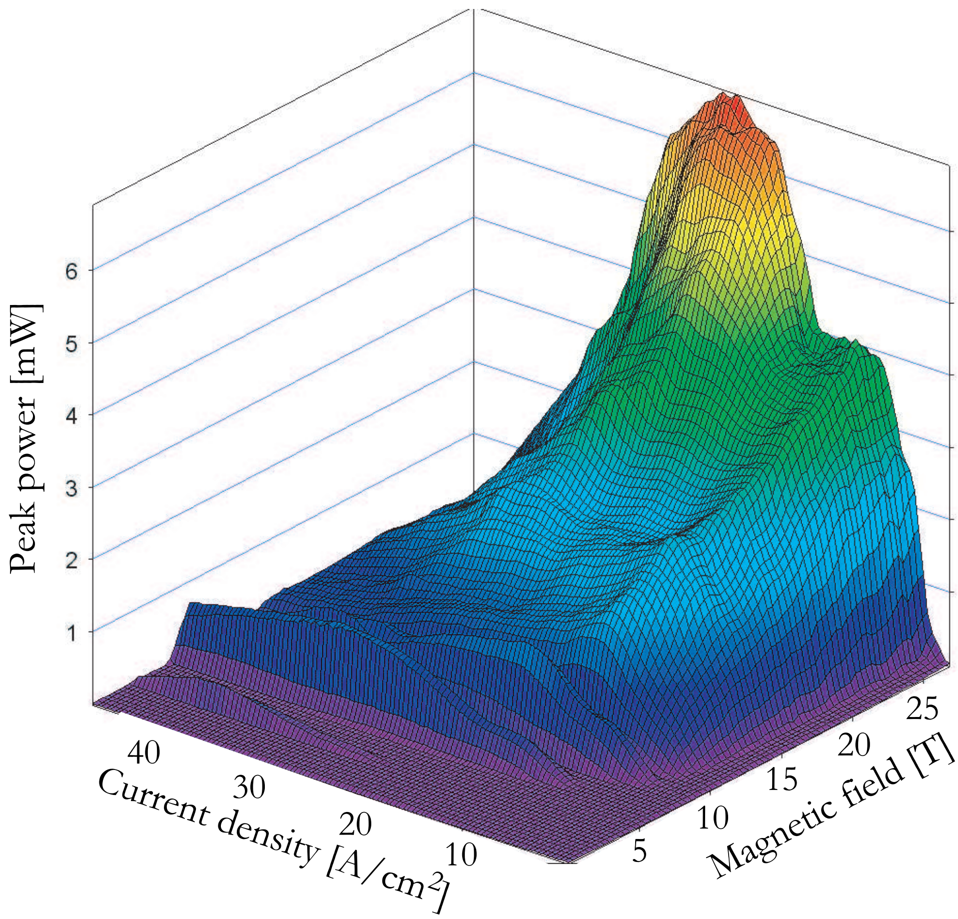

Figure 6.21: Laser emission of sample A3096 in magnetic field up to 27 T as a function of injected current density

of the system at high magnetic field we can analyze the slope efficiency dP/dI:

$$\frac{dP}{dI} = \frac{1}{2} N_p \frac{h\nu}{e} \frac{\alpha_m}{\alpha_w + \alpha_m} \left(1 - \frac{\tau_2}{\tau_{32}} \right) \tag{6.5.2}$$

In Fig.6.22 we plot the slope efficiency in function of the injected current density and the applied magnetic field. The increase after the last e-e scattering event and the constant increasing with the applied magnetic field is a signature of the lifetimes ratio that keeps improving. The value of the slope efficiency at B=27 T is 11 times the one we measure at 6.4 T. The spectral analysis of structure A3096 shows a redshift of about 1.5 cm^{-1} of the laser emission on the magnetic field range 6-27 T. This redshift will be analyzed in detail in Sec.6.6.2 where it will be compared to the same phenomenon detected on the other two long wavelength lasers.

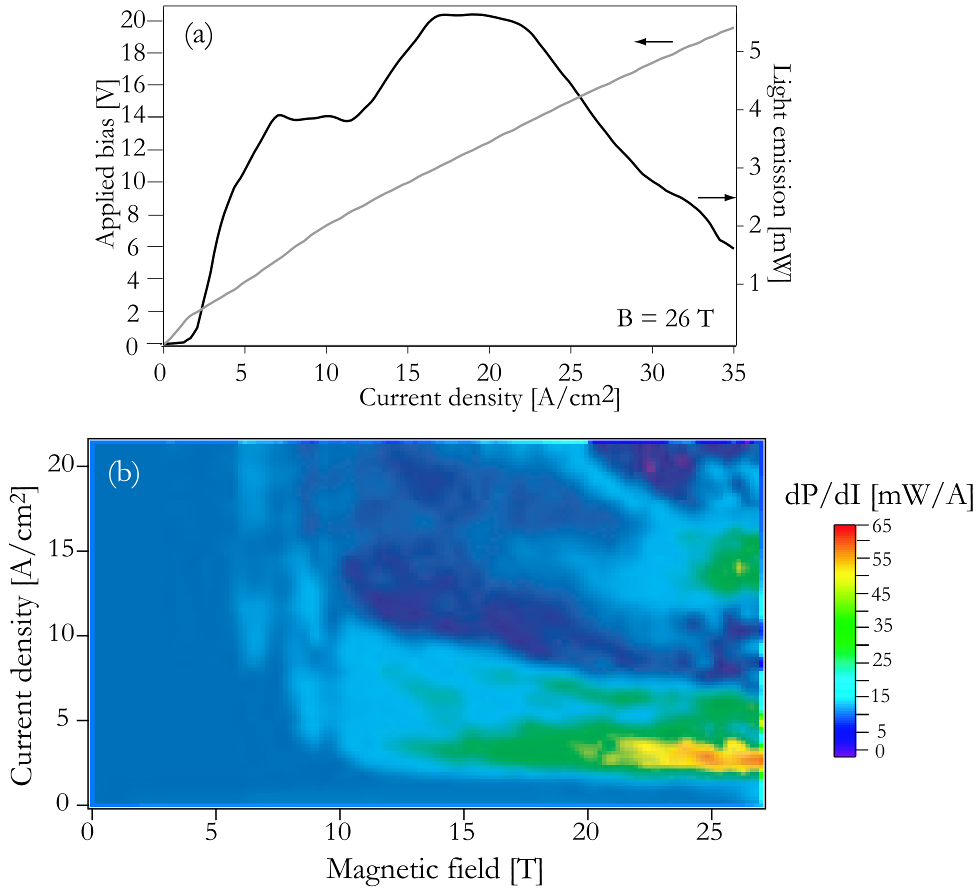

Figure 6.22: (a):L-I-V curve for sample A3096 at 26 T and 4.2 K. (b):Color plot of slope efficiency for sample A3096 as a function of injected current and applied magnetic field up to 27 T.

6.5.2 1.66 THz big well in strong magnetic field

The extension to longer wavelengths of the big well concept has been made trying to keep the designs as close as possible in the injector part, changing the widths of the big well and of the adjacent QW in order to tune the relevant levels of the structure accordingly to Eq. 6.2.1. A first structure with a photon energy of 7.1 meV (sample A3520)has been designed, exploiting

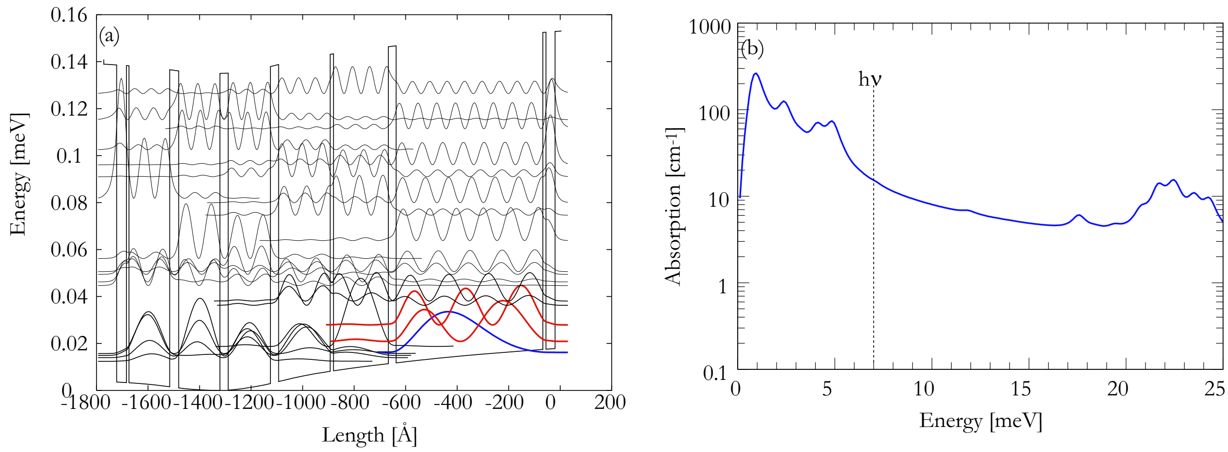

Figure 6.23: (a): Bandstructure for sample A3520 calculated self-consistently at T=10 K for an applied electric field of 0.86 kV/cm. (b): Absorption spectrum for structure A3520 calculated at T=10 K assuming a full width half maximum of 0.8 meV for the states. The vertical dashed line indicates the energy of the photon

a 57 nm wide undoped GaAs quantum well. One of the major difficulties in rescaling this kind of design towards longer wavelengths is to avoid the reabsorption between the many states that constitute the injector miniband, whose energy dispersion becomes closer to the photon energy and where the majority of the charge resides. In Fig.6.23 the bandstructure for sample A3520 together with the calculated absorption spectrum of the active region is reported supposing a thermal distribution of the carriers at T=10 K. With respect to structure A3096 there are no major changes in the injector, some wells have been shrink in order to keep the period length (1694 Å) at about the same value as the previous structure (1701 Å) since the gain scales as L^{-1} (see Formula 2.2.9). The dipole matrix element for the $|3\rangle \longrightarrow |2\rangle$ transition is z_{32} = 112.6 Å for an oscillator strength f_{32}=23.7 Spontaneous emission spectrum from a ridge structure together with transport characteristics at B=0 field are reported in Fig.6.24. The condition of resonant magnetic confinement should induce a strong population inversion for a field value of 2.8 T. Inspection of the lasing profile of the sample in magnetic fields up to 12 T (reported in Fig.6.25 together with a Landau fan of the active region) reveals that the laser switches on at 5 T and presents a maximum at 5.6

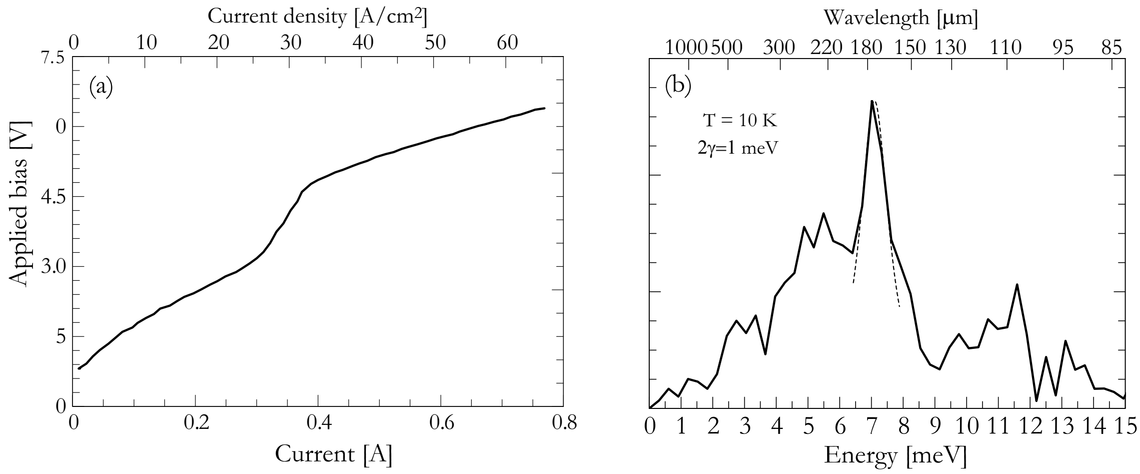

Figure 6.24: (a): I-V curve for sample A3520 at B=0. Device dimensions are 2.8 mm length and 420 μm width. (b): Electroluminescence spectrum for the same device at T=10 K for B=0 for an injected current density of 23 A/cm^2. Full width at half maximun is 2γ=1 meV.

T ($2E_{21} = 2 \cdot 4.85 = \hbar\omega_c(5.6T)$), where the resonant confinement condition is achieved by means of a 2-electron scattering process, as the second lasing maximum for sample A3096 at 6.1 T. The absence of lasing for the first resonant condition can be explained by the higher waveguide losses and the overall lower figure of merit of the second order single plasmon waveguide at 180 μm (see Section 3.3). The laser then switches off at 6.5 T and 8.24 T: those are the well known resonances on the $|3\rangle \longrightarrow |2\rangle$ transition due to single and 2-electron processes. The agreement of the first resonance at 6.5 T with the quenching of the laser emission is not as good as the one at higher field. For this sample there is no minimum of laser intensity (as in sample A3096) but a complete quenching of the laser action (several devices of different dimensions have been tested): this fact can be explained with the combination of the waveguide effects discussed above and of the increased strength of the lifetime modulation due to the closer energy spacing of the states involved. Afterwards the device enters the strong confinement regime and one more modulation of the laser emission is observed at 10.3 T. The corresponding cyclotron energy is 17.8 meV, that fits surprisingly well with the 3/2 of the overall energy spacing E_{31} = 11.9 meV. The evolution of the laser

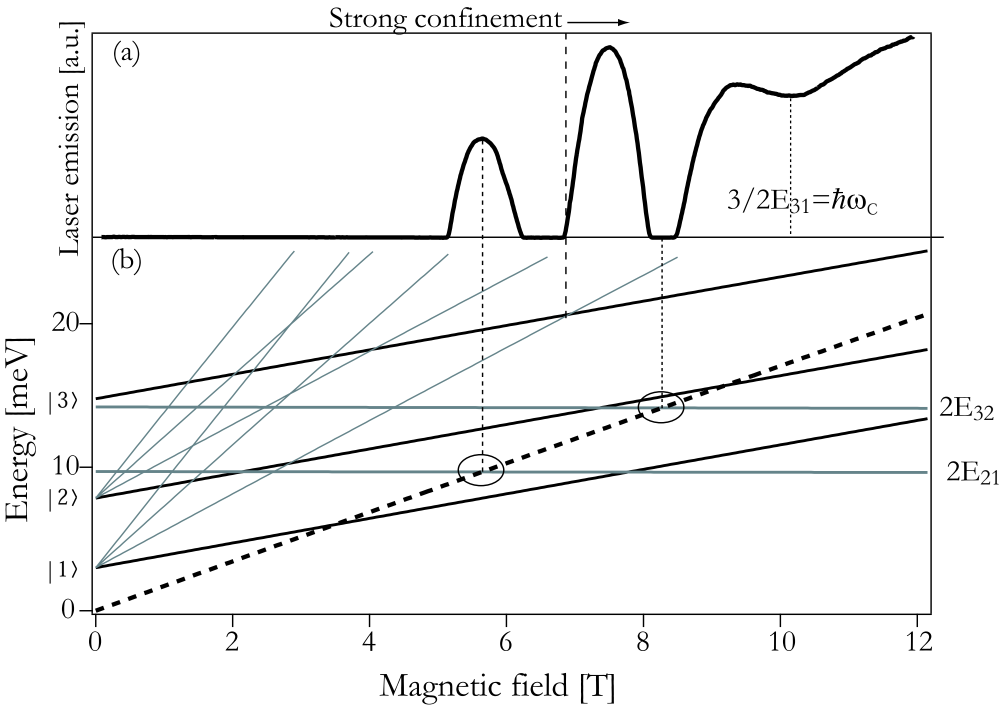

Figure 6.25: (a): L-B curve for sample A3520 at t=4.2 K for an injected current density of 16 A/cm^2. (b): Landau fan of the active region for sample A3520. Note the good agreement between the first lasing peak at 5.6 T and the 2-e scattering event involving the extraction levels $|1\rangle$ and $|2\rangle$. At 10.3 T there is a signature which energy spacing satisfy the relation $3/2\Delta E_{31} = \hbar\omega_c$.

emission in the range 6.5-28 T is shown in the color plot of Fig.6.26(a) for a 1.3 mm long, 420 μm wide laser ridge with high reflection backfacet coating (Al_2O_3/Au, 300/100 nm) in continuous wave operation. The dashed line indicates a local minimum of the light emission and a local maximum of threshold current attributed to the 2-electron resonance $|3\rangle \longrightarrow |1\rangle$ at 13.4 T. Threshold current density reaches values lower than 1 A/cm^2 at high magnetic fields.

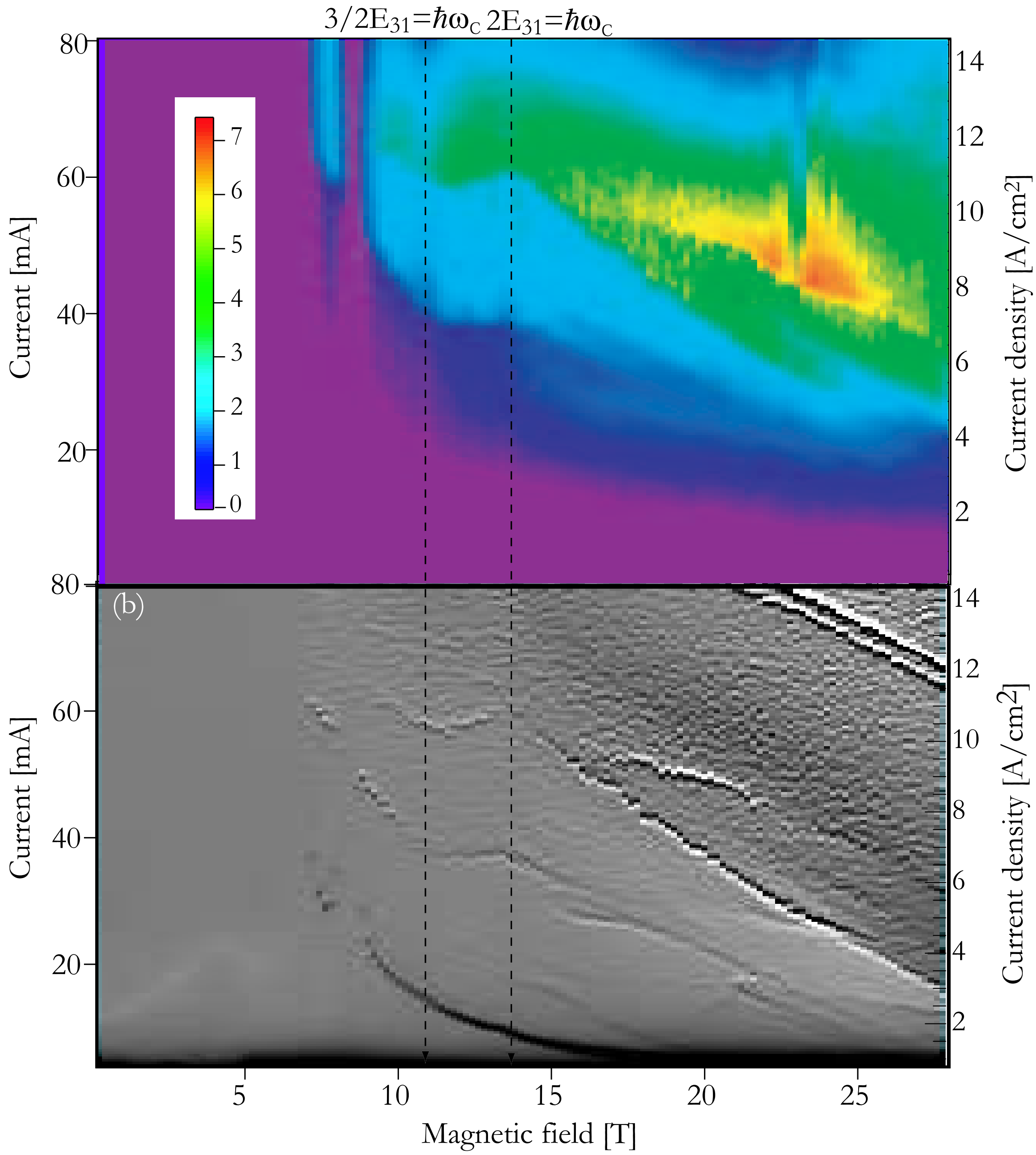

Figure 6.26: (a) Color plot of CW laser emission for sample A3520 (1.3 mm long, 420 μm wide with HR coating)in magnetic fields up to 28 T. The black arrow indicates the 2-electron resonance $|3\rangle \longrightarrow |1\rangle$ at 13.5 T. (b) Greyscale plot of $\frac{d^2V}{dI^2}$ for the same device in function of injected current and applied magnetic field. The discontinuity at threshold reveals as the deep (black) minimum and the features representing the successive couplings of the injector states are clearly evident. The 2-electron scattering event at 13.4 T is evident in all the transport features.

The dynamic range is wide but in this case the light emission presents a maximum as a function of the magnetic field, in the region around 22.5 T. The threshold current density continues to decrease even after the maximum emission value of 22.5 T. The presence of this maximum marks the condition of optimal radiative efficiency. A plot of the second derivative of the voltage in respect to the current $\frac{d^2V}{dI^2}$ in function of the magnetic field is reported in Fig. 6.26 for the same device as panel (a). The mapping of the transport features on the light emission features is striking: we can follow the evolution of the discontinuity at threshold from the first peak of CW lasing around 7.6 T up to 28 T. The size of the discontinuity increases with increasing magnetic field even after the maximum of light intensity: this demonstrates that the decrease in laser emission is not due to a degrading of the lifetime ratio. The careful inspection of the transport graphic reveals a threshold current density of 0.59 A/cm^2 for the highest field of 28 T. Signatures of successive alignement of injector states are present both in light emission and in transport: the 2-electron scattering event at 13.4 T ($2E_{31} = \hbar\omega_c$) is evident in all the transport features. A huge difference can be remarked looking at the non-lasing and lasing regions in the transport graph: the transport is strongly affected by the intense electromagnetic field present in the cavity generating strong oscillations in the I-V curves (and consequently in the second order derivative.)

6.5.3 1.39 THz big well in strong magnetic field

The lowest photon energy at which we achieved laser action is E_{32} = 5.9 meV (215 μm), obtained via a further rescaling of sample A3520 reaching a well width of 60.7 nm. From the bandstructure of sample V198 reported in Fig.6.27(a) we can see that the overall energy spacing E_{13} for this sample is reduced to 9.9 meV. The dipole matrix element for the $|3\rangle \longrightarrow |2\rangle$ transition is z_{32} = 106 Å for an oscillator strength f_{32}=21.3. The reaching of the strong confinement condition is achieved for a magnetic field of 5.7 T. The I-V curve (see Fig.6.27(b)) with no applied magnetic field still presents typical injection features, with a knee around 5 A/cm^2 and a typical NDR feature at 19 A/cm^2. Luminescence spectrum from a ridge structure is reported in Fig.6.27(c). The emission is centered around 6.2 meV, with a full-width-half-maximum linewidth of 2 meV.

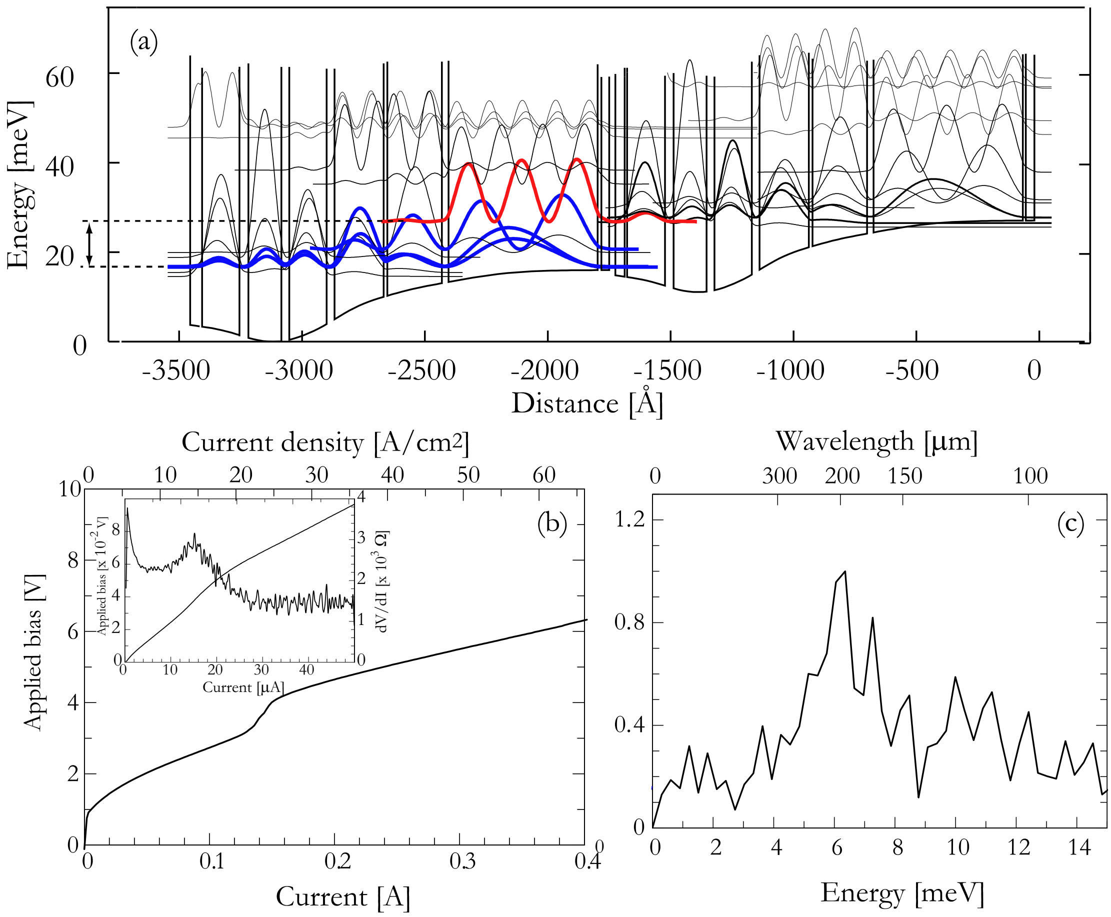

Figure 6.27: (a): Self-consistent calculation of bandstructure for sample V198 for an applied electric field of 0.72 kV/cm. Note the overall energy spacing $E_{31} < 10$ meV. (b):I-V curve for sample V198 at B=0 and T = 10K. Inset: zoom of the I-V curve in the low current region to highlight the peak in differential resistance that precedes the alignment of the injector with state $|2\rangle$. (c): Electroluminescence spectrum for a 3.8 mm long , 420 μm wide ridge at T=10 K for B=0 for an injected current density of 17 A/cm^2.

Laser emission is present for magnetic fields above 6 T, and a color plot of the emission intensity as a function of injected current and applied magnetic field on the interval 5.8-28 T is represented in Fig.6.28. Careful inspection of the figure reveals the first lasing peak around 6.4 T, when the condition of strong confinement is already reached. All the resonances occurring at lower fields are visible only in magnetotransport. Evidently, the degradation of the waveguide efficiency calls for a stronger population inversion ($\Gamma/\alpha = 0.023$ cm for this structure at this wavelength, see Sec.3.3.1) and lasing is possible only when waveguide losses are quenched by carriers localization [156]. Resonant modulation of upper state lifetime is evident in light emission and threshold current density features at 7 T (2-e on $|3\rangle \longrightarrow |2\rangle$ transition) and 11.5 T (2-e on $|3\rangle \longrightarrow |1\rangle$ transition).

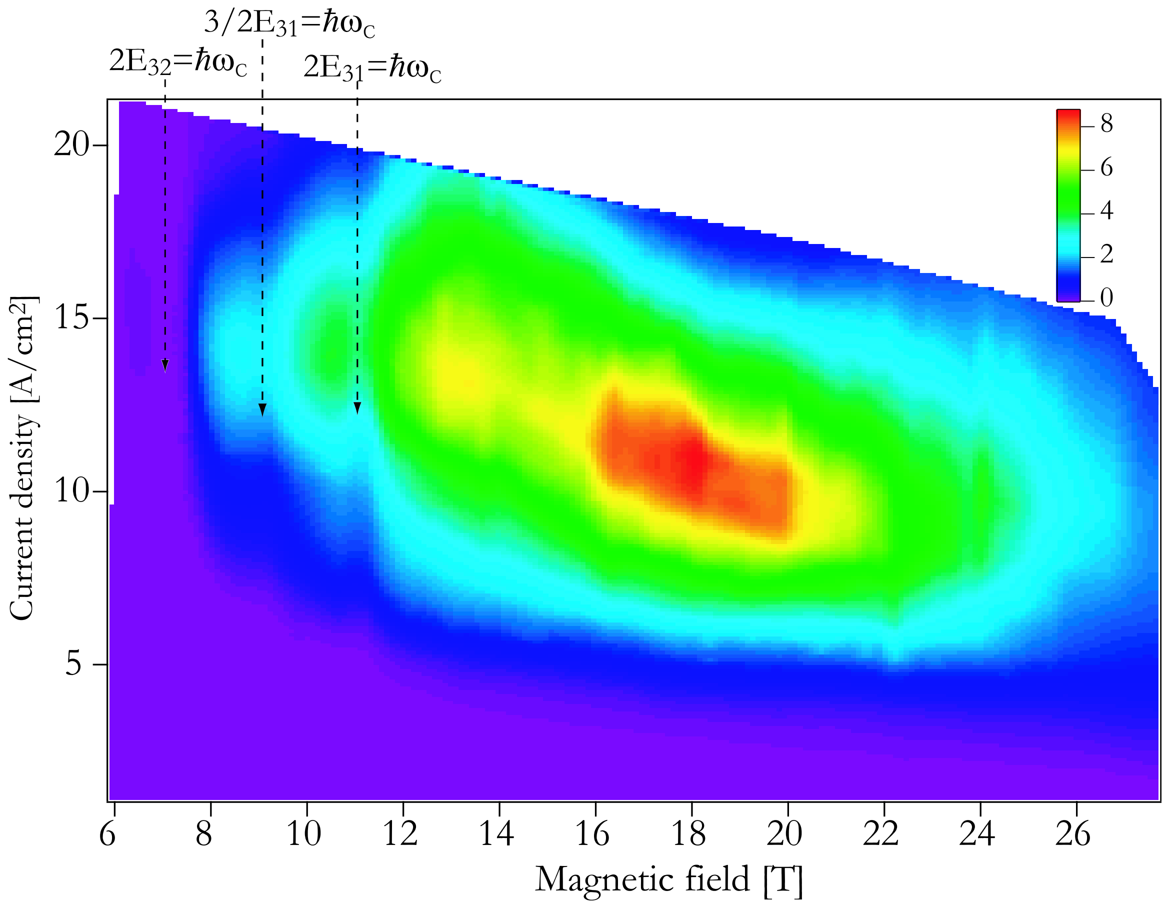

Figure 6.28: Color plot of laser emission for sample V198 (3.9 mm long, 520 μm wide with HR coating) in magnetic fields up to 28 T.

Again, as in sample A3520, we observe a quite strong feature at B= 9.12 T, where the condition $\frac{3}{2}E_{31} = \hbar\omega_c$ is satisfied. Inspection of the calculation of Kempa et al.[160] lead us to the hypothesis that this resonance is a signature for a 3-particle process, where for example two electrons gain $\hbar\omega_c/3$ and one electron loses $2/3\hbar\omega_c$. The lasing maximum as a function of the applied magnetic field covers a quite broad area of about 3.6 T width, centered around 18 T. As observed in the other samples, threshold current density continues to decrease as magnetic field is increased, reaching a value of 1.16 A/cm^2 at 28 T (see Fig.6.29). This value, in absolute very low, is nearly the double of what we found on the other devices at shorter wavelengths: the decreased overlap of the optical mode with the active region or maybe a non-optimal device can be the explanations for such a value. Spectral emission redshifts with the applied magnetic field (see Sec.6.6.2) and laser emission reaches 220 μm (1.35 THz) at B = 28 T (see inset of Fig.6.29). The maximum temperature attained for the laser emission is 40 K for an applied field of 12 T.

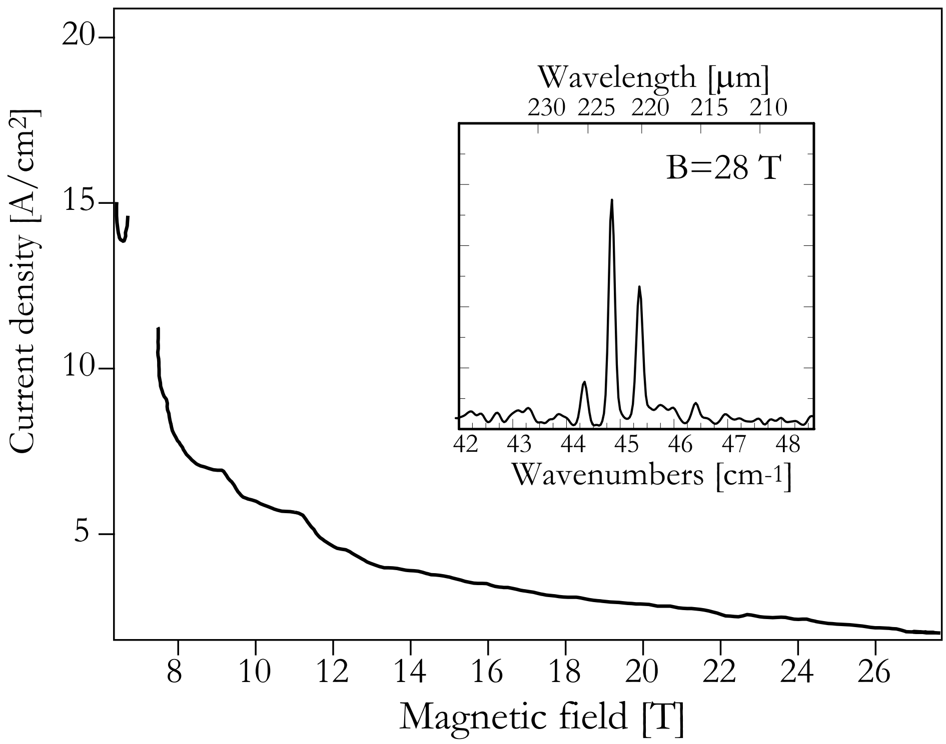

Figure 6.29: Threshold current for sample V198 as a function of the applied magnetic field in pulsed mode at T=4.2 K. Inset: spectral emission at B=28 T.

6.6 Comparative analysis

In this Section we will compare the three long wavelength structures that lase below 2 THz. The maximum emission in function of the applied magnetic field, the spectral emission and the magnetoresistance will be discussed.

6.6.1 Intensity maximum as a function of magnetic field

In the previous sections we have observed that the maximum emission for the three structures changes as a function of the applied magnetic field. For structure A3096 (λ =158 μm) the maximum intensity is above 27 T; for structure A3520 (λ =180 μm) the maximum occurs around 22 T and finally for sample V198 (λ =215 μm) we observe this feature around 18 T. From Table 6.2 we can observe that the fundamental parameters of doping and period length have been kept as close as possible throughout the three structure, in order to ease the comparison. The influence of the magnetic field is not limited to the lifetimes involved in the lasing action: also the in-plane dephasing time τ_p will increase with the applied magnetic field. This is confirmed by electroluminescence measurements in magnetic field where a narrowing of the spontaneous THz emission ($\tau_p \sim \hbar/\gamma_{32}$) was observed up to 12 T [122, 81] and attributed to a quenching of intra-subband relaxation processes.

	$E_{32}(0)$ (meV)	E^t_{32} (meV)	z_{32} (Å)	E^t_{21} (meV)	L_p (Å)	n_s (cm^{-2})	N_{avg} (cm^{-3})
A3096	7.9	7.55	119.3	5.07	1701	5.34×10^{10}	3.13×10^{15}
A3520	7.1	7.03	112.6	4.85	1694	5.23×10^{10}	3.08×10^{15}
V198	6.2	5.93	106.4	4.05	1730	5.08×10^{10}	2.94×10^{10}

Table 6.2: Relevant numbers for samples A3096, A3520 and V198. Energies E^t_{ij} are calculated and the values for the doping are the intentional ones.

If we assume that we can still employ the Kazarinov-Suris Formula 2.5.19 to describe the injection process, we know that the term that governs the injection coupling regime is $4|\Omega|^2\tau_3\tau_p$ (see Sec.2.5). When this term is much greater than unity, the injection barrier strongly couples the two states and the laser is in its optimal regime [135]. The localization induced by the magnetic field and disorder then helps the injector to couple strongly with the upper state of the lasing transition. At the same time the maximum current at resonance can be written (in the strong coupling regime) as $J_{max} = \frac{n_s\, e}{2\tau_3}$. When sweeping the magnetic field we improve the lifetime ratio for the threshold condition and also the injection coupling. If we continue to increase the magnetic field, we observe a reduction in the laser emission intensity and also in the dynamic range. The threshold current, on the contrary, still continues to decrease. Our interpretation is the following: the threshold term is governed only by the lifetimes $\tau_2(B)$, $\tau_{32}(B)$ and $\tau_3(B)$, as expressed by the Eq.2.4.18: hence it continues to improve because of the increasing of the lifetimes due to magnetic confinement. The laser efficiency, on the contrary, degrades because of carrier localization in the injector region: the transport time across the whole period will begin to greatly exceed the injection time ($\tau_{inj} \approx (2|\Omega_{i3}|^2\tau_p)^{-1}$) because of the localization of carriers. In some sense the laser will reach a roll-over induced by the localization: the carriers are very efficiently injected in the active well where they experience very long lifetimes and lase with extremely reduced threshold. At the same time the transport in the superlattice that constitutes the injector will be progressively quenched (see also the pronounced magnetoresistance, Sec.6.6.3), and the injection efficiency will decrease not for a lack of coupling but for a lack of carriers. It is important to note that the threshold still continues to decrease, supporting our hypothesis. The maximum of emission shifts towards low magnetic field values because the term that governs the injector coupling is higher in the long wavelength devices: this can be deduced from the transport characteristics of the three samples. A progressive diminution of the J_{max} (also governed by the term $4|\Omega|^2\tau_3\tau_p$) at zero magnetic field is observed: $J_{max}^{A3096} = 40$ A/cm^2, $J_{max}^{A3520} = 30$ A/cm^2 and $J_{max}^{V198} = 20$ A/cm^2.

6.6.2 Redshift of the laser emission and non parabolicity

The spectral measurements of the lasers analyzed in this Chapter and analogous measurements on superlattice structures presented in Chapter 7 show a redshift of the envelope of the modes of laser emission with increasing magnetic field of a few wavenumbers. Possible sources of shift of the intersubband transition energy are described by Helm in Ref.[27] who divides them in three categories:

1. Band structure effects, non parabolicity

2. Coulomb interaction on energy levels (Hartree self-consistent potential and exchange-correlation effects).

3. Coulomb interactions like depolarization shift and exciton shift.

We leave the non-parabolicity apart for the moment. Following Helm's analysis the most important effect for the shift of the intersubband transition among the Coulomb effects is the depolarization shift. This effect, in a system of two subbands thermally populated, blue-shifts the intersubband transition energy accordingly to the following formula (neglecting the exciton shift that in GaAs Qw is much smaller than the depolarization shift):

$$E'_{12} = E_{12}\sqrt{1+\alpha} \Longrightarrow \Delta E_{12} \approx E_{12}\frac{\alpha}{2} \qquad (6.6.3)$$

where α is defined as:

$$\alpha_{dep} = \frac{2e^2 n_s}{\epsilon\epsilon_0 E_{21}} S \qquad \text{with} \qquad S = \int_{-\infty}^{\infty} dz \left[\int_{-\infty}^{z} dz' \psi_2(z')\psi_1(z)\right]^2 \qquad (6.6.4)$$

S is called the depolarization integral and for an infinite QW of thickness a has the value S=$\frac{5}{9\pi^2}a$. The depolarization shifts the transition towards the blue and we actually observe a redshift, but our system is inverted and the sign of the depolarization shift changes (as shown in Refs.[195, 196]) giving finally a redshift of $\Delta E_{12} \approx \frac{e^2 n_s}{\epsilon\epsilon_0} S$ (note that the shift is independent from the energy). Let's evaluate the redshift giving an upper limit (we assume that the lower state is almost empty) for our structure A3096 based on an undoped 55 nm wide quantum well. The sheet carrier density of the upper state has been evaluated in Sec.6.4.1 to be $n_3 \simeq 1.05 \times 10^8$ cm^{-2} at 12 T. Calculation gives $\alpha = 0.00163$ that translates in a redshift of 0.005 meV ($\simeq 4 \times 10^{-2}$ cm^{-1}). As expected the correction is very small because the depolarization shift, being a collective effect, is proportional to the carrier density and our systems are extremely low density systems. It is true that the value of the carrier density is deduced at 12 T and higher field measurements demonstrate an improvement of the population inversion, but a change of at least two order of magnitude in the carrier density of the upper state would be necessary in order to have a sizeable redshift ($\Delta E \approx 0.5$ meV) from depolarization effects.

Let us come now to non-parabolicity: the parabolic approximation is valid only for low energies and close to the conduction band minimum (Γ point for GaAs). In Chapter 2 we treated the non-parabolicity through an energy-dependent effective mass (Eq.2.2.1). When we apply the magnetic field the energy spectrum of the electron is modified according to equation 2.6.30, that contains the effective mass in the cyclotron energy expression. In order to evaluate the effects of the non parabolicity in presence of magnetic field we have to solve the set of coupled equations 2.2.1 and 2.6.30 (neglecting the spin):

$$m^*(E) = m^*(0)\left(1 + \frac{E(B)}{E_G}\right) \tag{6.6.5}$$

$$E(B) = E_0 + \frac{\hbar e B}{m^*(E)}\left(n + \frac{1}{2}\right) \tag{6.6.6}$$

by substituting the first equation into the second one we end up with:

$$E(B) = E_0 + \left(n + \frac{1}{2}\right)\frac{\hbar e B}{m^*(0)}\frac{1}{(1 + E(B)/E_G)} \tag{6.6.7}$$

After a bit of algebra we obtain the solution for Landau levels with non-parabolicity correction:

$$E(B,n) = \frac{E_0 - E_G}{2} + \frac{1}{2}\sqrt{(E_G - E_0)^2 + 4E_G\left(E_0 + \left(n + \frac{1}{2}\right)\frac{\hbar e B}{m^*(0)}\right)} \tag{6.6.8}$$

The problem of non-parabolicity effects on the energy levels of a QW in a magnetic field has been treated also by Ekenberg [197] and his model gives very similar results for our range of energies and magnetic fields. With formula 6.6.8 we can calculate the Landau fan and the evolution of the energy difference $E_{32}(B)$ that gives us the photon emission energy up to high magnetic fields values. In order to compare the predicted shift with experimental data coming from structures that do not lase at B=0 we set our theoretical value of the laser emission in coincidence with the one measured at B=10 T, which is the starting point for our series of measurements. The center of gravity $< f >$ of the multimode spectrum of each laser has been calculate as:

$$< f >= \frac{\sum_i \prod_i f_i I_i}{\sum_i I_i} \tag{6.6.9}$$

where f_i is the frequency of the i-th mode of the spectrum and I_i its intensity. The experimental results, measured at 4.2 K, together with energy difference between the two lasing states calculated with Eq. 6.6.8 are plotted in Fig.6.30. A relevant discrepancy (about 1-1.5

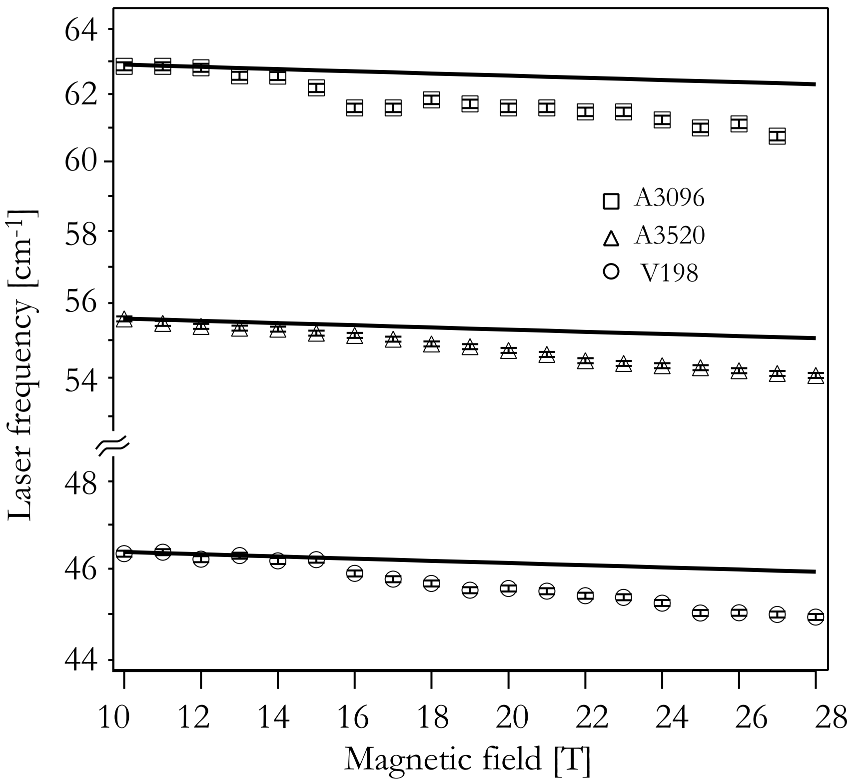

Figure 6.30: Laser frequency as a function of applied magnetic field for samples A3096 (squares), A3520 (triangles), V198 (circles) measured at T = 4.2 K together with theoretical calculation (continuous black lines).

cm^{-1} at the maximum applied magnetic field) is observed on all data between calculate value of the lasing transition and observed emission. Even when adding the many-body correction

	$\left(\frac{\Delta\nu}{\nu}\right)_{calc}$	$\left(\frac{\Delta\nu}{\nu}\right)_{exp}$
A3096	9.5×10^{-3}	3.41×10^{-2}
A3520	9.5×10^{-3}	2.73×10^{-2}
V198	9.5×10^{-3}	3.1×10^{-2}

Table 6.3: Calculated and experimental relative redshift for samples A3096, A3520 and V198

calculated before in the case of an higher inversion we could not explain the redshift: moreover in the case of samples A3520 and V198 the redshift is monotonous with the applied field even if the light intensity reaches a maximum and then decreases, as a consequences of the reduced number of carriers injected in the active well. This rules out many body contributions to the redshift. One possible explanation is the following: in the localized scenario the states lie in the tails of the Gaussian distribution (see Sec.2.6.3 and Fig.2.9) centered around the Landau levels. The optical transitions taking place between localized states will then be redshifted. An experiment aimed to test this hypothesis would be the measurement of spectral characteristics in function of the magnetic field and of the laser temperature. In Table 6.3 the experimental and calculated relative shifts for the three structures are reported

.

6.6.3 Magnetoresistance and threshold voltage oscillations

One aspect common to all the measurements in strong magnetic field is the huge magnetoresistance detected on the samples. To analyze the magnetoresistance, we propose two measurements: in the first one we fix a value for the current I_0 and then we plot the value of V/I as a function of the magnetic field, and the results are plotted in Fig.6.31 (a), normalized to the low field value. As expected, we observe the resonances due to magnetointersubband scattering already analyzed in the laser emission. Those resonances come from the transitions $|3\rangle \longrightarrow |2,1\rangle$ in the active region of the laser. We think that those resonances are superimposed on a background of magnetoresistance that comes from the quenching of the transport in the quasi-superlattice constituted by the injector. The second measurement is aimed to the smoothing of the resonance features in order to observe the general trend of the magnetoresistance. In this case the value of the resistance is measured on the part of the I-V curve after the turn on bias, at constant magnetic field. The results normalized to the zero field value are plotted for different magnetic fields in c. The resistance increases with the applied field and the three samples follow approximately the same trend. The relative increase of the resistance is very similar, reaching resistances that are around 5 times the zero field value. The problem of the longitudinal magnetoresistance and generally of current suppression in vertical transport has been treated by a number of authors in the case of regular superlattices with a magnetic field applied parallel to the growth axis and parallel to the current flow [152, 198]. We will give an interpretation to the observed behavior keeping in mind the differences between a real superlattice (Wannier-Stark basis) and our QC structure. The transport in the injector has to be assisted [152] because of the violation of Landau index conservation. In a semiclassical model [198] the miniband conduction of a superlattice is totally quenched in absence of inelastic scattering. In our case the cyclotron energy is much larger than the miniband energy width Δ which is also smaller than the LO phonon energy $\hbar\omega_{LO}$. The states are then well separated in energy and the only nonelastic

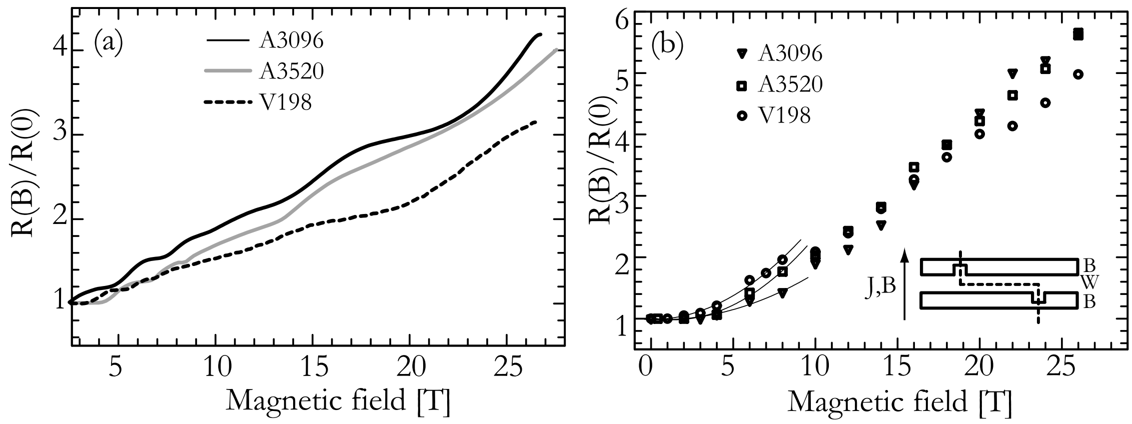

Figure 6.31: (a) Magnetoresistance for the three samples A3096, A3520 and V198 calculated at constant current. (b): averaged magnetoresistance for the three samples: note the superlinear dependence of the magnetoresistance at low fields (B< 10 T). Inset: serpentine conduction in the superlattice.

scattering source is represented by acoustic phonons, with very low probability. The increasing separation in energy induced by the magnetic field induces a suppression of the miniband current. Another effect that can play a role is the one highlighted by Lee et al.[199]. They investigate magnetotransport in superlattices with electron concentration similar to ours. They observe giant longitudinal magnetoresistance with a quadratic dependence form the magnetic field up to 9 T and a ratio of 4 between the high-field and the zero field resistance. The proposed transport mechanism is a mixture between direct vertical tunnelling and an in-plane transport due to interface fluctuations. The electrons will follow a "serpentine" pathway in order to tunnel where the interface fluctuations produce the narrowest barrier (see inset of Fig.6.31(b)). There will be then an in-plane contribution to the resistance that scales with B^2. At high values of the applied field this contribution will saturate. This behavior is shown also by our data, as visible from the second-order polynomial fits reported on the first 10 T of the measurements.

As stated before, the structure of the injector of the three samples A3096, A3520 and V198 has been kept as close as possible in order to ease the comparison of the experimental results. As already pointed out in Sec.6.4.3, in all three lasers there are three levels in the injector that can efficiently couple to the upper state of the lasing transition and give rise to marked features in light emission ("steps") as well as signatures in transport. Those features, being correlated to the injection process, reproduce the behavior of the lasing threshold and can be used to track magnetic field related phenomena. One interesting aspect that can be observed on the three laser structures is the oscillatory behavior of the threshold voltage and its related features when looking at the light emission in function of the magnetic field and of the applied voltage. In Fig.6.32 the L-V-B characteristics of the three lasers are plotted as a function of the applied magnetic field and applied voltage: the color plot helps to follow the oscillations of the threshold voltage and the steps induced by the successive alignment of the injector states. The filling factor of a 2 dimensional electron gas with the injector electron density ($\sim 5 \times 10^{10}$ cm^{-2}) is unity at B = 2 T: the observed features fall in the regime of the fractional Hall effect that is observable only at much lower temperatures. Nevertheless, this oscillatory behavior of the threshold voltage can be related to some in-plane transport phenomenon that couples the injector to the upper state of the lasing transition.

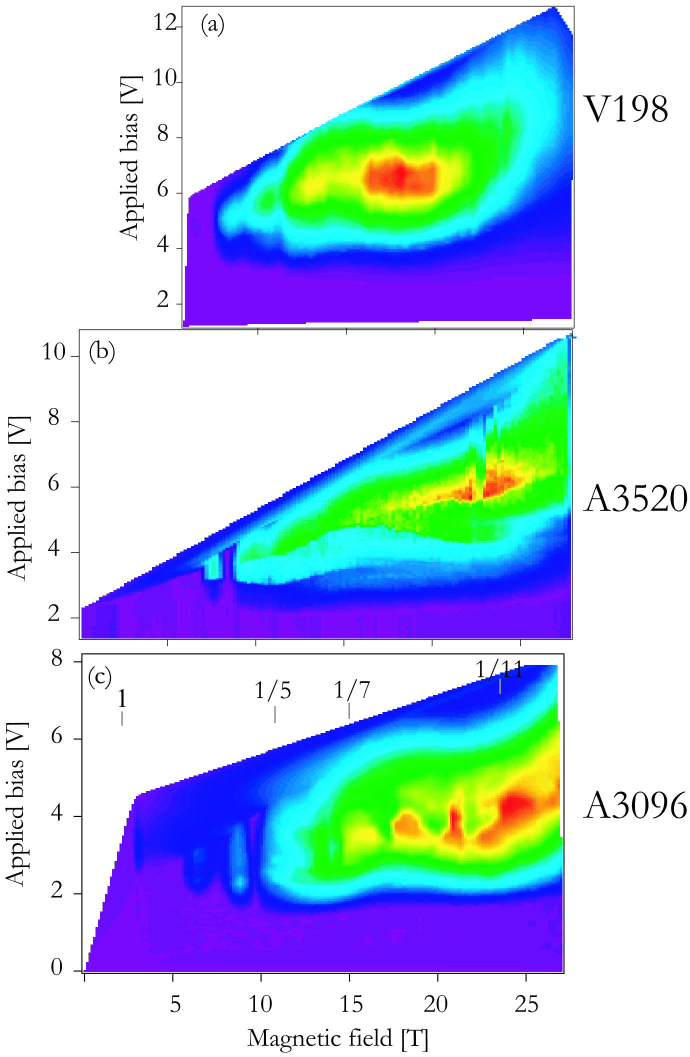

Figure 6.32: Laser emission as a function of applied bias and magnetic field for samples A3096 (160 mum), A3520 (180 mum), V198 (215 mum) together with relevant injector filling factors at different magnetic field values.

6.7 Two color laser emission in magnetic field: lasing on excited states

The energy spectrum of the single big quantum well that is used to achieve laser action at low frequencies suggests, in the localized picture in presence of a magnetic field, an atomic-like structure, with increasing dipole strength when considering photonic transitions between excited states. For example, the structure V198 emitting on the $|3\rangle \longrightarrow |2\rangle$ transition at 6 meV, presents a number of possible inter-excited state transitions with high dipole matrix elements. The idea is then to excite the photon emission also on high-order transitions, specifically injecting carriers in state number $|4\rangle$, the third excited state of the "big well". For sample V198, which lases on the $|3\rangle \longrightarrow |2\rangle$ transition at a wavelength of 215 μm, we find an energy spacing E_{43} = 8.7 meV at an electric field value where the ground state of the injector anticross with level $|4\rangle$.

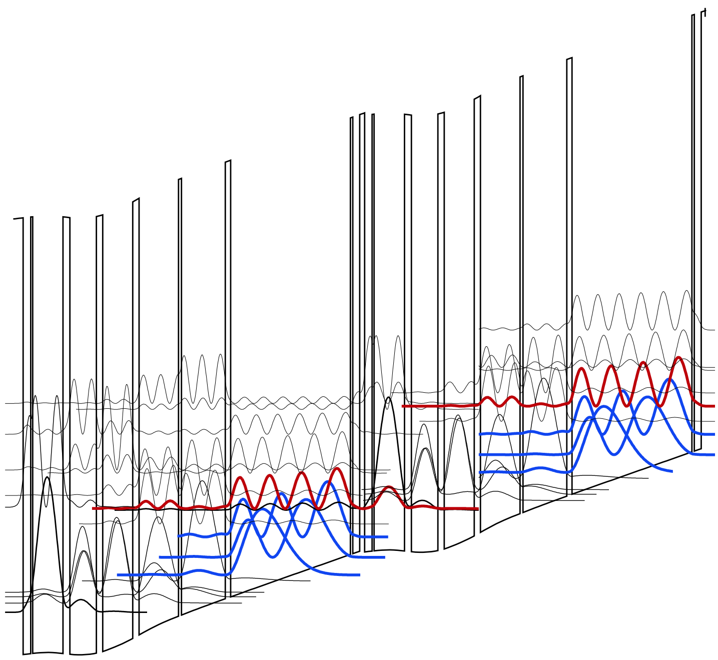

Figure 6.33: Bandstructure for sample V198 aligned on the $|4\rangle \longrightarrow |3\rangle$ transition, for an applied electric field of 1.89 kV/cm.

The coupling of those two states is even stronger than the one originally calculated for the

$|3\rangle \longrightarrow |2\rangle$ transition because as the states grow high in energy in the well the penetration in the barrier grows and consequently the overlap and the splitting $2\hbar\Omega_{4i}$ that now reads $2\hbar\Omega_{4i} = 0.37$ meV. In this case the dipole matrix element for the $|4\rangle \longrightarrow |3\rangle$ transition is $z_{43} = 112$ Å for an oscillator strength f_{43}=29. A plot of the light emission as a function of the applied magnetic field for sample V198 on a wide bias range is reported in Fig.6.34. Two distinct regions are evident: at high injection current densities ($J > 25$ A/cm^2) and starting from an applied magnetic field value of 3 T a strong laser emission is detected, which indeed corresponds to the $|4\rangle \longrightarrow |3\rangle$ transition. At higher magnetic fields (B > 7 T) and low injection currents, as already illustrated in Sec.6.5.3, we can observe the laser emission relative to the $|3\rangle \longrightarrow |2\rangle$ transition.

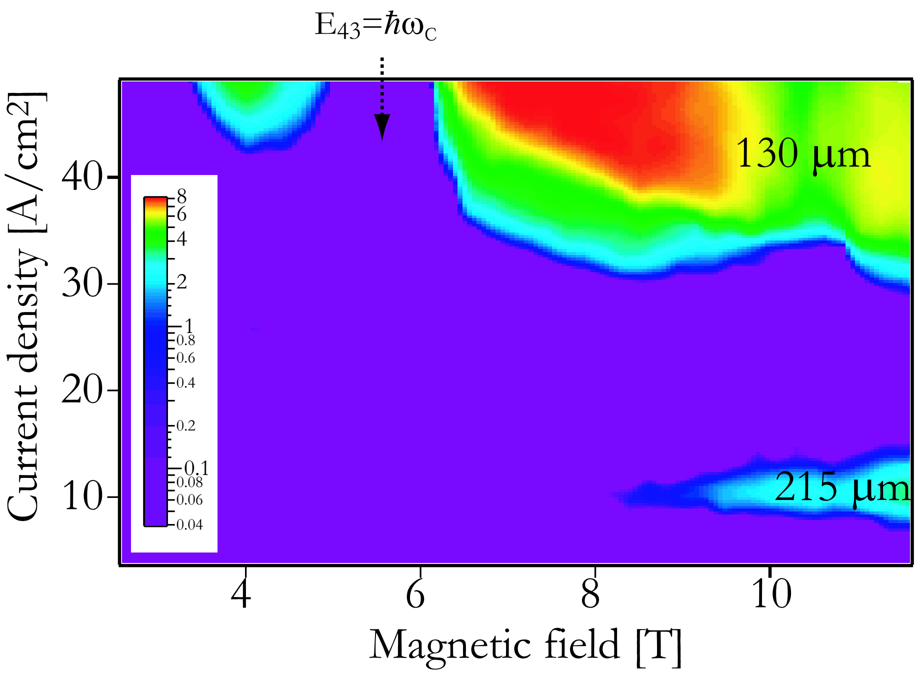

Figure 6.34: Color plot of the logarithm of laser emission as a function of injected current and magnetic field for sample V198: in the region with $J > 25$ A/cm^2 the sample is lasing on the $|4\rangle \longrightarrow |3\rangle$ transition (130 μm). Starting from 8 T and with $J < 25$ A/cm^2 laser emission is on the $|3\rangle \longrightarrow |2\rangle$ (220 μm). The quenching of laser emission for the shortest wavelength around 5 T is due to the resonance $\hbar\omega_c = E_{43}$.

The light emission has been represented in logarithmic scale in order to account for the huge intensity variations between the two regions. The laser emission relative to the second excited transition is more than 5 times stronger than the one of the $|3\rangle \longrightarrow |2\rangle$ transition (the detector is partially saturated in the region 6-9 T $J > 40$ A/cm^2). Spectral measurement yield an emission energy of 9.4-9.6 meV ($\lambda \simeq 130$ μm) depending on the applied magnetic field, in reasonable agreement with the calculated value of 8.7 meV. We can obviously observe lifetime modulation also on this "new" big well structure with 4 levels: the quenching of laser emission for the shortest wavelength around 5 T is due to the resonance $\hbar\omega_c = E_{43}$.

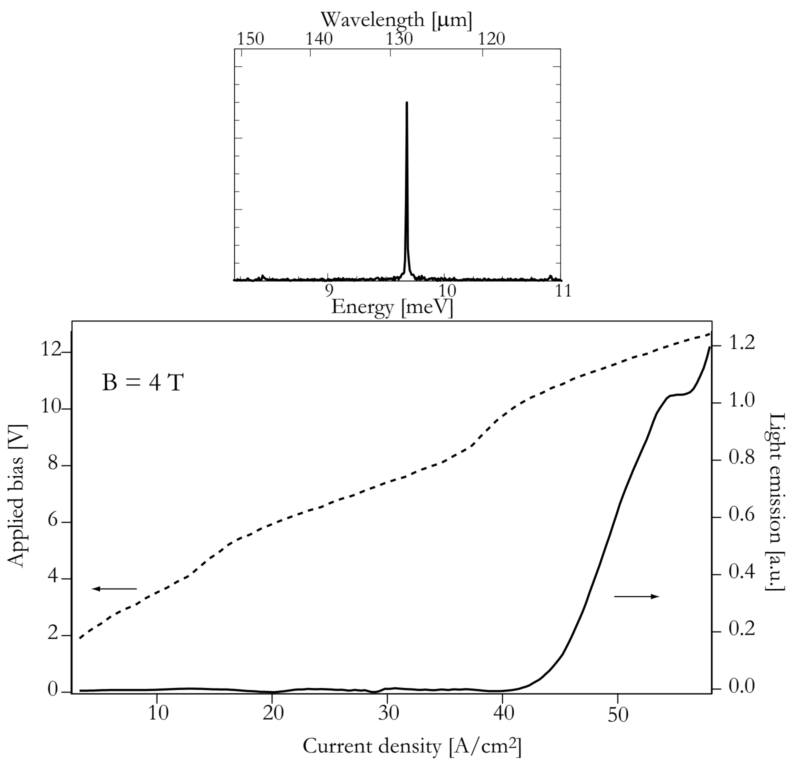

Figure 6.35: L-I-V curves and spectral emission for sample V198 at 4 T: note the two signatures of band alignment in the I-V curve.

It is instructive to plot L-I-V curves at constant values of magnetic field for two values of the applied field: one where only the 130 μm laser is operating (4 T, Figure 6.35) and the other where both transitions lase successively with increasing bias (11.5 T, Figure 6.36). The transport measurement at 4 T reveals clearly the presence of two point of band misalignment. The NDR feature at about 16 A/cm^2 is the injector that loses its anticrossing with state $|3\rangle$

of the big well.

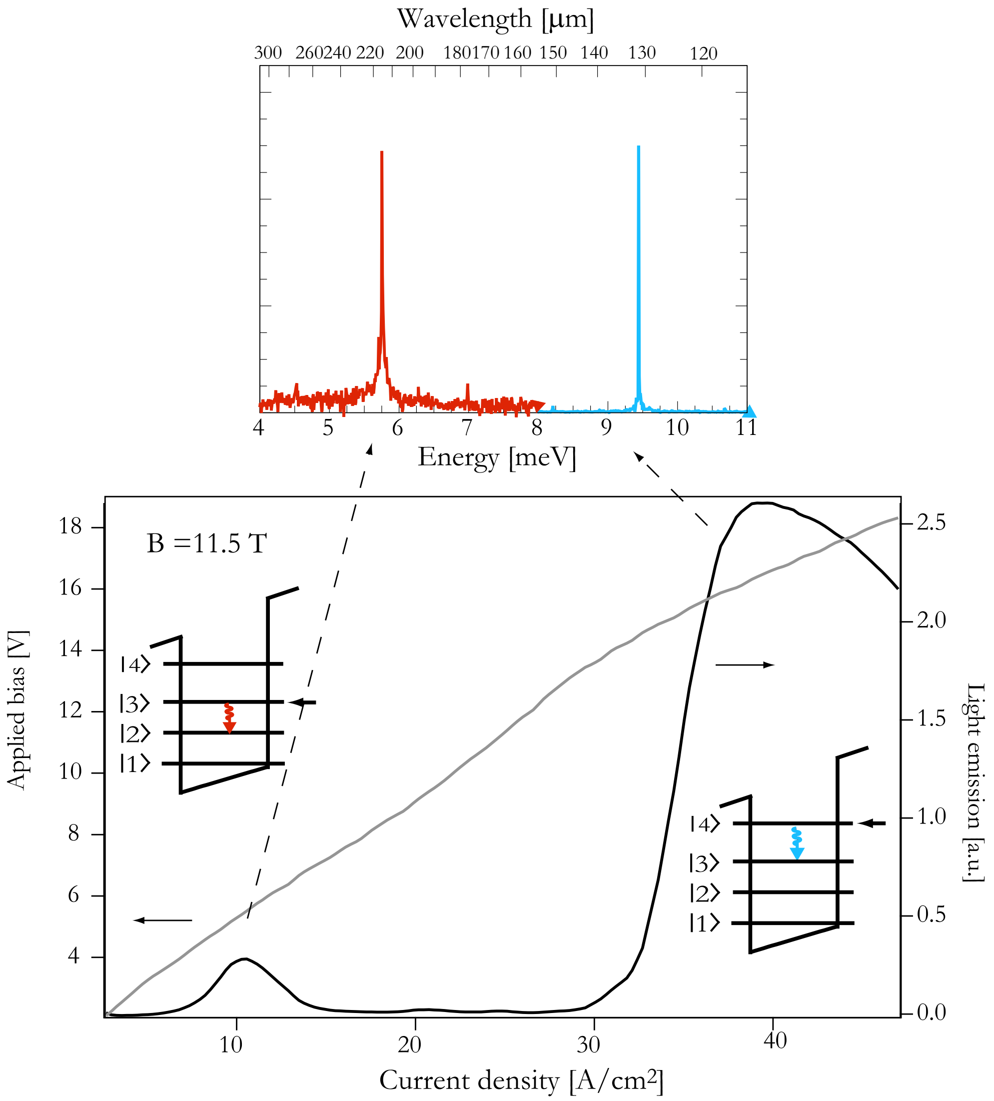

Figure 6.36: L-I-V curves and spectral emission for sample V198 at 11.5 T. Laser action takes place a first time starting from 5 A/cm^2 with the emission centered around 217 μm. Then, after rollover carriers are injected in state $|4\rangle$ and the new emission wavelength is centered around 130 μm.

The second NDR at about 40 A/cm^2 anticipate the strong coupling of the injector with the state $|4\rangle$ of the big well. Lasing threshold for the 130 μm transition is at 48 A/cm^2 at 3.4 T and reaches its minimum of 29 A/cm^2 at 12 T. If we look at the transport we can see that the "real threshold" for the $|4\rangle \longrightarrow |3\rangle$ transition is much lower if measured from the beginning of the I-V curve relative to the injection on state $|4\rangle$. Most of the injected current is necessary to achieve proper band alignement.

6.8 Conclusions

The study of vertical structures in strong magnetic field allowed the realization of low frequency THz lasers with very low threshold current densities. The problem of selective injection in closely spaced energy levels has been circumvented by employing a further confinement provided by the magnetic field. Our data show that extremely long intersubband lifetimes may be observed when well-separated Landau levels are localized by a disorder potential - typical conditions for the quantum Hall effect. As the devices are very large compared to the wavelength, the very low threshold current densities would lead to a "thresholdless" [200] device if structures could be fabricated in a microcavity configuration with a very high quality factor Q. Our data also open up the very interesting possibility of observing effects such as Coulomb charging relating to the discreteness of the charge residing in localized islands. This phenomenon could be observed reducing the temperature of the samples down to some hundreds of mK.

A number of interesting effects have been observed in the regime of low photon energy and high magnetic fields. The critical role of the transport is highlighted, and still a lot of work is needed to clearly interpret the data. From the point of view of electron lifetimes at low energy subband spacing, some remarks can be made. We have analyzed a series of quantum wells of increasing width (55, 57, 60.7 nm) all with very similar doping densities. If we estimate the lifetimes from the transport with the Kazarinov and Suris formula that accounts for the injector coupling (Formula 2.5.24) we obtain an increasing transport lifetime with increasing well width, respectively $\tau_3 \cong 95$ ps for sample A3096 (7.9 meV energy spacing), $\tau_3 \cong 120$ ps for sample A3520 (7 meV energy spacing) and $\tau_3 \cong 190$ ps for sample V198 (6 meV energy spacing). Besides the fact that those lifetimes are overestimated because we neglect the population of the lower state and of the injector, there is a clear trend of lifetime increase with the well width. Moreover, we find in literature lifetimes of the order of 1 ns measured by photovoltage and absorption [201]. From previous research we expected a lifetime that would have decreased with the energy spacing within the two states $|3\rangle$ and $|2\rangle$ because, keeping the electron density constant, the carrier-carrier scattering is more and more effective as the subband energy separation decreases. This results leads to the conclusion that interface roughness is actually an efficient scattering mechanism and, for these electron densities ($5\ 10^{10}\ \mathrm{cm}^{-2}$), is as efficient than electron-electron scattering. As we increase the well width and lower the energy states, the penetration of the wavefunction in the barrier diminishes and the electronic state is less and less sensitive to the interface roughness.

The achievement of well separated, multi-wavelength operation with clean electrical switching really demonstrates the flexibility of the QC concept. This kind of devices can in principle be operated without magnetic field and offer an interesting possibility to circumvent the problem of the tunability.

Chapter 7

Magnetic confinement on superlattice structures

In this Chapter we will present and analyze the results obtained measuring in strong magnetic field THz QC lasers not specifically designed for the magnetic confinement. Those designs are essentially superlattice-based lasers at different wavelengths (64, 82, 87 and 130 μm): the common aspect to all the devices and the main difference with respect to the design presented in Chapter 6 is the nature of the optical transition that is delocalized instead of intra-well. The Chapter is organized as follows: we will first present the results in magnetic fields up to 12 T on all the structures, then we will focus on two of them (bound-to-continuum with optical phonon extraction and long wavelength bound-to-continuum, see Chapter 5) presenting some results in high magnetic fields up to 28 T.

7.1 Chirped superlattice at 64 μm

The design studied is this section is the chirped-superlattice active region of Ref. [88, 178] (sample A2672). The computed band diagram and squared wavefunctions for this sample are displayed in Fig.7.1 together with L-I-V curves in pulsed mode. The device (2.7 mm-long, 200 μm-wide with HR backfacet coating) lased up to 60 K with a threshold current density of 140 A/cm^2 at T=10 K. This structure is very similar, but not identical, to the one of

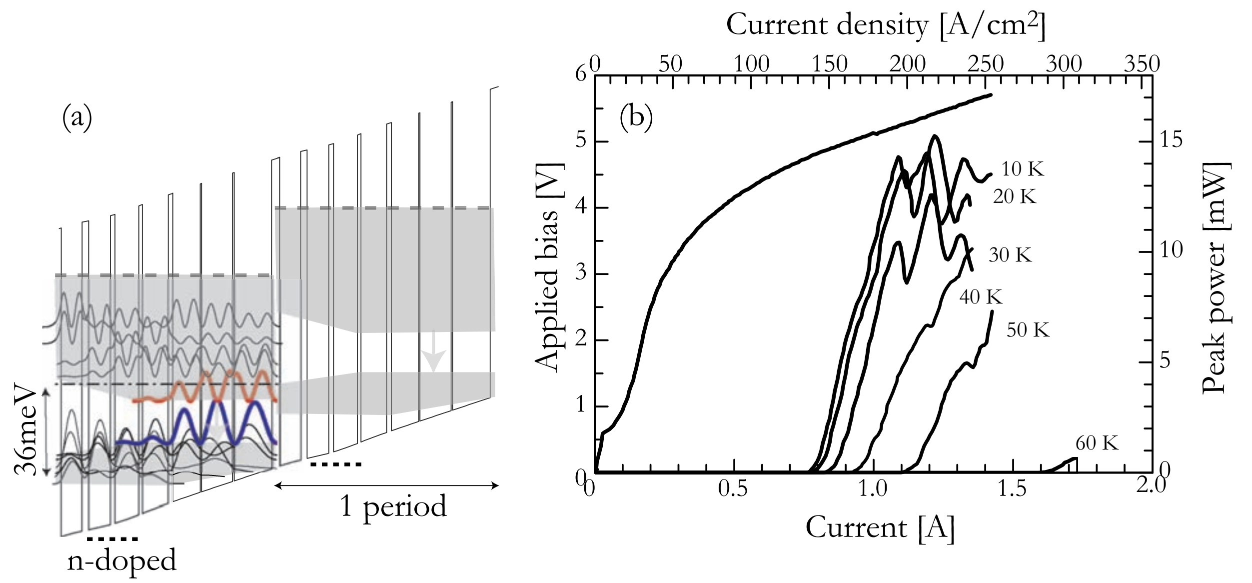

Figure 7.1: (a): Computed conduction band profile of one stage of the structure A2672 under an average applied electric field of 3.3 kV/cm. (b) L-I-V curves for sample A2672 (2.8 mm-long, 200 μm-wide with HR backfacet coating).

ref.[85] that has been investigated in magnetic field in its original version by Alton et al.[158] and in a re-grown version by Tamosiunas et al. [191]. We find slightly different results from the two cited references in the behavior of the laser emission as a function of the applied magnetic field. Those differences are mainly due to the structure of the lower miniband of our design, that is more a three-quantum well plus injector design than a real chirped superlattice. Magnetotransport measurements on a small mesa together with laser spectral emission enabled us to identify three states almost equally spaced in the lower miniband of the structure just computing the transition energy from field values at current peaks (where the resonance condition expressed by Eq.2.8.36 is satisfied) and then comparing it with the calculated energies of electronic states. The measured energy spacings are E_{43}=19.2 meV, E_{32}=6.3 meV, E_{21}=6.2 meV. The magnetotransport results are shown in Fig.7.2(a).

A Landau fan originating from the electronic states of the structure determined by magnetotransport measurements is shown in Fig. 7.2(b) together with laser emission as a function of the magnetic field. The magnetic field has a strong influence on the laser performance as

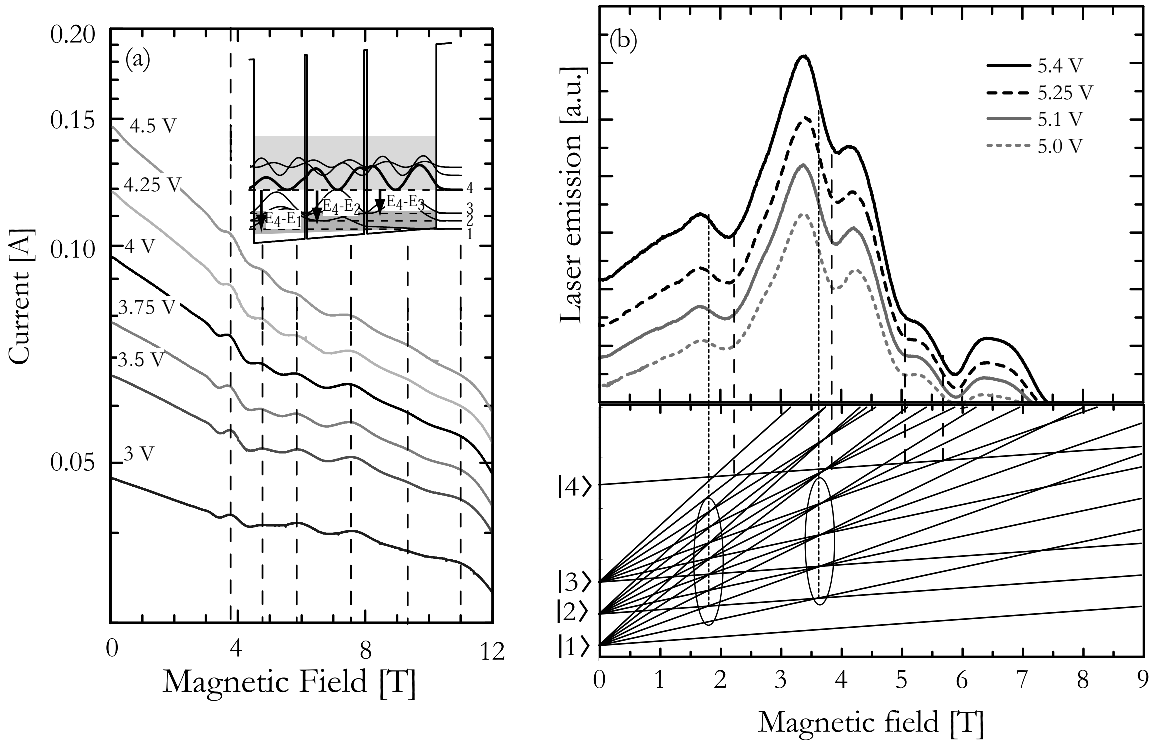

Figure 7.2: (a): Magnetotransport measurements on sample A2672 at different biases: dotted lines indicate current maxima corresponding to ISLR. Inset: calculated bandstructure of the active region of sample A2672. Relevant states deduced from magnetotransport are numbered starting from the bottom of the well. (b) Laser emission intensity of sample A2672 vs magnetic field for various applied biases measured at T = 4.2 K with InSb detector. Close-dotted lines and ellipses highlight resonance condition among extraction miniband states, while wide dotted lines correspond to resonances between states $|4,0\rangle \rightarrow |j,m\rangle$ where j= 1, 2, 3 and m = 1, 2,...

the signal undergoes several oscillations and the emission is enhanced also at low fields, with a maximum at 3.4 T. An increasing of light intensity is visible in proximity of resonances between the three levels of the lower miniband, as expected after the results illustrated in Chapter 6. The population inversion is enhanced by the matching of the miniband energy spacing with the cyclotron energy. On the contrary, when intersubband Landau scattering occurs between the levels attached to upper miniband edge and lower miniband Landau states ($|4,0\rangle \rightarrow |j,m\rangle$) a decrease in light intensity is observed [158, 191]. The observed resonances in light emission for this structure do not fall exactly on the corresponding Landau fan crossings: this is most probably due to the complex structure of the extraction miniband (three states) that generates many Landau levels closely spaced in energy. Moreover, resonance condition for the extraction miniband happen almost at the same field values as the resonances with the upper state of the lasing transition. The experimental data are then the result of two competing processes that shift the resonances due to their close spacing. Modulation of intersubband lifetimes is observed also for levels with high Landau index: the minimum in light emission at 2.1 T corresponds to a resonance with a Landau state n=5 ($|4,0\rangle \longrightarrow |3,5\rangle$). The quenching of laser action for fields higher than 7.5 T is due to a combination of effects: the reduction of the upper state lifetime with resonances with the Landau states of the injector and the magnetoresistance (see Fig.7.2(a)) that limits the number of carriers injected in the upper state preventing to reach threshold.

Together with increased emission there is a drastic reduction in threshold current. A plot of threshold currents measured at relevant magnetic field values is shown in Fig. 7.3 (a). Threshold current density oscillates with opposite phase with respect to light intensity and its value is always below the value at zero field ($J_{thB=0}$), except in the region around 6 T, where many resonances of the kind $|4,0\rangle \longrightarrow |(1,2,3),n\rangle$ occur. In detail, $J_{th}(B=1)$=0.75 $J_{th}(B=0)$ and for B = 4.1 T it reaches its minimum value, nearly 40% of $J_{thB=0}$ [1]. Minimum threshold current density for this device is 90 A/cm^2.

An analysis of slope efficiency dP/dI has also been carried out and is plotted in Fig.7.3(b). The value of the slope efficiency has been normalized to the values with no applied magnetic field. Slope efficiency is directly related to population inversion in the laser structure $dP/dI \propto \left(1 - \frac{\tau_3}{\tau_{43}}\right)$, and the measured value at zero magnetic field is 13 mW/A, much lower than the value (1W/A) extrapolated from an expression in which lower state population is neglected. This suggests that the laser action relies on a marginal population inversion probably limited by population of the lower state due to poor extraction. The observed increasing of the slope efficiency measured as a function of applied magnetic field (Fig. 7.3), with two local maxima at 2 T and 3.4 T, with a maximum increment of 2.7 times the zero field value, is consistent with an improved ratio of lifetimes $\frac{\tau_3}{\tau_{43}}$ coming both from an increasing of the

[1]Measurements on other laser ridges showed threshold reduction down to 50 % of the zero field value

upper state lifetime τ_{43} and a reduction of lower state lifetime τ_3 due to resonant magnetic confinement.

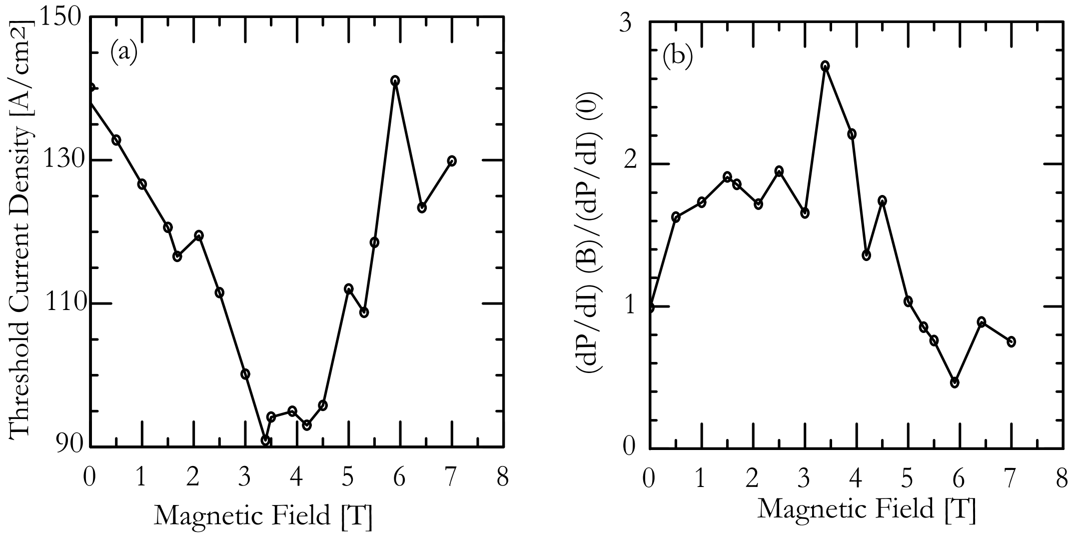

Figure 7.3: (a): Threshold current density as a function of the applied magnetic field for sample A2672. (b): slope efficiency normalized to zero field value as a function of the applied magnetic field for sample A2672.

7.2 Bound-to-continuum design in magnetic field

7.2.1 Bound-to-continuum at 87 μm

The next superlattice-based structure examined in magnetic field is sample A2771 , the bound-to-continuum design emitting at 87 μm extensively described in Section 5.1. In such an active region, the radiative transition takes place between a bound state and a miniband. This configuration of states enables a better population inversion in respect to the chirped superlattice and indeed the laser operated in pulsed mode up to T = 100 K [173]. The application of a magnetic field should not improve the performances in this structure since the lower laser level exhibits a quasi-continuum of states (7 states separated by an average of 1.3 meV). The closest spacing of the states of the injector gives rise to a magnetotransport spectrum with less pronounced features: in Fig.7.4(a) the current as a function of the magnetic field for two values of the applied bias is reported together with its second derivative with respect to the magnetic field $\frac{d^2I}{dB^2}$. The second derivative analysis is useful to evidence hidden features. The intersubband Landau resonance with index n=2 is clearly visible at 4.1 T ($\hbar\omega_c = 7.2meV = h\nu/2 = E_{87}/2$) and also the n=1 resonance is present at 8.2 T. The weak resonances at lower fields are attributed to n=3 ($h\nu/3 = 4.8 = \hbar\omega_c(2.7)$) and n=7 ($h\nu/7 = 2 = \hbar\omega_c(1.17)$). The weak resonance at 1.8 T is attributable to the index n=5. The

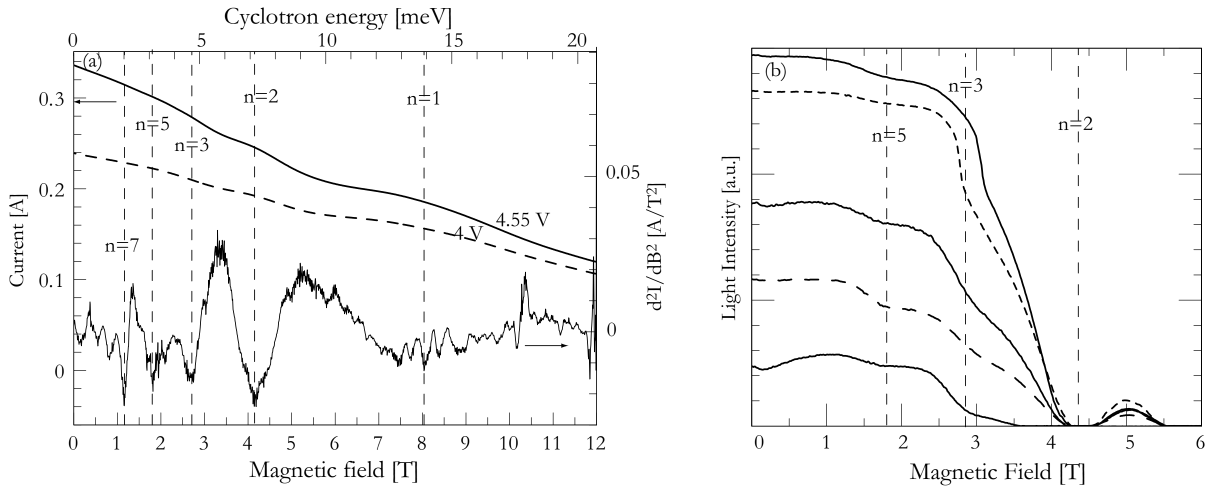

Figure 7.4: (a): Current as a function of the magnetic field for an applied bias of 4 V (dashed line) and 4.55 V (continuous line) for sample A2771. (b): Light emission as a function of the magnetic field for different applied biases for sample A2771.

same weak resonances can be observed also in laser emission in function of the magnetic field reported in Fig.7.4(b). The only strong feature is the quenching of the laser emission for n=2 resonance. No laser action is observed above 6 T, most probably due to the strength of the resonance n=1 (8 T) that efficiently depopulates the upper state of the lasing transition. Measurements on this device showed neither a significative reduction of the threshold current nor an increase of the slope efficiency in a magnetic field, as visible from Fig.7.5(a). An interesting comparison comes from the measurement in magnetic field of the same structure with the thickened injection barrier and the augmented doping (sample A2986, already discussed in Section 5.1.4). L-B curves for sample A2986 are reported in Fig.7.5(b) in function of the temperature: general behavior is the same as sample A2771, but the strong resonance at 4.1 T (n=2) is not quenching laser action anymore. This is a direct proof of an improved ratio of lifetimes for this structure with respect to sample A2771. The device also stops lasing at 7 T instead of 6 T. The persistence of the resonances up to high temperatures (86

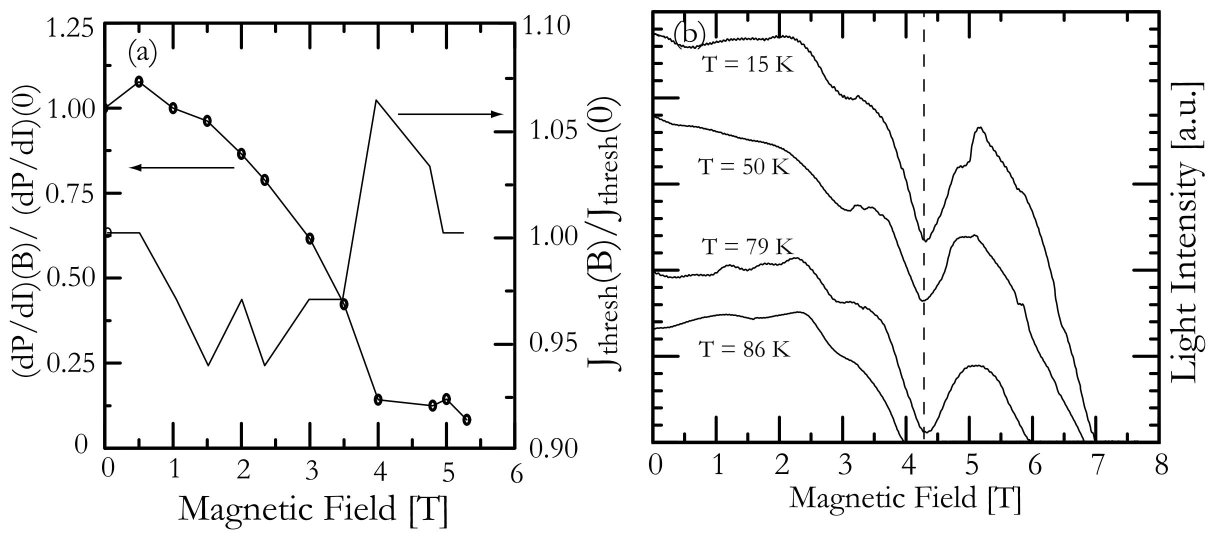

Figure 7.5: (a): threshold current density and slope efficiency normalized to the zero field value as a function of the applied magnetic field (b): light emission as a function of the magnetic field for different temperatures for sample A2771.

K) confirms the Fermi-level independence of the magnetointersubband scattering [155].

7.2.2 Bound-to-continuum with LO phonon at 82 μm

The evolution of the bound-to-continuum design is structure N314 , object of Sec.5.2, which relies on an improved injection-relaxation region that allows a phonon scattering of the carriers. The investigation of such a structure in magnetic field is of relevant interest because the active region where the optical transition occurs is almost identical to the bound-to-continuum analyzed in the previous section, which did not show any improvement with the application of magnetic field. A plot with the light emission and threshold current density for sample N314 as a function of the magnetic field up to 12 T is shown in Fig.7.6. A 2.66 mm-long, 110 μm ridge in a double metal waveguide had been used in order to investigate also possible maximum temperature increase.

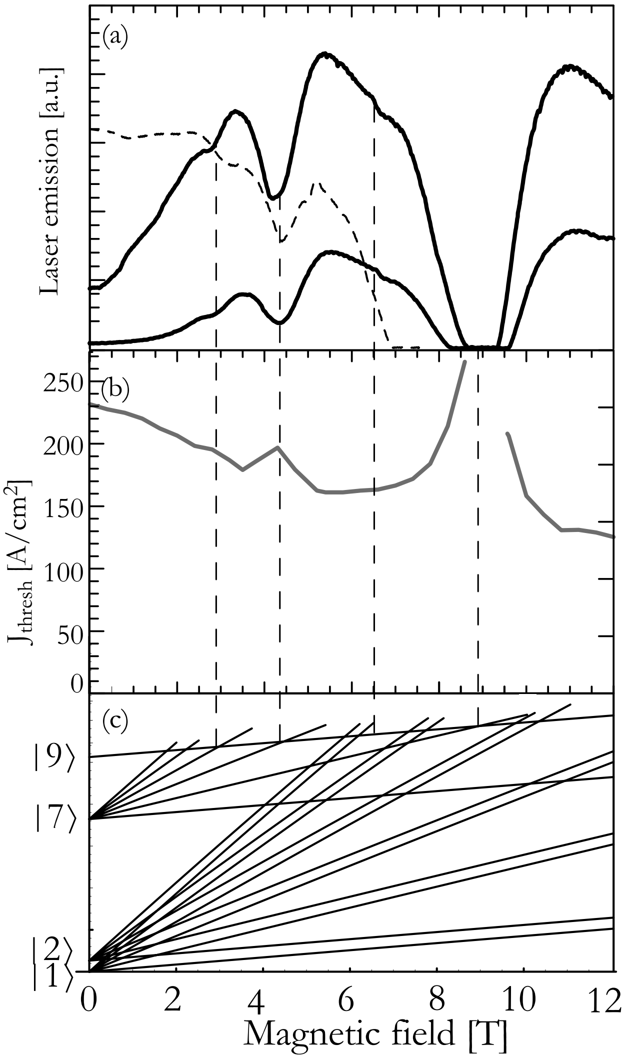

Figure 7.6: (a): Light emission as a function of the magnetic field for sample N314 (full line, 2 different applied biases) and for sample A2986 (dashed line). (b): threshold current density. (c): reduced Landau fan of the active region (states $|7\rangle$ and $|9\rangle$) plus injector (states $|1\rangle$ and $|2\rangle$) for sample N314. Resonance conditions which enhance electron extraction from state $|7\rangle$ are highlighted with grey rectangles.

The Landau fan employed to understand the lifetime modulation is a reduced version: the complete one includes to many states and would result in a loss of clarity. We employed the two bottom levels of the system of coupled wells that opens the phononic gap in the extraction miniband (levels $|1\rangle$ and $|2\rangle$). Then we reported the lower ($|7\rangle$) and upper state ($|9\rangle$) of the lasing transition. In order to compare the effect the field on both structures an L-B curve for sample A2986 (bound-to-continuum design) hase been reported (dashed line)[2]. Structure N314 shows great improvement when the magnetic field is increased: the resonance at the photon energy at 4.2 T is the same as sample A2986 but after this point, instead of observing a quenching of laser action we observe an increase of lasing efficiency together with a diminution of threshold current density. This demonstrates the efficiency of the phonon-assisted depletion of the lower miniband for design N314 with respect to the bound to continuum where the miniband dispersion is $\sim$ 13 meV. The LO phonon emission reduces the lower state lifetime and is effective also at low temperatures, as demonstrated by the measurements of Smirnov et al. [149]. The complete quenching of laser action

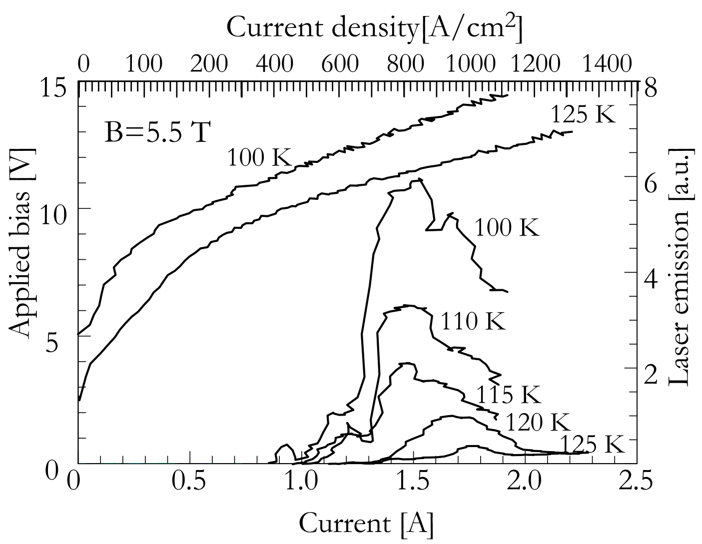

Figure 7.7: L-I-V curves as a function of temperature at 5.5 T for sample N314, 2.66 mm-long, 110 μm wide laser ridge in a double metal waveguide.

happens in a region centered around 8.9 T, where the cyclotron energy matches the photon

[2]The photon energy for these two structures is a bit different, hν_{A2986} =14.4 meV and hν_{N314} =14.9 meV but they display a minimum attributable to the condition $h\nu/2 = \hbar\omega_c$ at the same magnetic field value.

energy ($\hbar\omega_c(8.9T) = 15.3meV = h\nu$, we recall that the optical transition is partly diagonal and the Stark shift reflects in the width of the region where magnetic field suppress laser action). After this point the laser switches on again and the threshold current density reaches its lowest value of 119 A/cm^2 at 12 T, which is almost half of the value with no applied magnetic field (220 A/cm^2). A series of measurements in function of temperature have been performed: the best results where obtained for an applied magnetic field of 5.5 T and are visible in Fig.7.7. The maximum operating temperature for that particular device without applied magnetic field results of 113 K: at 5.5 T the lasing was observed up to 125 K. The 10 % improvement in T$_{max}$ is due to the reduced threshold. Temperature measurements have been performed also at 12 T, in correspondence of the minimum value of threshold current, but no temperature improvement was observed. The dynamic range also decreases with magnetic field, due to carrier localization, and at 12 T this effect prevents the observation of an increased temperature operating range.

7.3 High magnetic field measurements

The results obtained on sample N314 up to 12 T and the effects observed in Chapter 6 on low-energy THz Qc lasers motivated us to investigate sample N314 and sample A2985 (130 μm bound-to-continuum [173]) in high magnetic field in order to reach the strong confinement limit also on superlattice structures.

7.3.1 Bound-to-continuum with LO phonon at 82 μm

A color plot of the laser emission for sample N314 as a function of the applied magnetic field up to 27 T is presented in Fig.7.8. The low field part ($B < 12$ T) has already been analyzed: starting from a field value of 9.3 T the system enters the strong confinement region, in the sense that the cyclotron energy exceeds the photon energy. In this case the condition is less stringent than in the case of the big well system: the energy dispersion of the whole period (active region plus injector)is still larger than the cyclotron energy. Moreover, the active region is delocalized over several wells (at least three) and it is not so clear which of the state of the injector has to be taken into account. Another complete quench of lasing action is present for a field value of 13 T, that again matches surprisingly well with the relation $3/2E_{97} = 3/2h\nu = \hbar\omega_c(13T)$. A feature is also present in the transport characteristics in this region of applied magnetic fields (see Fig.7.9(a)). After this point another oscillation of laser emission is present, with a local maximum for B= 16.3 T and a local minimum for B=19.4 T. The maximum at 16.3 T is really surprising because we would have expected a minimum at 17.3 T, due to the resonance condition $2h\nu = 30meV = \hbar\omega_c(17.3)$. In fact this value lies approximately in the middle between the maximum at 16.3 T and the minimum at 19.4 T. Spectral measurement in that region do not show particular changes of the emission

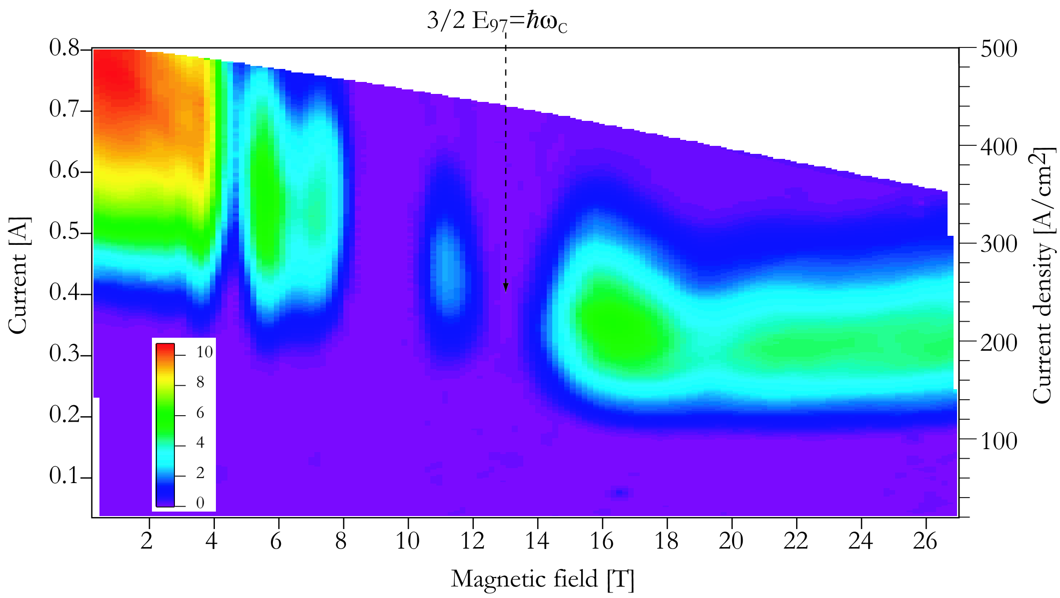

Figure 7.8: Light emission in function of the applied magnetic field from 0-28 T for sample N314, 1 mm long, 160 μm wide laser ridge.

wavelength that is centered on 14.7 meV. This behavior is still unexplained and marks one significant difference with what was observed on the vertical structures analyzed in Chapter 6. The threshold current reaches its minimum value of 100 A/cm^2 for an applied magnetic field of 17.6 T and not in correspondence of the maximum of light emission at 16.3 T. Threshold current then begins to rise again very slowly in function of the magnetic field: the measured threshold at 27 T is 104 A/cm^2. Laser action is present, with modulations, over the whole magnetic field sweep 0-28 T: this is a remarkable fact that marks a fundamental difference with respect the bound-to-continuum design object of Sec. 7.2.1. A representation of one section at constant injection current together with the reduced Landau fan is presented in Fig.7.9(b),(c).

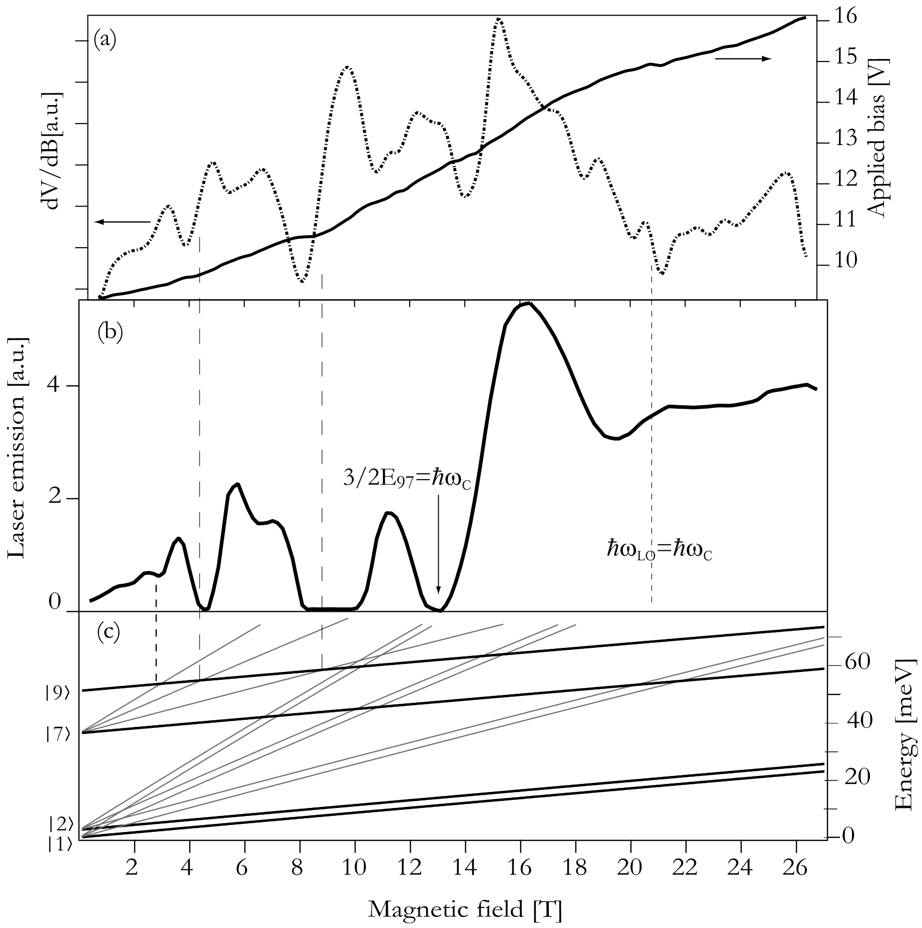

Figure 7.9: (a): Applied bias and its derivative with respect to the magnetic field for I=360 mA (b): Laser emission at constant current (I=360 mA) as a function of the magnetic field. (c): Landau fan for sample N314.

The possibility to observe a magnetophonon resonance for this active region design is extremely reduced: the energy spacing that will allow the equation 2.7.35 $\Delta E_{21} - \hbar\omega_{LO} = n\hbar e\frac{B}{m^*(E)}$ to be satisfied is $E_{91} = 51$ meV . States $|9\rangle$ and $|1\rangle$ are strongly separated in real space, and the coupling will result very small. Moreover the resulting energy $E_{91} - \hbar\omega_{LO} = 15$ meV happens to be coincident with the energy of the photon. The series of oscillation induced by the magnetophonon effect would then be superimposed to the one due to the elastic resonances between Landau levels. The resonance condition $\hbar\omega_{LO} = \hbar\omega_c$ between the optical phonon energy and the cyclotron energy is matched at 20.8 T. Laser emission presents a local minimum at 19 T, and an analysis of the transport as a function of the magnetic field reported in Fig.7.9 (a) shows a diminution of the slope dV/dB, i.e. a diminution of the magnetoresistance in correspondence with the resonance of with the LO-phonon energy. After the minimum at 19 T, that can be attributable to the resonance at twice the photon energy ($\hbar omega_c(19\ T) = 32.8\ meV = 2 \cdot h\nu$) the laser emission slowly increases with the applied magnetic field.

7.3.2 Bound-to-continuum at 130 μm

The structure object of the measurement of this Section is a rescaling of the bound-to-continuum design presented in Sec.5.1.1 and its performances without applied magnetic field are extensively described in Ref.[173]. The calculated bandstructure and the L-I-V curves at B = 0 for sample A2985 are plotted in Fig.7.10: the layer sequence is reported in App.C. The low energy of the photon emitted $h\nu \approx 9.6$ meV (130 μm) and the overall energy spacing of its period (E_{81}=21 meV) make this device suitable for a comparison with the low energy structures of Chapter 6 because it will enter the strong confinement region at approximately 12.6 T.

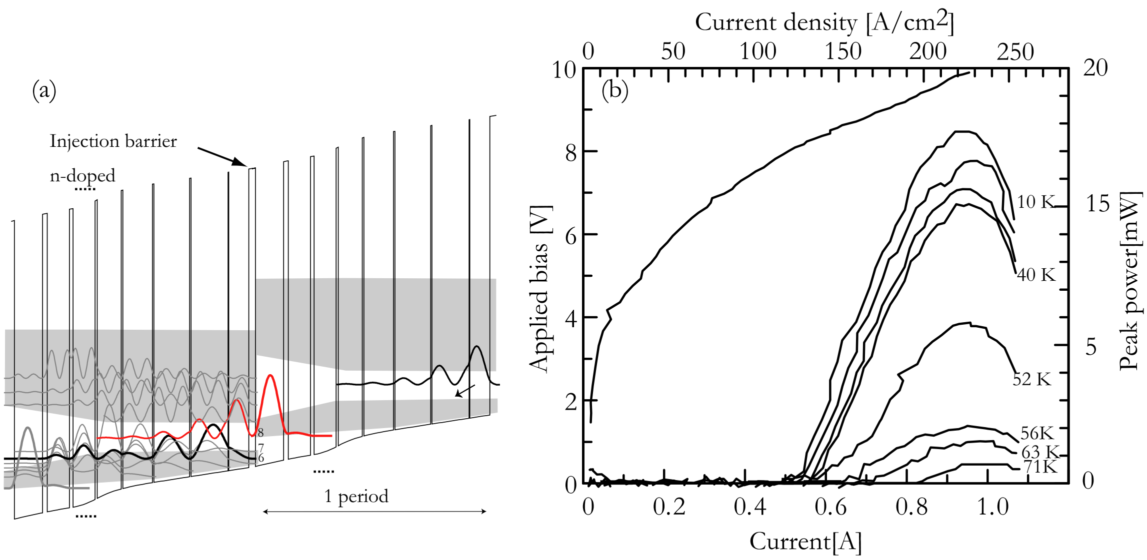

Figure 7.10: (a): Calculated bandstructure for sample A2985 emitting at $\lambda \simeq 130\ \mu$m. (b): L-I-V curves for sample A2985 without applied magnetic field (laser ridge 2 mm long 210 μm wide)

Due to the differences in laser intensity at low and high magnetic fields, the data relative to the low field portion are plot in Fig.7.11 (a) while the high field part of the measurements is reported in panel (b) of the same figure. The ratio between the maximum intensity at zero field and the maximum intensity at high magnetic field is $I_{0\ T}/I_{20.8\ T} \cong 16$. Also in this case laser action is present on the whole magnetic field sweep, and as in the case of sample N314 the laser emission results to be much weaker at high magnetic fields. The diminution of light intensity at 2.85 T is attributed to the resonance $|8,0\rangle \longrightarrow |7,2\rangle$ and the successive quenching of laser action is due to the resonance of one photon with the cyclotron energy $h\nu = 9.7$ meV $= \hbar\omega_c(5.6T)$.

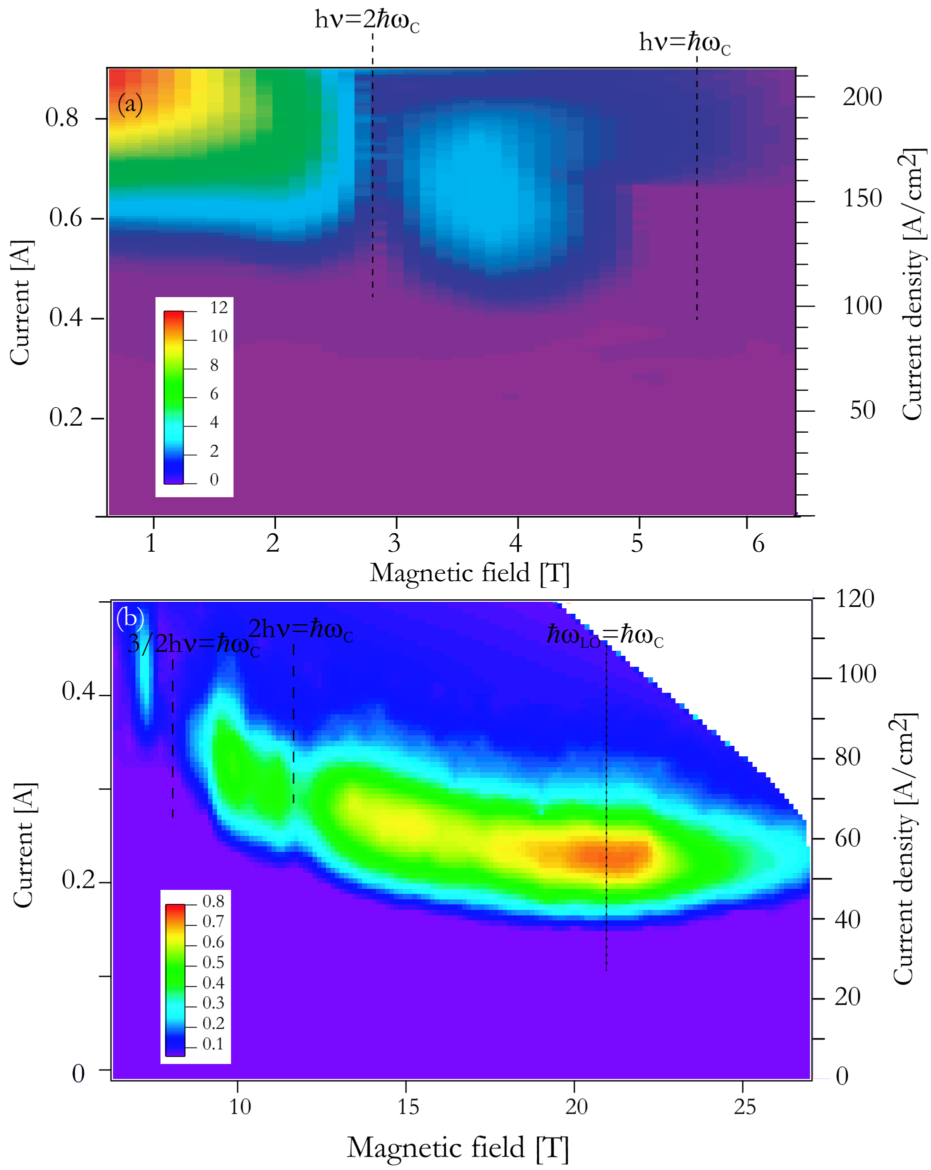

Figure 7.11: (a) Light emission in function of injected current and applied magnetic field from 0-6.5 T for sample A2985. (b) Light emission in function of injected current and applied magnetic field from 6-27 T for sample A2985

Laser action is present again for a small peak around 7 T, then another quenching occurs. This quenching can be identified with the resonance $3/2h\nu = \hbar\omega_c$, already observed in the other structures. Starting from 8.3 T lasing is always present with low threshold with respect to the low field part. A weak signature in the threshold current density and in light emission is present around 12 T, where the cyclotron energy matches twice the photon energy ($\hbar\omega_c(12)$=20.7 meV $\approx 2h\nu$ = 19.4 meV). The slight detuning of this feature could be due the matching of the resonance condition for the overall energy spacing of the active region E_{81}=21 meV $\cong \hbar\omega_c(12)$=20.7 meV, although the states $|8\rangle$ and $|1\rangle$ are hugely spatially separated and their coupling is strongly reduced by the several barriers present.

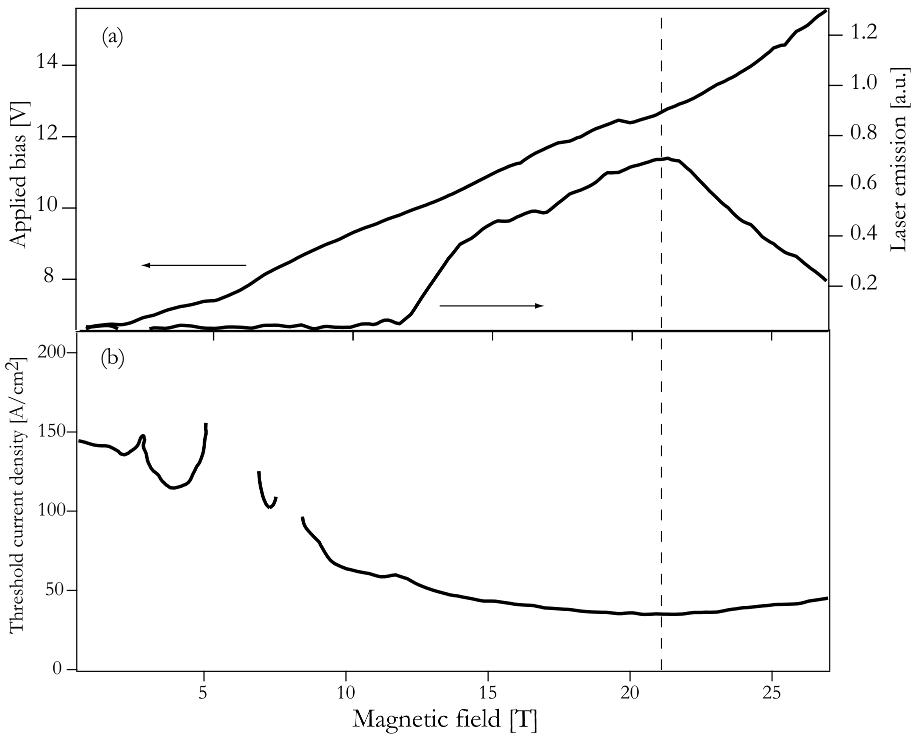

Figure 7.12: (a):Applied bias and laser emission at a constant injected current density of 65 A/cm^2 for sample A2985. (b): Threshold current density as a function of the applied magnetic field from 0-27 T for sample A2985

In the other superlattice-like structures and at higher photon energy we never observed such an elastic coupling between states so widely separated in real space. Light emission undergoes several modulations and presents a pronounced maximum (for the region where $B > 6.5$ T) at 20.9 T. The cyclotron energy at this magnetic field matches the optical phonon energy in GaAs $\hbar\omega_c(20.9T) \cong 36$ meV. An analysis of the transport reported in Fig.7.12 (a) reveals a decrease in the positive magnetoresistance at 19.9 T which is probably related to the maximum in laser emission. The threshold current density is plotted on the whole magnetic field sweep in Fig.7.12(b) and shows the minimum value at 20.8 T, in correspondence of the local maximum in laser emission. The value of 30 A/cm^2 is roughly 1/3 of the zero field value. Threshold current rises again to 37 A/cm^2 at the maximum field of 26.7 T.

7.4 Comparative analysis

Despite the different photon energies ($h\nu_{N314} = 14.8$ meV, $h\nu_{A2985} = 9.6$ meV) and the presence of a much wider miniband that encloses the LO phonon energy (sample N314), the two superlattice-based structures analyzed in strong magnetic field present many similarities. If we take a look at the threshold current density as a function of the applied magnetic field for the two samples, reported together in Fig.7.13, the two samples behave exactly in the same way except for the location of the resonances that are obviously shifted because of the different photon energy. In particular, in these data there is no evidence of a direct magnetic-field modulation of the lifetime of the lower state of the lasing transition. This is in agreement with what observed at lower fields in this same Chapter (Section 7.2.1): there is no special arrangement in the levels of the lower miniband of sample A2985 and the strength of the scattering of the LO phonon for sample N314 do not allow the observation of modulation of the lifetime in the active region of the laser. All the features are identified with resonances that involve only the upper and the lower state of the lasing transition. There is no dramatic reduction of the threshold current as observed in the big well samples: here the threshold current is reduced by a factor of 3 and not by a factor of 20-25. The coupling of the energy states of both lasers with the LO phonon is not direct as in the case of Mid-IR QCL's [120] where the upper state lifetime is regulated via LO phonon emission. In the Far-IR the upper state lifetime is determined by the complex interplay of different scattering mechanisms. However, in both samples we noticed the presence of weak features in transport and light emission where the cyclotron energy roughly matches the GaAs LO phonon energy. This is the condition for the magnetopolaron effect [202, 203], very important in the study of the strong interaction between electron and phonons both in the bulk and

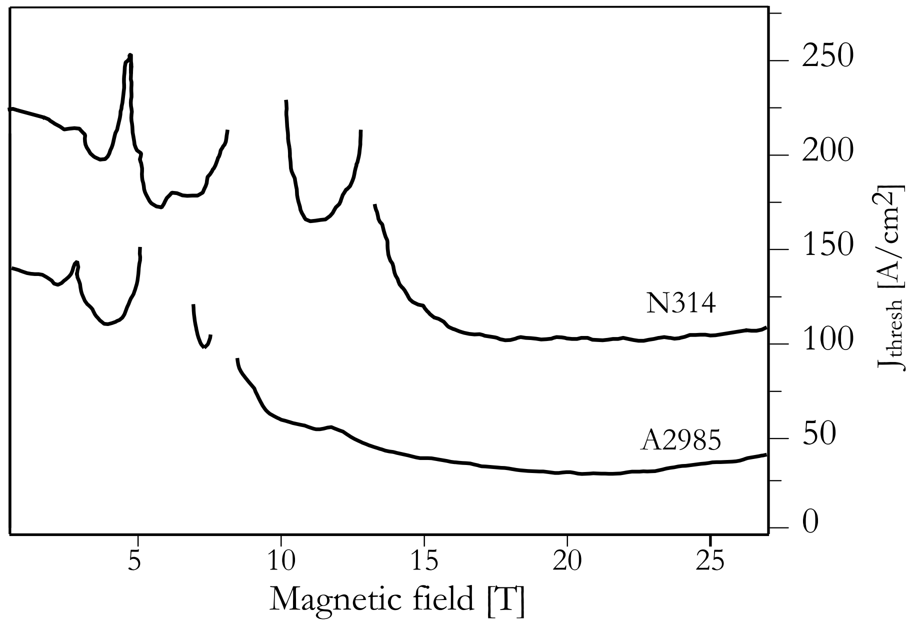

Figure 7.13: Threshold current density as a function of the applied magnetic field for samples A2985 and N314 at T = 4.2 K.

in systems of reduced dimensionality. The observation of such signatures in the superlattice based structures and the absence of any signature for the big well structures could indicate that the vertical, low energy structures are completely decoupled from the LO phonon at least at the low temperatures where we carried on the investigation.

7.5 Conclusions

The study of superlattice-based structures in strong magnetic field brings interesting information especially if compared with the results obtained with vertical transition structures analyzed in Chapter 6. Lasers with very different transition energy and different lower miniband architecture show very similar behavior of threshold current as a function of the magnetic field. The dominating effect in these superlattice structures is the modulation of the upper state lifetime: there is no evidence of a lifetime modulation in the lower miniband that affects laser action for the bound-to-continuum structures. The lower miniband of these devices does not present a regular dispersion in energy and resonant magnetic confinement, observed on chirped superlattice with a more regular miniband, are absent. Threshold current density are reduced by a factor of 2-3 with respect to zero field value in contrast to the factor of 20-30 observed in vertical structures between high and low magnetic field. It is clear that the delocalized nature of the wavefunction limits the increase of the electronic lifetime. The quenching of the transport due to electron localization is observed also in these bound-to-continuum structures. At the same time light emission intensity for strong applied magnetic fields is always much weaker than the zero field value. A new resonance in light emission is observed also in these structures, corresponding to the condition where 1.5 times the energy spacing between subbands equals the cyclotron energy. This effect, also present in vertical transition structures, needs an adequate theoretical description.

Chapter 8

Conclusions and perspectives

In this thesis work we have studied different gain mechanisms in order to obtain laser action in the Terahertz region using intersubband transitions in semiconductor quantum wells. The motivation for such a research is twofold: the exploration of a new region of laser frequencies generated by a semiconductor device and the realization of sources of coherent radiation that can fill the gap existing between optics and electronics.

The first approach we have used is based on the conventional quantum cascade laser technology: the optical transitions are engineered between conduction band states with quasi-parabolic dispersion. We have demonstrated laser action in three different new designs, each one with different performances. The single quantum well 3.5 THz laser object of Chapter 4, closely related to the original Kazarinov and Suris proposal for the quantum cascade laser, is an extremely useful model system to understand the interplay between resonant tunnelling and intersubband scattering dynamics for subband with energy spacing below the LO phonon. Modellization based on resonant tunnelling current flow calculated with density matrix approach and rate equations quantitatively account for the observed results and yield values for the relevant lifetimes in the structure. The laser device showed a very low threshold current density of 29 A/cm^2, the lowest among QC lasers without employing magnetic field.

Superlattice-based design employing a bound-to-continuum optical transition (Chapter 5) has been profitably used to achieve laser emission at 3.4 THz with high output optical power and pulsed operating temperature of 100 K, above the technologically important barrier of liquid nitrogen temperature (77 K). A detailed study of the temperature dependence of the threshold current together with spontaneous emission has highlighted the crucial role of a fast extraction of carriers in the lower miniband. This issue has been addressed with an improved version of the bound-to-continuum design that employs scattering from optical phonons as a mechanism to deplete the lower state of the lasing transition. Such a structure, studied in two different waveguide configurations, lased up to 116 K in pulsed operation: the design looks very promising and an active region optimization aimed to increase injection efficiency together with improvement of the double metal waveguide technology could lead to significant improvement both in pulsed and CW operation. The degradation of the performances with increasing wavelength is evident, making difficult the realization of high temperatures lasers emitting below 2 THz.

The core of this thesis work is the study of low energy-long wavelength quantum cascade structures. In this case the gain mechanism is based on the modification of the lifetimes by the additional in-plane confinement induced via an intense magnetic field perpendicular to the layers, in the spirit of the research on quantum boxes and low dimensional semiconductor devices. The intra-well vertical transition joined with an outstanding quality of the grown material makes those structure unique systems where extremely long intersubband lifetimes are observed. This design approach has led to the demonstration of laser action at 1.39 THz (220 μm ca.), the lowest frequency reported for any quantum-cascade laser to-date. The threshold current density exhibited by this class of devices is below 1 A/cm^2, among the lowest observed on any semiconductor-based laser, including last-generation quantum dots at cryogenic temperatures. This extremely reduced value of the threshold current density is attributed to the combined effect of the quenching of scattering and dephasing mechanisms together with the huge reduction of the waveguide losses due to carrier localization. As in the quantum Hall effect, electrons are localized by the combined action of magnetic field and residual disorder in the sample. The structures have been studied in very high magnetic fields up to 28 T: very interesting and peculiar phenomena are observed, that demonstrate the strong link between optical and transport characteristics in a quantum cascade laser. The comparative study of superlattice based active region in very high magnetic field points out the fundamental difference between an intra-well optical transition and an optical transition based on delocalized states. The threshold current density in the case of superlattices shows important reduction in function of the applied magnetic field, but there is not a dramatic effect as observed on the vertical transitions. Those results can be useful also for establishing the relative importance of the various diffusion mechanisms as electron-electron scattering and interface roughness scattering.

The achievement of high temperature, long wavelength THz QC lasers will strongly depend on the ability to manage in-plane scattering. If employing conventional QC structures with parabolic subband dispersion, then the use of LO phonon to deplete the lower state of the lasing transition seems to be unavoidable. Lots of improvement are still possible from the point of view of the design. The choice of the waveguide resonator will be essentially application-driven: the double metal solution is the best choice for high temperature performances but when high power is needed (imaging applications for example) the single plasmon waveguide is the optimal compromise, at the expenses of a lower operating temperature (still above liquid nitrogen).

The study of multi dimensional confined intersubband lasers offers a huge variety of interesting research themes. On one side the complex phenomena related to localization, electron dynamics and interaction between transport and laser emission are far from being understood. The exploration of the low temperature ($\sim$ 100 mK) regime and the in-plane transport characteristics could bring new elements for the comprehension of the carrier dynamics. On the other side the possibility to combine electron and photon confinement can lead to envision multi-wavelength microlasers emitting at THz frequencies. In light of the results exposed in Chapter 6, it is particularly attractive to look at the possibility to produce optical resonators where all the spontaneous emission is coupled into one cavity mode and test the system in the ideal condition for the achievement of a thresholdless laser. The realization of structures with a three dimensional physical confinement is strongly connected to technological issues. The accuracy needed for such structures is very high: the uncertainty on the MBE growth for the long wavelength structures is below 1%.

Acknowledgements

It is a real challenge to express with my words the gratitude to Prof. Jérôme Faist, my thesis director, for having given me the opportunity to work with him. It is rare to find such a mixture of scientific and human qualities in only one person: I really thank him for his patience, his trust, his incredible enthusiasm, his every-day encouragement and for being disponible every time I needed help. His deep and intuitive vision of the physics has been really inspiring and has always provided solutions to the many problems we have faced.

I am really grateful to Prof. Daniel Hofstetter and Prof. Piero Martinoli (Uni Neuchâtel), Prof. Carlo Sirtori (Université Paris VII) and Prof. Karl Unterrainer (Technical University of Vienna) for the critical reading of the manuscript and for being present and active part of the jury at the thesis defense.

Prof. Daniel Hofstetter has been a reference during the first years: we shared the same office for a long time and I particularly admire his rigorous and efficient work. I especially thank him for the careful correction of the manuscript also on the English language side.

Prof. Piero Martinoli is a model of enthusiasm and competence in the research field: I would like to thank him also for communicating me the good news of the SPS award!

I would like to warmly thank Prof. Carlo Sirtori for the many discussions, the constant encouragement and the support that he gave me throughout all my thesis work. It has been really a pleasure to have a scientific exchange with such an expert that showed interest and appreciated my work.

Many thanks also to Prof. Karl Unterrainer for the constant scientific exchange and the clarifications he gave me about THz intersubband transitions in high magnetic fields.

Many of the results presented in this thesis work would not have been possible without the extraordinary quality of the epitaxial growth. I am really grateful to Prof. Edmund Linfield of the University of Leeds and especially to Prof. David Ritchie and Dr. Harvey Beere of the Cavendish Laboratory for the excellent samples produced during our collaborations in the different EU projects.

Many thanks to Dr. Marcella Giovannini, Mr. Nicolas Hoyler and Dr. Mattias Beck for the friendship and for the excellent layers coming from our in-house growth facility, that arrived together with me in October 2001!

I would like to thank Dr. Marcin L. Sadowski at the Grenoble High Magnetic Field Laboratory for the support and help during the very "intense" days (and especially nights!!) we spent together trying to make M10 work together with the FTIR!

The PhD thesis is really something that can change your life, not only in the professional sense but also on the human side. I had the real privilege to have excellent colleagues, but mostly important, excellent persons and friends that created a very special working environment.

Many many thanks to Thierry R. "chopper" Aellen for all the discussions, beers, skying days, laughs and for the excellent friendship we built in these years: grazie amico!

Thanks a lot to Dr. Stephane "organizer" Blaser for the many good moments spent together and for having taught me a lot about the magnetic field cryostat.

Thanks a lot to Dr. Lorenzo "fondue" Sirigu for being such a good scientist and a good person. We spent also two weeks together in Grenoble without getting mad and one week in L.A. without getting too overweight!!

Many "Merssi" to Christoph Walther for having been an outstanding diploma student and for the occasional sailing on the lake. As a team member of the Grenoble expedition you learned quite quickly how to eat a steak for breakfast!

Thanks so much to Lassaad Ajili, my collegue on the THz project: we shared the labs and the clean room with a sane competition but always with a big respect.

Grazie mille to Romain "jesuisnaze" Terazzi, for the many many interesting discussions and for being so disponible at any time for my theoretical questions.

Merci beaucoup to Dr. Laurent "Larry" Diehl also for his great hospitality in Boston.

Thanks a lot to Marcel Graf for the nice discussions and the fun time we had working on the detector. Marcel and Tobias, the "GNU" team, deserve a big thank also for their invaluable job in providing us with a nice working server and backup system: the life is much easier thanks to MESO!

It is my pleasure to thank all the other members (past and present) of the mesoscopic group, the Hofstetter group and Alpes Lasers for their help, for the discussions and for bearing me for all this time! Thanks to "Angus" Richard, Yuriy, Michel, Arun, Maria, Maxi, Esther, Fabrizio, Antoine, Lubos, Sophie.

The technical staff of the Physics Institute deserves acknowledgement for the excellent and immediate support in solving technical problems and realizing our proposals.

A special thought to my dear friend Harald that meant so much for me and to whom this work

is dedicated. He taught me a lot of things, introducing me to many aspects of this work with an enthusiasm and a friendship that I'll never forget.
Many thanks to Dr. L. Andrea Dunbar for her work within the collaboration on photonic crystal structures.
The fruitful collaborations on the THz imaging projects with Prof. Jim Harris and Dr. Seongsin Kim at Stanford University and Dr. Danielle Chamberlin, Dr. Peter Robrish and Dr. Rick Trutna at Agilent Technologies are gratefully acknowledged.
I would also like to acknowledge scientific discussions with Dr. Alessandro Tredicucci, Dr. Rudeger Kohler, Dr. Stefano Barbieri, Dr. Benjamin Williams, Prof. Qing Hu, Sushil Kumar, Dr. Angela Vasanelli, Dr. Cristiano Ciuti, Dr. Sukhdeep Dhillon, Dr. Hans Sigg, Prof. Gottfried Strasser.
Thanks to all my close friends (old and new!) that have been aside me during this adventure in Switzerland: Piero, Giuseppe, Cate, Miriam, Rolf, Maurizio, Marta (e Lorenzino), Fabio, Tupytan, Annalisa, Marcello, Veronica, Elena, Lollone.
Many special thanks go to Dr. Raffaele MT Colombelli for his long-term friendship, the scientific support and for strongly encouraging me when I applied for Jerome's group ("...Faist? seriously??!! ...GO FOR IT!!!!")
My dear family has been an enormous support for me, always encouraging me and being constantly at my side with their love without making me feel too much the sadness of the distance. Grazie infinite a Mamma Nicoletta, Babbo Ferruccio e Nonna Luciana: siete eccezionali.
Thanks so much also to Giuliano and Sonia for their affection and for really making me feel part of the family.
..at last, we are there! the biggest thanks and a loving kiss go to my life companion Sara: after all these years of trains and trips and movings we are together!! I love You, my dear, and I couldn't have made it without all your help, your understanding, all the love you give me everyday and without your wonderful smile that enlightens my life.

This thesis was funded by the Swiss National Science Foundation

Appendix A

Magneto spectroscopy with THz QCL's

In this Appendix we will illustrate two simple magneto-spectroscopy experiments carried out with the laser devices developed during this thesis work. The first one is the detection of electron spin resonance on the conduction electrons of InSb and the second one is the magneto-spectroscopy of a quantum well THz photodetector also developed in our laboratory.

A.1 Electron spin resonance on InSb

A system with an angular momentum $\vec{J} = \hbar\vec{I}$, where $\vec{I}$ is the spin momentum, presents an associated magnetic momentum $\vec{\mu} = \gamma\hbar\vec{I}$, where γ is the gyromagnetic factor. The interaction energy of an isolated spin system with a static magnetic field $\vec{B}$ is then given by :

$$E = -\vec{\mu}\vec{B} \tag{A.1.1}$$

If we choose the quantization axis for $\vec{J}$ parallel to the field $\vec{B}$ the system will admit an ensemble of 2I+1 Zeeman levels separated by an energy $\Delta E = \gamma\hbar B$. For the electrons in a semiconductor we will have I=1/2 and the gyromagnetic factor will take the form of an effective gyromagnetic factor g^*, as already described in Chapter 2. The Zeeman splitting for the electrons in a semiconductor is then $\Delta E_{Zeeman} = |g^*|\mu_B B$ and he effective g-factor is defined by the band structure parameters of the materials involved, especially the spin-orbit energy splitting of the valence band Δ_{SO}. Electron spin resonance (ESR) is traditionally performed in the microwave region of the electromagnetic spectrum because the g-factors of many materials are almost equal to the one of the free electron, that for an applied magnetic field of 1 T will give rise to a Zeeman splitting of $\Delta E/\hbar \cong 28$ GHz. In Fig.A.1(extracted from Ref.[204])is reported a diagram that plots the g-factor in function of the lattice constant for the III-V semiconductors. The experimental points have been interpolated by a theoretical calculation of the effective g factor via the formula [205]:

$$\frac{g^*}{g_0} = 1 - \frac{\Delta_{SO}}{3E_g + 2\Delta_{SO}} \left(\frac{m_0}{m^*} - 1\right) \tag{A.1.2}$$

where g_0 and m_0 are the free electron values and E_g is the bandgap.

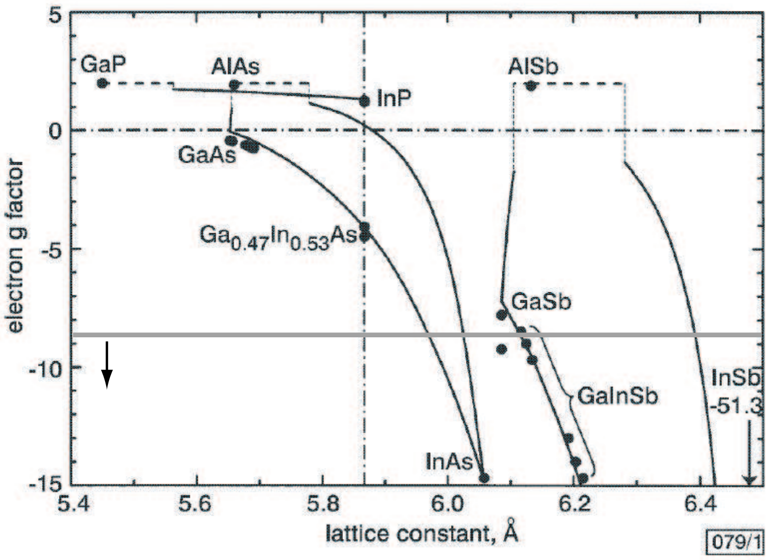

Figure A.1: g factors for conduction electrons in III-V semiconductors against lattice constant (reprinted from [204]). The horizontal grey line represents the limit of systems that can be investigated in the Neuchâtel apparatus, $B_{max} = 12\ T, \lambda_{max} = 215\ \mu$m.

Understanding the physical mechanisms underlying the manipulation of electronic spin in semiconductors may ultimately lead to multifunction devices based on the synthesis of photonics, electronics and magnetics. At present, in electronics it is predominantly the charge of the electrons which is used in applications, e.g. in field-effect transistors where the voltage on a gate controls the charge in an inversion layer and so the current through the device. Recently, it was proposed that it is also possible to use the spins of the electrons to perform electronic functions, extending electronics into spintronics. Electron spin resonance (ESR) allows one to investigate the properties of spin systems. In addition, it can also be applied to manipulate spins: with a pulse at the ESR frequency of controlled duration and intensity (π pulse, $\pi/2$ pulse, see [206])it is possible to reverse the orientation of a spin, e.g. from $|\uparrow\rangle$ to $|\downarrow\rangle$ or even to construct a quantum mechanical superposition state. The possibility to have a compact, electrically injected laser source which can be used to probe the spin degree of freedom of several III-V materials is attractive, combined to the inherently high sensitivity of a spin resonance process detected with high values of the applied magnetic field.

The long wavelength THz QCL's developed in this thesis work and described in Chapter 6 are good candidates to perform this kind of spectroscopy due to their long wavelength, their low electrical power consumption and their working principle based on the presence of a magnetic field that optimize the coupling with the examined sample. In order to check the feasibility of such an experiment, we arranged an experimental setup in order to perform electron spin resonance with a long wavelength THz QCL as a source. Inspection of Fig.A.1 reveals that the materials that can be investigated with our apparatus where B_{max} = 12 T and $\lambda_{max} = 215$ μm are the ones with $|g^*| > 8.7$.We currently use in our setup an InSb cyclotron resonance detector: InSb has a g^* of about -50, depending on the doping and on the quality of the material, then well above our detection limit. The idea is then to use our detector as a sample and perform an experiment of electrically detected ESR [207]: we will detect the spin resonance phenomenon as a change in the conductivity of our InSb detector. In this case the small superconducting coil that usually tunes the Landau states of the detector will be used as the polarizing field. The long wavelength THz QC is immersed in the main magnetic field that this time will be kept fixed at a value where the laser presents good emission power with low threshold. In order to induce transitions between spin states we need the magnetic field of the AC field to be perpendicular to the polarizing field [206]: this condition is fulfilled by our experimental arrangement. We employed a 1.66 THz laser based on the big well design described in Sec.6.5.2. The results of the measurement is shown in Fig.A.2. The peak in the magnetoresistance is due to spin-flip transitions of the conduction electrons: the increasing background of the magnetoresistance has been subtracted. In the inset is visible the complete field sweep of the small superconducting coil that shows the laser spectrum due to Landau level absorption (usual "detector" configuration, then $\hbar\omega_c = 8.324 \cdot B[meV]$ and from the inset $h\nu_{las} = 0.85 \cdot 8.324 = 7$ meV) with the circle highlighting the ESR contribution.

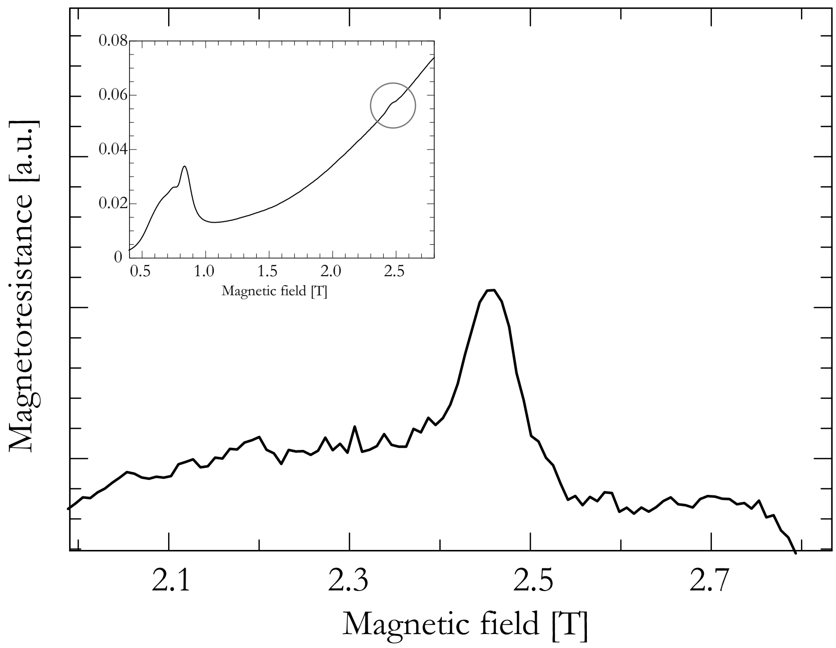

Figure A.2: Electron spin resonance signal observed as a variation in the magnetoresistance of the InSb detector (the background has been subtracted). Inset: complete field sweep for the InSb detector, where is visible the signal due to the laser and, in the grey circle, is highlighted the ESR contribution.

From the expression of the Zeeman energy it is possible to deduce the $|g^*|$ for our InSb detector:

$$|g^*| = \frac{h\nu_{las}}{\mu_B\ B_{res}} = \frac{180.4}{\mu_B\ 2.45} = 48.5 \pm 1.5 \tag{A.1.3}$$

The deduced value of the g^* is in excellent agreement with what found in literature [208], provided that we do not know the exact doping concentration for our sample.

A.2 THz quantum well photodetector in magnetic field

In the framework of our study of the electronic state lifetimes below the LO phonon energy in function of the applied magnetic field, we examined the possibility to measure the transport properties of a cascade-like structure in a magnetic field when illuminated by terahertz radiation. The structure tested is actually a THz range quantum well infrared photodetector , described in detail in Ref.[209] and designed to operate at 3.4 THz. The detector, whose self-consistently calculated bandstructure is reported in Fig.A.3 , is a QCL-like structure grown in the $Al_{0.15}Ga_{0.85}As/GaAs$ material system on a semi-insulating structure. The structure is designed in order to work under zero bias condition in order to avoid additional noise due to dark current. The operating principle is based on photoexcitation of electrons firstly residing in state $|0\rangle$ into the doublet formed from states $|4\rangle$ and $|5\rangle$ (the calculated energies are $E_{50} = 16$ meV and $E_{40} = 13.7$ meV). Once excited in state 4 or 5 the electrons have a certain probability to tunnel into state 3 (ground state of the adjacent well) and then to slide down in the cascade of ground states formed by the chirped superlattice.

The idea of the experiment is the following: the magnetic field, applied perpendicularly to the plane of the layers, will enhance the lifetime $\tau_{5,4\rightarrow 0}$ thus favoring the probability for the electron to tunnel in the adjacent well contributing to the photocurrent. The lifetime of states 4 and 5 will be modulated by the elastic processes examined in Chapter 2 and observed extensively on lasing systems. The experimental arrangement is the following: a THz quantum cascade emitting at 87 μm ($h\nu$ =14.4 meV, sample A2771, Sec.5.1.1) and maintained at constant power shines on the detector placed inside the magnetic field cryostat. The detector photocurrent is then recorded sweeping the magnetic field. To rule out any possible influence of the stray field of the magnet on the excitation laser we monitored the laser parameters in function of the applied field controlling their stability throughout all magnetic field sweep. The detector is grown on a semi-insulating structure and processed

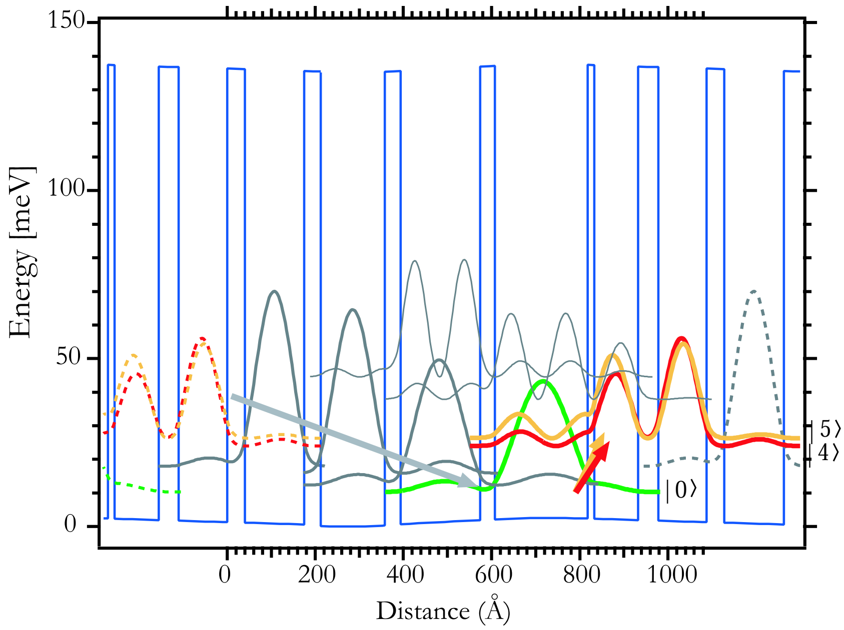

Figure A.3: Self-consistently calculated conduction band structure for sample A2879 at 10 K. One full period, surrounded by adjacent parts of the previous/next period is shown. The observed transitions take place between the ground state $|0\rangle$ and the states $|4\rangle$ and $|5\rangle$.

as a mesa structure with a diffraction grating on top that allows the coupling of both polarizations. The results of a typical measurement are shown in Fig.A.4, with the detector temperature kept at T=10 K. the lower panel of the same figure contains a Landau fan of the significant levels of the structure: the energy values are the calculated ones. In the region from 0 to 7 T the detector photocurrent shows some strong oscillations in function of the applied magnetic field, with minima located at 1.9 T, 2.6 T and 4 T. In the region 2.8-5.2 T the detector photocurrent is higher than the value at zero magnetic field. The minima are attributed to elastic resonances between the Landau levels $|4,0\rangle$ and $|5,0\rangle$ and the Landau states $|1,j\rangle$ that shorten the lifetime of the excited states increasing the probability of a recapture of the electron in the state $|0\rangle$ and subsequent loss of responsivity. The minimum at 4 T marks the condition where the energy spacing E_{40} approximately matches two times the cyclotron energy $\hbar\omega_c(4T)$. The deduced value of this energy spacing is 13.7 meV and

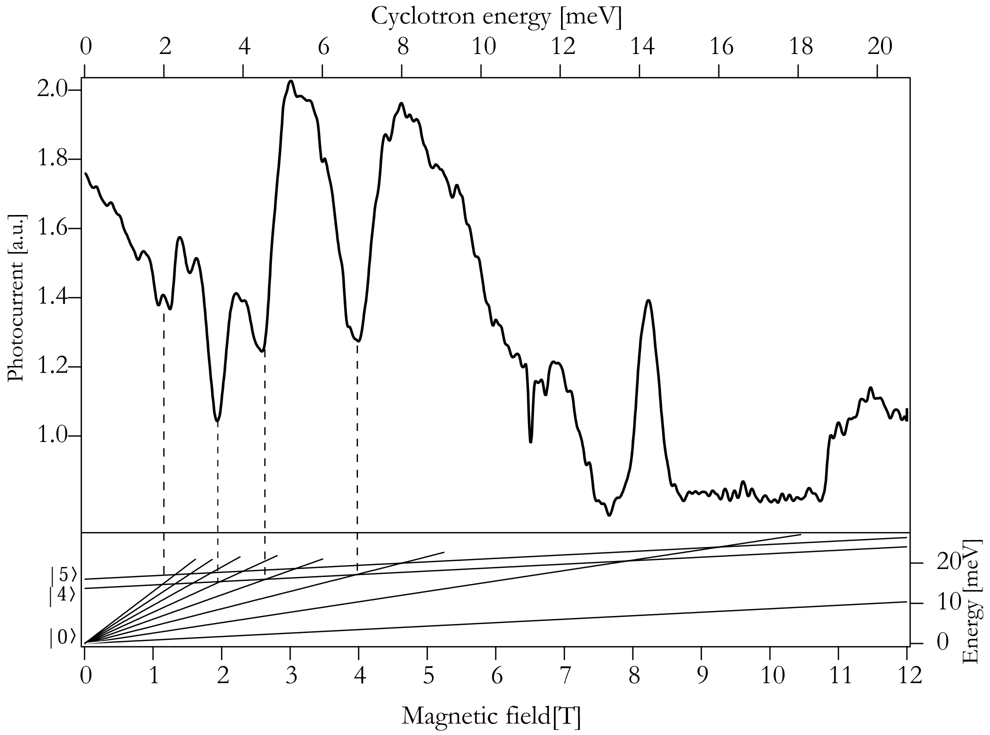

Figure A.4: (a): Photocurrent signal form sample A2879 in function of the applied magnetic field. (b) Landau fan for the three levels 0, 4 and 5 of the photodetector. The energy values are the calculated ones.

matches surprisingly well the one *calculated* from the bandstructure simulation, and is in disagreement with the one deduced from spectral measurement (14.7 meV [209]). Also the other resonances observed fit with an energy spacing E_{40} of 13.7 meV. The responsivity then drops and after we observe a clean and narrow peak at 8.2 T: this is the cyclotron resonance peak that provide us with the spectral information about the laser emission frequency. The deduced energy $E_{las} = \hbar\omega_c(8.2T) = 14.3$ meV matches very well the typical value for the center of gravity of the mode enevelope for a Fabry-Pérot ridge of sample A2771 (14.4 meV). The observed data can be interpreted as follows: the responsivity of the detector will depend on the interplay from the lifetime $\tau_{5,4\rightarrow 0}$ of one electron in the doublet of states 4,5 with the tunnelling time of the same electron to the adjacent well and thus its contribution to the photocurrent. The magnetic field acts in both directions: the lifetime $\tau_{5,4\rightarrow 0}$ is increased by the reduction of the non radiative processes due to Landau quantization in the x-y plane (outside the resonant conditions where we observe the minima in photocurrent). At the

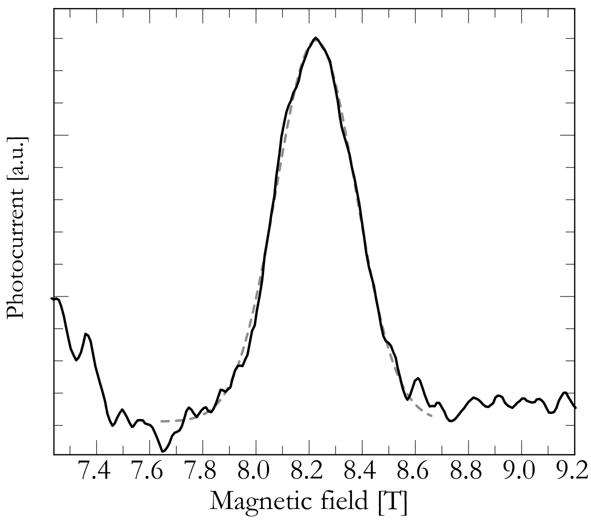

Figure A.5: Cyclotron resonance peak (full line) for sample A2879 with an illumination at 14.2 meV. The dashed line is a Gaussian fit that yields a full-width at half max of 0.4 T

same time, the localization of carriers induced by an increasing magnetic field will quench the transport, resulting in a poor detector efficiency for high values of applied magnetic fields. The region where the detectivity is higher in respect to the zero field value is the results of the trade-off between the described phenomena: the lifetime $\tau_{5,4\rightarrow 0}$ is increased and the transport across the structure is not yet suppressed. The discrepancy between the energy difference value of the subbands measured with the FTIR spectrum and the one deduced with the magnetospectroscopy can be ascribed to the depolarization shift (see Sec.6.6.2). With the value nominal value of the sheet carrier density $n_s = 8.7 \cdot 10^9$ cm^{-2} we obtain a shift $\Delta E \simeq 0.5$ meV, in good agreement with what observed. From a Gaussian fit of the cyclotron resonance peak, reported in Fig.A.5 we can deduce a full width at half maximum of 0.4 T that translates into a cyclotron resonance linewidth of 0.69 meV. This value represents the convolution of the cyclotron resonance transition linewidth with the multimode spectrum of the laser. Typical value for cyclotron resonance full widths measured on GaAs/AlGaAs heterostructures [210] lie in the $10^{-2} \div 4 \cdot 10^{-3}$ T range. What we observe is then the spectral width of the laser emission that will dominate the detected linewidth: the value of 0.69 meV matches very well typical values observed on this kind of devices (see Fig.5.6).

Appendix B

Grenoble high magnetic field experimental setup

The experimental setup for magnetic field measurement that has been built at the Institute of physics of Neuchâtel university (see Section 3.2) is limited to a maximum field of 14 T. The experimental results obtained up to that field value motivated the investigation of THz quantum cascade lasers with higher values of applied field, up to 28 T. The experiments where then carried out at the Grenoble High Magnetic Field Laboratory (GHMFL-CNRS, 25, Avenue de Martyrs BP166 38042 Grenoble cedex 9, FRance. http://ghmfl.grenoble.cnrs.fr). The magnet where the experiments were carried out (M10) is a resistive magnet made with copper-based windings of mixed Bitter type and "polyhelix" type. The bore is 34 mm wide. The magnet is supplied with a voltage of about 400 V at full power and the maximum electrical power is 20 MW. and the current is provided by power rectifiers with a stability of 10 ppm over a period of time of about 10 minutes. The cooling is provided by a circulation of deionized and deoxygenized water, with a flow reaching up to 1000 m^3/h at full power.

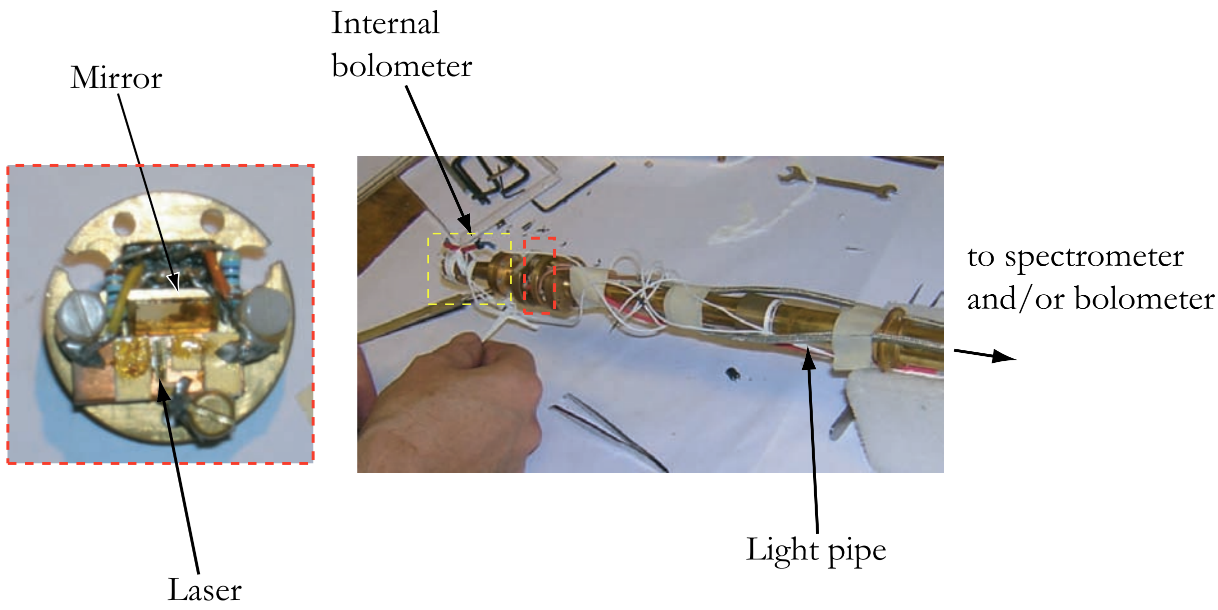

Figure B.1: Left: laser holder with 50 Ω charge resistors and mirror for launching the laser emission to the internal bolometer or to the spectrometer. Right: complete mount with internal bolometer, laser holder and hollow cryo probe that constitutes the light pipe.

The optical mesurements were carried out with three different setups: an internal bolometer has been used (Infrared research Inc. put specs) and placed directly in front of the laser (see fig. B.1). The laser mount is equipped of a 45 ° mirror because the magnetic field has to be applied perpendicularly to the plane of the layers and then the edge emission will be orthogonal to the field (intersubband selection rule). With this setup were possible light-current-voltage-magnetic field measurements, with the whole assembly immersed in liquid He. Put some words and a graph about the calibration of the internal bolometer with the magnetic field. The second setup allowed us to extract the light from the bore of the magnet and perform also spectral measurement. The experimental setup is shown in figs B.1 and B.2: the laser mount is inverted by 180 ° with respect to the horizontal direction and the light is guided via a light pipe that constitute the measurement probe. At the end we placed a mirror that reflected the radiation into a second light pipe that feeded an under vacuum Bruker FTIR. The whole path outside the measurement probe, included the spectrometer, was kept under vacuum in order to avoid water absorption especially strong at those long wavelength. The same purged light pipe was also used to perform the CW measurements; at the end of the light pipe was placed a window and then a chopper allowing the use of an He-cooled bolometer that detected the CW laser emission from the sample. Special care was employed in order to keep the equipment outside of the strong stray field that can cause serious problems to the electronics when the magnet reaches the highest values of the field (28 T). The power supply allows great flexibility in the control of the field sweep rate that can be adjusted between the maximum value of 919 Gauss/s (that translates in a complete sweep 0-28 T in about 5 minutes!!) and some Gauss per second. Our typical sweep rate for obtaining a complete characterization of the laser on the whole field range was 50 Gauss/s resulting in a total acquisition time of about 90 minutes.

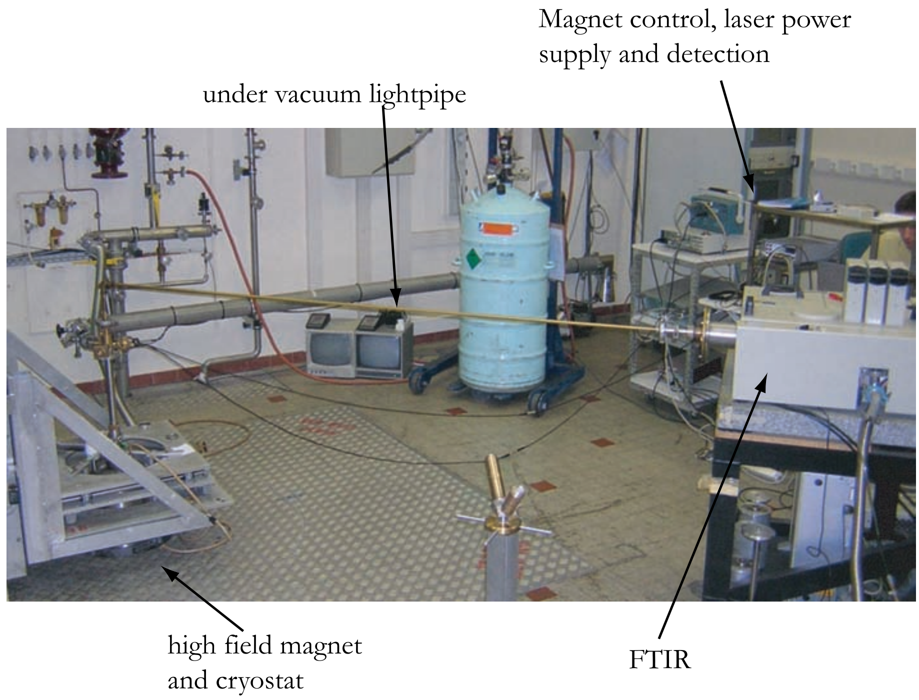

Figure B.2: Experimental setup for spectral measurements with pumped light pipe and FTIR spectrometer. The magnet is one floor below.

Appendix C

Samples parameters

The layer sequence of one period of the different GaAs/AlGaAs THz structures measured during this thesis are given in the following table, starting from the injection barrier. Also indicated are the doping levels, the nominal sheet density n_s induced by this doping and the number of periods N_p. The doped layers are underlined and the thickness of the barriers are in bold. Sample names staring either with an "A" or a "V" come from the Cavendish laboratory in Cambridge, UK. Samples whose identifier starts with "N" come from the inhouse MBE facility of the Faist group at the University of Neuchâtel, CH.

Sample	Layer sequence of one period, thickness in nm. $Al_{0.15}Ga_{0.85}As$ barriers are in bold, n-doped layers are underlined.	n [cm^{-3}]	n_s [cm^{-2}]	N_a [cm^{-3}]	N_p
A2664	**3.0**/3.0/**1.0**/36.0/**3.0**/14.5/**1.0**/ 13.0/**3.0**/13.0/**3.2**/<u>13.0</u>/**3.5**/11.0/**1.0**/3.0	$2 \cdot 10^{16}$	$2.6 \cdot 10^{10}$	$2.07 \cdot 10^{15}$	120
A2770	**2.2**/3.0/**1.0**/36.0/**2.2**/15.0/**1.0**/ 13.0/**2.5**/12.0/**3.0**/<u>10.0</u>/**3.5**/10.0/**1.0**/3.0	$3 \cdot 10^{16}$	$3.0 \cdot 10^{10}$	$2.53 \cdot 10^{15}$	120
A2771	**3.5**/9.0/**0.6**/16.3/**0.9**/16.0/**1.0**/ 13.8/**1.2**/12.0/**1.5**/<u>11.0</u>/**2.4**/ 11.0/**2.4**/11.0/**3.2**/12.1	$2.5 \cdot 10^{16}$	$2.75 \cdot 10^{10}$	$2.38 \cdot 10^{15}$	120
A2985	**4.0**/12.0/**0.5**/22.3/**0.8**/21.5/**.9**/ 17.8/**1.0**/14.5/**1.3**/<u>13.2</u>/**2.2**/13.4/**2.8**/17.0/	$2.5 \cdot 10^{16}$	$3.3 \cdot 10^{10}$	$2.27 \cdot 10^{15}$	120
A2986	**4.2**/9.0/**0.6**/16.3/**0.9**/16.0/**1.0**/ 13.8/**1.2**/12.0/**1.5**/<u>11.0</u>/**2.4**/ 11.0/**2.4**/11.0/**3.2**/12.1	$3 \cdot 10^{16}$	$3.3 \cdot 10^{10}$	$2.83 \cdot 10^{15}$	120
A3096	**2.5**/3.5/**1.2**/55.0/**3.0**/21.0/**1.0**/ 20.0/**3.2**/<u>16.4/**3.2**/16.0</u>/**3.5**/15.8/**1.0**/3.8/	$1.5 \cdot 10^{16}$	$5.34 \cdot 10^{10}$	$3.13 \cdot 10^{15}$	100
A3520	**2.5**/3.5/**1.2**/57.0/**3.0**/21.3/**1.3**/ 20.0/**3.2**/<u>15.6/**3.2**/13.9</u>/**3.5**/15.4/**1.0**/3.8/	$1.6 \cdot 10^{16}$	$5.23 \cdot 10^{10}$	$3.08 \cdot 10^{15}$	100
V198	**2.5**/3.5/**1.2**/60.7/**2.7**/22.2/**1.5**/ 20.0/**3.2**/<u>15.2/**3.2**/13.4</u>/**3.5**/15.4/**1.0**/3.8/	$1.6 \cdot 10^{16}$	$5.08 \cdot 10^{10}$	$2.94 \cdot 10^{15}$	95
N310	**4.5**/9.0/**0.6**/16.3/**0.9**/16.0/**1.0**/ 13.8/**1.2**/12.0/**1.5**/<u>11.0</u>/**2.4**/ 11.0/**2.4**/11.0/**3.2**/12.1	$8 \cdot 10^{16}$	$1.68 \cdot 10^{11}$	$7.54 \cdot 10^{15}$	120
N314	**4.2**/10.0/**0.7**/18.3/**1.0**/15.2/**1.3**/12.7/**1.7**/10.5/**2.7**/ <u>21.1</u>/**2.4**/ 16.5/	$3.8 \cdot 10^{16}$	$8.0 \cdot 10^{10}$	$6.77 \cdot 10^{15}$	120
N470	**3.7**/10.0/**0.7**/18.3/**1.0**/15.2/**1.3**/12.7/**1.7**/10.5/**2.7**/ <u>21.1</u>/**2.4**/ 16.5/	$3.8 \cdot 10^{16}$	$8.0 \cdot 10^{10}$	$6.77 \cdot 10^{15}$	120
N471	**4.7**/28.0/**2.3**/18.0/**2.3**/16.5/**2.3**/<u>16.0</u>/**2.3**/15.5/	$2.4 \cdot 10^{16}$	$3.84 \cdot 10^{10}$	$3.55 \cdot 10^{15}$	140

Table C.1: Layer sequence of THz QC samples based on $Al_{0.15}Ga_{0.85}As$ material system.

Bibliography

[1] M. Sherwin, C. Schmuttenmaer, and P. Bucksbaum. Opportunities in thz science. Technical report, 2004. Report of a DOE-NSF-NIH workshop Arlington, VA.

[2] P.H. Siegel. Terahertz technology. *IEEE Trans. Microwave Theory Tech.*, 50(03):910–928, 2002.

[3] D. Mittelman, R. Jacobsen, and M. Nuss. T-ray imaging. *IEEE J. Select. Topics Quantum Electron.*, 2(3):679–692, 1996.

[4] D. Chamberlin, P. Robrish, W. Trutna, G. Scalari, M. Giovannini, L. Ajili, and J. Faist. Imaging at 3.4 thz with a quantum-cascade laser. *Appl. Opt.*, 44(1):121–125, 2005.

[5] G.A. Krafft. Compact high-power terahertz radiation source. *Phys. Rev.*, 7:060704–1–060704–6, 2004. special topics ACCELERATORS AND BEAMS.

[6] A. Maestrini, J. Ward, J. Gill, H. Javadi, E. Schlecht, G. Chattopadhyay, F. Maiwald, N.R. Erickson, and I. Mehdi. A 1.7-1.9 thz local oscillator source. *IEEE Microwave Wireless Comp. Lett.*, 14(06):253–255, 2004.

[7] W. Knap, J. Lusakowski, T. Parenty, S. Bollaert, A. A.Cappy, V. Popov, and M.S. Shur. Terahertz emission by plasma waves in 60 nm gate high electron mobility transistors. *Appl. Phys. Lett.*, 84(13):2331–2333, 2004.

[8] D. Auston, K.P. Cheung, and P. Smith. Picosecond photoconducting hertzian dipoles. *Appl. Phys. Lett.*, 45(3):284–286, 1984.

[9] E. Brown, K. McIntosh, K. Nichols, and C. Dennis. Photomixing up to 3.8 thz in low-temperature-grown gaas. *Appl. Phys. Lett.*, 66(3):285–287, 1995.

[10] B. Lax. New York, Columbia University, 1960.

[11] A.A. Andronov, I.V. Zverev, V.A. Kozlov, Y.N. Nozdrin, S.A. Pavlov, and V.N. Shastin. Stimulated emission in the long-wavelength ir region from hot holes in ge in crossed electric and magnetic fields. *JETP Lett.*, 40(2):804–807, 1984.

[12] H. Hubers, S. Pavlov, and V. Shastin. Terahertz lasers based on germanium and silicon. *Semicond. Sci. Technol.*, 20:S211–S221, 2005.

[13] K. Unterrainer, C. Kremser, E. Gornik, C.R. Pidgeon, Y.L. Ivanov, and E.E. Haller. Tunable cyclotron-resonance laser in germanium. *Phys. Rev. Lett.*, 64(19):2277–2280, 1990.

[14] E. Brundermann, D. Chamberlin, and E. Haller. High duty cycle and continuous terahertz emission from germanium. *Appl. Phys. Lett.*, 76(21):2991–2993, 2000.

[15] S.G. Pavlov, R.K. Zhukavin, E.E. Orlova, V.N. Shastin, A.V. Kirsanov, H.W. Hubers, K. Auen, and H. Riemann. Stimulated emission from donor transitions in silicon. *Phys. Rev. Lett.*, 84(22):5220–5223, 2000.

[16] S.G. Pavlov, H.W. Hubers, H. Riemann, R.K. Zhukavin, E.E. Orlova, and V.N. Shastin. Terahertz optically pumped si:sb laser. *J. Appl. Phys.*, 92(10):5632–5634, 2002.

[17] E. Rosencher and B. Vinter. *Optoélectronique.* Masson, Paris, 1998.

[18] T. Tanabe, K. Suto, . Nishizawa, K. Saito, and . Kimura. Tunable terahertz wave generation in the 3- to 7-thz region from gap. *Appl. Phys. Lett.*, 83(2):237–239, 2003.

[19] C. Cohen-Tannoudji, B. Diu, and F. Laloë. *Mécanique quantique I et II.* Hermann, Paris, 1973.

[20] G. Bastard. *Wave mechanics applied to semiconductor heterostructures.* Les éditions de physique, Les Ulis, France, 1988.

[21] A. Cho. *Molecular Beam Epitaxy.* AIP Press, Woodbury, NW, 1994.

[22] L.L. Chang, L. Esaki, and R. Tsu. Resonant tunneling in semiconductor double barriers. *Appl. Phys. Lett.*, 24:593–595, 1974.

[23] R. Dingle, W. Wiegmann, and C.H. Henry. Quantum states of confined carriers in very thin al$_x$ga$_{1-x}$as-gaas-al$_x$ga$_{1-x}$as heterostructures. *Phys. Rev. Lett.*, 33:827–, 1974.

[24] L. Esaki and R. Tsu. Superlattice and negative differential conductivity in semiconductors. *IBM J. Res. Develop.*, 14(61):61–65, 1970.

[25] A. Kamgar, P. Kneschaurek, G. Dorda, and J.F. Koch. Resonance spectroscopy of electronic levels in a surface accumulation layer. *Phys. Rev. Lett.*, 32(22):1251–1254, 1974.

[26] L.C. West and S.J. Eglash. First observation of an extremely large-dipole infrared transition within the conduction band of a gaas quantum well. *Appl. Phys. Lett.*, 46(12):1156–1158, 1985.

[27] M. Helm. The basic physics of intersubband transitions. In H.C. Liu and F. Capasso, editors, *Intersubband transitions in quantum wells: Physics and device applications I*, volume 62, chapter 1, pages 1–99. Academic Press, 2000.

[28] F. Capasso. Band-gap engineering: from physics and materials to new semiconductor-devices. *Science*, 235:172–176, 1987.

[29] A. Yariv. *Quantum electronics.* John Wiley & Sons, New-York, 3^{rd} edition, 1989.

[30] Z.I. Alferov. Nobel lecture: The double heterostructure concept and its applications in physics, electronics and technology. *Rev. Mod. Phys.*, 73:767–782, 2001.

[31] R.F. Kazarinov and R.A. Suris. Possibility of the amplification of electromagnetic waves in a semiconductor with a superlattice. *Sov. Phys. Semicond.*, 5(4):707–709, 1971.

[32] F. Capasso, K. Mohammed, and A.Y. Cho. Resonant tunneling through double barriers, perpendicular quantum transport phenomena in superlattices, and their device applications. *IEEE J. Quantum Electron.*, 22(9):1853–1869, 1986.

[33] A. Kastalsky, V.J. Goldman, and J.H. Abeles. Possibility of infrared laser in a resonant tunneling structure. *Appl. Phys. Lett.*, 59(21):2636–2638, 1991.

[34] H.C. Liu. A novel superlattice infrared source. *J. Appl. Phys.*, 63(8):2856–2858, 1988.

[35] P. Yuh and K.L. Wang. Novel infrared band-aligned superlattice laser. *Appl. Phys. Lett.*, 51(18):1404–1406, 1987.

[36] V. Berger. Three-level laser based on intersubband transitions in asymmetric quantum wells: a theoritical study. *Semicond. Sci. Technol.*, 9:1493–1499, 1994.

[37] M. Helm, P. England, E. Colas, F. DeRosa, and S.J. Allen. Intersubband emission from semiconductor superlattices excited by sequential resonant tunneling. *Phys. Rev. Lett.*, 63(1):74–77, 1989.

[38] J. Faist, F. Capasso, D.L. Sivco, C. Sirtori, A.L. Hutchinson, and A.Y. Cho. Quantum cascade laser. *Science*, 264:553–556, 1994.

[39] C. Weisbuch and B. Vinter. *Quantum semiconductor structures.* Academic Press, San Diego, CA, 1991.

[40] K. Unterrainer. Photon-assisted tunneling in semiconductor quantum structures. In H.C. Liu and F. Capasso, editors, *Intersubband transitions in quantum wells: Physics and device applications II*, volume 66, chapter 1, pages 127–186. Academic Press, 2000.

[41] C. Sirtori, F. Capasso, J. Faist, D.L. Sivco, S.G. Chu, and A.Y. Cho. Quantum wells with localized states at energies above the barrier height. a fabry-perot electron filter. *Appl. Phys. Lett.*, 61(8):898–900, 1992.

[42] J. Faist, F. Capasso, C. Sirtori, D.L. Sivco, A.L. Hutchinson, and A.Y. Cho. Vertical transition quantum cascade laser with bragg confined excited state. *Appl. Phys. Lett.*, 66(5):538–540, 1995.

[43] G. Scamarcio, F. Capasso, C. Sirtori, J. Faist, A.L. Hutchinson, D.L. Sivco, and A.Y. Cho. High-power infrared (8 - micrometer wavelength) superlattice lasers. *Science*, 276:773–776, 1997.

[44] J. Faist, F. Capasso, C. Sirtori, D.L. Sivco, A.L. Hutchinson, and A.Y. Cho. Laser action by tuning the oscillator strength. *Nature*, 387:777–782, 1997.

[45] J. Faist, F. Capasso, C. Sirtori, D.L. Sivco, A.L. Hutchinson, M.S. Hybertsen, and A.Y. Cho. Quantum cascade lasers without intersubband population inversion. *Phys. Rev. Lett.*, 76(3):411–414, 1996.

[46] A. Tredicucci, C. Gmachl, F. Capasso, D.L. Sivco, A.L. Hutchinson, and A.Y. Cho. A multiwavelength semiconductor laser. *Nature*, 396:350–353, 1998.

[47] M. Beck, D. Hofstetter, T. Aellen, J. Faist, U. Oesterle, M. Ilegems, E. Gini, and H. Melchior. Continuous wave operation of a mid-infrared semiconductor laser at room temperature. *Science*, 295:301–305, 2002.

[48] D. Hofstetter, M. Beck, T. Aellen, J. Faist, U. Oesterle, M. Ilegems, E. Gini, and H. Melchior. Continuous wave operation of a 9.3 μm quantum cascade laser on a peltier cooler. *Appl. Phys. Lett.*, 78(14):1964–1966, 2001.

[49] M. Beck, J. Faist, C. Gmachl, F. Capasso, D.L. Sivco, J.N. Baillargeon, and A.Y. Cho. Buried heterostructure quantum cascade lasers. In *SPIE Proceedings*, volume 3284, pages 231–236, 1998.

[50] A. Tredicucci, F. Capasso, C. Gmachl, D.L. Sivco, A.L. Hutchinson, and A.Y. Cho. High performance interminiband quantum cascade lasers with graded superlattices. *Appl. Phys. Lett.*, 73(15):2101–2103, 1998.

[51] J. Faist, M. Beck, T. Aellen, and E. Gini. Quantum cascade lasers based on a bound-to-continuum transition. *Appl. Phys. Lett.*, 78(2):147–149, 2001.

[52] J. Faist, F. Capasso, C. Sirtori, D.L. Sivco, A.L. Hutchinson, S.G. Chu, and A.Y. Cho. Narrowing of the intersubband electroluminescent spectrum in coupled-quantum well heterostructures. *Appl. Phys. Lett.*, 65(1):94–96, 1994.

[53] J. Faist, F. Capasso, C. Sirtori, D.L. Sivco, and A.Y. Cho. Quantum cascade lasers. In H.C. Liu and F. Capasso, editors, *Intersubband transitions in quantum wells: Physics and device applications II*, volume 66, chapter 1, pages 1–83. Academic Press, 2000.

[54] C. Sirtori, P. Kruck, S. Barbieri, P. Collot, J. Nagle, M. Beck, J. Faist, and U. Oesterle. Gaas/al$_x$ga$_{1-x}$as quantum cascade lasers. *Appl. Phys. Lett.*, 73(24):3486–3488, 1998.

[55] C. Pflügl, W. Schrenk, S. Anders, G. Strasser, C. Becker, C. Sirtori, Y. Bonetti, and A. Muller. High-temperature performance of gaas-based bound-to-continuum quantum-cascade lasers. *Appl. Phys. Lett.*, 83(23):4698–4700, 2003.

[56] K. Ohtani and H. Ohno. Inas/alsb quantum cascade lasers operating at 10 μm. *Appl. Phys. Lett.*, 82(7):1003–1005, 2003.

[57] R. Teissier, D. Barate, A. Vicet, C. Alibert, A.N. Baranov, X. Marcadet, C. Renard, M. Garcia, C. Sirtori, D. Revin, and J. Cockburn. Room temperature operation of inas/alsb quantum cascade lasers. *Appl. Phys. Lett.*, 85(02):167–169, 2004.

[58] D.G. Revin, L.R. Wilson, E.A. Zibik, R.P. Green, J.W. Cockburn, M.J. Steer, R.J. Airey, and M. Hopkinson. Ingaas/alassb quantum cascade lasers. *Appl. Phys. Lett.*, 85(18):3992–3994, 2004.

[59] J.S. Roberts, R.P. Green, L.R. Wilson, E.A. Zibik, D.G. Revin, J.W. Cockburn, and R.J. Airey. Quantum cascade lasers grown by metalorganic vapor phase epitaxy. *Appl. Phys. Lett.*, 82(24):4221–4223, 2003.

[60] M. Troccoli, D. Bour, S. Corzine, G. Höfler, A. Tandon, D. Mars, D.J. Smith, L. Diehl, and F. Capasso. Low-threshold continuous-wave operation of quantum-cascade lasers grown by metalorganic vapor phase epitaxy. *Appl. Phys. Lett.*, 85(24):5842–5844, 2004.

[61] M. Troccoli, S. Corzine, D. Bour, J. Zhu, O. Assayag, L. Diehl, B. Lee, G. Höfler, and F. Capasso. Room temperature continuous-wave operation of quantum-cascade lasers grown by metal organic vapour phase epitaxy. *IEE Elect. Lett.*, 41(19):1059–1060, 2005.

[62] O. Gauthier-Lafaye, P. Boucaud, F.H. Julien, S. Sauvage, S. Cabaret, J.M. Lourtioz, and R. Planel. Long-wavelength ($\approx$ 15.5μm) unipolar semiconductor laser in gaas quantum wells. *Appl. Phys. Lett.*, 71(25):3619–3621, 1997.

[63] G. Dehlinger, L. Diehl, U. Gennser, H. Sigg, J. Faist, K. Ensslin, D. Grützmacher, and E. Müller. Intersubband electroluminescence from silicon-based quantum cascade structures. *Science*, 290:2277–2280, 2000.

[64] S.A. Lynch, R. Bates, D.J. Paul, D.J. Norris, A.G. Cullis, Z. Ikonic, R.W. Kelsall, P. Harrison, D.D. Arnone, and C.R. Pigeon. Intersubband electroluminescence from si/sige cascade emitters at terahertz frequencies. *Appl. Phys. Lett.*, 81(9):1543–1545, 2002.

[65] J. Faist, F. Capasso, D.L. Sivco, A.L. Hutchinson, S.G. Chu, and A.Y. Cho. Short wavelength ($\lambda \sim 3.4$ μm) quantum cascade laser based on strained compensated ingaas/alinas. *Appl. Phys. Lett.*, 72(6):680–682, 1998.

[66] R. Colombelli, F. Capasso, C. Gmachl, A.L. Hutchinson, D.L. Sivco, A. Tredicucci, M.C. Wanke, A.M. Sergent, and A.Y. Cho. Far-infrared surface-plasmon quantum-cascade lasers at 21.5 μm and 24 μm wavelengths. *Appl. Phys. Lett.*, 78(18):2620–2622, 2001.

[67] J.S. Yu, S. Slivken, S.R. Darvish, and M. Razeghi. Short wavelength ($\lambda \sim 4.3\mu$m) high-performance continuous-wave quantum-cascade lasers. *IEEE Photon. Technol. Lett.*, 17(06):1154–1156, 2005.

[68] A. Evans, J.S. Yu, J. David, L. Doris, K. Mi, S. Slivken, and M. Razeghi. High-temperature, high-power, continuous-wave operation of buried heterostructure quantum-cascade lasers. *Appl. Phys. Lett.*, 84(03):314–316, 2004.

[69] T. Aellen, S. Blaser, M. Beck, D. Hofstetter, J. Faist, and E. Gini. Continuous-wave distributed-feedback quantum-cascade lasers on a peltier cooler. *Appl. Phys. Lett.*, 83(10):1929–1931, 2003.

[70] J.S. Yu, S. Slivken, S.R. Darvish, A. Evans, B. Gokden, and M. Razeghi. High-power, room-temperature, and continuous-wave operation of distributed-feedback quantum-cascade lasers at lambda ~ 4.8 $/mu$m. *Appl. Phys. Lett.*, 87:041104–1–041104–3, 2005.

[71] C. Gmachl, D.L. Sivco, R. Colombelli, F. Capasso, and A.Y. Cho. Ultra-broadband semiconductor laser. *Nature*, 415(6874):883–887, 2002.

[72] R. Maulini, M. Beck, J. Faist, and E. Gini. Broadband tuning of external cavity bound-to-continuum quantum-cascade lasers. *Appl. Phys. Lett.*, 84(10):1659–1661, 2004.

[73] N. Owschimikow, C. Gmachl, A. Belyanin, V. Kocharovsky, D.L. Sivco, R. Colombelli, F. Capasso, and A.Y. Cho. Resonant second-order nonlinear optical processes in quantum cascade lasers. *Phys. Rev. Lett.*, 90(4):043902–1–043902–4, 2003.

[74] J.Y. Bengloan, A.D. Rossi, V. Ortiz, X. Marcadet, M. Calligaro, I. Maurin, and C. Sirtori. Intracavity sum-frequency generation in gaas quantum cascade lasers. *Appl. Phys. Lett.*, 84(12):2019–2021, 2004.

[75] H. Willenberg, G.H. Döhler, and J. Faist. Intersubband gain in a bloch oscillator and quantum cascade laser. *Phys. Rev. B*, 67:085315–1–085315–10, 2003. in press.

[76] Q. Hu and S. Feng. Feasibility of far-infrared lasers using multiple semiconductor quantum wells. *Appl. Phys. Lett.*, 59(23):2923–2925, 1991.

[77] S.I. Borenstain and J. Katz. Evaluation of the feasibility of a far-infrared laser based on intersubband transitions in gaas quantum wells. *Appl. Phys. Lett.*, 55(7):654–656, 1989.

[78] B. Xu, Q. Hu, and M.R. Melloch. Electrically pumped tunable terahertz emitter based on intersubband transition. *Appl. Phys. Lett.*, 71(4):440–442, 1997.

[79] M. Rochat, J. Faist, M. Beck, U. Oesterle, and M. Ilegems. Far-infrared ($\lambda = 88$ μm) electroluminescence in a quantum cascade structure. *Appl. Phys. Lett.*, 73(25):3724–3726, 1998.

[80] J. Ulrich, R. Zobl, N. Finger, K. Unterrainer, G. Strasser, and E. Gornik. Terahertz-electroluminescence in a quantum cascade structure. *Physica B*, 272:216–218, 1999.

[81] J. Ulrich, R. Zobl, W. Schrenk, G. Strasser, K. Unterrainer, and E. Gornik. Terahertz quantum cascade structures: Intra- versus interwell transition. *Appl. Phys. Lett.*, 77(13):1928–1930, 2000.

[82] B.S. Williams, B. Xu, Q. Hu, and M.R. Melloch. Narrow-linewidth terahertz intersubband emission from three-level systems. *Appl. Phys. Lett.*, 75(19):2927–2929, 1999.

[83] J. Ulrich, R. Zobl, K. Unterrainer, G. Strasser, E. Gornik, K.D. Maranowski, and A.C. Gossard. Temperature dependence of far-infrared electroluminescence in parabolic quantum wells. *Appl. Phys. Lett.*, 74(21):3158–3160, 1999.

[84] M. Rochat, M. Beck, J. Faist, and U. Oesterle. Measurement of far-infrared waveguide loss using a multisection single-pass technique. *Appl. Phys. Lett.*, 78(14):1967–1969, 2001.

[85] R. Köhler, A. Tredicucci, F. Beltram, H.E. Beere, E.H. Linfield, A.G. Davies, D.A. Ritchie, R.C. Iotti, and F. Rossi. Terahertz semiconductor-heterostructure laser. *Nature*, 417:156–159, 2002.

[86] A. Tredicucci, C. Gmachl, F. Capasso, A.L. Hutchinson, D.L. Sivco, and A.Y. Cho. Single-mode surface-plasmon laser. *Appl. Phys. Lett.*, 76(16):2164–2166, 2000.

[87] C. Sirtori. Bridge for the terahertz gap. *Nature*, 417:132–133, 2002.

[88] M. Rochat, L. Ajili, H. Willenberg, J. Faist, H. Beere, G. Davies, E. Linfield, and D. Ritchie. Low-threshold terahertz quantum-cascade lasers. *Appl. Phys. Lett.*, 81(8):1381–1383, 2002.

[89] G. Scalari, L. Ajili, J. Faist, H. Beere, E. Linfield, D. Ritchie, and G. Davies. Far-infrared ($\lambda \simeq 87\mu$m) bound-to-continuum quantum-cascade lasers operating up to 90 k. *Appl. Phys. Lett.*, 82(19):3165–3167, 2003.

[90] B.S. Williams, H. Callebaut, S. Kumar, Q. Hu, and J.L. Reno. 3.4-thz quantum cascade laser based on longitudinal-optical-phonon scattering for depopulation. *Appl. Phys. Lett.*, 82(7):1015–1017, 2003.

[91] G. Scalari, S. Blaser, L. Ajili, J. Faist, H. Beere, E. Linfield, D. Ritchie, and G. Davies. Population inversion by resonant magnetic confinement in terahertz quantum-cascade lasers. *Appl. Phys. Lett.*, 83(17):3453–3455, 2003.

[92] R. Kohler, A. Tredicucci, C. Mauro, F. Beltram, H.E. Beere, E.H. Linfield, A.G. Davies, and D.A. Ritchie. Terahertz quantum-cascade lasers based on an interlaced photon-phonon cascade. *Appl. Phys. Lett.*, 84(8):1266–1268, 2004.

[93] G. Scalari, N. Hoyler, M. Giovannini, and J. Faist. Terahertz bound-to-continuum quanutm-cascade lasers based on optical-phonon scattering extraction. *Appl. Phys. Lett.*, 86:181101–1–181101–3, 2005.

[94] B.S. Williams, S. Kumar, H. Callebaut, Q. Hu, and J.L. Reno. Terahertz quantum-cascade laser at $\lambda \sim 100\mu$m using metal waveguide for mode confinement. *Appl. Phys. Lett.*, 83(11):2124–2126, 2003.

[95] K. Unterrainer, R. Colombelli, C. Gmachl, F. Capasso, H.Y. Hwang, A.M. Sergent, D.L. Sivco, and A.Y. Cho. Quantum cascade lasers with double metal-semiconductor waveguide resonators. *Appl. Phys. Lett.*, 80(17):3060–3062, 2002.

[96] B.S. Williams, S. Kumar, Q. Hu, and J.L. Reno. Operation of terahertz quantum-cascade lasers at 164 k in pulsed mode and at 117 k in continuous-wave mode. *Optics Express*, 13:3331–3339, 2005.

[97] J. Alton, S.S. Dhillon, C. Sirtori, A.d. Rossi, M. Calligaro, S. Barbieri, H. Beere, E.H. Linfield, and D.A. Ritchie. Buried waveguides in terahertz quantum cascade lasers based on two-dimensional surface plasmon modes. *Appl. Phys. Lett.*, 86:071109–1–071109–3, 2005.

[98] S. Dhillon, J. Alton, S. Barbieri, C. Sirtori, A.d. Rossi, M. Calligaro, H.E. Beere, and D. Ritchie. Ultralow threshold current terahertz quantum cascade lasers based on double-metal buried strip waveguides. *Appl. Phys. Lett.*, 87:071107–1–071107–3, 2005.

[99] S. Barbieri, J. Alton, H. Beere, J. Fowler, E. Linfield, and D. Ritchie. 2.9 thz quantum cascade lasers operating up 70 k in continuous wave. *Appl. Phys. Lett.*, 85(10):1674–1676, 2004.

[100] R. Colombelli, K. Srinivasan, M. Troccoli, O. Painter, C.F. Gmachl, D.M. Tennant, A.M. Sergent, D.L. Sivco, A.Y. Cho, and F. Capasso. Quantum cascade surface-emitting photonic crystal laser. *Science*, 302:1374–1377, 2003.

[101] A. Dunbar, V. Moreau, R. Ferrini, R. Houdr, L. Sirigu, G. Scalari, M. Giovannini, N. Hoyler, and J. Faist. Design, fabrication and optical characterisation of quantum cascade lasers at terahertz frequencies using photonic crystal reflectors. *Optics Express, in press*, 2005.

[102] L. Ajili, G. Scalari, N. Hoyler, M. Giovannini, and J. Faist. Ingaasalinas/inp terahertz quantum cascade laser. *Appl. Phys. Lett.*, 87:141107–1–141107–3, 2005.

[103] Y. Arakawa and H. Sakaki. Multidimensional quantum well laser and temperature dependence of its threshold current. *Appl. Phys. Lett.*, 40(11):939–941, 1982.

[104] Y. Arakawa, H. Sakaki, M. Nishioka, and N. Miura. Two-dimensional quantum-mechanical confinement of electrons in dh lasers by strong magnetic fields. *IEEE J. Quantum Electron.*, 19(8):1255–1257, 1983.

[105] E. Kapon, D.M. Hwang, and R. Bhat. Stimulated emission in semiconductor quantum wire heterostructures. *Phys. Rev. Lett.*, 63(4):430–433, 1989.

[106] N. Kirstaedter, N. Ledentsov, M. Grundmann, D. Bimberg, V. Ustinov, S. Ruvimov, M. Maximov, P. Kop'ev, Z. Alferov, U. Richte, P. Werner, U. Gösele, and J. Heydenreich. Low threshold, large t0 injection laser emission from (inga)as quantum dots. *IEE Elect. Lett.*, 30(17):1416–1417, 1994.

[107] H.Y. Liu, D.T. Childs, T.J. Badcock, K.M. Groom, I.R. Sellers, M. Hopkinson, R.A. Hogg, D.J. Robbins, D.J. Mowbray, and M.S. Skolnick. High-performance three-layer 1.3 μm inasgaas quantum-dot lasers with very low continuous-wave room-temperature threshold currents. *IEEE Photon. Technol. Lett.*, 10(06):1139–1141, 2005.

[108] H. Benisty, C.M. Sotomayor-Torres, and C. Weisbuch. Intrinsic mechanism for the poor luminescence properties of quantum-box systems. *Phys. Rev. B*, 44(19):10945–10948, 1991.

[109] H. Aoki. Novel landau level laser in the quantum hall regime. *Appl. Phys. Lett.*, 48(9):559–560, 1986.

[110] A. Kastalsky and A.L. Efros. Magnetic field-induced suppression of acoustic phonon emission in a superlattice. *J. Appl. Phys.*, 69(2):841–845, 1991.

[111] A. Blank and S. Feng. Suppression of intersubband nonradiative transitions by magnetic field in quantum well laser devices. *J. Appl. Phys.*, 74(7):4795–4797, 1993.

[112] V.M. Apalkov and T. Chakraborty. Influence of dimensionality on the emission spectra of nanostructures. *Appl. Phys. Lett.*, 83(18):3671–3673, 2003.

[113] I. Keck, S. Schmult, W. Wegscheider, M. Rother, and A.P. Mayer. Quantum wire intersubband emitter. *Phys. Rev. B*, 67:125312–1–125312–8, 2003.

[114] S. Schmult, I. Keck, T. Herrle, W. Wegscheider, M. Bichler, D. Schuh, and G. Abstreiter. Field-effect-induced midinfrared electroluminescence of a quantum-wire-cascade structure by remote δ-doping. *Appl. Phys. Lett.*, 83(10):1909–1911, 2003.

[115] C. Hsu, J. O, P. Zory, and D. Botez. Intersubband quantum-box semiconductor lasers. *IEEE J. Select. Topics Quantum Electron.*, 6(3):491–503, 2000.

[116] N.S. Wingreen and C.A. Stafford. Quantum-dot cascade laser: proposal for an ultralow-threshold semiconductor laser. *IEEE J. Quantum Electron.*, 33(07):1170–1173, 1997.

[117] I.A. Dmitriev and R.A. Suris. Quantum cascade lasers based on quantum dot superlattice. *phys. stat. sol.*, 202(6):987–991, 2005.

[118] S. Anders, L. Rebohle, F.F. Schrey, W. Schrenk, K. Unterrainer, and G. Strasser. Electroluminescence of a quantum dot cascade structure. *Appl. Phys. Lett.*, 82(22):3862–3864, 2003.

[119] N. Ulbrich, J. Bauer, G. Scarpa, R. Boy, D. Schuh, G. Abstreiter, S. Schmult, and W. Wegscheider. Midinfrared intraband electroluminescence from alinas quantum dots. *Appl. Phys. Lett.*, 83(08):1530–1532, 2003.

[120] C. Becker, C. Sirtori, O. Drachenko, V. Rylkov, D. Smirnov, and J. Leotin. Gaas quantum box cascade lasers. *Appl. Phys. Lett.*, 81(16):2941–2943, 2002.

[121] J. Ulrich, R. Zobl, K. Unterrainer, G. Strasser, and E. Gornik. Magnetic-field-enhanced quantum-cascade emission. *Appl. Phys. Lett.*, 76(1):19–21, 2000.

[122] S. Blaser, M. Rochat, M. Beck, D. Hofstetter, and J. Faist. Terahertz intersubband emission in strong magnetic fields. *Appl. Phys. Lett.*, 81(1):67–69, 2002.

[123] C. Sirtori, F. Capasso, J. Faist, and S. Scandolo. Nonparabolicity and a sum rule associated with bound-to-bound and bound-to-continuum intersubband transitions in quantum wells. *Phys. Rev. B*, 50(12):8663–8674, 1994.

[124] R. Köhler, A. Tredicucci, F. Beltram, H.E. Beere, E.H. Linfield, A.G. Davies, and D.A. Ritchie. High-intensity interminiband terahertz emission from chirped superlattices. *Appl. Phys. Lett.*, 80(11):1867–1869, 2002.

[125] J. Faist, F. Capasso, L. Pfeiffer, and K.W. West. Phonon limited intersubband lifetimes and linewidths in a two-dimensional electron gas. *Appl. Phys. Lett.*, 64(7):872–874, 1994.

[126] K.L. Campman, H. Schmidt, A. Imamoglu, and A.C. Gossard. Interface roughness and alloy-disorder scattering contributions to intersubband transition linewidths. *Appl. Phys. Lett.*, 69(17):2554–2556, 1996.

[127] R. Ferreira and G. Bastard. Evaluation of some scattering times for electrons in unbiased and biased single-and multiple-quantum-well structures. *Phys. Rev. B*, 40(2):1074–1086, 1989.

[128] J.H. Smet, C.G. Fonstad, and Q. Hu. Intrawell and interwell intersubband transitions in multiple quantum wells for far-infrared sources. *J. Appl. Phys.*, 79(12):9305–9320, 1996.

[129] M. Hartig, J.D. Ganière, P.E. Selbmann, B. Deveaud, and L. Rota. Density dependence of carrier-carrier-induced intersubband scattering in gaas/alxga1-xas quantum wells. *Phys. Rev. B*, 60(3):1500–1503, 1999.

[130] P. Hyldgaard and J.W. Wilkins. Electron-electron scattering in far-infrared quantum cascade lasers. *Phys. Rev. B*, 53(11):6889–6892, 1996.

[131] M. Rochat, M. Beck, J. Faist, U. Oesterle, and M. Ilegems. Electrically pumped terahertz quantum well sources. *Physica E*, 7(1-2):44–47, 2000.

[132] H. Callebaut, S. Kumar, B.S. Williams, Q. Hu, and J.L. Reno. Analysis of transport properties of terahertz quantum cascade lasers. *Appl. Phys. Lett.*, 83(02):207–209, 2003.

[133] H. Callebaut, S. Kumar, B.S. Williams, Q. Hu, and J.L. Reno. Importance of electron-impurity scattering for electron transport in terahertz quantum-cascade lasers. *Appl. Phys. Lett.*, 84(05):645–647, 2004.

[134] R.F. Kazarinov and R.A. Suris. Electric and electromagnetic properties of semiconductors with a superlattice. *Sov. Phys. Semicond.*, 6(1):120–131, 1972.

[135] C. Sirtori, F. Capasso, J. Faist, A.L. Hutchinson, D.L. Sivco, and A.Y. Cho. Resonant tunneling in quantum cascade lasers. *IEEE J. Quantum Electron.*, 34(9):1722–1729, 1998.

[136] T. Heinzel. *Mesoscopic electronics in solid state nanostructures*. Wiley-VCH GmbH, Weinheim, DE, 2003.

[137] D.K. Ferry and S.M. Goodnick. *Transport in nanostructures*. Cambridge University Press, Cambridge, UK, 1997.

[138] T. Ando, A.B. Fowler, and F. Stern. Electronic properties of two-dimensional systems. *Rev. Mod. Phys.*, 54(2):437–446, 1982.

[139] J.P. Eisenstein, H.L. Stormer, V. Narayanamurti, A.Y. Cho, A.C. Gossard, and C.W. Tu. Density of states and de haas-van alphen effect in two-dimensional electron systems. *Phys. Rev. Lett.*, 55(08):875–878, 1985.

[140] K.v. Klitzing, G. Dorda, and M. Pepper. New method for high-accuracy determination of the fine-structure constant based on quantized hall resistance. *Phys. Rev. Lett.*, 45(6):494–497, 1980.

[141] R. Willett, J.P. Eisenstein, H.L. Stormer, D.C. Tsui, A.C. Gossard, and J.H. English. Observation of an even-denominator quantum number in the fractional quantum hall effect. *Phys. Rev. Lett.*, 59(15):1776–1779, 1987.

[142] R. Dingle, H.L. Störmer, A.C. Gossard, and W. Wiegmann. Electron mobilities in modulation-doped semiconductor heterojunction superlattices. *Appl. Phys. Lett.*, 33(7):665–667, 1978.

[143] A.L. Efros. Density of states of 2d electron gas and width of the plateau of iqhe. *Solid State Commun.*, 65(11):1281–1284, 1988.

[144] V.J. Goldman, M. Santos, M. Shayegan, and J.E. Cunningham. Evidence for 2-dimensional quantum wigner crystal. *Phys. Rev. Lett.*, 65(17):2189–2192, 1990.

[145] N.B. Zhitenev, T.A. Fulton, A. Yacoby, H.F. Hess, L.N. Pfeiffer, and K.W. West. Imaging of localized electronic states in the quantum hall regime. *Nature*, 404:473–476, 2000.

[146] S. Ilani, J. Martin, E. Teitelbaum, J.H. Smith, D. Mahalu, V. Umansky, and A. Yacoby. The microscopic nature of localization in the quantum hall effect. *Nature*, 427:328–332, 2004.

[147] J.H. Smet, C.G. Fonstad, and Q. Hu. Magnetotunneling spectroscopy in wide $in_{0.53}ga_{0.47}as$ / $in_{0.52}al_{0.48}as$ double quantum wells. *Appl. Phys. Lett.*, 63(16):2225–2227, 1993.

[148] P.D. Buckle, J.W. Cockburn, M.S. Skolnick, R. Grey, G. Hill, and M.A. Pate. Magnetic-field-induced modulation of intersubband scattering in a double-barrier resonant-tunneling structure. *Phys. Rev. B*, 53(20):13651–13655, 1996.

[149] D. Smirnov, O. Drachenko, J. Leotin, H. Page, C. Becker, C. Sirtori, V. Apalkov, and T. Chakraborty. Intersubband magnetophonon resonances in quantum cascade structures. *Phys. Rev. B*, 66:125317–1–125317–4, 2002.

[150] D. Smirnov, C. Becker, O. Drachenko, V.V. Rylkov, H. Page, J. Leotin, and C. Sirtori. Control of electron-optical phonon scattering rates in quantum box cascade lasers. *Phys. Rev. B*, 66:121305–1–121305–4, 2002.

[151] C. Becker, A. Vasanelli, C. Sirtori, and G. Bastard. Electron-longitudinal optical phonon interaction between landau levels in semiconductor heterostructures. *Phys. Rev. B*, 69:115328–1– 115328–6, 2004.

[152] R. Ferreira. Resonances in the hopping probability between flexible quantum dots: the case of superlattices under parallel electric and magnetic field. *Phys. Rev. B*, 43(11):9336–9338, 1991.

[153] L. Canali, M. Lazzarino, L. Sorba, and F. Beltram. Stark-cyclotron resonance in a semiconductor superlattice. *Phys. Rev. Lett.*, 76(19):3618–3621, 1996.

[154] S. Blaser, M. Rochat, M. Beck, J. Faist, and U. Oesterle. Far-infrared emission and stark-cyclotron resonances in a quantum cascade structure based on photon-assisted tunneling transition. *Phys. Rev. B*, 61(12):8369–8374, 2000.

[155] M.E. Raikh and T.V. Shabazyan. Magnetointersubband oscillations of conductivity in a two-dimensional electronic system. *Phys. Rev. B*, 49(8):5531–5540, 1994.

[156] G. Scalari, S. Blaser, J. Faist, H. Beere, E. Linfield, D. Ritchie, and G. Davies. Terahertz emission from quantum cascade lasers in the quantum hall regime: evidence for many body resonances and localization effects. *Phys. Rev. Lett.*, 93:237403–1–237403–4, 2004.

[157] S. Blaser, M. Rochat, L. Ajili, M. Beck, J. Faist, H.E. Beere, A.G. Davies, E.H. Linfield, and D.A. Ritchie. Terahertz interminiband emission and magneto-transport measurements from a quantum cascade chirped superlattice. *Physica E*, 13(2-4):854–857, 2002.

[158] J. Alton, S. Barbieri, J. Fowler, H.E. Beere, J. Muscat, E.H. Linfield, D.A. Ritchie, G. Davies, R. Köhler, and A. Tredicucci. Magnetic field in-plane quantization and tuning of population inversion in a thz superlattice quantum cascade laser. *Phys. Rev. B*, 68:081303–1–081303–4, 2003.

[159] K. Kempa, P. Bakshi, J. Engelbrecht, and Y. Zhou. Intersubband electron transitions due to electron-electron interactions in quantum-well structures. *Phys. Rev. B*, 61(16):11083–11087, 2000.

[160] K. Kempa, Y. Zhou, J. Engelbrecht, and P. Bakshi. Electron-electron scattering in strong magnetic fields in quantum well systems. *Phys. Rev. B*, 68:085302–1–085302–5, 2003.

[161] K. Kempa, Y. Zhou, J.R. Engelbrecht, P. Bakshi, H.I. Ha, J. Moser, M.J. Naughton, J. Ulrich, G. Strasser, E. Gornik, and K. Unterrainer. Intersubband transport in quantum wells in strong magnetic fields mediated by single- and two-electron scattering. *Phys. Rev. Lett.*, 88(22):226803–1–226803–4, 2002.

[162] J.J. Sakurai. *Modern quantum mechanics*. Addison Wesley, Boston, MA, 2^{rd} edition, 1994.

[163] A. Tredicucci. Marriage of two device concepts. *Science*, 302:1346–1347, 2003.

[164] E. Gornik. Landau emission. In G. Landwehr and E. I. Rashba, editors, *Landau level spectroscopy*, chapter 16, pages 911–996. Elsevier Science, New-York, 1991.

[165] E. Gornik. Recombination radiation from impact-ionized shallow donors in n-type insb. *Phys. Rev. Lett.*, 29(9):595–597, 1972.

[166] N.W. Ashcroft and N.D. Mermin. *Solid state physics*. Harcourt Brace College Publishers, Fort Worth, 1976.

[167] D.C. Larrabee, G.A. Khodaparast, F.K. Tittel, J. Kono, G. Scalari, L. Ajili, J. Faist, H. Beere, G. Davies, E. Linfield, D. Ritchie, Y. Nakajima, M. Nakai, and S. Sasa. Application of terahertz quantum-cascade lasers to semiconductor cyclotron resonance. *Opt. Lett.*, 29(01):122–124, 2004.

[168] S. Blaser. *Quantum cascade structures based on photon-assisted tunneling transitions in strong magnetic fields*. PhD thesis, Université de Neuchâtel, 2002.

[169] M. Rochat. *Far-infrared emission in quantum cascade structures*. PhD thesis, Université de Neuchâtel, 2002. unpublished.

[170] T. Ikegami. Reflectivity of mode at facet and oscillation mode in double-heterostructure injection lasers. *IEEE J. Quantum Electron.*, 8(6):470–476, 1972.

[171] S. Kohen, B. Williams, and Q. Hu. Electromagnetic modeling of terahertz quantum cascade laser waveguides and resonators. *J. Appl. Phys.*, 97:053106–1–053106–9, 2005.

[172] S. Barbieri, J. Alton, S.S. Dhillon, H.E. Beere, M. Evans, E.H. Linfield, A.G. Davies, D.A. Ritchie, R. Köhler, A. Tredicucci, and F. Beltram. Continuous-wave operation of terahertz quantum-cascade lasers. *IEEE J. Quantum Electron.*, 39(4):586–591, 2003.

[173] L. Ajili, G. Scalari, J. Faist, H. Beere, E. Linfield, D. Ritchie, and G. Davies. High power quantum-cascade lasers operating at $\lambda \sim 87$ and 130 μm. *Appl. Phys. Lett.*, 85(18):3986–3988, 2004.

[174] J.I. Pankove. *Optical processes in semiconductors.* Dover Publications, Inc., New York, US, 1971.

[175] R. Colombelli, F. Capasso, C. Gmachl, A. Tredicucci, A.M. Sergent, A.L. Hutchinson, D.L. Sivco, and A.Y. Cho. Intersubband electroluminescence from long-side-cleaved quantum-cascade lasers above threshold: Investigation of phonon bottleneck effects. *Appl. Phys. Lett.*, 77(24):3893–3895, 2000.

[176] A. Bonvalet, J. Nagle, V. Berger, A. Migus, J. Martin, and M. Joffre. Femtosecond infrared emission resulting from coherent charge oscillations in quantum wells. *Phys. Rev. Lett.*, 76(23):4392–4395, 1996.

[177] J.R. Gao, J.N. Hovenier, Z.Q. Yang, J.J. Baselmans, A. Baryshev, M. Hajenius, T.M. Klapwijk, A.J. Adam, T.O. Klaassen, B.S. Williams, S. Kumar, Q. Hu, and J.L. Reno. Terahertz heterodyne receiver based on a quantum cascade laser and a superconducting bolometer. *Appl. Phys. Lett.*, 86:244104–1–244104–3, 2005.

[178] L. Ajili, G. Scalari, D. Hofstetter, M. Beck, J. Faist, H. Beere, G. Davies, E. Linfield, and D. Ritchie. Continuous-wave operation of far-infrared quantum cascade lasers. *IEE Elect. Lett.*, 38(25):1675–1676, 2002.

[179] R. Köhler, A. Tredicucci, F. Beltram, H.E. Beere, E.H. Linfield, A.G. Davies, D.A. Ritchie, S.S. Dhillon, and C. Sirtori. High-performance continuous-wave operation of superlattice terahertz quantum-cascade lasers. *Appl. Phys. Lett.*, 82(10):1518–1520, 2003.

[180] M. Rochat, D. Hofstetter, M. Beck, and J. Faist. Long-wavelength ($\lambda \sim 16\mu$m), room-temperature, single-frequency quantum-cascade lasers based on a bound-to-continuum transition. *Appl. Phys. Lett.*, 79(26):4271–4273, 2001.

[181] J. Faist, D. Hofstetter, M. Beck, T. Aellen, M. Rochat, and S. Blaser. Bound-to-continuum and two-phonon resonance quantum cascade lasers for high duty cycle, high temperature operation. *IEEE J. Quantum Electron.*, 38(6):533–546, 2002.

[182] E.D. Palik. Gallium arsenide (gaas). In Edward D. Palik, editor, *Handbook of optical constants of solids*, pages 429–443. Academic Press, Inc., Orlando, Florida, 1985.

[183] S. Blaser, L. Diehl, M. Beck, J. Faist, U. Oesterle, J. Xu, S. Barbieri, and F. Beltram. Characterization and modeling of quantum cascade lasers based on photon-assisted tunneling transition. *IEEE J. Quantum Electron.*, 37(3):448–455, 2001.

[184] B.S. Williams, S. Kumar, H. Callebaut, Q. Hu, and J.L. Reno. Terahertz quantum-cascade laser operating up to 137k. *Appl. Phys. Lett.*, 83(25):5142–5144, 2003.

[185] S. Kumar, B.S. Williams, S. Kohen, Q. Hu, and J.L. Reno. Continuous-wave operation of terahertz quantum-cascade lasers above liquid-nitrogen temperature. *Appl. Phys. Lett.*, 84(14):2494–2496, 2004.

[186] L. Ajili, G. Scalari, N. Hoyler, M. Giovannini, and J. Faist. *unpublished*, 2005.

[187] D. Indjin, P. Harrison, R.W. Kelsall, and Z. Ikonic. Mechanisms of temperature performance degradation in terahertz quantum-cascade lasers. *Appl. Phys. Lett.*, 82(9):1347–1349, 2003.

[188] M. Vitiello, G. Scamarcio, V. Spagnolo, B. Williams, S. Kumar, Q. Hu, and J. Reno. Measurement of subband electronic temperatures and population inversion in thz quantum-cascade lasers. *Appl. Phys. Lett.*, 86:111115–1–111115 –3, 2005.

[189] C. Sirtori, A. Tredicucci, F. Capasso, J. Faist, D.L. Sivco, A.L. Hutchinson, and A.Y. Cho. Dual-wavelength emission from optically cascaded intersubband transitions. *Opt. Lett.*, 23(6):463–465, 1998.

[190] G. Scalari, S. Blaser, M. Rochat, L. Ajili, H. Willenberg, D. Hofstetter, J. Faist, H. Beere, A. Davies, E. Linfield, and D. Ritchie. Low threshold thz qc lasers in strong magnetic field. In *Proceeding of the 26th International Conference on the Physics of Semiconductors*, pages CD–, 2002.

[191] V. Tamosiunas, R. Zobl, J. Ulrich, K. Unterrainer, R. Colombelli, C. Gmachl, K. West, L. Pfeiffer, and F. Capasso. Terahertz quantum cascade lasers in a magnetic field. *Appl. Phys. Lett.*, 83(19):3873–3875, 2003.

[192] G.S. Boebinger, A.F. Levi, S. Schmitt-Rink, A. Passner, L.N. Pfeiffer, and K.W. West. Direct observation of two-dimensional magnetopolarons in a resonant tunnel junction. *Phys. Rev. Lett.*, 65(2):235–238, 1990.

[193] V.M. Gvozdikov and R. Vega-Monroy. Electromagnetic waves in layered conductors and superlattices in a magnetic field. *Low Temp. Phys.*, 25(10):802–809, 1999.

[194] E.D. Palik. *Handbook of optical constants of solids.* Academic Press, Inc., Orlando, Florida, 1985.

[195] M.V. Kisin, M.A. Stroscio, G. Belenky, and S. Luryi. Electron-plasmon relaxation in quantum wells with inverted dubband occupation. *Appl. Phys. Lett.*, 73(15):2075–2077, 1998.

[196] H.C. Liu and A.J. SpringThorpe. Optically pumped intersubband laser: Resonance positions and many-body effects. *Phys. Rev. B*, 61(23):15629–15632, 2000.

[197] U. Ekenberg. Nonparabolicity effects in a quantum well: Sublevel shift, parallel mass, and landau levels. *Phys. Rev. B*, 40(11):7714–7726, 1989.

[198] A. Patané, N. Mori, D. Fowler, L. Eaves, M. Henini, D.K. Maude, C. Hamaguchi, and R. Airey. Magnetic-field-induced suppression of electronic conduction in a superlattice. *Phys. Rev. Lett.*, 93(14):146801–1–146801–4, 2004.

[199] M. Lee, N.S. Wingreen, S.A. Solin, and P.A. Wolff. Giant growth axis longitudinal magnetoresistance form in-plane conduction in semiconductor superlattices. *Solid State Commun.*, 89(8):687–691, 1994.

[200] I. Protsenko, P. Domokos, V. Lefevre-Seguin, J. Hare, J. J.M.Raimond, and L. Davidovich. Quantum theory of a thresholdless laser. *Phys. Rev. A*, 59(2):1667–1682, 1999.

[201] J. Heynman, K. Unterrainer, K. Craig, B. Galdrikian, M. Sherwin, K. Campman, P. Hopkins, and A. Gossard. Temperature and intensity dependence of intersubband relaxation rates from photovoltage and absorption. *Phys. Rev. Lett.*, 74(14):2682–2685, 1995.

[202] J. Devreese. *Polarons in ionic crystals and polar semiconductors.* North Holland publishing company, Amsterdam, Netherlands, 1972.

[203] Y.J. Wang, Y.A. Leem, B.D. McCombe, X.G. Wu, F.M. Peeters, E.D. Jones, J.R. Reno, X.Y. Lee, and H.W. Jiang. Strong three-level resonant magnetopolaron effect due to the intersubband coupling in heavily modulation-doped gaas/al$_x$ga$_{1-x}$as single quantum wells at high magnetic field. *Phys. Rev. B*, 64(16):161303–1–161303–4, 2001.

[204] H. Kosaka, A. Kiselev, F. Baron, K. Kim, and E. Yablonovitch. Electron g factor engineering in iii-v semiconductors for quantum communications. *IEE Elect. Lett.*, 37(7):464–465, 2001.

[205] C. Weisbuch and C. Hermann. Optical detection of conduction-electron spin resonance in gaas, ga$_{1-x}$in$_x$as, and ga$_{1-x}$al$_x$as. *Phys. Rev. B*, 15(2):816–822, 1977.

[206] C.P. Slichter. *Principles of magnetic resonance.* Springer-Verlag, Berlin, Ge, 1978.

[207] R. Meisels. Electron spin resonance and related phenomena of low-dimensional electronic systems in iiiv compounds. *Semicond. Sci. Technol.*, 20(1):R1–R18, 2005.

[208] R.A. Isaacson. Electron spin resonance in n-type insb. *Phys. Rev.*, 169(2):312–314, 1968.

[209] M. Graf, G. Scalari, D. Hofstetter, J. Faist, H. Beere, E. Linfield, D. Ritchie, and G. Davies. Terahertz range quantum well infrared photodetector. *Appl. Phys. Lett.*, 84(4):475–477, 2004.

[210] M.A. Hopkins, R.J. Nicholas, D.J. Barnes, M.A. Brummell, J.J. Harris, and C.T. Foxon. Temperature dependence of the cyclotron-resonance linewidth in gaas-ga1-xalxas heterojunctions. *Phys. Rev. B*, 39(18):13302–13309, 1989.

Index

Published work

1. G. Scalari, C. Walther, J. Faist, H. Beere and D. Ritchie **Electrically switchable, two-color quantum cascade laser emitting at 1.39 and 2.3 THz**, *Appl. Phys. Lett.*, vol. 88, pp. 141102–1–141102–3 (2006).
2. S. Kim and F. Hatami and J. Harris and A. Kurian and J. Ford and D. King and G. Scalari and M. Giovannini and N. Hoyler and J. Faist and G. Harris, C. Walther, **Biomedical terahertz imaging with a quantum cascade laser**, *Appl. Phys. Lett.*, vol. 88, pp. 153903–1–153903–2 (2006).
3. E. Bründermann, M. Havenith, G. Scalari, M. Giovannini, J. Faist, J. Kunsch, L. Mechold, M. Abraham , **Turn-key compact high temperature terahertz quantum cascade lasers: imaging and room temperature detection**, *Optics Express*, vol. 14, pp. 1829–1841 (2006).
4. L. A. Dunbar, V. Moreau, R. Ferrini, R. Houdré, L. Sirigu, G. Scalari, N. Hoyler, M. Giovannini, and J. Faist, **Design, fabrication and optical characterization of quantum cascade lasers at terahertz frequencies using photonic crystal reflectors**, *Optics Express*, vol. 13, pp. 8960–8968 (2005).
5. L.Ajili, G. Scalari, N. Hoyler, M. Giovannini, and J. Faist, **An InGaAs-AlInAs/InP Terahertz Quantum Cascade Laser**, *Appl. Phys. Lett.*, vol. 87, pp. 141107–1–141107–3 (2005).
6. H. Beere, J. Fowler, J. Alton, E. Linfield, D. Ritchie, R. Kohler, A. Tredicucci, G. Scalari, L. Ajili, J. Faist, and S. Barbieri, **MBE growth of terahertz quantum cascade lasers**, *J. Cryst. Growth*, vol. 278, pp. 756–764 (2005).
7. G. Scalari, N. Hoyler, M. Giovannini, and J. Faist, **Terahertz bound-to-continuum quanutm-cascade lasers based on optical-phonon scattering extraction**, *Appl. Phys. Lett.*, vol. 86, pp. 181101–1–181101–3 (2005).
8. D. Chamberlin, P. Robrish, W. Trutna, G. Scalari, M. Giovannini, L. Ajili, and J. Faist, **Imaging at 3.4 THz with a quantum-cascade laser**, *Appl. Opt.*, vol. 44, no. 1, pp. 121–125 (2005).
9. J. Faist, L. Ajili, G. Scalari, M. Giovannini, M. Beck, M. Rochat, H. Beere, G. Davies, E. Linfield, and D. Ritchie, **Terahertz quantum cascade lasers**, *Philos. T. Roy. Soc. A*, vol. 362, no. 1815, pp. 215–229 (2004).

10. G. Scalari, S. Blaser, J. Faist, H. Beere, E. Linfield, D. Ritchie, and G. Davies, **Terahertz emission from quantum cascade lasers in the quantum Hall regime: evidence for many body resonances and localization effects**, *Phys. Rev. Lett.*, vol. 93, pp. 237403–1–237403–4 (2004).

11. L. Ajili, G. Scalari, J. Faist, H. Beere, E. Linfield, D. Ritchie, and G. Davies, **High power quantum-cascade lasers operating at $\lambda \sim$ 87 and 130 μm**, *Appl. Phys. Lett.*, vol. 85, no. 18, pp. 3986–3988 (2004).

12. S. Barbieri, J. Alton, H. Beere, E. Linfield, D. Ritchie, S. Whithington, G. Scalari, L. L.Ajili, and J. Faist, **Heterodyne mixing of two far-infrared quantum cascade lasers by use of a point-contact Schotky diode**, *Opt. Lett.*, vol. 29, no. 14, pp. 1632–1634 (2004).

13. A. Barkan, F.K. Tittel, D.M. Mittelman, R. Dengler, P.H. Siegel, G. Scalari, L. Ajili, J. Faist, H.E. Beere, E.H. Linfield, A. Davies, and D.A. Ritchie, **Linewidth and tuning characteristics of terahertz quantum cascade lasers**, *Opt. Lett.*, vol. 29, no. 6, pp. 575–577 (2004).

14. L. Lenci, D. Bertolini, D. Friselli, M. Martinelli, and G. Scalari, **Magnetic resonance force microscopy: nonlinear processes and influence of relaxation times**, *Phys. Rev. B*, vol. 69, pp. 094426–1–094426–8 (2004).

15. M. Graf, G. Scalari, D. Hofstetter, J. Faist, H. Beere, E. Linfield, D. Ritchie, and G. Davies, **Terahertz range quantum well infrared photodetector**, *Appl. Phys. Lett.*, vol. 84, no. 4, pp. 475–477 (2004).

16. D.C. Larrabee, G.A. Khodaparast, F.K. Tittel, J. Kono, G. Scalari, L. Ajili, J. Faist, H. Beere, G. Davies, E. Linfield, D. Ritchie, Y. Nakajima, M. Nakai, and S. Sasa, **Application of terahertz quantum-cascade lasers to semiconductor cyclotron resonance**, *Opt. Lett.*, vol. 29, no. 01, pp. 122–124 (2004).

17. G. Scalari, S. Blaser, L. Ajili, J. Faist, H. Beere, E. Linfield, D. Ritchie, and G. Davies, **Population inversion by resonant magnetic confinement in terahertz quantum-cascade lasers**, *Appl. Phys. Lett.*, vol. 83, no. 17, pp. 3453–3455 (2003).

18. G. Scalari, L. Ajili, J. Faist, H. Beere, E. Linfield, D. Ritchie, and G. Davies, **Far-infrared ($\lambda \simeq 87\mu$m) bound-to-continuum quantum-cascade lasers operating up to 90 K**, *Appl. Phys. Lett.*, vol. 82, no. 19, pp. 3165–3167 (2003).

19. L. Ajili, G. Scalari, D. Hofstetter, M. Beck, J. Faist, H. Beere, G. Davies, E. Linfield, and D. Ritchie, **Continuous-wave operation of far-infrared quantum cascade lasers**, *IEE Elect. Lett.*, vol. 38, no. 25, pp. 1675–1676 (2002).

20. A. Menciassi, G. Scalari, A. Eisinberg, C. Anticoli, P. Francabandiera, M. Carrozza, and P. Dario, **An instrumented probe for mechanical characterization of soft tissues**, *Biomed. Microdev.*, vol. 3, no. 2, pp. 149–156 (2001).

21. G. Alzetta, C. Ascoli, P. Baschieri, I. Betti, B.D. Masi, L. Lenci, M. Martinelli, and G. Scalari, **Simultaneous micromechanical and electromagnetic detection of electron paramagnetic resonance**, *J. Mag. Res.*, vol. 141, no. 1, pp. 148–158 (1999).